

Surface-confined and Bulk Reactions of Alkynes

Zur Erlangung des akademischen Grades eines

DOKTORS DER NATURWISSENSCHAFTEN

(Dr. rer. nat.)

von der KIT-Fakultät für Chemie und Biowissenschaften

des Karlsruher Instituts für Technologie (KIT)

genehmigte

DISSERTATION

von

M.Sc. Zhi Chen

aus

Hunan, China

KIT-Dekan: Prof. Dr. Willem M. Klopper

Referent: Prof. Dr. Mario Ruben

Korreferent: Prof. Dr. Johannes V. Barth

Tag der mündlichen Prüfung: 10.02.2017

Die vorliegende Arbeit wurde in Zeitraum vom 2012 bis zum 2016 am Institut für Nanotechnologie am Karlsruher Institut für Technologie (KIT) in der Arbeitsgruppe von Prof. Dr. Mario Ruben angefertigt.

Hiermit erkläre ich, die vorliegende Arbeit selbstständig und nur unter Verwendung der angegebenen Quellen angefertigt zu haben. Zitate und Inhalte aus anderen Arbeiten wurden als solche kenntlich gemacht.

Karlsruhe, den 22.12.2016

Zhi Chen

Table of Contents

Abstract	1
Zusammenfassung	4
1. Introduction	8
1.1 Alkyne and its derivatives	8
1.2 Graphdiyne	14
1.3 On-surface assembly and reactions	24
1.4 Mechanically controllable break junctions	35
1.5 Lithium batteries and organic batteries	47
2. Aim of the thesis	55
3. Alkyne derivatives for on-surface assembly and reactions	56
3.1 Synthesis of graphdiyne wires by surface templating	56
3.2 Polymerization of alkyne and enyne containing compounds on metal surfaces	64
3.3 Alkynenitriles as ligand for surface 2D coordination network	76
4. Synthesis of graphdiyne at the liquid-solid interface	83
5. Alkyne derivatives for molecular junction applications	93
6. Alkyne substituted porphyrins for battery applications	103
7. Experimental part	127
7.1 Materials and equipment	127
7.2 Syntheses of the compounds	129
4,4''-diethynyl-1,1':4',1''-terphenyl (1)	129
4-(but-3-en-1-ynyl)-4'-ethynyl-1,1'-biphenyl (2)	132
3,3'-([1,1':4',1''-terphenyl]-4,4''-diyl)dipropiolonitrile (3)	133
3-([1,1':4',1''-terphenyl]-4-yl)propiolonitrile (4)	134
hexakis[4-(ethynyl)phenyl]benzene (5)	135
Graphdiyne 6	136
1,4-diethynylbenzene (7)	137
4,4'-diethynyl-1,1'-biphenyl (8)	138
4,4'''-diethynyl-1,1':4',1''':4'',1'''-quaterphenyl (9)	139

[5,15-bis(ethynyl)-10,20-diphenylporphinato]copper(II) (10)	141
7.3 Crystal structures.....	142
3,3'-([1,1':4',1''-terphenyl]-4,4''-diyl)dipropiolonitrile (3)	143
3-([1,1':4',1''-terphenyl]-4-yl)propiolonitrile (4)	144
5,15-bis(trimethylsilanylethynyl)-10,20-diphenyl-21 <i>H</i> ,23 <i>H</i> -porphyrin (10a).....	145
[5,15-bis(trimethylsilylethynyl)-10,20-diphenylporphinato]copper(II) (10b)	148
[5,15-bis(ethynyl)-10,20-diphenylporphinato]copper(II) (10)	150
8. Summary	152
9. References	154
10. Appendix	168
10.1 Abbreviations	168
10.2 Publications	171
11. Acknowledgements.....	172

Abstract

Alkyne compounds containing at least one carbon-carbon triple bond have attracted much interest as extremely valuable building blocks in organic synthesis and material science. In this thesis, five series of novel alkyne derivatives were designed and synthesized and their applications such as on-surface assembly and reactions, molecular junctions and batteries were explored.

Firstly, a series of diethynyl-oligophenyls was designed and synthesized, and the on-surface homo-coupling reaction of compound 4,4''-diethynyl-1,1':4',1''-terphenyl was investigated. On the flat Ag(111) surface the thermal activation of 4,4''-diethynyl-1,1':4',1''-terphenyl triggered a variety of side-reactions resulting in irregularly branched polymeric networks. To improve the chemoselectivity of the linking process, the templating approach with the vicinal surface Ag(877) was used, where the 4,4''-diethynyl-1,1':4',1''-terphenyl molecules aligned along the step-edges of the Ag(877) surface. After annealing at 400 K, 1D extended graphdiyne (GDY) wires with lengths reaching 30 nm were obtained. The first characterization of its electronic properties by means of DFT calculations qualified the new material as a 1D semiconductor with a presumably simple band structure.

The single-molecule conductance of this series of compounds was also determined by using the mechanically controllable break junction (MCBJ) technique. The molecules bind to the gold electrodes through the endstanding *sp*-hybridized carbon atom at each side without the need for deprotective agents or toxic leaving groups. Compound 4,4''-diethynyl-1,1':4',1''-terphenyl and the new compound 4,4'''-diethynyl-1,1':4',1''':4'',1'''-quaterphenyl can bind nicely to Au electrodes and their conductance values showed an exponential decay with $\beta \approx 0.45 \text{ \AA}^{-1}$; a value which was similar to the value of sp^3 C–Au junctions with the same molecular backbone (oligophenylene). The conductance of molecules contacted via an *sp*-hybridized carbon atom was lower than the ones with sp^3 hybridization due to differences in the coupling of the conducting orbitals with the gold electrodes. Interestingly, the compound 4,4'-diethynyl-1,1'-biphenyl showed two values of conductance corresponding to the two features appearing in the 2D histogram, whereby the higher one was approximately the same as found in 4,4''-diethynyl-1,1':4',1''-terphenyl. These two values may be associated with the presence of dimers of the molecule and/or to π - π stacking of two molecules each attached to one electrode. The unexpected low conductance of 4,4'-diethynyl-1,1'-biphenyl may be attributed to rotation of phenyl rings breaking the conjugation of backbone or a change of anchoring to a more sp^2 like character.

Secondly, we designed and synthesized a novel compound 4-(but-3-en-1-ynyl)-4'-ethynyl-1,1'-biphenyl containing both an alkyne and an enyne group and investigated its on-surface reactions. The results showed that the Au(111) surface cannot activate the enyne group yielding as main reaction path the cyclotrimerization of the alkynes, while on Cu(111) surface the enyne groups can cross-couple with alkyne groups giving access to a 2D infinite covalent network. After annealing at 160 °C Cu atoms are coordinated to the alkyne-alkene-alkyne linkages forming organometallic polymer chains. This work reports the first alkyne and alkene cross-coupling reaction on surface, which opens a new way for surface-confined synthetic protocols of covalent polymers.

Thirdly, we inserted an alkyne group between a phenyl ring and a CN group forming a novel terphenyl-4,4''-dipropiolonitrile linker. The self-assembly of terphenyl-4,4''-dipropiolonitrile on the Ag(111) surface showed chevron arrangement with a Moiré pattern. Gd-directed assembly revealed an irregular metal-organic pattern with variable coordination motifs. The high reactivity of the $-C\equiv C-$ bonds in propiolonitrile groups prevented from formation of any regular metal-organic architecture and caused formation of reticulated Ln-organic networks with only local order.

Fourthly, for the first time, a new route of a modified Glaser-Hay homo-coupling reaction of a stable alkyne compound hexakis[4-(ethynyl)phenyl]benzene was used to synthesize large area of a GDY nanofilm on Cu foil. The vanishing 3293 cm^{-1} peak of typical C-H stretching vibration in $-C\equiv C-H$ terminal alkyne in the IR spectra as well as the shift of the alkyne peak to 2212 cm^{-1} in the Raman spectra proved that the homo-coupling of alkyne has occurred. Optic microscopy (OM), scanning electron microscopy (SEM) and atomic force microscopy (AFM) revealed that this nanofilm was very flat. Moreover, AFM images determined the average thickness of the produced GDY nanofilms with 117 nm. The high-resolution transmission electron microscopy (HR-TEM) images exhibited that there were curved streaks with the lattice fringe of 0.37 nm at the edge regions of the films, revealing that the GDY nanofilms grew in 2D manner on the copper foil. The measurement of a device based on GDY nanofilm showed that this GDY nanofilm had a conductivity of $5.15 \times 10^{-6}\text{ S m}^{-1}$ indicating semiconducting properties.

Finally, considering the structural rigidity and electronic conductivity of a terminal alkyne group to exert on the electrochemical properties of the porphyrins, we designed and synthesized a alkyne substituted porphyrin as [5,15-bis(ethynyl)-10,20-diphenylporphinato]copper(II) (CuDEPP) and investigated its electrochemical performance as

electrode material for rechargeable batteries. Three different cell designs were tested and investigated in detail.

First, a Li/LiPF₆/CuDEPP cell delivered an initial discharge capacity of 210 mAh g⁻¹ and the capacity retention of approximately 85% and 60% was maintained within 2000 and 8000 cycles, respectively, at a high current density of 4 A g⁻¹ demonstrating excellent cyclability. Notably, a stable reversible discharge capacity of 115 mAh g⁻¹ was achieved at a current of 10 A g⁻¹ within 42 seconds, offering energy density of 345 Wh kg⁻¹ at a high specific power of 29 kW kg⁻¹.

Second, CuDEPP served as an anode-active material in a Li free CuDEPP/PP₁₄TFSI/graphite cell, in which a discharge capacity of 94 mAh g⁻¹ was obtained at a current density of 1 A g⁻¹ and with good cyclability and rate capability. The reversible intercalation of the TFSI⁻ anion into (from) the graphite cathode was indicated by *ex-situ* XRD and EDX spectroscopy.

Third, in an all-organic symmetric configuration, the ambipolar redox reactivity of the CuDEPP electrode enabled a four-electron transfer. Therefore, an energy storage device with CuDEPP as electrode-active material as both cathode and anode will be able to bridge the gap between the batteries and the supercapacitors.

Zusammenfassung

Alkinverbindungen enthalten zwei orthogonal zueinander stehende π -Bindungen und sind äußerst wertvolle Bausteine in der organischen Synthese. Durch ihr breites Anwendungsspektrum unter anderem in der Polymerisation haben Alkinverbindungen in den Materialwissenschaften viel Aufmerksamkeit auf sich gezogen. In dieser Arbeit wurden fünf Reihen von neuartigen Alkinderivaten synthetisiert, um diese hinsichtlich drei verschiedener Aspekte zu untersuchen: a) Ihre generelle Selbstorganisation und chemische Reaktivität auf planaren Oberflächen, b) ihre Fähigkeit als leitfähige molekulare Verbindungen zu agieren und c) ihre Anwendung als Elektrodenmaterial in Batterien.

Eine Reihe von Oligo(phenylethynylen) wurde synthetisiert, um auf der Oberfläche C–C Homokupplungsreaktionen vom Glaser-Hay-Typ zu untersuchen. So wurde beobachtet, dass auf einer Ag(111)-Oberfläche thermische Aktivierung von 4,4''-Diethynyl-1,1':4',1''-terphenyl eine Vielzahl von Nebenreaktionen auslöst, die zu unregelmäßig verzweigten Polymernetzwerken führen. Um die Chemoselektivität des Verknüpfungsprozesses zu erhöhen, wurde der Templatansatz mit der vicinalen Oberfläche Ag(877) genutzt. Die 4,4''-Diethynyl-1,1':4',1''-terphenylmoleküle richten sich dabei entlang den Stufenrändern der Ag(877)-Oberfläche aus. Nach weiterem Erwärmen auf 400 K wurden 1-dimensionale Graphdiynketten mit alternierenden terphenyl und Butadiynyleinheiten mit einer Länge von ca. 30 nm erhalten. DFT-Berechnungsergebnisse zeigen, dass diese Graphdiynketten eine Bandlücke von 1,6 eV aufweisen und halbleitende Eigenschaften besitzen.

Weiterhin wurde die Einzelmolekültransport dieser Verbindungen mittels mechanisch kontrollierten Bruchkontakte (mechanically controllable break junction, MCBJ) studiert. Die synthetisierten Moleküle können durch Deprotonieren von einem sp -hybridisiertes Kohlenstoffatom an jeder Seite Goldelektroden kontaktieren. Vorteilhafterweise besitzen die verwendeten Moleküle keine sperrigen Schutzgruppen, so dass problematisches Entschützen oder die Verwendung von toxischen Abgangsgruppen von vermieden wird. Die Verbindungen 4,4''-Diethynyl-1,1':4',1''-terphenyl und 4,4'''-Diethynyl-1,1':4',1''':4'',1''-quaterphenyl binden so stabil an Gold. Der experimentell bestimmte Leitwert zeigt einen exponentiellen Abfall $\beta \approx 0,45 \text{ \AA}^{-1}$, der einen ähnlichen Wert zu sp^3 -C–Au-Übergängen mit gleichem Oligophenylmolekülrückgrat aufweist. Allerdings ist die Leitfähigkeit von Molekülen, die über ein sp -hybridisiertes Kohlenstoffatom kontaktiert werden, niedriger als derjenigen, die vorher für eine sp^3 -Hybridisierung bestimmt wurde. Als Ursache für diesen überraschenden Befund werden Unterschieden in der Kopplung der leitenden Orbitale mit den Goldkontakten herangezogen. Interessanterweise wurden im Fall von 4,4'-Diethynyl-1,1'-biphenyl zwei

unterschiedliche Leitfähigkeitswerte in der Messung ermittelt, welche auch reproduziert werden konnten. Der höhere von beiden weist in etwa den gleichen Wert wie 4,4''-Diethynyl-1,1':4',1''-terphenyl auf. Das Auftreten von zwei verschiedenen Werten kann entweder mit der Anwesenheit von σ -Dimeren des Moleküls oder mit der π - π -wechselwirkung von zwei Molekülen erklärt werden, die jeweils an einer Elektrode befestigt sind. Die unerwartete niedrigere Leitfähigkeit von 4,4'-Diethynyl-1,1'-biphenyl kann auf die Verdrehung der Phenylringen zurückgeführt werden, was die Konjugation des aromatischen Rückgrats bricht oder die Bindungskonfiguration zu einem sp^2 -ähnlichen Charakter verändert.

Desweiteren wurde die bisher unveröffentlichte Alkin-Enin-funktionalisierte Verbindung 4-(But-3-en-1-ynyl)-4'-ethynyl-1,1'-biphenyl synthetisiert, um anschließend ihr C-C Kopplungserhalten und ihre Reaktivität auf verschiedenen Oberflächen zu untersuchen. Die Ergebnisse zeigen, dass die Au(111)-Oberfläche die Enin-Gruppe nicht gut aktiviert werden kann, weswegen jeweils drei Alkine in einer Cyclotrimerisierungsreaktion zum identifizierten Hauptprodukt reagieren. Dagegen kann die Cu(111)-Oberfläche Enin-Gruppen sehr gut aktivieren und diese mit Alkingruppen kreuzkuppeln. Daraus ergibt sich ein 2-dimensionales unendliches kovalentes Netzwerk. Nach dem Erwärmen auf 160 °C koordinierten die Cu-Atome der Oberfläche zu den Alkin-Alken-Alkin-Bindungen und bildeten metallorganische Polymerketten aus. Diese Arbeit stellt die erste Alkin- und Alken-Kreuzkupplungsreaktion auf Metalloberflächen vor, was einen neuen Weg für die kovalente Oberflächenpolymerisation eröffnet.

Drittens insertierten wir die Alkingruppe zwischen der Phenylgruppe und einer CN-Gruppe, wobei ein Terphenyl-4,4''-dipropiolonitril-Linker gebildet wurde. Die Selbstorganisation von Terphenyl-4,4''-dipropiolonitril bildet auf der Ag(111)-Oberfläche eine Monoschicht mit Fischgrätenanordnung, welche zusätzlich ein Moiré-Muster mit der hexagonalen Oberfläche bildet. Gadolinium-Koordination führt zu einer sehr unregelmäßigen metallorganischen Monolage mit variablen Koordinationsmotiven, einschließlich Clustering. Die hohe Reaktivität der $C\equiv C$ Bindungen in den Propiolonitril-Gruppen verhindert die Bildung einer regulären metallorganischen Architektur und führt zu vernetzten Ln-organischen Netzwerken mit nur kurzreichweitiger Ordnung.

Viertens wurde zum ersten Mal ein neuer Weg einer modifizierten Glaser-Hay-Homokupplungsreaktion einer stabilen Alkinverbindung Hexakis [4-(ethynyl)phenyl]benzol verwendet, um größere Flächen von Graphdiyn-Nanofilmen auf Cu-Folie zu synthetisieren. Das Verschwinden der typischen C-H-Streckschwingung (bei 3293 cm^{-1}) im IR-Spektrum des $-C\equiv C-H$ -terminalen Alkins und die Verschiebung der Alkinbande auf 2212 cm^{-1} im

Raman-Spektrum beweisen, dass die Homokupplung der Alkine stattfindet. Optische Mikroskopie (OM), Rasterelektronenmikroskopie (SEM) und Atomkraftmikroskopie (AFM) zeigen übereinstimmend, dass diese Nanofilme sehr dünn sind; insbesondere zeigen AFM-Bilder, dass die durchschnittliche Dicke der GDY-Nanofilme 117 nm beträgt. Die hochauflösenden Transmissionselektronenmikroskopie-Bilder (HR-TEM) zeigen, dass es an den Randbereichen der Folien gekrümmte Streifen mit dem Gitterstreifen von 0,37 nm gibt, die darauf hinweisen, dass die Graphdiin-Nanofilme 2-dimensional auf der Kupferfolie wachsen. Eine auf Graphdiin-Nanofilmen-basierende Vorrichtung zur Messung der elektrischen Eigenschaften wurde hergestellt und führt zu einer Messung der Leitfähigkeit von $5,15 \times 10^{-6} \text{ S m}^{-1}$, typisch für einen Halbleiter.

Zusätzlich wurde die neuartige alkinsubstituierte Porphyrinverbindung [5,15-Bis(ethinyl)-10,20-diphenylporphinato]-Kupfer(II) (CuDEPP) synthetisiert. Dabei wurde zum einen die strukturelle Rigidität und zum anderen die elektrische Leitfähigkeit endständiger Alkingruppen berücksichtigt, die bekanntlich die elektrochemischen Eigenschaften der Porphyrine beeinflussen können. Das so hergestellte modifizierte Cu-Porphyrin wurde dann bezüglich seiner elektrochemischen Eigenschaften in Batteriekonfigurationen untersucht. Dabei wurden drei verschiedene Zellkonfigurationen ausgewählt und untersucht:

Eine Li/LiPF₆/CuDEPP-Zelle lieferte eine anfängliche Entladungskapazität von 210 mAh g⁻¹ bei einer hohen Stromdichte von 4 A g⁻¹, die über 2000 (bzw. 8000) Zyklen zu ungefähr 85% (bzw. 60%) erhalten werden konnte, was das ausserordentliche Zyklisierungsverhalten der elektrochemischen Zelle beweist. Bemerkenswert ist eine stabile reversible Entladungskapazität von 115 mAh g⁻¹ innerhalb von 42 Sekunden bei einer Stromdichte von 10 A g⁻¹, was einer gravimetrischen Energiedichte von 345 Wh kg⁻¹ bei einer hohen spezifischen Leistung von 29 kW kg⁻¹ entspricht.

Des Weiteren wurde CuDEPP als anodenaktives Material in einer Li-freien CuDEPP/PP₁₄TFSI/Graphit-Zelle eingesetzt. In dieser Anordnung konnte bei einer Entladungskapazität von 94 mAh g⁻¹ eine Stromdichte von 1 A g⁻¹ und ebenfalls ein gutes Zyklisierungsverhalten nachgewiesen werden. Die reversible Interkalation der TFSI-Anionen in bzw. aus der Graphitkathode wurde durch *ex-situ* Röntgendiffraktometrie und energiedispersive Röntgenmikroanalyse nachgewiesen.

In dem dritten untersuchten Zellaufbau, einer symmetrischen und komplett organischen Konfiguration, ermöglichte die ambipolare Redoxaktivität der CuDEPP-Elektroden einen Vierelektronentransfer. Energiespeichersysteme, die CuDEPP als elektrodenaktives Material

verwenden, könnten so eventuell elegant die Lücke zwischen Batterien und den Superkondensatoren schließen.

1. Introduction

1.1 Alkyne and its derivatives

An alkyne is an unsaturated hydrocarbon containing at least one carbon-carbon triple bond which is formed by two sp -hybridized carbon atoms. In the past decades, alkyne compounds have attracted much interest as extremely valuable building blocks in organic synthesis and material science.^[1]

As the simplest alkyne molecule, the $C\equiv C$ bond distance of acetylene is 1.20 Å with very strong bond strength of 839 kJ/mol, and the $C\equiv C-H$ bond angle is 180° (Figure 1.1). The $C\equiv C$ bond contains one σ and two sets of orthogonal π bonds.

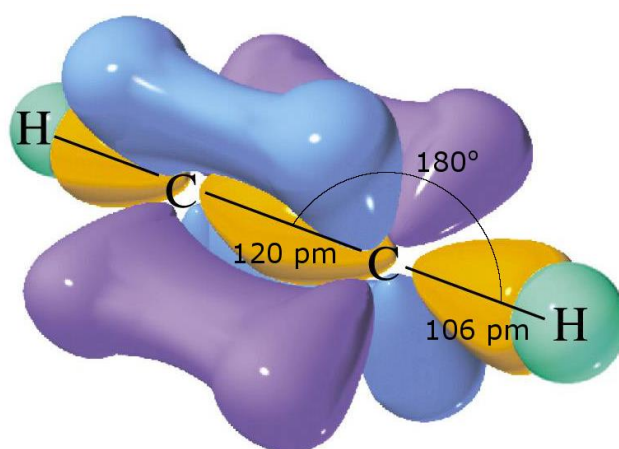
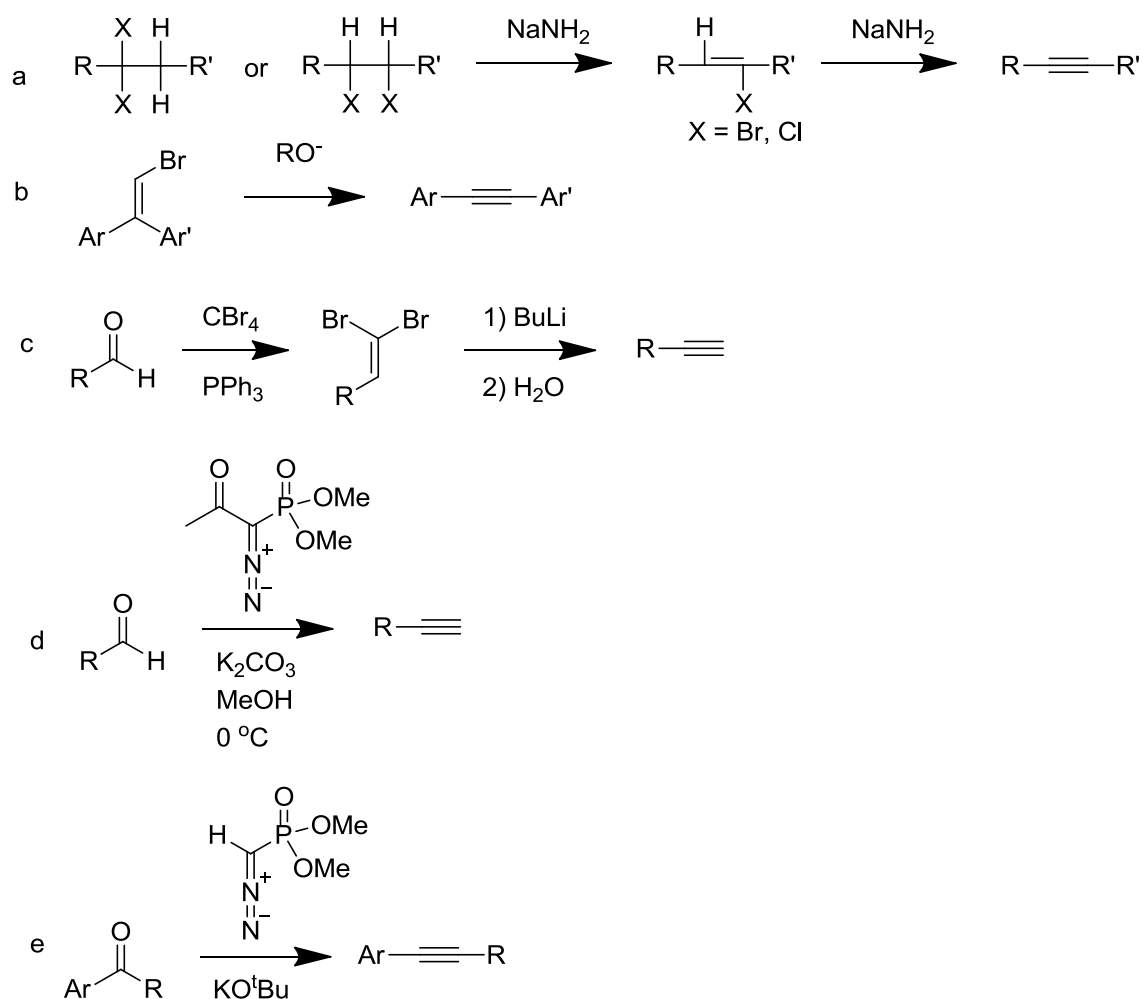


Figure 1.1 Structure of acetylene with σ and π bonds.

Because the sp -hybridized carbon atoms have 50% s character and are more electronegative than sp^2 and sp^3 carbon atoms, the terminal alkyne compounds are more acidic (pKa about 25) than alkene and alkane compounds.^[2] They can react with a strong base such as n -butyllithium yielding the anion of the terminal alkyne (RCC^-), and are often used as nucleophiles in synthesis.

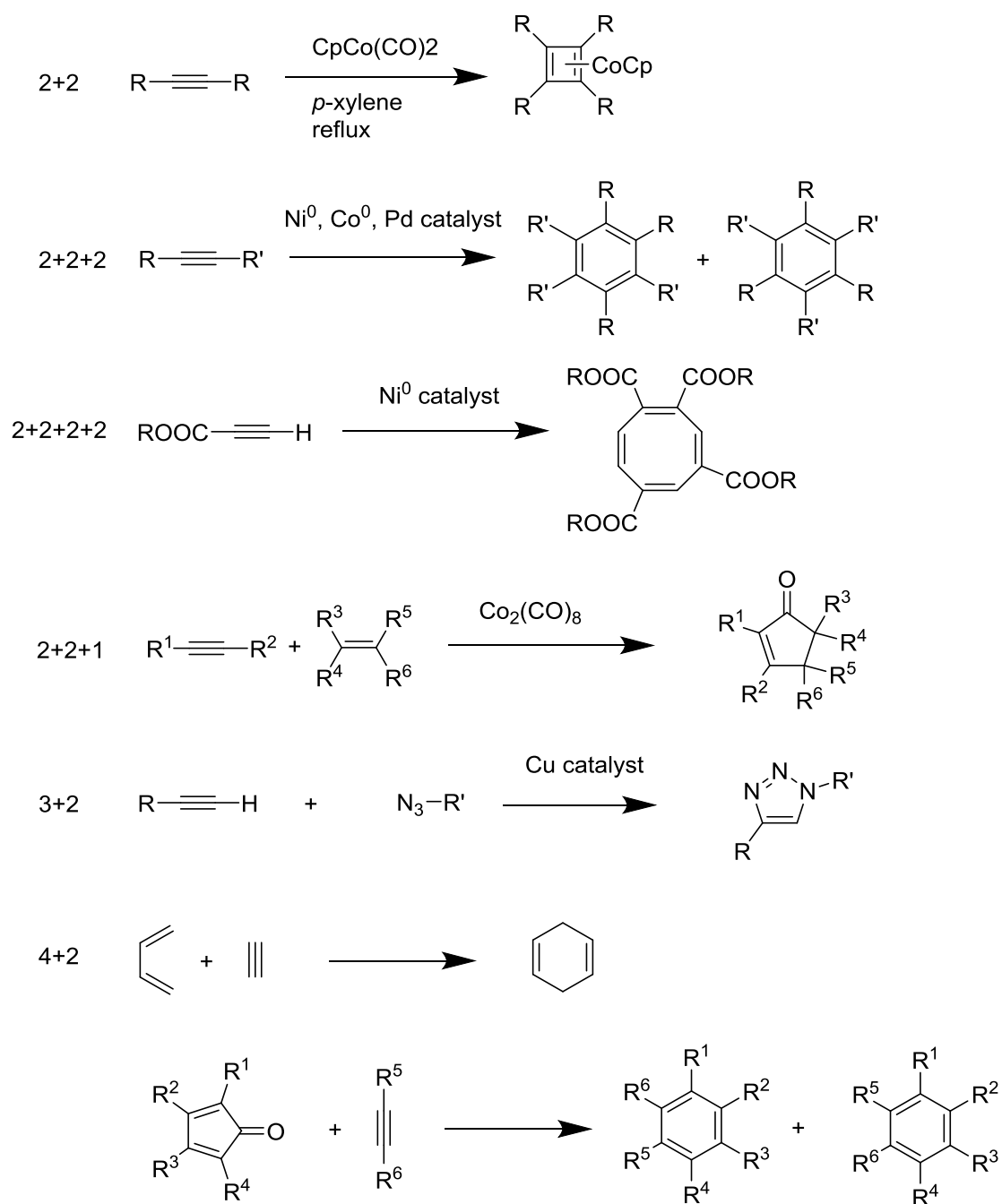
As shown in Scheme 1.1, alkynes can be prepared by dehydrohalogenation of vicinal alkyl dihalides or vinyl halides (Scheme 1.1a).^[3] But this kind of reaction needs very strong bases to dehydrohalogenate the intermediate haloalkenes, which limits its generality. Alkynes can also be synthesized starting from vinyl bromides via the Fritsch-Buttenberg-Wiechell rearrangement (Scheme 1.1b).^[4] The Corey-Fuchs reaction is a widely used procedure to prepare alkynes through aldehydes (Scheme 1.1c).^[5] With a Seyferth-Gilbert reagent, aldehydes and ketones can form alkynes (Scheme 1.1d,e).^[6]



Scheme 1.1 Different synthetic routes for alkynes.

Similar to the π -electron bond activity of alkenes, alkynes can undergo reactions such as the addition of hydrogen, the addition of halogens, the addition of hydrogen halides, metathesis, oxidation and polymerization in the presence of metal compounds.

Besides these, alkynes undergo diverse cyclization reactions including cyclooligomerizations and cycloadditions.^[7] Frequent cyclooligomerizations of alkynes are cyclotrimerization^[8] and cyclotetramerization (Scheme 1.2)^[9]. Many catalysts for the cyclotrimerization have been found, such as metals or compounds contain U (Group 3),^[10] Ti (Group 4),^[11] Nb (Group 5),^[12] Cr^[13] and W^[14] (Group 6), Fe^[15] and Ru^[16] (Group 8), Co^[17], Rh^[17] and Ir^[18] (Group 9), Ni^[8] and Pd^[9,19] (Group 10), and Au (Group 11)^[20].



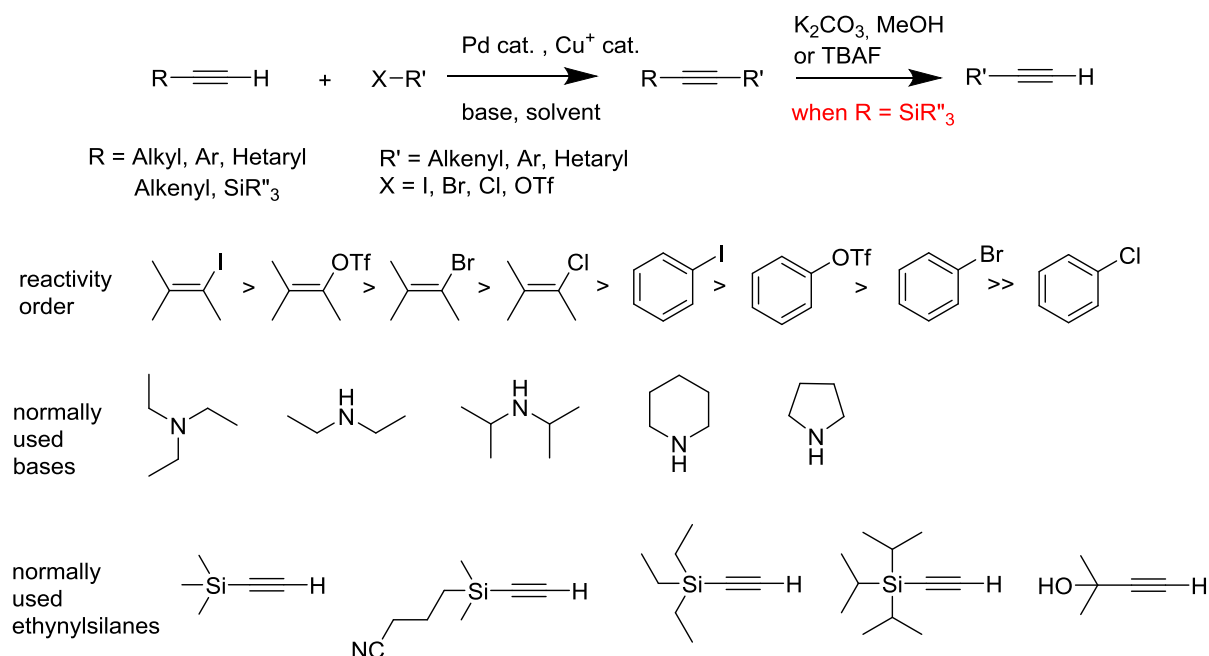
Scheme 1.2 Different cycloadditions of alkynes.

The description of cycloadditions can be expressed as [2 + 2], [2 + 2 + 1], [2 + 2 + 2], [3 + 2], [4 + 2], etc., type cycloadditions (Scheme 1.2). The representative [2 + 2 + 1] cycloaddition is the Pauson-Khand reaction employing the cyclization of alkynes with alkenes and carbon monoxide in the presence of cobalt carbonyls.^[21] The famous [3 + 2] cycloaddition is the azide-alkyne Huisgen cycloaddition, also named as “click reaction”, which means the cycloaddition of alkyne and azide in the presence of a copper catalysts to render 1,2,3-triazole.^[22] The most notable [4 + 2] cycloaddition is the Diels-Alder reaction with 1,3-dienes to give 1,4-cyclohexadienes. The Diels-Alder reaction of a phenyl- or

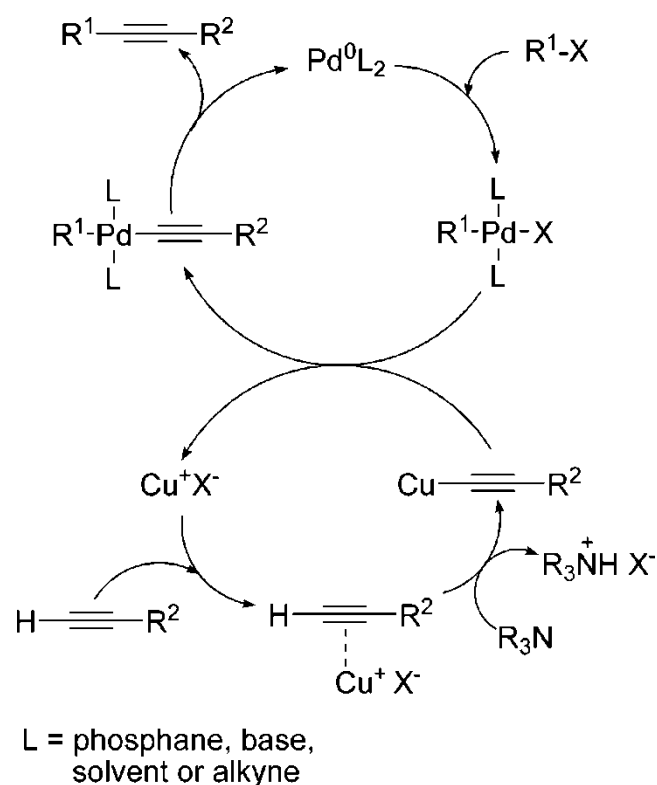
diphenylacetylene containing molecules and tetraphenylcyclopentadienone has proven to be very useful for the syntheses of conductive materials.^[23] Certain of these reactions were also investigated on surface and characterized by STM.^[20]

Because of the strong nucleophilicity of terminal alkyne anions and the orthogonality of the two sets π -bonds, alkynes can undergo coupling reactions with aryl or vinyl halides, carbon monoxide, carbon dioxide, aldehydes, ketones, alkenes, allenes and nitriles in the presence of transition metal compound catalyst.^[7]

Sonogashira cross-coupling and Glaser-Hay homo-coupling reactions are two widely used coupling reactions of alkynes. These reactions yield the rigid and conjugated products as poly(*p*-phenylene-ethynylene)s and poly(arylenebutadiynylene)s, respectively, which have good luminescence and electronic activity favoured by material scientists.^[24]



Scheme 1.3 The Sonogashira reaction and its used halogenides, bases and ethynylsilanes.



Scheme 1.4 Schematic representation of the proposed mechanism of the Sonogashira reaction. Reproduced with permission from [25], Copyright (2007) American Chemical Society.

The Sonogashira cross-coupling reaction was first reported by Kenkichi Sonogashira et al. in 1975.^[26] It employs a palladium catalyst to form a carbon-carbon bond between a terminal alkyne and an aryl or vinyl halide (the reaction, typical reactants and reagents are shown in Scheme 1.3; the proposed mechanism is given in Scheme 1.4).^[25,27] The general reactivity order of the sp^2 species is vinyl iodide > vinyl triflate > vinyl bromide > vinyl chloride > aryl iodide > aryl triflate > aryl bromide \gg aryl chloride.^[25] Examples of such palladium catalysts including $\text{Pd}(\text{PPh}_3)_4$, $\text{Pd}(\text{PPh}_3)_2\text{Cl}_2$, $\text{Pd}(\text{dppp})\text{Cl}_2$ and $\text{Pd}(\text{dppf})\text{Cl}_2$. Amines (such as triethylamine, diethylamine, diisopropylamine, piperidine^[28] and pyrrolidine^[29]) are the typically employed bases in this reaction to neutralize the byproduct hydrogen halide.

Trialkylsilylacetylenes are often used as convenient reactants for introduction of an acetylenic unit.^[30] In particular, different protective silane groups can be selectively cleaved.^[31] Trimethylsilyl (TMS) and triisopropylsilyl (TIPS) are the widely used as protection groups. The former is easy to remove by a plethora of reagents, such as K_2CO_3 or KOH or KF with methanol, KF with 18-crown-6, and TBAF. The cleavage of the latter is normally presented in THF or DCM solution of TBAF. [(3-Cyanopropyl)dimethylsilyl] (CPDMS)^[32] and 2-hydroxypropyl^[33] can increase the polarity of the alkyne derivative, improving the chromatographic purification of the product.

Additionally, with the pKa around 25 and two set π -bonds, after deprotonation, the terminal alkynes can coordinate to transition metal or metal ions via formation of a coordinative σ -bond. With more noble metal ions such as Au,^[34] Rh,^[35] Ru,^[36] Co,^[37] and Pt^[38], they give transition metal acetylide complexes that are considered as linear conjugated molecules showing interesting applications as e.g. luminescence.

1.2 Graphdiyne

Carbon plays a special important role in human's daily life. With various hybridized states (sp , sp^2 , sp^3) it exhibits different allotropes (Figure 1.2): the carbon in diamond is sp^3 -hybridized; sp^2 -hybridized carbon atoms are present in fullerenes,^[39] carbon nanotubes,^[40] graphene^[41] and graphite; the linear carbyne is formed by only sp -hybridized carbon atoms.^[42] When sp^2 and sp hybridized carbon atoms are combined, a new family of carbon allotropes, graphyne (GY)^[43] and graphdiyne (GDY)^[44] will be obtained.^[45]

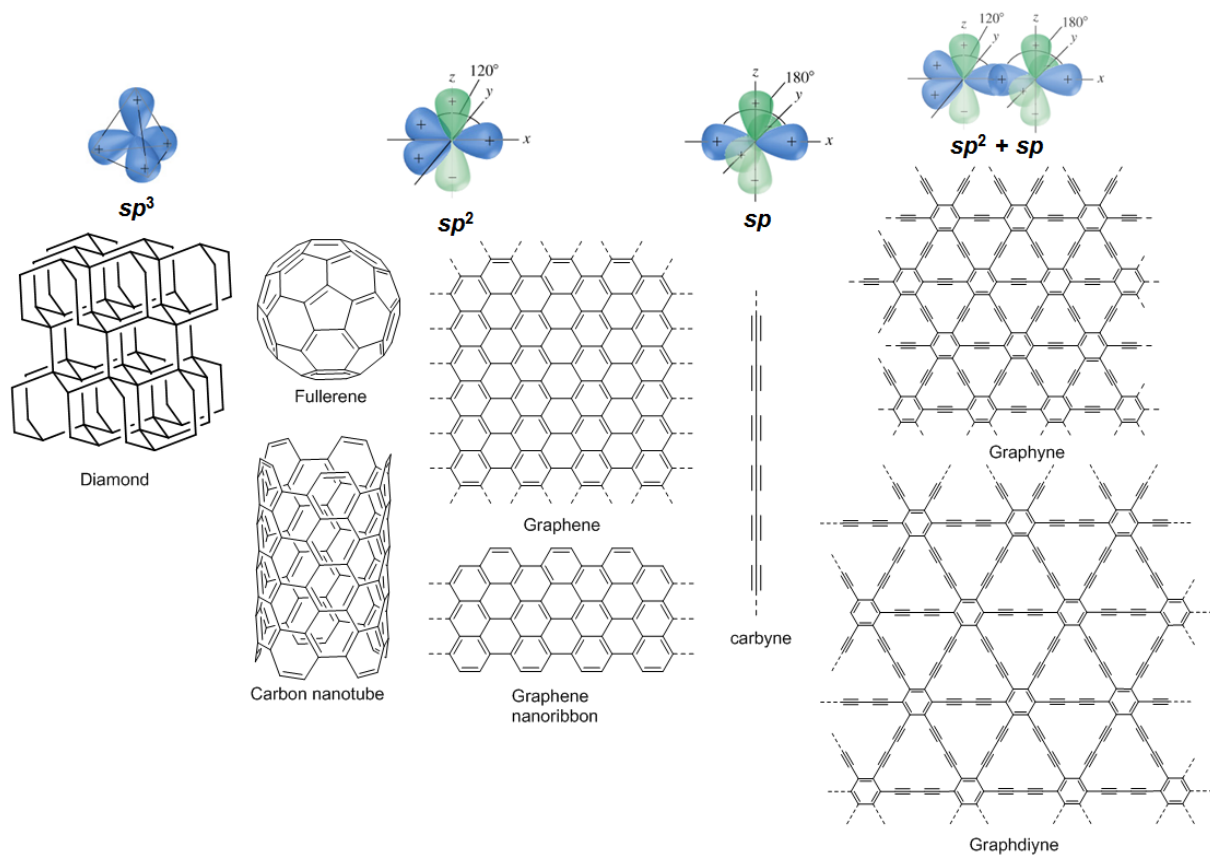
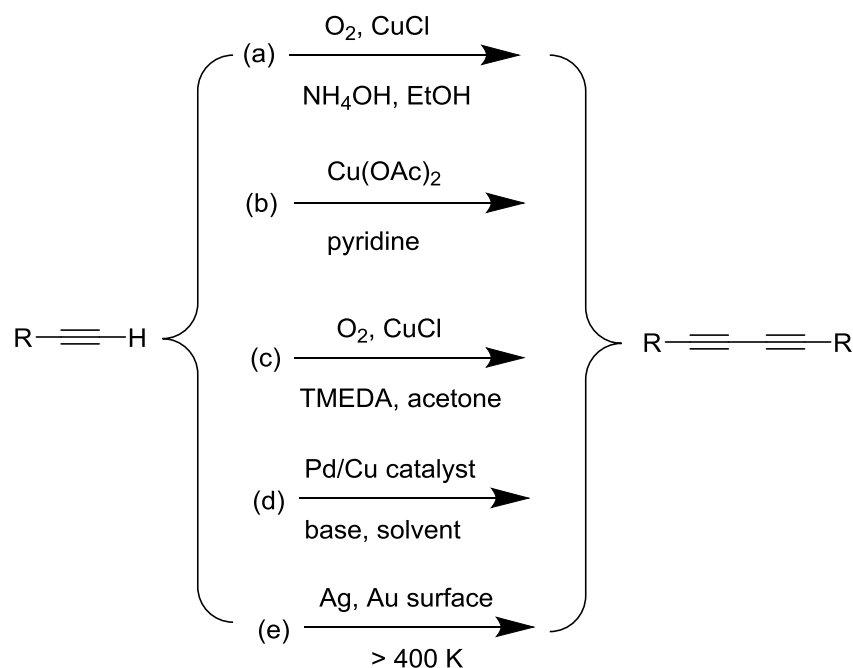


Figure 1.2 Representation of carbon allotropes with differently hybridized carbon atoms.

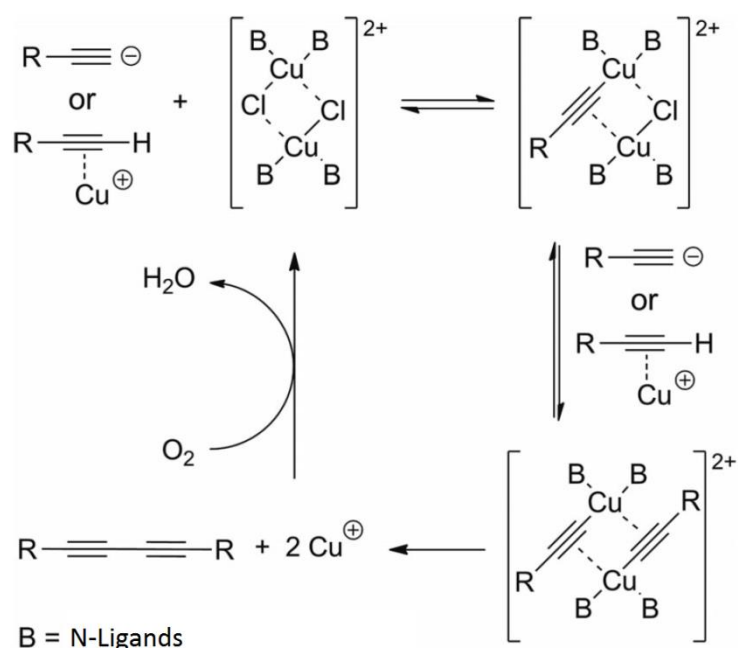
Due to the particular reactivity of acetylenic linkages, the chemical bottom-up route is the only one available to synthesize GY and GDY. With directional anisotropy and nonequivalent Dirac points, GY and GDY are predicted to exhibit a tunable band gap beyond graphene with a range from 0.46 to 1.22 eV, depending on the applied methods and exchange-correlation functionals.^[45a] These compounds are predicted to have highly interesting electronic properties, as they can form uniform pores and contain activated triple bonds; in some aspects, they are supposed to be more versatile than graphene. A lot of theoretical investigations have calculated the structure,^[45a] electronic,^[46] optical^[47] and mechanical

properties^[48] of GY and GDY, proposing applications as hole-transporting materials,^[49] transistors,^[50] field emission devices,^[51] batteries,^[46c,52] gas separation,^[53] desalination,^[54] catalysis^[55] and sensors^[56].

For the synthetic approach, chemists have made lot efforts to synthesize some small *sp*² conjugated subunits of GY and GDY such as annulene.^[57] Compared with GY, there are more routes to achieve the butadiyne unites for GDY, particularly by the on-surface approach (Scheme 1.5).^[58] Early in 1869, Glaser firstly found the alkyne homo-coupling, using copper(I) salts in the presence of ammonium hydroxide and under ambient conditions (Scheme 1.5).^[59] Later in 1956, Eglinton and Galbraith introduced pyridine as base as well as ligand for the Cu catalyst. In 1962, Hay^[60] started to use *N,N,N',N'*-tetramethylethylenediamine (TMEDA) to modify the reaction giving improved selectivities and yields^[61]; this is the so-called Glaser-Hay coupling reaction. The proposed mechanism of the Glaser-Hay coupling is shown in Scheme 1.6. Recently, Pd/Cu catalyst systems have been shown to afford good yield in this homo-coupling reaction.^[62] Interestingly, Ag^[63] and Au^[64] have been shown to act as both, catalyst and template, in the homo-coupling reaction after annealing up to 400 K.



Scheme 1.5 Syntheses of butadiynes by C–C homo-coupling via (a) Glaser, (b) Eglinton-Galbraith and (c) Hay couplings reaction, (d) Pd-catalysed reactions, and (e) metal surface catalysis.



Scheme 1.6 Mechanism for the Glaser-Hay coupling reaction suggested by Bohlmann et al.^[65] Reproduced with permission from [66], Copyright (2012) John Wiley and Sons.

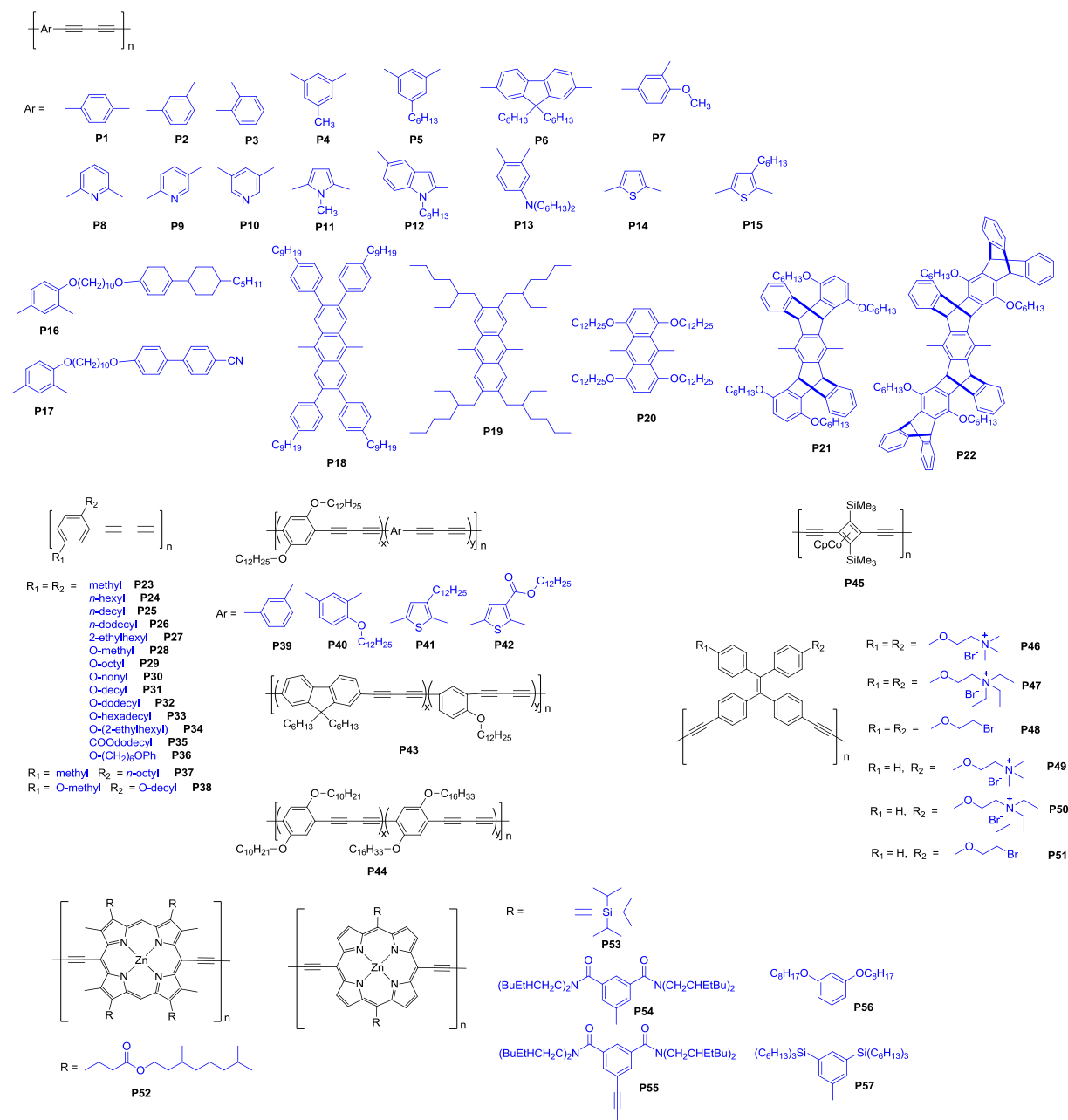
1D Poly(arylenebutadiynylene)s polymers as the GDY analogue also exhibit butadiyne units and π -conjugated backbones endowing them electronic, optic and photonic activities with applications such as liquid crystals and LED. Introducing different side groups as pendants to the polymer chains can change the solubility and functions of the poly(arylenebutadiynylene)s. A summary of a series of poly(arylenebutadiynylene)s structures is listed in Scheme 1.7. These results were mainly obtained by the Bunz group, the Kijima group, the Swager group, the Anderson group, and the Tang group.^[66-70]

As early as in 1995, the Bunz group^[67] has reacted the 2,4-diethynyl-1,3-bis(trimethylsilyl)-substituted cobalt complex as monomer obtaining a well soluble and stable polymer **P45** (as shown in Scheme 1.7).

The Kijima group^[68] has reported a series of poly(arylenebutadiynylene)s using a Glaser-Hay reaction, thereby the used arylene groups include phenylene, fluorene, pyridine, thienylene, pyrrole and N-alkylindole. The results of photoluminescence studies showed that **P12**, **P25**, **P27**, **P31**, **P34**, **P35**, **P36** and **P39-P43** exhibited intense light emissions ranging from 416 to 596 nm (blue to orange-red color) with very good quantum yields.^[68d,68f-h] **P12**, **P39**, **P42**, **P43** were also used for LED applications.^[68f,68h]

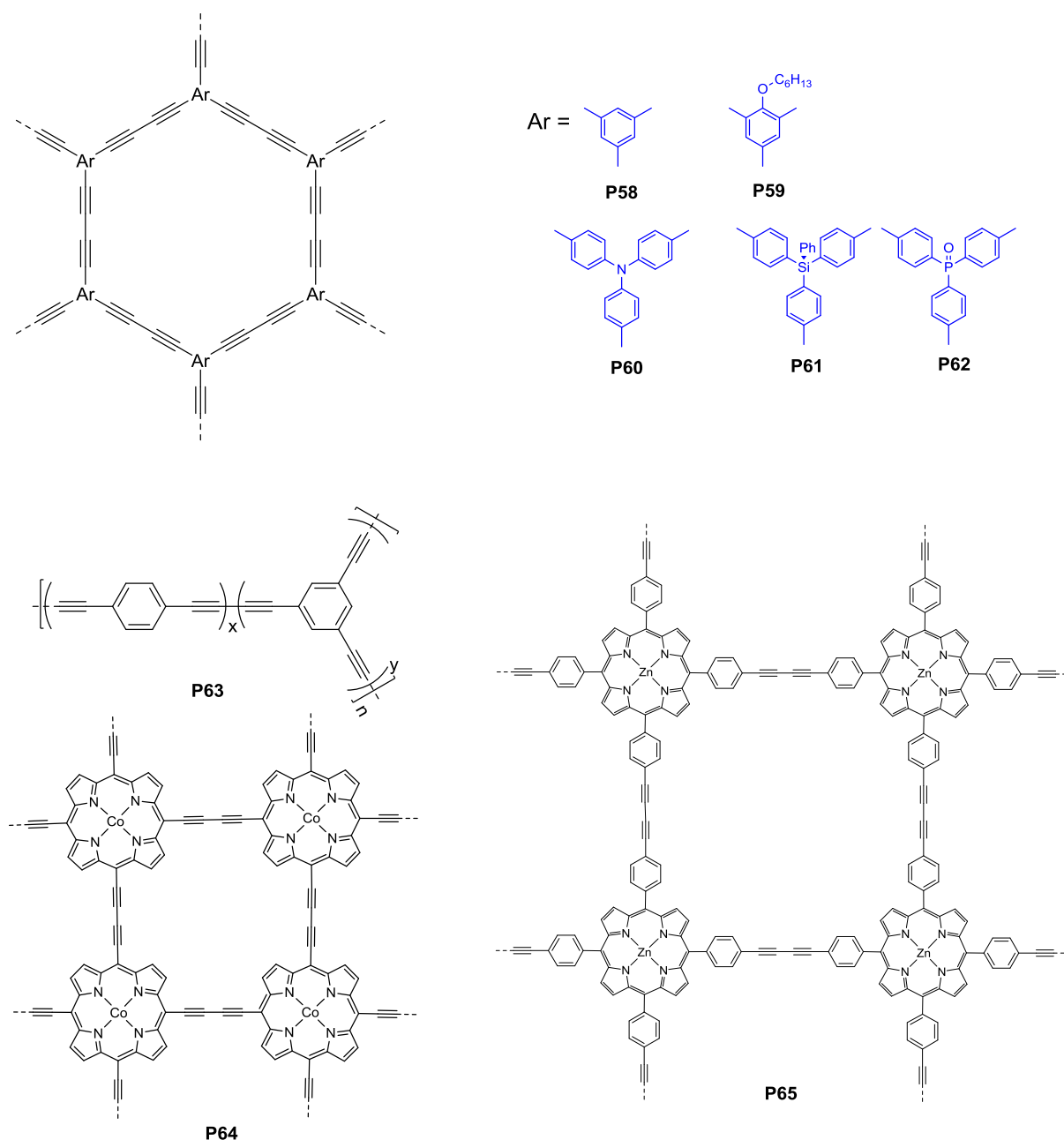
In 2000, the Swager group^[69] improved the yield and chemical selectivity of the Pd/Cu catalyzed homo-coupling alkyne reaction by introducing benzoquinone as oxidant. With this method, the poly(arylenebutadiynylene)s **P31**, **P33** and **P44** were synthesized. The \bar{M}_n of **P33**

and **P44** (x:y = 2:1) can reach to 14000 and 154000 respectively. As we know, **P44** has the highest molecular weight \bar{M}_n for the reported poly(arylenebutadiynylene)s.



Scheme 1.7 Overview of different poly(arylenebutadiynylene)s.

Finally, Anderson group^[70] synthesized a series of 1D butadiyne-linked porphyrin polymers **P52-P57**. Except **P53**, these compounds are soluble in common organic solvents. **P52**, **P54**, **P55** showed good third-order nonlinear optical properties.^[70a,70c] After introducing 4,4'-bipyridine, **P54** and **P57** self-assembled to double-strand ladder complexes, respectively.^[70b,70d] The ladder complex of **P57** showed good positive charges mobility along the molecular wires. Polymer **P56** was also observed in molecular level by UHV-STM using electro spray deposition.^[70e]



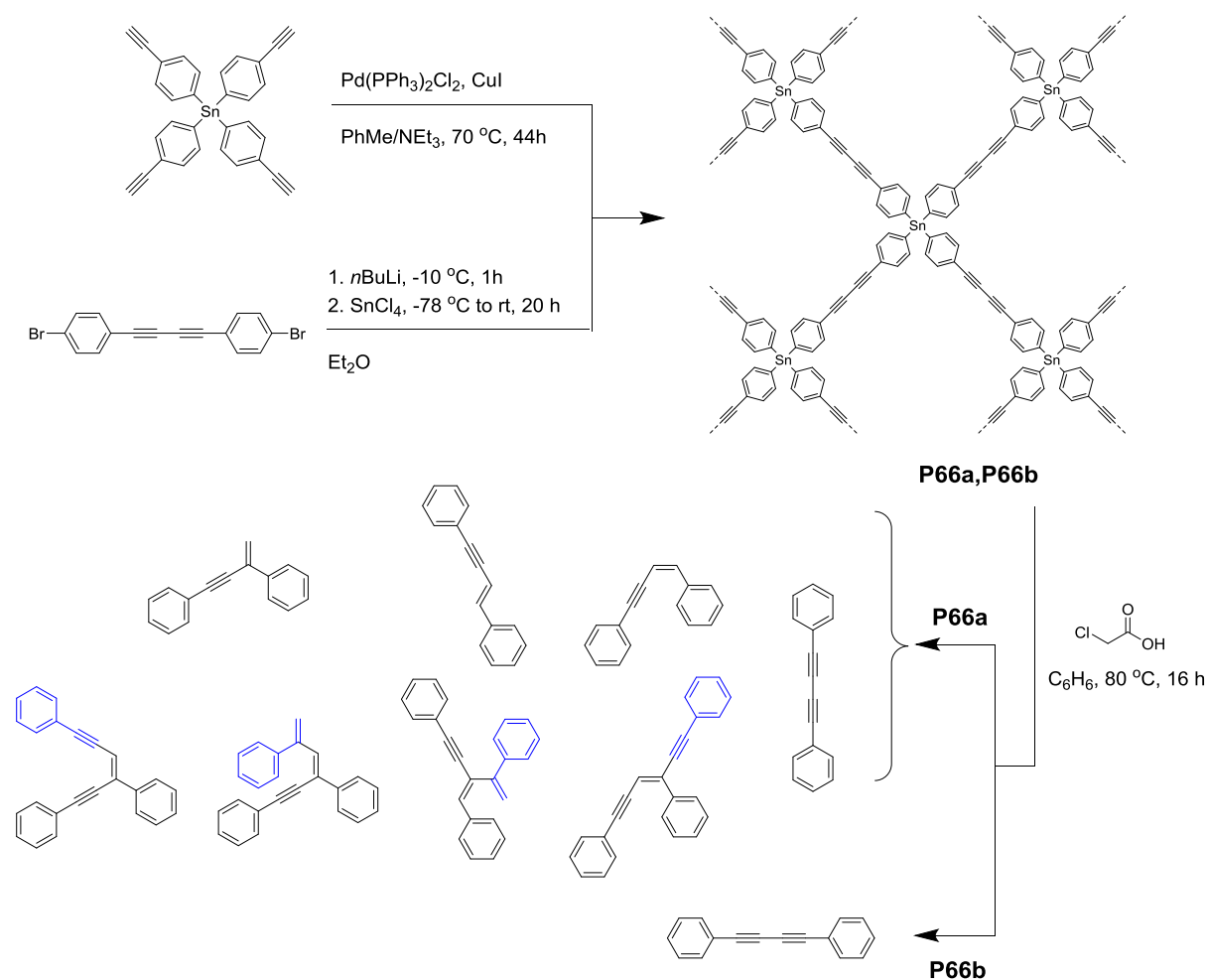
Scheme 1.8 Structures of different butadiyne conjugated microporous polymers.

Beside the 1D conjugated polymers, 2D and 3D conjugated microporous polymers (CMPs) have also attracted intense interest. As a new member of the microporous framework materials, such as metal-organic frameworks (MOFs), covalent organic frameworks (COFs) and zeolites, CMPs with optoelectrical response of π -conjugated rigid frameworks and tunable pore size are supposed to have versatile applications in photoluminescence, gas adsorption, heterogeneous catalysis, energy storage and so on. The butadiyne linked CMPs is an import branch of this material.

The Tang group^[71] synthesized the hyperbranched network polydiyne **P58-P62** by using triyne monomers containing various functional groups such as ether, amine, silane and

phosphorus oxide by Glaser-Hay coupling reactions. **P59** and **P60** exhibited good solubility and high molecular weight (\bar{M}_n 8500 and 15000 respectively), while **P60** showed bright blue fluorescence and high light refractivity.

The Cooper group^[72] synthesized the CMPs **P1** and **P58** by a Pd catalyzed reaction, and investigated their gas adsorption properties. **P1** also had the cross-linked 1,3-disubstituted enynes reaction under the synthetic conditions. The BET surface was found to be 827 and 842 $\text{m}^2 \text{g}^{-1}$ for **P1** and **P58**, respectively. At 77.3 K, **P1** and **P58** can adsorb up to 131 and 107 $\text{cm}^3 \text{g}^{-1} \text{H}_2$, respectively.



Scheme 1.9 Syntheses and cleavage of the CMPs **P66a** and **P66b**.^[73]

Furthermore, two different CMPs **P66a**, **P66b** based on tetrakis(4-ethynylphenyl)stannane as the repeating units were synthesized by the Bunz group (Scheme 1.9).^[73] These CMPs showed high BET surfaces (747 and $385 \text{m}^2 \text{g}^{-1}$ for **P66a** and **P66b**, respectively) and high thermal stability. Interestingly, after using chloroacetic acid to quantitatively cleave the tin-carbon bonds, GC-MS and NMR results showed that, except for a small amount of diphenylbutadiyne, the main products were enyne-based dimers, trimers, and tetramers of

phenylacetylene for **P66a**. But for **P66b**, the respective reaction product was exclusively diphenylbutadiyne. This cleavage approach is a powerful method to elucidate the subordinated structure of CMPs. This work also suggests that Pd catalyzed homo-coupling reaction does not show a high selectivity, but it is efficient to obtain high specific surface area.

Hijazi et al.^[74] *in situ* synthesized CMPs **P64** with cobalt meso-tetraethynylporphyrin units on the multi-walled carbon nanotubes (MWNTs) surfaces through the Glaser-Hay coupling reaction and the multiple π - π interactions between the porphyrin and MWNT. Wu et al.^[75] used a miniemulsion-template approach and Pd(II)-Cu(I) catalysed homo-coupling of terminal alkyne groups of 5,10,15,20-tetra(4-ethynylphenyl)porphyrin-Zn(II) to synthesize the Zn-porphyrin-based conjugated microporous polymer **P65** (Zn-Por NCMPs) as nanoparticles, which was shown to be used as a colorimetric sensor of SO₂.

In 2010, the Li group^[76] reported the first GDY synthesis which was carried out on Cu foil via a homo-coupling reaction using hexaethynylbenzene (HEB) in the presence of pyridine (Figure 1.3a). The AFM images showed that the GDY films had the thickness of 970 nm (Figure 1.3c). The HR-TEM images indicated that the GDY films had very high crystallinity and clear lattice fringes of 4.19 Å (Figure 1.3d). The device based on GDY films fabricated on Cu foil showed Ohmic behavior with conductivity of $2.516 \times 10^{-4} \text{ S m}^{-1}$, demonstrating the GDY films had outstanding semiconducting properties in comparison to silicon (Figure 1.3f).

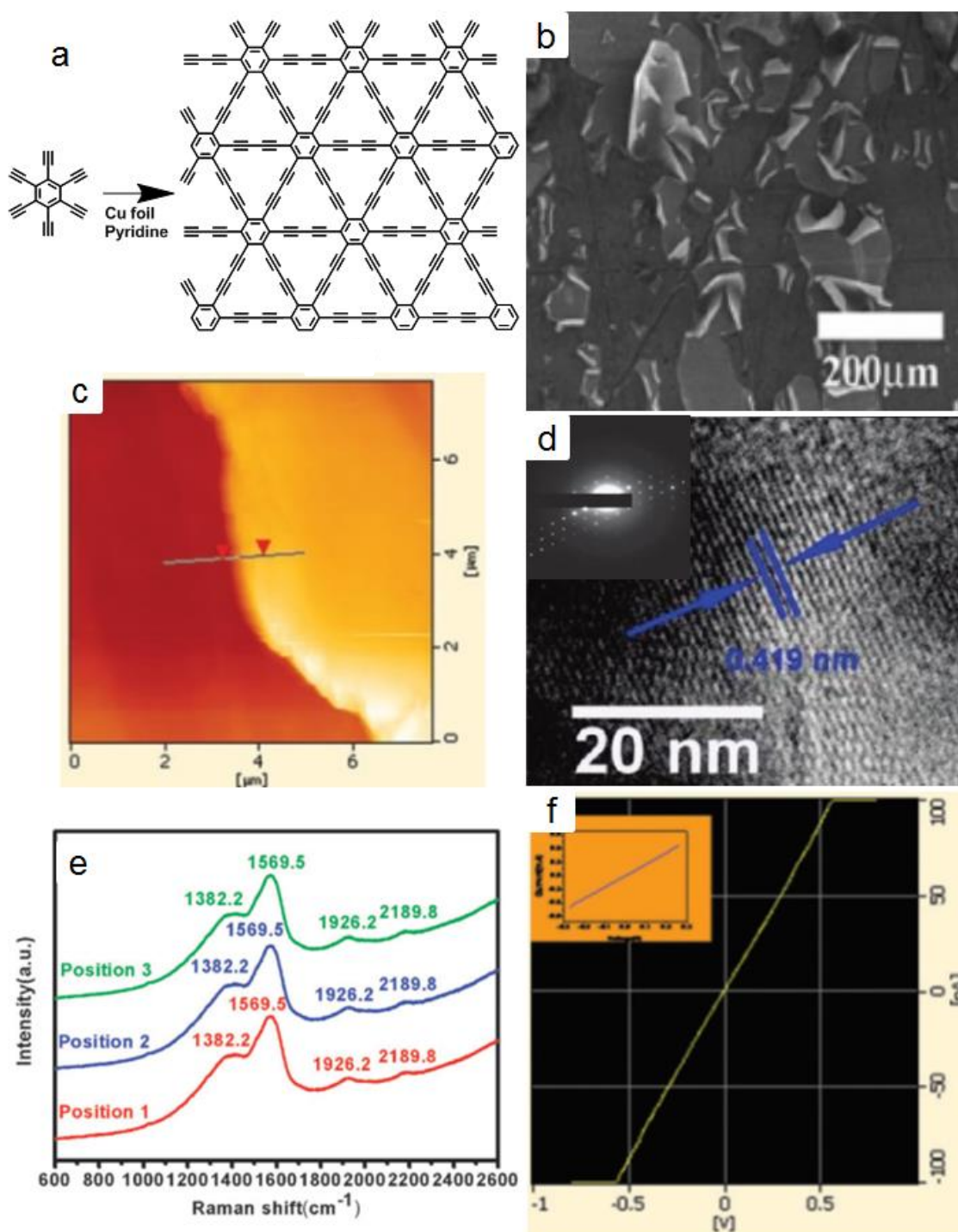


Figure 1.3 (a) Representation of the route of synthesis of GDY films on Cu foil. (b) SEM image of GDY films on Cu foil. (c) AFM image of GDY film (average thickness = 970 nm). (d) HR-TEM of GDY film with clear lattice fringes of 4.19 Å. (e) Raman spectra of GDY films on three different positions. (f) *I-V* curve of GDY films. Reproduced with permission from [76], Copyright (2010) Royal Society of Chemistry.

After the successful *in situ* synthesis of GDY films on Cu foil, in 2015, Zhang's group^[77] synthesized the first GDY nanowalls through a modified Glaser-Hay coupling reaction (Figure 1.4a). The measurements of the thickness of the nanowalls film were achieved by AFM on mechanical exfoliated films transferred on a silicon surface revealing a thickness of

15.5 nm (Figure 1.4c). The selected area electron diffraction (SAED) patterns indicated high crystallinity in certain areas of the nanowalls films (Figure 1.4d). HR-TEM images showed that the value of the lattice fringe was 0.466 nm and another crystal form was simultaneously present in the film; namely curved GDY sheets with a lattice parameter (0.365 nm), which can be assigned to the spacing between two carbon layers (Figure 1.4d). These GDY nanowalls also exhibited excellent and stable field-emission properties (Figure 1.4f,g).

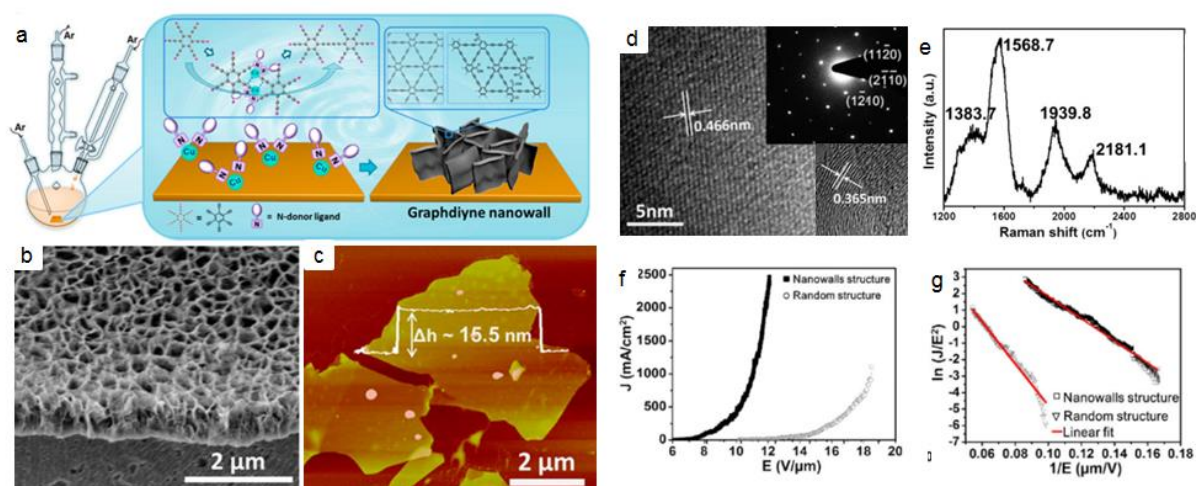


Figure 1.4 (a) Schematic illustration of the experimental setup. (b) Cross-sectional view of SEM image of GDY nanowalls on Cu substrate. (c) AFM image of an exfoliated sample on Si/SiO₂ substrate. The height profile is taken along the white line, representing a 15.5 nm thick film. (d) HR-TEM images of GDY nanowalls; related SAED patterns are in corresponding insets. (e) Raman spectra of GDY nanowalls. (f) Typical plots of the electron-emission current density J as a function of applied electric field E . (g) Corresponding $F-N$ plots and linear fitting. Reproduced with permission from [77], Copyright (2015) American Chemical Society.

Regarding its natural band gap, uniform pores, and highly activated triple bonds, different applications of GDY have been proposed. GDY can form composites with TiO₂, ZnO, Pd and CdSe (Figure 1.5a), and contributes greatly in raising the catalytic properties such as the photocatalytic degradation of dyes, electrocatalysis for water splitting and O₂ reduction.^[78] GDY also shows very high capacities and long-time cycle performance in Li ion batteries (Figure 1.5c)^[79] and can improve the polymer and perovskite solar cell performances (Figure 1.5d).^[80] GDY oxide synthesized by the acid-treatment method was applied as fluorescence sensor of biomolecules such as DNA, since the GDY oxide quenches efficiently the fluorescence of an organic dye labelled single-stranded DNA (Figure 1.5b).^[81] GDY nanowalls with high specific surface roughnesses were also synthesized on a 3D commercially available and low-cost copper foam surface, and then coated with poly(dimethylsiloxane) (PDMS). An extraordinary superhydrophobicity material was formed and used for oil/water separation (Figure 1.5e).^[82]

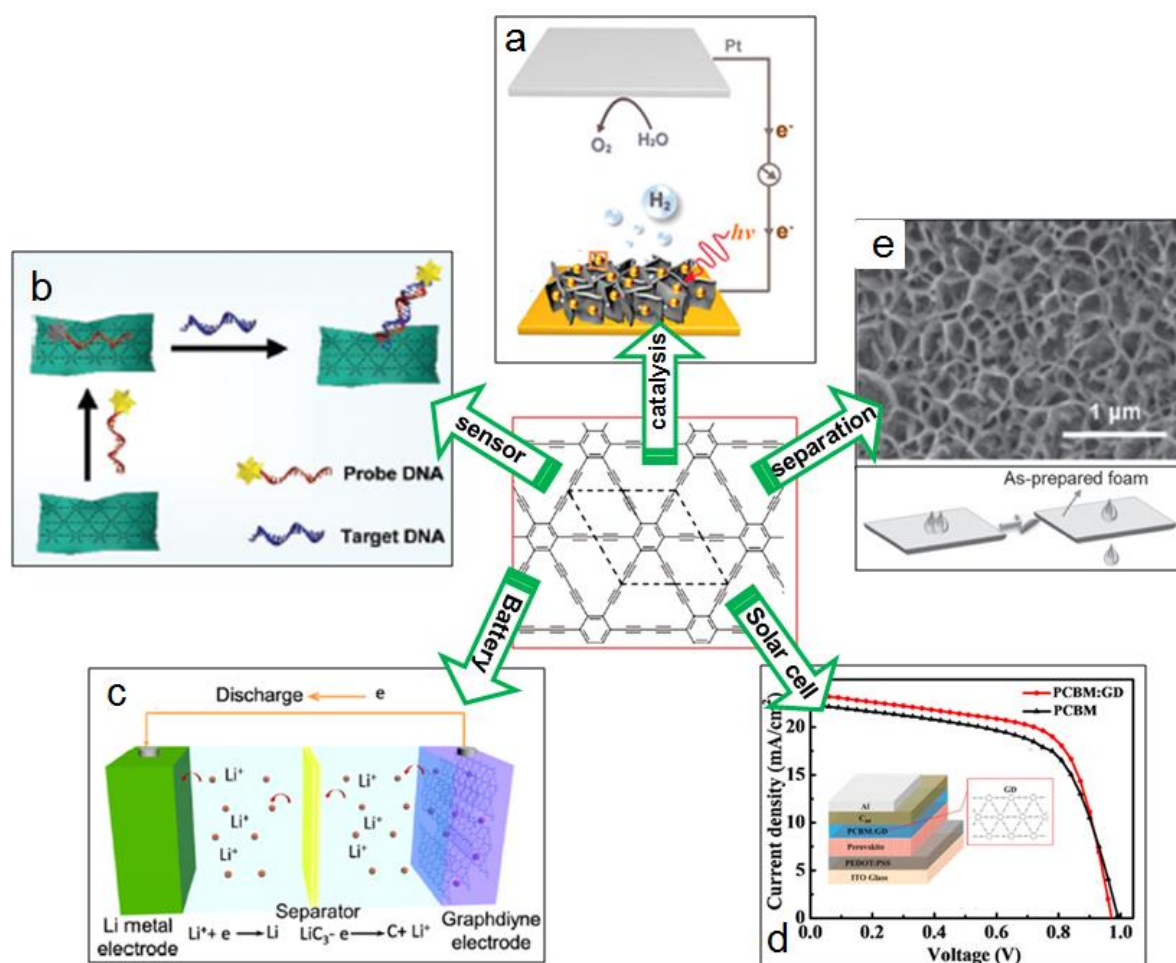


Figure 1.5 (a) Schematic diagram of the photoelectrochemical water splitting cell using CdSe QDs/GDY. Reproduced with permission from [78f], Copyright (2016) American Chemical Society. (b) Schematic illustration of the GDY-based fluorometric DNA assay. Reproduced with permission from [81], Copyright (2016) Royal Society of Chemistry. (c) A representation of an assembled GDY-based battery. Reproduced with permission from [79b], Copyright (2015) Elsevier. (d) Device architecture of perovskite solar cell with GDY and its solar cell performance. Reproduced with permission from [80b], Copyright (2015) American Chemical Society. (e) SEM image of the PDMS-modified GDY-grown copper foam and its oil/water separation mechanism. Reproduced with permission from [82], Copyright (2015) John Wiley and Sons.

On metal surfaces under UHV condition, several conjugated butadiyne polymers have been synthesized and characterized by STM. These will be discussed in next section.

1.3 On-surface assembly and reactions

Early in 1960s, Giaever showed that if the distance of two metal pieces becomes smaller than 10 nm, the electrons can tunnel the gap and a so called tunnel current flows.^[83] Based on this phenomenon, scanning tunneling microscopy (STM) was later developed by Binnig and Rohrer at the IBM Zurich Research Laboratory in Switzerland in 1982.^[84] The importance of STM was soon recognized and the Nobel Prize in Physics was attributed to them in 1986. With this technology, for the first time, atomic resolution of solid surfaces had become possible to be observed.

Early STM works deal mainly with the investigation of the clean, bare surfaces under UHV conditions. Later, STM started to be used in alternative environments and media, such as air, water, and various other liquid or gas atmospheres.

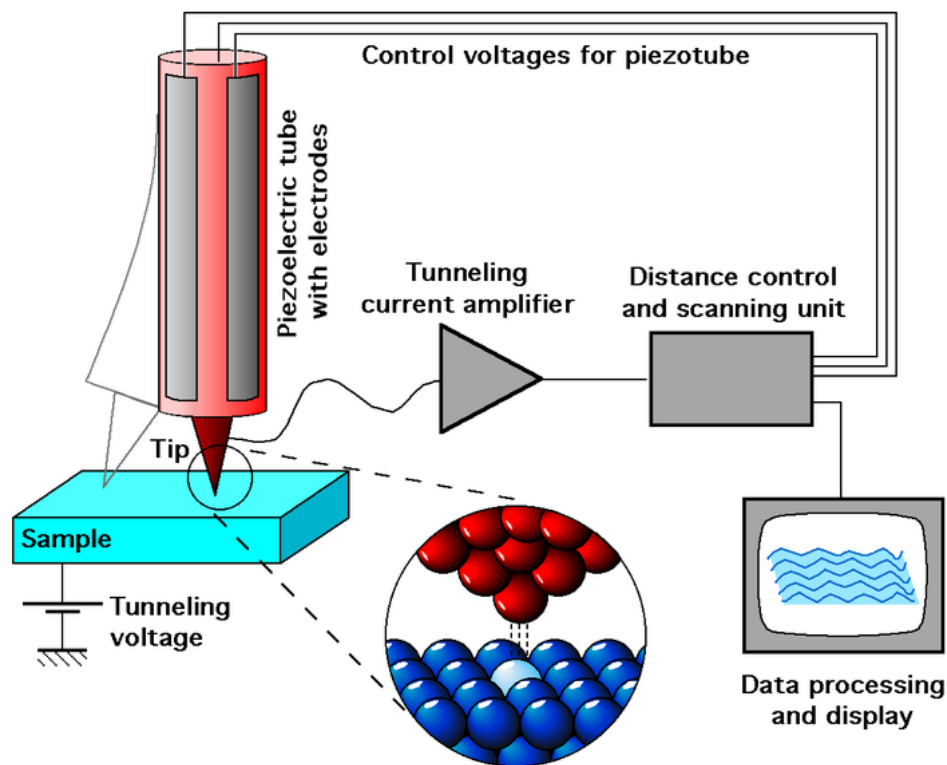


Figure 1.6 Schematic representation of the working principle of STM. Source: https://en.wikipedia.org/wiki/Scanning_tunneling_microscope#/media/File:ScanningTunnelingMicroscope_schematic.png

Figure 1.6 shows the working scheme of an STM. An STM contains an atomically-sharp tip, an atomic flat surface sample, a piezoelectric tube, a controlling digit circuit system and a compute supporting system. The tips are either mechanically formed Pt/Ir (4:1) alloy tips or electrochemically etched Pt/Ir or W-tips. The surface samples normally consist typically of single crystals of Au, Ag, Cu, Ni, Pd, Ru, and HOPG.

The x , y and z movements of the tip can be picometer-precisely controlled by changing the voltages applied on the piezoelectric tube. When the tip is close enough to the sample (typically at 5-10 Å), a measurable tunneling current I can flow between the tip and the sample, after applying a bias voltage. The tunneling current I depends in first approximation exponentially on z (typically, a 1 Å displacement in z implies a ten-fold variation in I). This endows the STM atomic resolution with typically 0.1 nm lateral resolution and 0.01 nm depth resolution.

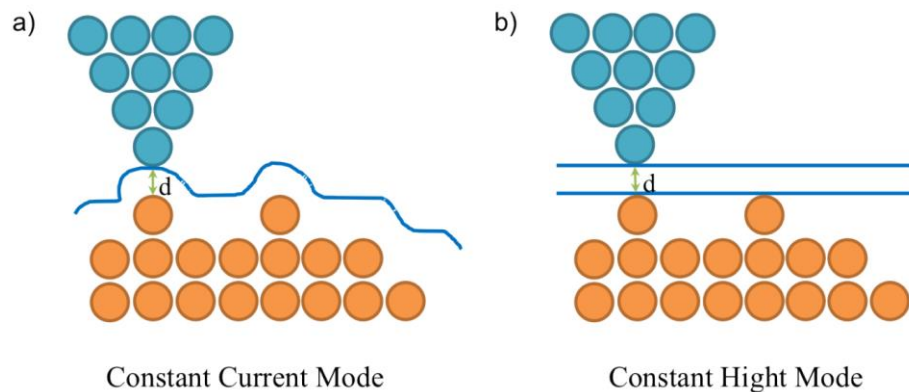


Figure 1.7 Schematic representations of (a) constant current mode and (b) constant height mode of the STM.

The constant current mode and the constant height mode are two different scanning modes of STM (Figure 1.7). In the constant current mode, the tunneling current is kept constant by using a feedback mechanism to change the distance between the tip and the sample. Recording the feedback signal as a function of the lateral tip position yields a 3D map of the surface topography. In this way, the acquired STM topographies show the better coincidence with theoretical predictions than the constant height mode.

The constant height mode can scan faster than the constant current mode, but it still needs a weak feedback to keep the average tip sample distance constant. Under not particular low temperature and small size (< 100 nm) scanning conditions, the higher scan rates are very helpful to reduce the influence of thermal and mechanical drift. However, this mode is only suitable for very flat surfaces; otherwise it is easy to cause the crash of the tip with the surface.

Under (i) small bias, (ii) low temperature, and the assumption of (iii) a spherical tip represented solely by an s -wave function, Tersoff and Hamann indicated that the tunneling current was only proportional to the surface local density of states (LDOS) near the Fermi level, E_F .^[85]

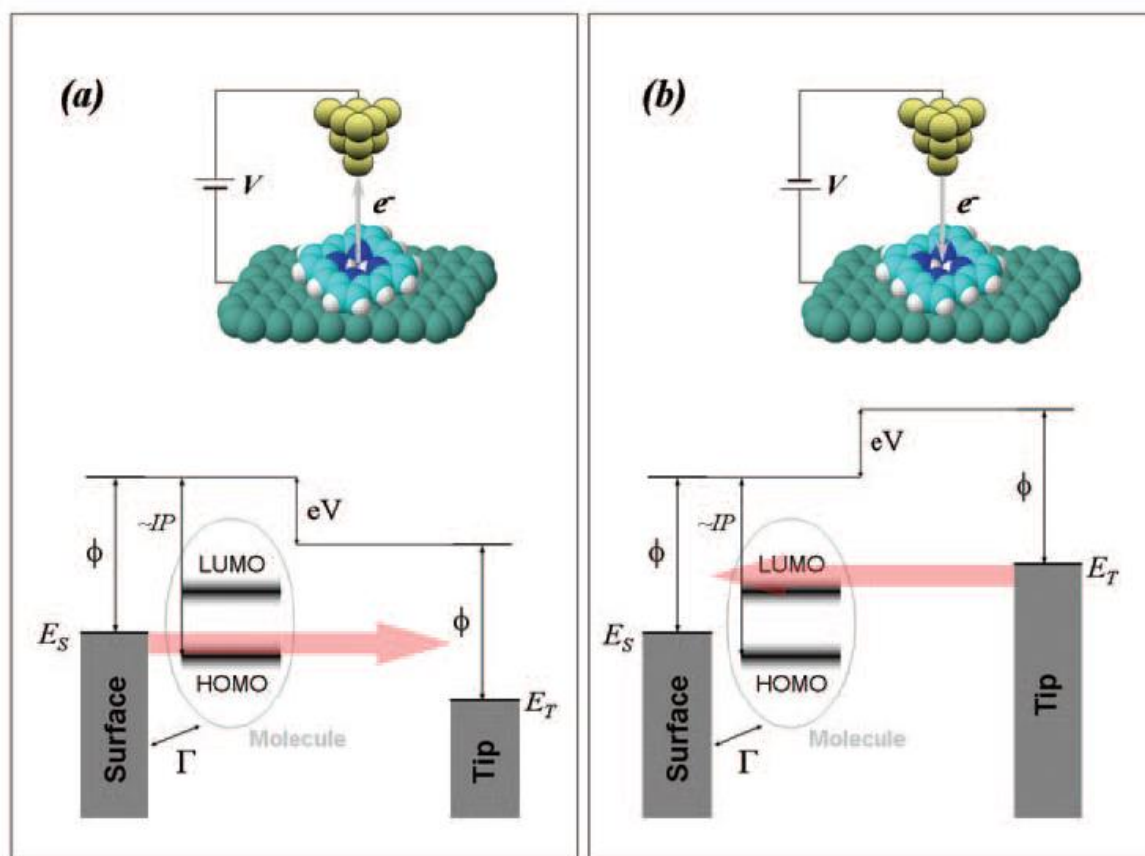


Figure 1.8 (a) When applying a negative sample bias, the electron transport goes through the HOMO of the adsorbate. (b) When a positive bias added, the charge transport is dominated by the LUMO. Fermi levels of substrate (E_S), tip (E_T) and electronic coupling (I) are indicated. The Fermi level of the substrate and the HOMO of a free molecule are referred to the vacuum level by the work function, Φ , and ionization potential, IP , respectively. Source: <http://www.bruker.co.jp/axs/nano/imgs/pdf/AN085.pdf>

When considering the density of states (DOS) of the overall system, the frontier orbitals of the molecular adsorbate must be taken into account (Figure 1.8). Normally, the E_F of the metal is between the HOMO and LUMO energy level of organic adsorbate. When a negative sample bias is applied, and if the HOMO is near to the E_F of the surface metal, the electron transmission is mainly through the HOMO of the adsorbate. When an appropriate bias voltage is applied, the scanning tunneling spectroscopy (STS) mapping reveals the shape of individual molecular HOMO orbital. Conversely, when a positive sample bias is used, the LUMO of adsorbate dominates the electrons transport and the shape of the LUMO can be observed in STS mapping.

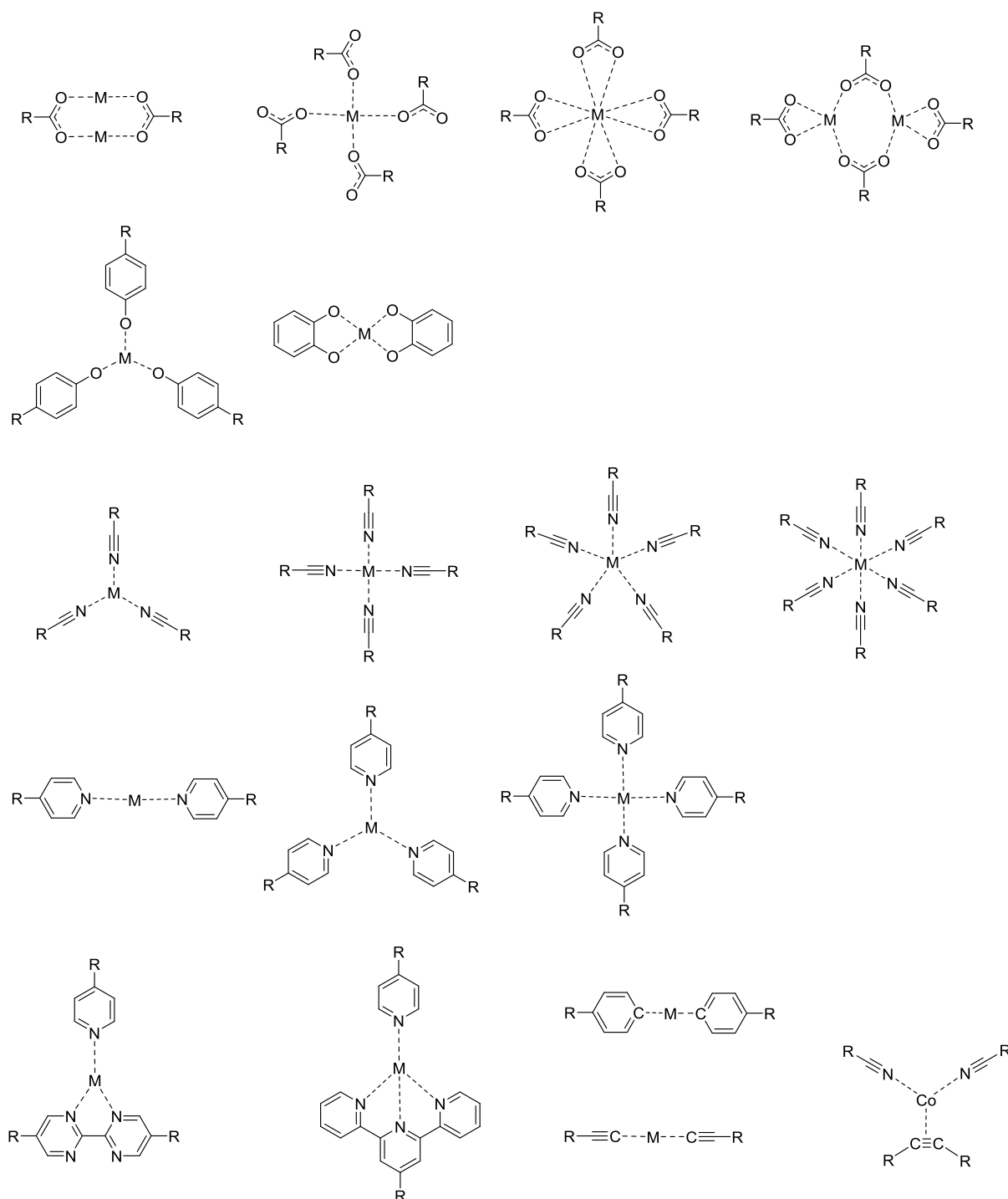
However, the influences of electronic coupling (I) between the adsorbate and substrate, and the tip and sample interactions will also affect the shape of the adsorbates. For example, alkali metal atoms are sometimes transparent in STM images due to the tip and sample interactions.^[86]

In another way, STS can show the electron DOS at local positions of the tip. During the measurement, the STM tip is placed above a particular position on the sample, then the bias is varied, and the tunneling current is recorded. The dI/dV peaks of the data will reveal the HOMO and LUMO energy level of the adsorbates and other properties such as Kondo effect.^[87]

Accounting to the atomic resolution and electron transport indicating LDOS, STM has been a powerful tool for many scientific research areas, especially for nanoscience. Taking profit from the bottom-up self-assembly of single layer of molecules on single crystals of metals or HOPG, STM is a very useful tool to address single molecules. After addition of a magnetic field, it has even become a tool for investigations of quantum and spintronic devices.^[88] With introduction of thermal or light treatment, STM has become adapted to elucidating chemical reactions paths and catalytic mechanisms closed to metal surface.^[58] Syntheses of 2D coordinated networks^[89] and 1D or 2D covalent conjugated polymers^[90] on metal surface has also become very common by the use of STM.

2D supramolecular self-assembly on surface has been enabled through formation of weak and reversible non-covalent interactions, such as hydrogen bonding, dipole-dipole, van der Waals interactions and coordination bonding. Meanwhile, the interaction between substrate and adsorbate, so called chemi- or physisorption, depending on its strength, is also a very important factor steering the self-assembly under surface confinement.

Thus, various hydrogen bond systems have been studied on solid surfaces, such as hydrogen bonds between carboxylic groups ($C=O\cdots H-O$),^[91] carbonyl groups and hydrogen atoms on amino groups ($C=O\cdots H-N$),^[92] carbonitrile groups and phenyl groups ($CN\cdots H-Ph$),^[93] pyridyl groups and hydrogen atoms of aryl group ($N\cdots H-Ar$),^[94] etc.



Scheme 1.10 Library of coordinated models of metals and ligands on surfaces.^[89,95]

Coordination bonds (about 0.5-2 eV) show an increased bonding energy compared to hydrogen bonds (about 0.05-0.7 eV), and endow 2D coordination polymer networks with high thermal stability on surfaces.^[95f] When the metal and ligands are varied, the coordination number of the metal ion or atom on the surface can range from 2 to 6 (Scheme 1.10). The transition metal atoms normally prefer the coordination numbers 2 to 4, while lanthanide metal atoms prefer more coordination numbers ranging from 3 to 6.^[95b,95g,95h] When the ratio

of europium (Eu) atoms and *para*-quaterphenyl-dicarbonitrile (qdc) ligands is carefully controlled, Urgel et al. could obtain different kinds of porous networks, including the simultaneous expressions of four-fold, five-fold and six-fold vertices on Au(111) surfaces.^[95h] STM results show that there are four kinds of Eu-qdc networks formed by controlling different Eu:qdc ratios: (1) random string networks based on three-fold coordination nodes (Figure 1.9b,f Eu:qdc \approx 2:3), (2) reticular four-fold assemblies (Figure 1.9c,g Eu:qdc \approx 2:4), (3) complex tiling schemes (Figure 1.9d,h Eu:qdc \approx 2:5) and (4) a hexagonal lattice stabilized by six-fold nodes (Figure 1.9e,i Eu:qdc \approx 2:6). Interestingly, the open-porous networks obtained for a \sim 2:5 Eu:qdc stoichiometry show dodecagonal random-tiling with quasicrystallinity features.

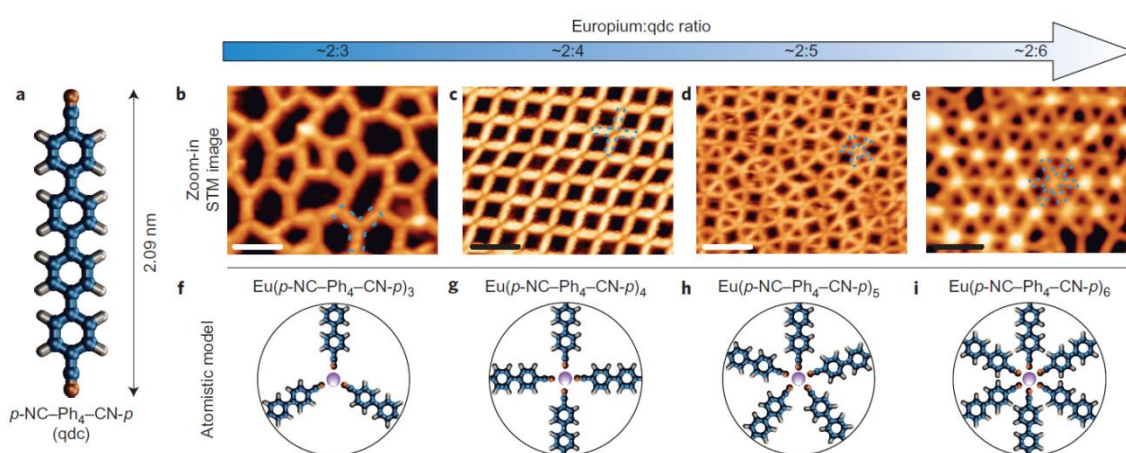
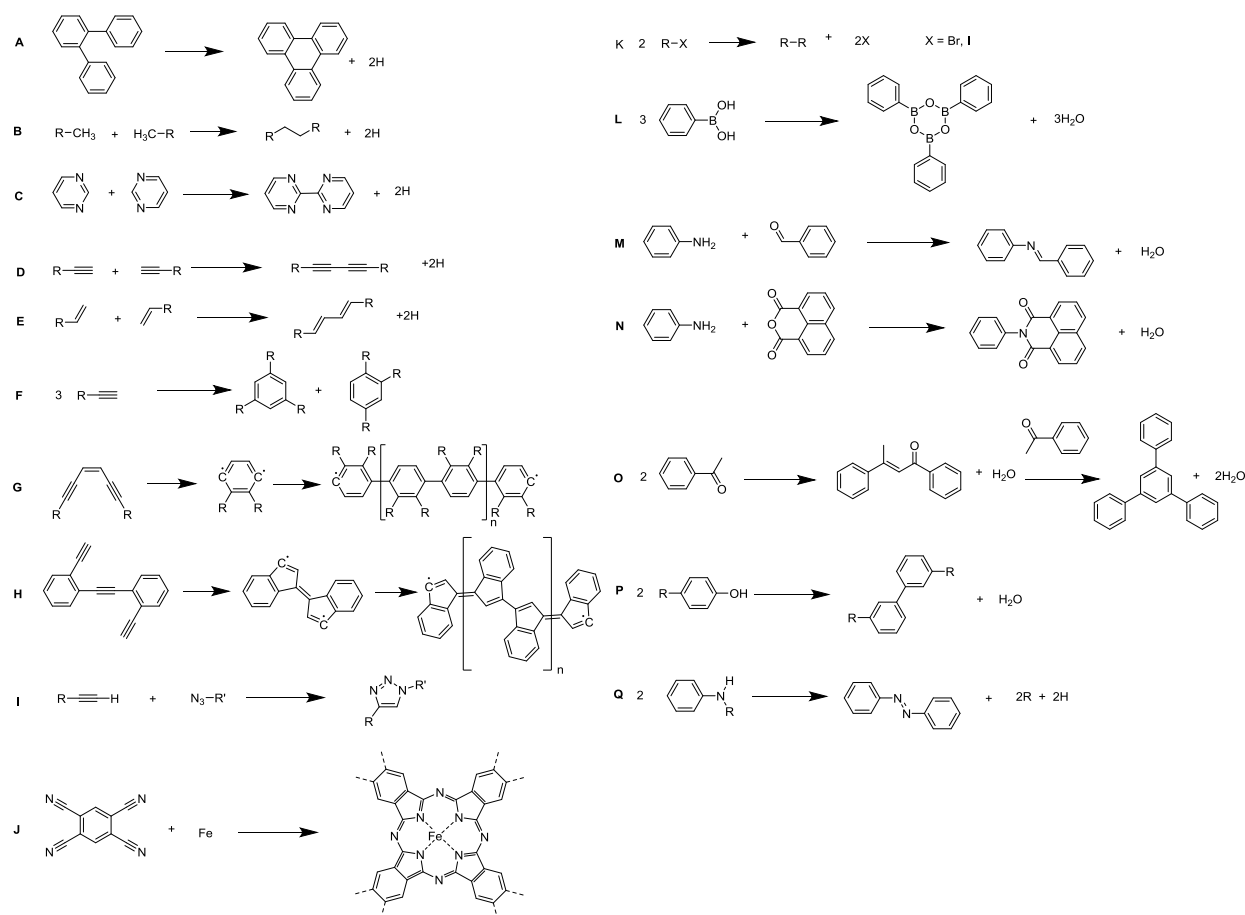


Figure 1.9 Eu-directed assembly of metal-organic coordination networks on Au(111). (a) The *para*-quaterphenyl-dicarbonitrile (qdc) molecule. (b-e), High-resolution STM images of the distinct coordination networks designed at varying Eu:linker stoichiometry. (Scale bar, 5 nm.) (f-i), Atomistic models of (b-e) highlighting the distinct coordination nodes that stabilize the assemblies: three-fold (f), four-fold (g), five-fold (h) and six-fold (i). Reproduced with permission from [95h], Copyright (2016) Nature Publishing Group.



Scheme 1.11 Summary of different chemical reactions researched under metal surface confinement.^[90]

Surface-assisted organic reactions, studied by STM, have been an appealing way to understand precise reaction mechanisms, because some reaction intermediates can be observed atomically. It also provides an innovative route for the bottom-up fabrication of 1D and 2D covalent organic frameworks and some graphene analogues may show potential for applications in molecular electronics and optoelectronics. Various reactions have been introduced in surface, which are non-exhaustively listed in Scheme 1.11.^[90]

The Ullmann reaction is the most popular approach to obtain 1D and 2D conjugated polymers on surface (Scheme 1.11K).^[96] In 2007, Grill et al. firstly reported utilizing this method to synthesize 1D and 2D porphyrins polymer on Au(111).^[96c] By combining Ullmann and cyclodehydrogenation reactions (Scheme 1.11B), Fasel's group designed the brominated precursors and fabricated atomically precise graphene nanoribbons on Au(111) surface.^[97]

In another way, the byproduct free reactions or reactions only releasing H_2 or other small gas molecules on surface are preferred and chased by scientists.

With its active H atom in C–H, pyrimidine can form 1D tetraazaperopyrenes polymer through pyrimidine-pyrimidine coupling on Cu(111) surface after thermal treatment (Scheme 1.11C).^[98]

On Ag(111), Au(111) and Cu(111) surfaces, the homo-coupling and cyclotrimerization of terminal alkynes can be triggered (Scheme 1.11D,F). On Ag(111), the homo-coupling is the preferred reaction,^[63b] while on Au(111) the cyclotrimerization is the dominant reaction.^[20] On Cu(111), the two reactions and other side reactions will occur simultaneously resulting in variable product distributions.^[99] Several approaches such as sterically hindered substitutions, surface templates, organometallic intermediates and irradiation by UV light, have been proposed and realized in order to avoid these side reactions, aiming to achieve homo-coupling products such as longer 1D GDY wires and larger areas of 2D GDY nanosheets.^[58]

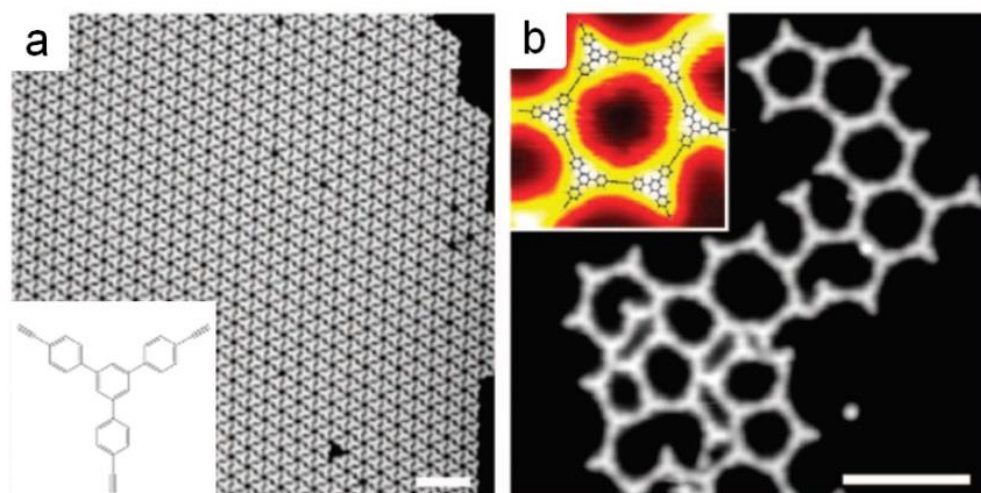


Figure 1.10 (a) STM image of the densely packed phase of unreacted 1,3,5-tris-(4-ethynylphenyl)benzene molecules on Ag(111) with substrate temperature of 152 K. (Scale bar 50 Å) (b) In the magnified area an open reticular structure from the merged ethynyl moieties prevails after 400 K annealing. The inset shows a single honeycomb nanopore superimposed with a HYPERCHEM calculated model. (Scale bar 50 Å). Reproduced with permission from [63], Copyright (2012) Nature Publishing Group.

The first example of an on-surface synthesized GDY structure analysed by STM was achieved in 2012.^[63b] Barth's group introduced the 1,3,5-tris-(4-ethynylphenyl)benzene to Ag(111) surfaces (Figure 1.10). After annealing at 400 K, the molecular precursors with endstanding alkyne groups coupled to a 2D conjugated open-porous network (Figure 1.10b), whereby the dominant linear homo-coupling reaction introduced repeated honeycomb units. However, due to the formation kinetics involving flexible monomers and the non-reversibility of the C–C coupling, beside hexagons, also pentagons and heptagons were formed and spurious side reactions occurred involving more than two alkyne bond fading away the long-range order of the network.

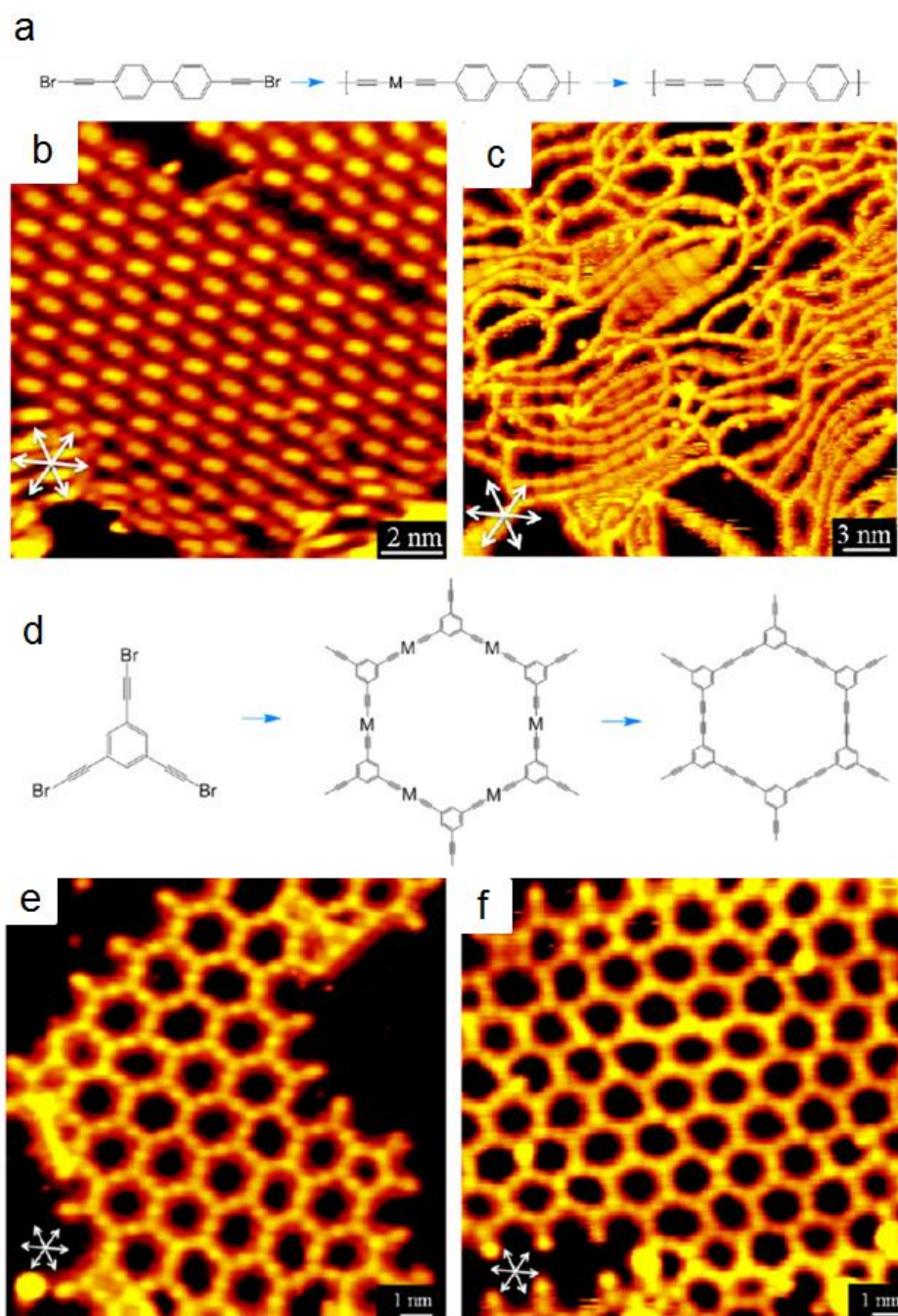


Figure 1.11 (a,d) Schematic illustrations of dehalogenative homo-couplings of 4,4'-di(bromoethynyl)-1,1'-biphenyl (bBEBP) (a) and 1,3,5-tris(bromoethynyl)benzene molecule (tBEP) (d). (b,e) STM images showing the formation of the C–Au–C organometallic network after deposition of bBEBP (b) and tBEP (e) molecules on Au(111) at RT and slight annealing to 320 K. (c,f) STM images showing the formation of molecular wires and networks mainly with acetylenic scaffoldings after annealing the bBEBP (c) and tBEP (f) to 425 K and 450 K respectively. Reproduced with permission from [100], Copyright (2016) American Chemical Society.

Xu's group^[100] introduced a terminal alkynyl bromide onto Au(111). After thermal treatment of the organic layer at 320 K, a large area of C–Au–C organometallic network formed (Figure 1.11b,e). After increasing the temperature up to 420 K, 1D molecular wires (Figure 1.11a,c) and 2D molecular networks (Figure 1.11d,f) evolved exhibiting acetylenic

scaffoldings. The 2D network showed a very regular honeycomb structure being first example of a large area of 2D GDY structure observed at molecular level. The C–Au–C organometallic intermediates are obviously good templates for the dehalogenative homo-coupling reactions to form large area GDY.

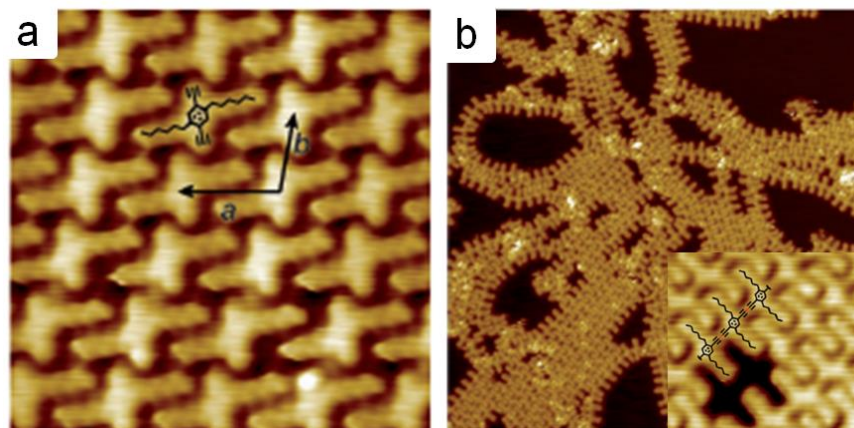


Figure 1.12 (a) High-resolution STM image of 1,4-diethynyl-2,5-dihexylbenzene on Au(111) (0.5 V, 100 pA, 6 nm × 6 nm). (b) STM image and high-resolution image (inset) of 1,4-diethynyl-2,5-dihexylbenzene on Ag(111) after 398 K annealing (0.5 V, 50 pA, 40 nm × 40 nm and 5 nm × 5 nm). Reproduced with permission from [64], Copyright (2013) John Wiley and Sons.

Fuchs' group^[64] used the molecule 1,4-diethynyl-2,5-dihexylbenzene with a lateral hexyl substitution at the conjugated alkyne backbone to increase the steric shielding of the alkyne to suppress side reactions during the Glaser coupling obtaining long linear polymer chains after annealing at 398 K (Figure 1.12). The self-assembled structure (Figure 1.12a) is a good template for the homo-coupling reaction. The results on different metal surfaces resume that the homo-coupling reaction is more efficient on the Ag(111) surface than on Au(111) and Cu(111).

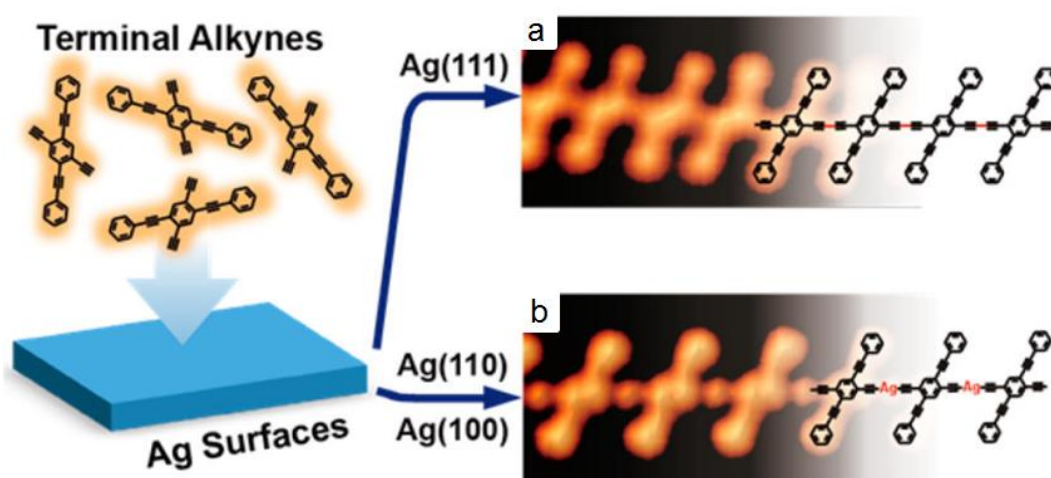


Figure 1.13 (a) High-resolution STM images of 1D GDY wire after annealing at about 350 K with the chemical structure superimposed. (b) High-resolution STM image of organometallic chain after

annealing at about 350 K on Ag(110) achieved by using a CO-modified tip. Reproduced with permission from [101], Copyright (2015) American Chemical Society.

Following same strategy as the work of Fuchs' group^[64], Wu's group^[101] used the phenylethynyl group with steric hindrance. After annealing at 350 K, the 2,5-diethynyl-1,4-bis(phenylethynyl)benzene precursors formed successfully on Ag(111) 1D GDY wires (Figure 1.13a). Interestingly, on Ag(110) and Ag(100), the terminal alkynes reacted with surface metal atoms, leading to 1D organometallic nanostructures (Figure 1.13b). Detailed experimental and theoretical analyses revealed that such a lattice dependence of the terminal alkyne reaction at surfaces originated from the epitaxial matching of the produced molecular wires with the substrate lattice structures.

Several precursors that possess two alkyne groups in ortho positions of a phenyl ring or alternatively two alkyne groups in *E*-positions of an alkene are going to form radicals that further polymerize, after annealing, to 1D chains in a so-called Bergmann reaction (Scheme 1.11G,H).^[102] Condensation reactions such as Schiff base reactions (Scheme 1.11M),^[103] boronic acid-based couplings (Scheme 1.11L),^[104] acylation reactions (Scheme 1.11N)^[105] and Aldol condensations (Scheme 1.11O)^[106], have been used on surfaces. Click reactions between azides and alkynes have successfully approached on Au(111) surfaces at room temperature conditions (Scheme 1.11I) mainly leading the dimeric and trimeric products.^[107] The protecting-group activation approach uses precursors in which, during annealing process, the protecting groups can be removed giving access to the *in-situ* coupling reactions (Scheme 1.11Q).^[108]

1.4 Mechanically controllable break junctions

Molecular electronics investigations focus mainly on the research of the charge transport properties of single molecule junctions and ensembles such as self-assembled single layer of molecules. The electrodes are normally made of metal such as Au, Ag, W, Pd and Pt, or nonmetal materials such as carbon nanotubes, graphene, polymer-consisted or silicon-based materials.^[109] The break junction (BJ) technique as an important set-up for single-molecule junctions and can be classified into (i) scanning tunneling microscope break junction (STM-BJ) and (ii) mechanically controllable break junction (MCBJ).

The first report about the use of MCBJ for measuring the transport through a single molecules was given by Reed in 1997.^[110] Later this technique has been widely used by several groups for various molecular conductance measurements.

The MCBJs exhibit several advantages: (1) The MCBJ setup can be easily integrated with other systems, such as a Raman spectrometer or high vacuum TEM system due to its small size and flexible configuration. (2) It has less impurity of electrodes due to the *in situ* formation of the junctions by breaking of Au bridges without chemical treatments. (3) With advanced lithographical techniques the electrodes can be scaled down to molecular dimensions, which make them well suitable for single-molecule measurements. (4) A high mechanical stability compared to other techniques, due to the picometer accuracy of the motion of the push rod causing an attenuated horizontal displacement in the electrodes by several magnitudes, suspended the disturbing effects through the piezoelectric components, such as mechanical vibration, thermal expansion, or voltage instability. Thus, the gap size can be controlled with nanometer resolution.

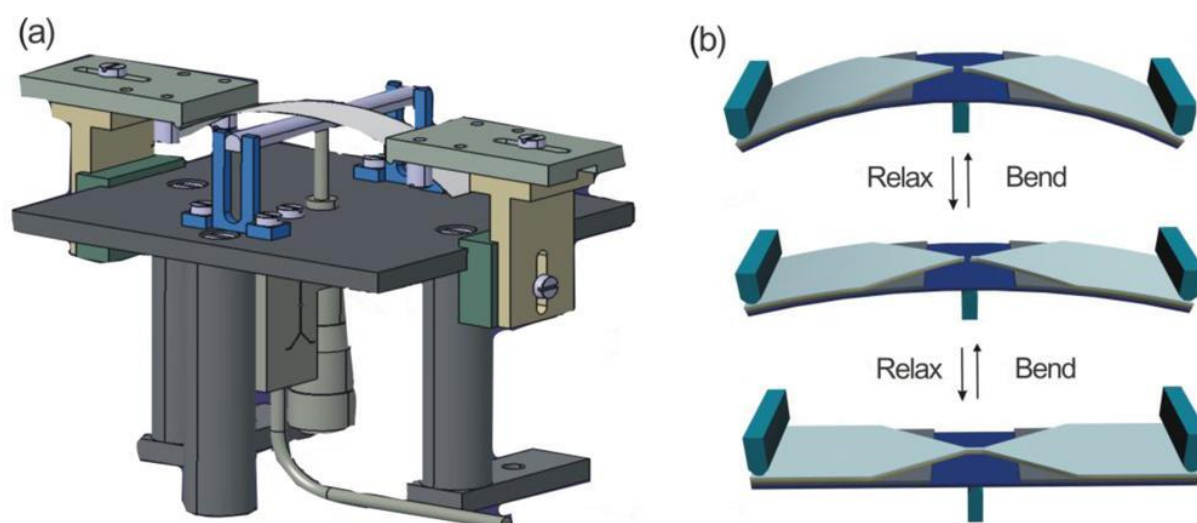


Figure 1.14 (a) Schematic representation of the MCBJ setup. (b) Working principle of the MCBJ setup. Reproduced with permission from [109], Copyright (2016) American Chemical Society.

An MCBJ setup typically consists of three parts: a flexible substrate containing a macro-fabricated metal wire, a push rod to break the nanostructure, and a counter support to bend the substrate (Figure 1.14).

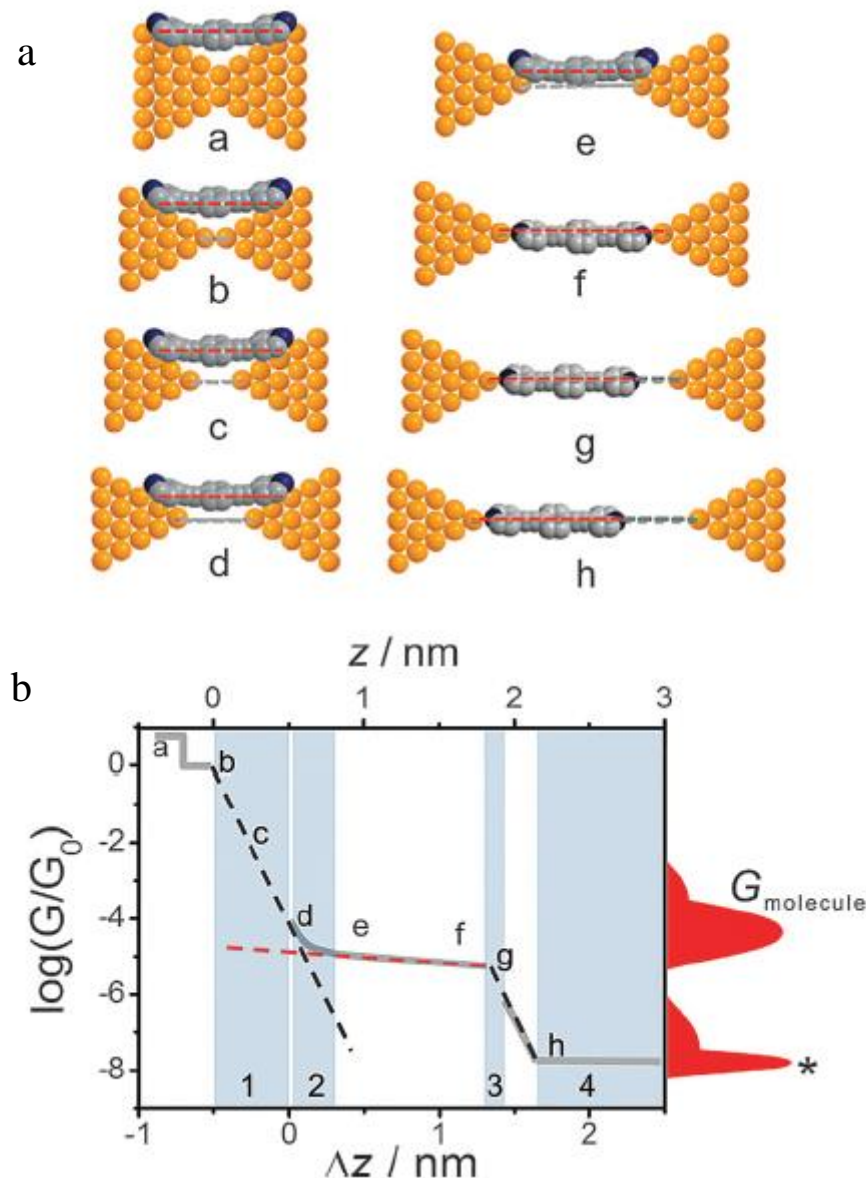


Figure 1.15 (a) Schematic representation of the process of formation of a molecular junction during MCBJ measurements. (b) Simplified schematic representation of a measured conductance trace (solid light gray line) with conductance contributions from direct tunneling (gray dashed lines) and from the molecule (red dashed line). A 1D conductance histogram is depicted in the red color on the right side of (b). Reproduced with permission from [111], Copyright (2015) Royal Society of Chemistry.

As shown in Figure 1.15, the process of formation of a molecular junction during MCBJ measurements can be divided into five steps.

Step 1: fabrication of Au bridge.

(a) A Au bridge with a notch is microfabricated onto the substrate by advanced lithographic techniques exhibiting a conductance G higher than G_0 .

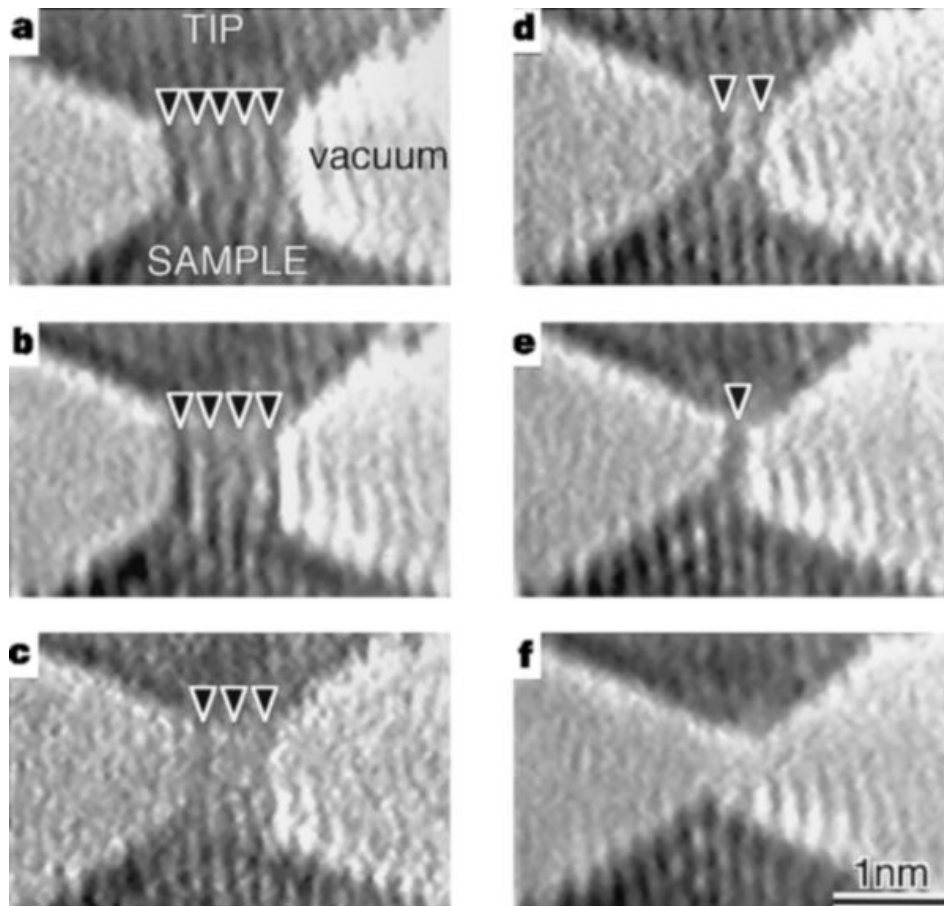


Figure 1.16 TEM images of gold bridge formation by a small STM setup. A gold bridge formed between the gold tip (top) and the gold substrate (bottom), thinned from (a) to (e) and ruptured at (f), with observation time of 0, 0.47, 1.23, 1.33, 1.80 and 2.17 s, respectively. Reproduced with permission from [112], Copyright (1998) Nature Publishing Group.

Step 2: Breaking of the metal-metal contact.

(b) When the substrate is bent, the metal wire starts to elongate, resulting in a decrease of the cross section at the notch. A further elongation will slowly lead to a complete fracture of the metal wire at the notch point. The electrodes form an atomic contact, lower than G_0 . This breaking procedure was observed by Ohnishi et al. in atomic resolution using a HR-TEM with a miniature STM inside (Figure 1.16).^[112] Firstly, they put the gold tip inside the gold sample surface, and then slowly retracted the gold tip. The HR-TEM results showed that along the [110] direction, the number of atomic rows in the connecting nanowire gradually decreased to one atom strand, and the conductance decreased simultaneously to $2e^2/h$.

(c) After the bridge is broken, freshly cleaved electrodes are generated. The conductance in a very short distance cannot be measured because of the fast snap-back processes (region 1 in Figure 1.15b).

Step 3: Sliding of molecules along the electrodes.

(d) When the distance of the electrodes keeps on to be elongated, an electrode-molecule-electrode junction is formed. The observed conductance is attributed to direct tunneling through the molecule (region 2 in Figure 1.15b).

Step 4: Formation of a molecular junction.

(e) As the electrode-molecule-electrode junction is elongated, the anchoring groups of the molecules nicely attach to the opposite electrodes surfaces and bridge the gap. Most of the conductance is attributed to the molecule and a conductance plateau is observed. (f) At the end of the plateau, a junction with the fully extended molecule is formed.

Step 5: Breaking of a molecular junction.

(g) Further bending of the substrate leads to a snap-back of the molecular junction and the conductance decreases sharply. This sharp decrease in conductance (region 3 in Figure 1.15b) may be attributed to intermolecular interactions, such as π - π interaction or hydrogen-bonds between neighboring molecules. (h) An enlarged nanogap is formed in the electrode-molecule junction and the other electrode (gray dashed line). The conductance measurement is limited by the sensitivity of the current detection in the MCBJ set-up (usually with range from $10^{-5} G_0$ to $10^{-9} G_0$, region 4 in Figure 1.15b).

Because of the different conditions of each breaking in a metal-metal contact and observed instabilities of the assembly and the binding, the shape of each conductance trace will be rather different. The statistical analysis of thousands of individual stretching traces is required to determine the most probable conductance, the plateau length and the junction formation probability. Thus, so-called 2D histograms, 1D logarithmic conductance histograms and the plateau length histograms have been widely used to acquire quantitative information from break junctions (Figure 1.17).^[113]

When numerous conductance (stretching) traces are plotted in the 1D conductance histogram, the peak (or peaks) may reveal indicating the most probable single-molecule conductance (Figure 1.17b). Logarithmic scale plots of the conductance can distinguish the different conductance features. When putting thousands of individual conductance-distance traces overlaid together in 2D space, 2D histograms are generated (Figure 1.17c) providing additional information about the conductance evolution during the stretching process. A plateau length histogram can reveal the distance distribution of the molecular plateau (Figure 1.17d). Normally, the stretching length is calculated by taking the relative zero position and the end of the high conductance feature into account. This actual separation is usually comparable to the molecular length indicating of a single-molecule junction.

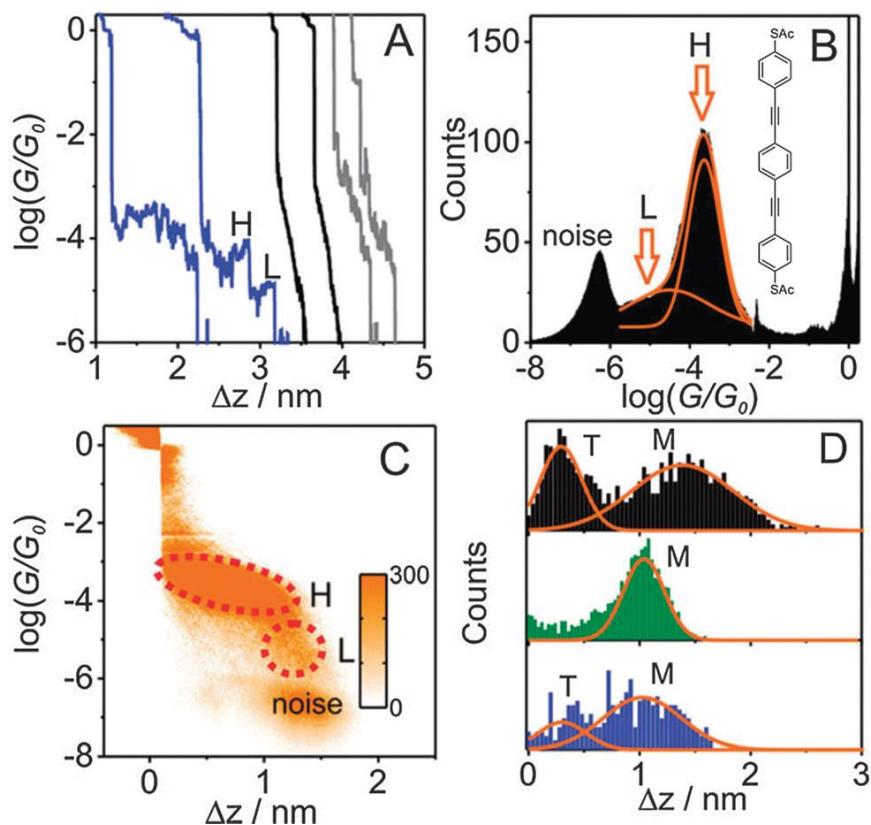


Figure 1.17 Different statistical analysis methods for the conductance measurements of the OPE3-dithiol (the molecular structure is shown in panel (b)). (a) Typical conductance distance traces recorded at $V_{\text{bias}} = 0.1$ V. (b) 1D conductance histogram and (c) 2D histogram generated from 2000 individual curves. High and low conductance features are marked as H and L, respectively. (d) Characteristic length distributions for the stretching of molecular junctions, with stretching rates of 145 (black), 58 (green), and 1.45 nm s^{-1} (blue), $V_{\text{bias}} = 0.10$ V. Reproduced with permission from [113], Copyright (2012) American Chemical Society.

The conductance mechanism is generally determined by Γ and U . Γ represents the coupling parameter of the molecule and electrode. U is the HOMO-LUMO gap energy of the molecule.^[114]

When $\Gamma \ll U$, the system is in the weak coupling regime. The anchor group is weakly coordinated with the electrodes, and the wavefunctions of molecules have little mixing with the electronic states of the electrodes (Figure 1.18a). The charge transfer is described by a two steps hopping process. At low temperature, the Coulomb-blockade phenomenon occurs: without matched energy levels of molecule and electrodes, the electron transport is blocked unless a gate voltage is applied.

When $\Gamma \gg U$, the molecules are covalent bonded to the electrodes and the system belongs to strong coupling regime. The wavefunctions of the molecule overlap with the electronic states of the electrodes broadening the energy levels of the molecule (Figure 1.18c). The electron transport occurs through the molecule by a one-step process.

When Γ and U are not differing too much, the system is in the intermediate coupling regime. The molecular energy levels are partially broadened (Figure 1.18b).

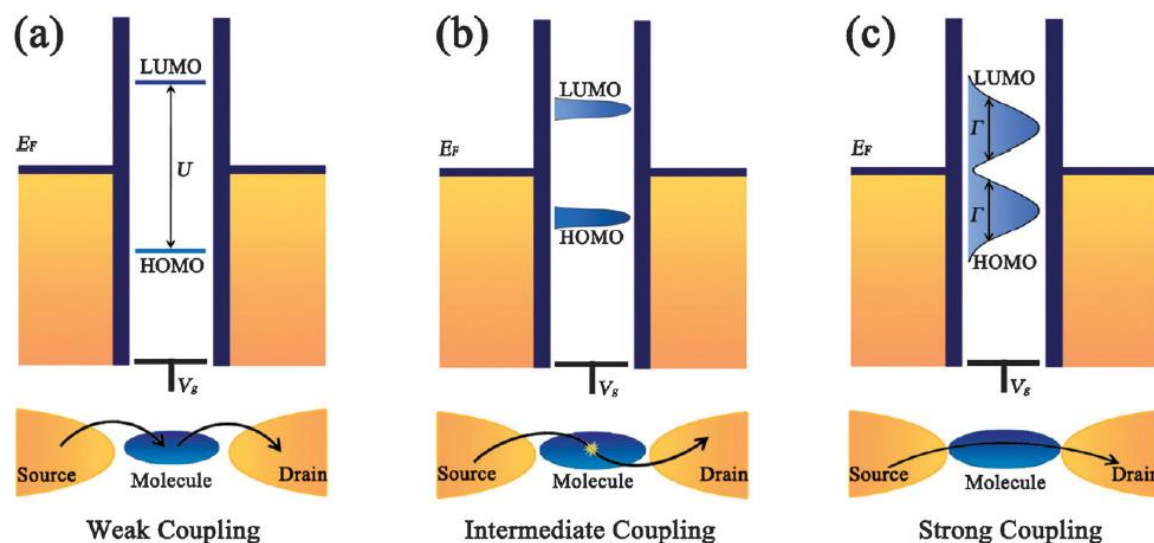
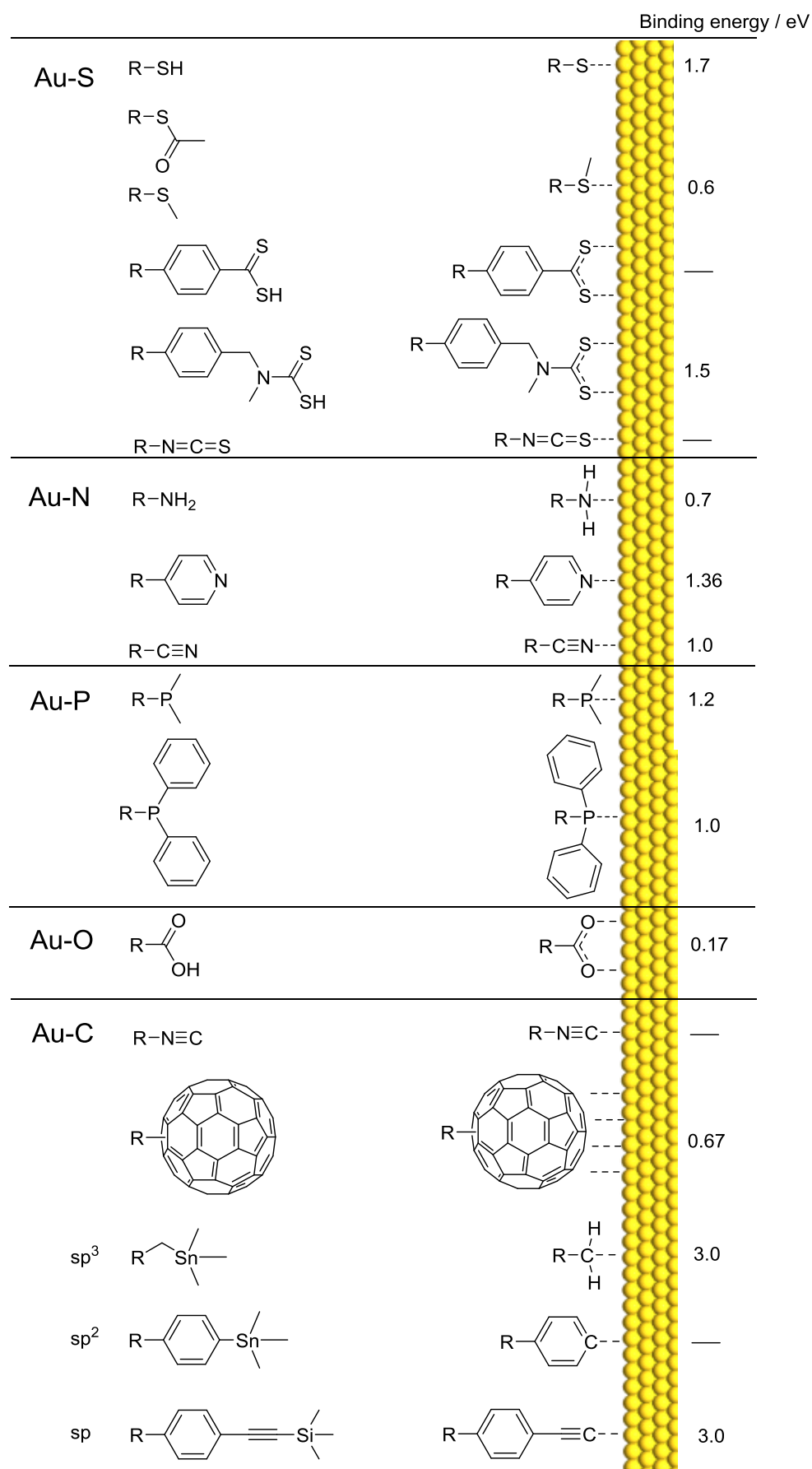


Figure 1.18 Schematic representation of the conductance mechanism affected by Γ . (a) In the weak coupling regime, electron transport takes place in a two-step process. (b) In the intermediate coupling regime, the HOMO and LUMO become broader and closer to Fermi energy of electrodes (E_F), and electron transport through the molecules interacting with the electrons on the molecules. (c) In the strong coupling regime, a large broadening of molecular energy levels occurs, and electrons move from the source to the drain through a one-step process. Reproduced with permission from [114], Copyright (2013) Royal Society of Chemistry.

For the weak coupling regime, the electron doping pathway is normally through the LUMO of the molecule, such as the anchor groups as $-\text{CN}$ and pyridine. For the intermediate and strong coupling systems, the electron transport pathway is normally through the HOMO of the molecule, such as $-\text{NH}_2$, $-\text{SH}$ and $-\text{SMe}$ anchor groups.^[111]

The electrodes materials, anchor groups and molecule backbones are three important features varying the transport through a molecule. The Fermi level (E_F) decreases in the order $\text{Ag} > \text{Au} > \text{Pd} > \text{Pt}$, with work functions of 4.26 eV, 5.10 eV, 5.12 eV and 5.65 eV, respectively.^[111] The Fermi energy of the electrodes decreases considerably when the work function increases. When applied in MCBJ, they show opposite order in the conductance with $\text{Ag} < \text{Au} < \text{Pd} < \text{Pt}$. The lower the E_F of the electrode, the smaller is the energy gap between E_F of electrode and the HOMO of molecule resulting in a faster charge transport step through the molecule-electrode interface and an increased junction conductance. Because in Pt and Pd the p and d orbitals are partially mixed, the coupling strength of the molecule and electrode is increased resulting in the higher conductance values. Contrarily, the s-character binding is predominant in Au electrodes.



Scheme 1.12 Overview of different types of anchor groups with their respective binding energies to Au. ^[109,115]

Because of the good malleability of the Au electrodes, Au remains the preferred material in MCBJ experiments. The trend in the molecule-electrode binding strength as well as conductance is from Au-O, Au-N, Au-S, Au-P to Au-C increasing (Scheme 1.12),^[114] while the anchor group binding strengths increase following $-\text{CN} < -\text{COOH} < -\text{Py} < -\text{NH}_2 < -\text{SH} < -\text{SMe} < -\text{PPh}_2 < -\text{PMe}_2 < \text{C}-\text{Au}$.^[111]

Au-S

The covalent Au-S is the most widely used anchor group-electrode combination. Its charge transport is normally through HOMO of the molecules.^[110,116] Thiol groups ($-\text{SH}$) are widely used as anchor groups for MCBJ, because they can form Au-S covalent bonds with binding energies around 0.45-1.72 eV. However, the S atom can bind to Au at different sites, which varies the conductance. Another problem is that $-\text{SH}$ groups can polymerize yielding disulfide formation during the measuring time. In addition, the relatively covalent Au-S bonds will reconstruct the surface of the gold-electrode. When using the $-\text{SAc}$ (Ac = acetyl) group, the Ac group can be *in situ* removed preventing from disulfide formation.^[113,117] The carbodithioate ($-\text{CS}_2\text{H}$) group forms a bidentate with the Au electrode via its two terminal sulfur atoms.^[118] The s and p states of carbodithioate groups ($-\text{CS}_2$) hybridize with d states of gold creating a π -back donation, which enhances the electronic coupling and results in a higher conductance than observed in the thiol group.

The characteristics of the dithiocarbamate ($-\text{NCS}_2$) group are similar to those of the $-\text{CS}_2$ moiety.^[119] Due to the electron donating effect nonbonding electron pair of the nitrogen to the S-Au antibonding states, the bond strength of the S-Au bond is enhanced, and the energy offset between the HOMO and the E_F is also reduced. Therefore, molecules anchored by the dithiocarbamate combine higher conductance values with increased mechanical stability. The $-\text{SMe}$ group and the dihydrobenzo[b]thiophene group ($-\text{BT}$) are rigidly locked due to the preorientation of the lone pair, and the cyclability of the junction is so improved.^[120] The thiocyanate $-\text{NCS}$ headgroup can strongly bind to the Au electrodes with strong π orbital contributions, but it exhibits only low conductance values.^[121]

Au-N

Amine groups ($-\text{NH}_2$) can be used to coordinate the Au electrodes via the lone electron pair of the N.^[122] Compared to $-\text{SH}$, the amine group has a weaker bond strength. However, due to the single lone pair electrons, the direction of the coordination bond to Au is locked, which results in narrow distributions in the conductance histograms. The electron-donating amine group lifts the HOMO of the molecules closer to the E_F resulting in HOMO charge transport. However, when the amine group is integrated into an aromatic ring system, the lone pair

electrons of N atom are partly delocalized into the molecular π -system. Thus, the Au–N bond of pyridine is stronger than that of amine due to the sp^2 -derived lone pair of pyridine decreasing the LUMO and enabling charge transport through the LUMO. The nitrile group (–CN) can form a weak coordination bond with Au and shows a much weaker conductance and much less stability than the –SH group.^[123] It was also shown to be electron-withdrawing group favouring the LUMO to transport charge.

Au–P

In comparison with Au–N and Au–S bonds, phosphine (–PMe₂ and –PPh₂) anchor groups show the strongest single σ -donation from the lone electron pair to the Au atom, and also the strongest π -back-donation from Au atom to the d states of the ligand.^[122,124] This π -back-donation provides an additional channel for electron transport leading to an increased conductance.

Au–O

Carboxylic acid (–COOH) group has very weak interaction with the Au electrodes and exhibits a bond energy of 0.17 eV.^[125]

Au–C

The bond of isocyanides (–NC) and Au has a bond strength that is comparable to that of thiols, but with an about three times lower conductance.^[126] The LUMO is the predominant charge path for this system. As anchoring groups, C₆₀ moieties can strongly be adsorbed on gold surfaces via a hexagonal benzene unit or a [6,6] double bond through partial charge transfer and strong hybridization between C₆₀ and surface gold atoms.^[127]

Au–C σ -bonds currently seem to be the best anchoring motifs to achieve low-ohmic contacts between the molecular backbone and the metal electrodes. The contacted carbon can be classified to sp^3 , sp^2 , and sp hybridizations, and the conductance is reported to follow in the order $sp^3 > sp > sp^2$.

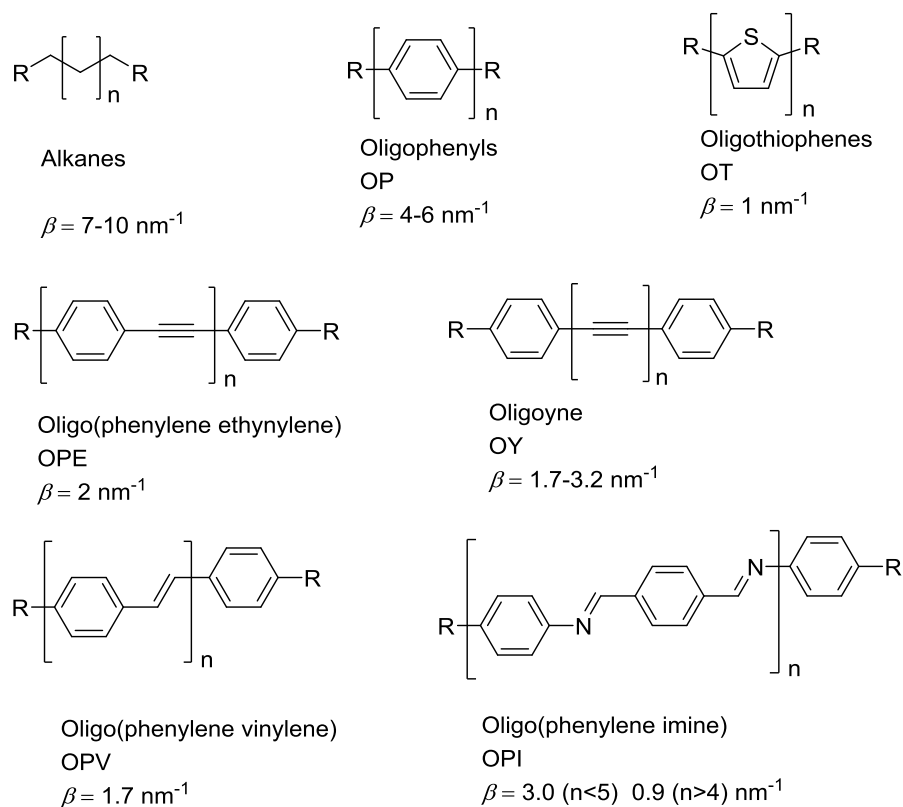
For sp^3 -hybridized carbons, Venkataraman's group used trimethyl tin (–SnMe₃) terminated polymethylene molecules to form *in situ* covalent Au–C σ -bond connections by directly displacing the SnMe₃ linkers at the molecular ends with gold atoms.^[128] Due to the high electronic coupling of Au–C σ -bond orbitals, the conductance of direct Au–C bonded alkanes is about 100 times larger than those of analogous alkanes with most other terminal groups. Later, the same group studied a family of highly conductive oligophenylenes (OP_n, n = 1-4) molecules.^[129] When n = 1, the conductance reached up to 0.9 G₀.

For sp^2 -hybridized carbons, the same group tried the para-phenyl (OP1) molecule connected by an sp^2 -hybridized carbon to the gold using the same SnMe₃ leaving groups.^[128]

Tao's group formed *in situ* an Au-biphenyl-Au sp^2 C–Au junction by an electrochemical cleavage of diazonium groups in a STM-break junction in solution.^[130] However, the benzene π system was not well coupled with the σ channel of Au–C bonds, while in case of the sp^3 -hybridized carbon atom, a conjugated system with a terminal methylene groups was shown to exhibit strong electronic coupling between the electrodes and the molecular π system.

For sp -hybridized carbons, Hong et al. performed measurements on the trimethylsilyl oligophenylethylene (TMS–OPEn, $n = 1, 2, 3$) family of molecules.^[131] The tetrabutylammonium fluoride (TBAF) was used as a deprotecting agent cleaving the TMS end group from the oligophenylethylene backbone and leaving the sp -hybridized carbon free to form a Au–C σ -bond. This anchoring system showed an enhanced conductance of one order of magnitude compared with conventional Au–S bonds.

Nevertheless, there are also considerable drawbacks in the reported Au–C approaches. The SnMe_3 terminal group requires rather toxic precursors, and the TMS group needs TBAF to be cleaved off that makes the handling of the MCBJ more complicated.



Scheme 1.13 Different types of backbones for single molecule molecular wires with the corresponding conductance decay factors, β .^[115]

The characters of the molecular backbones can be divided into non-conjugated systems (such as alkanes), broken conjugation systems, weakly and fully conjugated systems (such as oligophenylenes and cross conjugated systems) (Scheme 1.13). The conjugation of the

electronic system and its separation from the metal states determines the voltage drop and the field gradient across the molecular junction. The conductance change with molecular length is given by $G = G_c e^{-\beta L}$, where G_c is the contact conductance, which depends on the electrode-molecule interface, β is the decay constant and L is length of the molecular backbone. Different backbones show different decay constants β .

The widely studied alkane backbones (Scheme 1.13a), which are considered insulating because of their large HOMO-LUMO gap, are reference models for MCBJ experiments and theoretical studies.^[132]

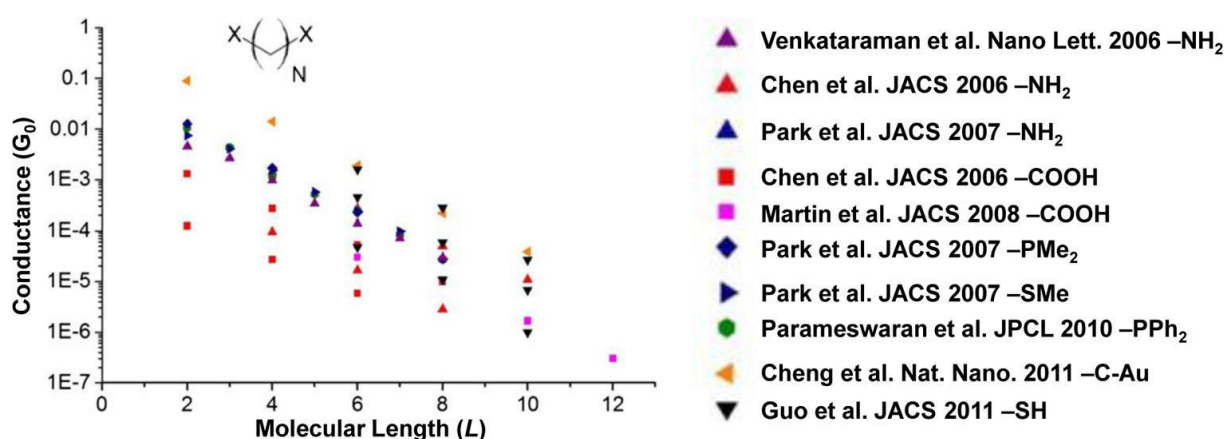


Figure 1.19 Conductance length-dependent studies on alkane chains with different anchor groups. Different anchor groups show similar β value. Reproduced with permission from [132a], Copyright (2014) IOP Publishing Ltd.

Figure 1.19 displays the conductance of several single-alkane chains of different lengths and linker groups by plotting $\log(G)$ versus L .^[132a] Different anchor group sets show the similar slope, meaning similar β value. Because of the large HOMO-LUMO gap, the difference in conductance for different molecular sets is mainly affected by the anchor groups. The higher conductance system should supposedly exhibit the stronger covalent bonding. The results in Figure 1.19 show a conductance trend $-\text{COOH} < -\text{NH}_2 < -\text{SH} < -\text{SMe} < -\text{PPh}_2 < -\text{PMe}_2 < \text{C-Au}$.

For oligophenyl backbones, the twisting angle of phenyl rings, Φ , between π -conjugated units is an important factor for the conductance variety.^[129,133] When Φ is small, it is a planar system with large conjugation overlap, resulting in high conductance. Whereas, when Φ is large, especially in almost perpendicular rings arrangements, the conjugation is broken resulting in a lower conductance. This opens a channel to tune the electron transport. But longer molecular backbones which are structurally rigid are less sensitive to microscopic details of the molecule's alignment within the junction. The β values of oligophenyls backbones are in the range from 4-6 nm^{-1} .

Oligo(*p*-phenylene ethynylene)s (OPEs) is a cross-conjugated backbone.^[113,131,134] When measured incorporating 1-3 benzene rings, tunneling is the main charge transport mechanism of OPEs with $\beta = 2.0 \text{ nm}^{-1}$. With more repeating units the hopping mechanism dominates the transport with $\beta = 0.3 \text{ nm}^{-1}$ which is strongly affected by temperature.

Compared to OPEs, oligo(phenylene vinylene) (OPV) have a little lower HOMO-LUMO gap exhibiting slightly higher conductance with a decay constant $\beta = (1.7-1.8) \text{ nm}^{-1}$.^[135]

The heteroatomic conjugated backbone oligothiophenes show an even lower decay constant with $\beta = 1.0 \text{ nm}^{-1}$. Like OPEs, oligothiophenes also show two kinds of β value with increasing number of repeating units.^[136]

Similar to OPEs, oligophenyleneimine (OPI) exhibits the higher decay constant $\beta \approx 3.0 \text{ nm}^{-1}$ for short molecular wires (OPI 1-4) and lower decay constant $\beta \approx 0.9 \text{ nm}^{-1}$ for long molecular wires (OPI 5-10).^[137]

1.5 Lithium batteries and organic batteries

The pollution of the environment and high demand for efficient energy storage have been turned out to be urgent global problems. The fossil-fuel based economics is considered not sustainable, since too much release of CO_2 gas resulting in global warming effects. The development of renewable energy sources with sustainable energy storage technologies provides an effective route to solve these problems. Rechargeable batteries although developed and used for very long time, are here clearly in the focus of future developments.

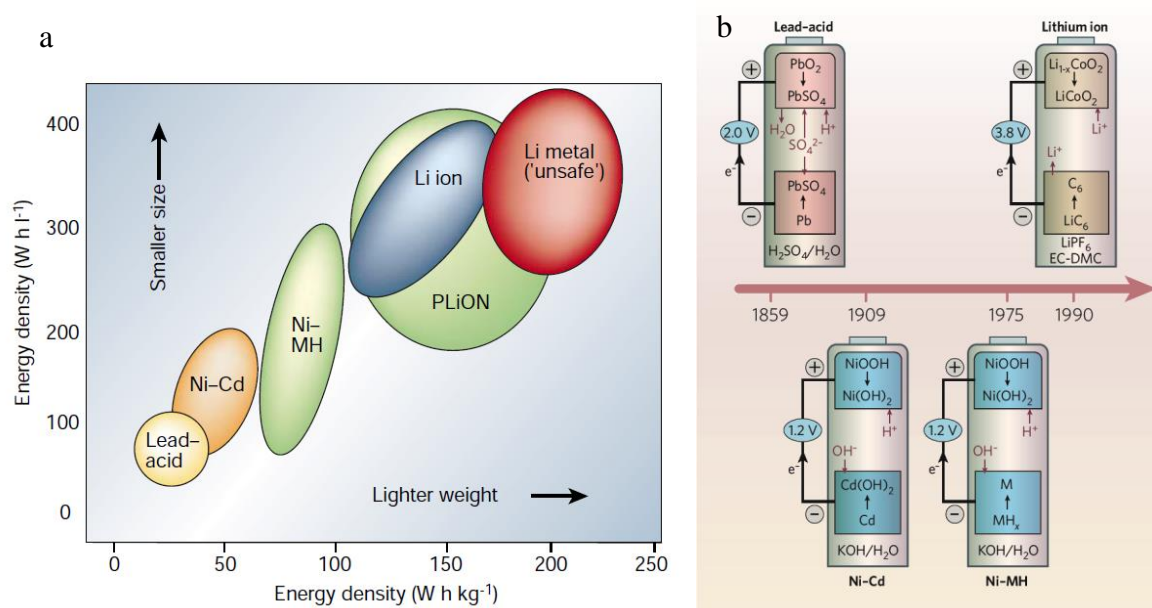


Figure 1.20 (a) Comparison of the energy densities of different rechargeable battery systems. (b) Representation of the structure of these batteries. The share of worldwide sales for Ni-Cd, Ni-MH and Li-ion portable batteries is 23, 14 and 63%, respectively. Reproduced with permission from [138], Copyright (2001) Nature Publishing Group.

Batteries can be divided into primary batteries and secondary batteries. The former can be used only once and cannot be recharged. The classic primary batteries such as zinc-manganese batteries, alkaline batteries, silver button cell and zinc-air button cell have been widely used in past few decades.^[139] In contrast, secondary batteries can be charged and discharged a certain number of times. Some commercial rechargeable batteries are shown in Figure 1.20. The first rechargeable battery was the lead-acid battery invented in 1859. Subsequently, nickel-cadmium batteries were developed in 1899. Later the cadmium-free batteries nickel-metal hydride batteries (1967) and lithium ion batteries (LIBs, 1985) were developed. In 1991, the Sony Corporation firstly commercialized the LIBs. With the development of information technology, LIBs have been widely applied in portable devices, electric vehicles, and even large grid storage fields.

However, due to the challenge on storage capabilities, sustainability, safety and high cost, conventional rechargeable batteries are not able to satisfy the ever increasing demand for energy storage, especially in the field of electric vehicles. These attracted great interest of scientists in development of the batteries technologies.

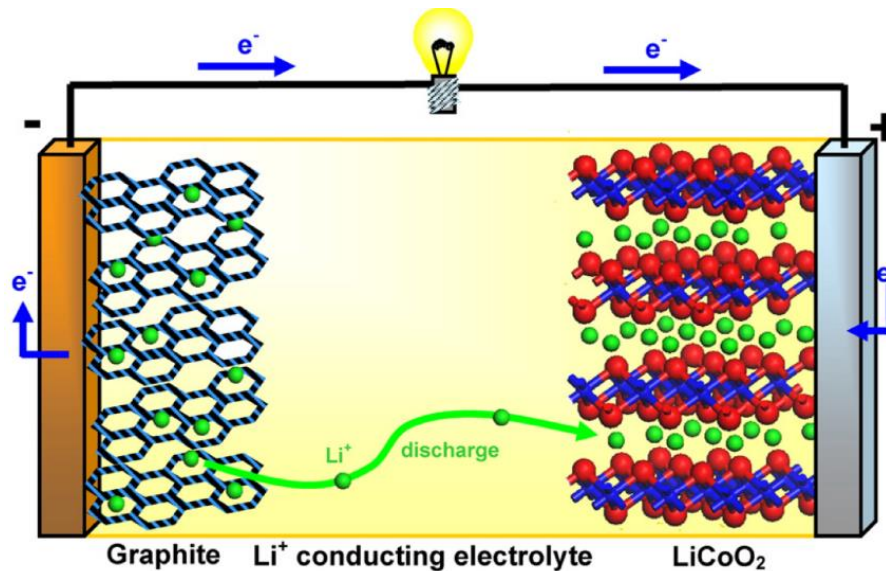
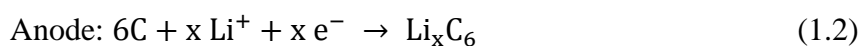
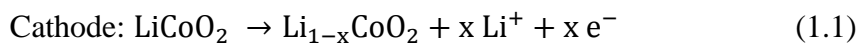


Figure 1.21 Schematic illustration of a LIB (anode: graphite, cathode: LiCoO₂). Reproduced with permission from [140], Copyright (2008) Elsevier.

As a model to understand the reversible recharging of batteries, the example of the LIB will be herein discussed. The electrochemical reaction of LIB (LiCoO₂ as a cathode, graphite as an anode) during the charge process can be written as follows:



For the cathode, compounds exhibiting intercalation are commonly used as shown in Figure 1.22. They can be divided into three types: (i) layered transition metal materials with a 2D ion diffusion path (e.g. LiCoO₂, theoretical capacity is 274 mAh g⁻¹),^[141] (ii) a spinel structural material with a 3D ion diffusion path (e.g. LiMn₂O₄, 147 mAh g⁻¹),^[142] and (iii) olivine structural materials with a 1D ion diffusion path (e.g. LiFePO₄, 170 mAh g⁻¹).^[143] In addition, pure carbon cathodes for the Li–O₂ battery and sulfur cathodes for the Li–S battery are very promising to satisfy the next generation energy storage devices due to their high theoretical capacities of 3350 and 1672 mAh g⁻¹, respectively.^[144]

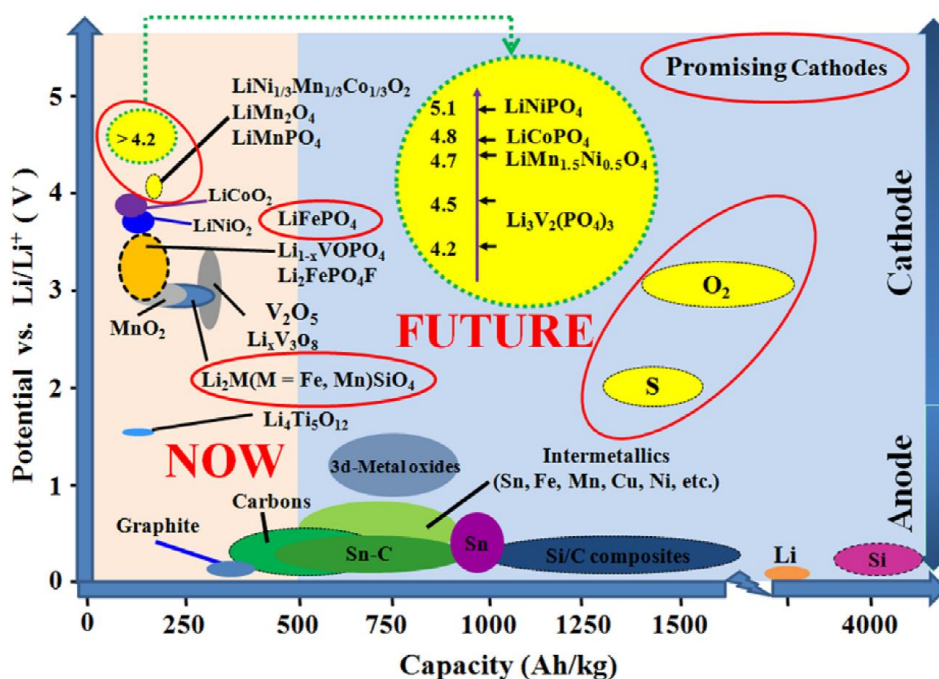


Figure 1.22 Different electrode materials and their corresponding electrochemical performance in current LIBs technologies. Reproduced with permission from [145], Copyright (2013) Elsevier.

As anode, different carbon materials can be used. The commercialized graphite anode has a theoretical capacity of 372 mAh g^{-1} based on the formation of LiC_6 units upon insertion of lithium ions into graphite inter-layers.^[146] Other carbon materials such as nanotubes (1100 mAh g^{-1}),^[147] carbon nanofibers (450 mAh g^{-1}),^[148] graphene (960 mAh g^{-1}),^[149] porous carbon ($800\text{--}1100 \text{ mAh g}^{-1}$)^[150] were also investigated.

As mentioned in the first section, also GDY has been tested as LIBs anode showing high capability of Li ion storage performance (520 mAh g^{-1} at current density 500 mA g^{-1}).^[79b,79c] After nitrogen doping, it showed an even better performance (740 mAh g^{-1} at current density 500 mA g^{-1}).^[79a]

Metal-organic frameworks (MOFs), with a high degree of order at the nanoscale and uniform distribution channels, have been applied as LIBs anode materials showing excellent performance.^[151]

Beside lithium ion batteries, recently sodium ion batteries (SIBs) also attract much attention due to the abundant sodium resources which may be suitable for large grid application.^[152] Additionally, K,^[153] Ca,^[154] Mg^[155] and Al-ion^[156] batteries have been studied due to their abundance.

The organic batteries are regarded as promising candidates for the next generation electrochemical energy storage due to their low-cost, recyclability, resource sustainability, environmental friendliness, structural diversity and flexibility. Meanwhile, there are still a lot

of challenges to overcome to commercialize them, such as low mass density, low electronic conductivity and dissolution of active material to electrolyte.^[157]

Organic electrode materials can be classified into n-type organics, p-type organics and bipolar-type organics as shown in Figure 1.23 and Table 1.1.^[157a]

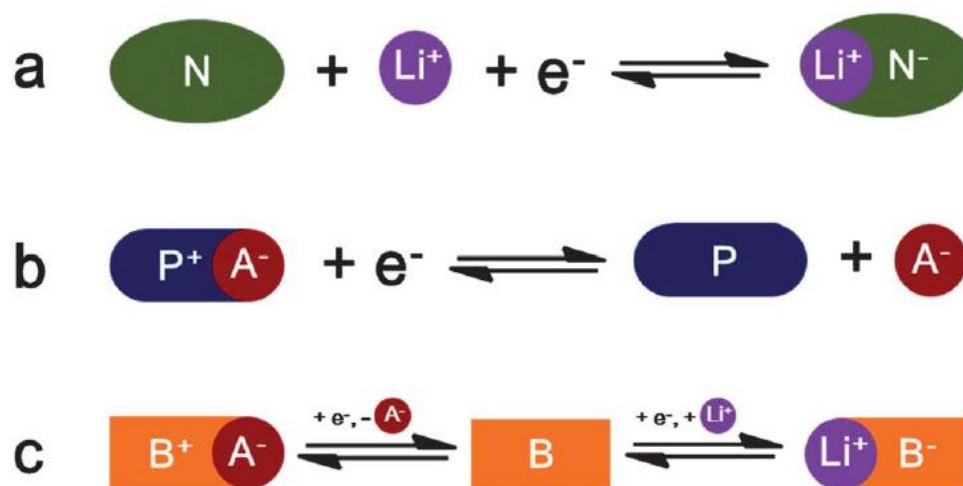


Figure 1.23 The redox reactions of three types of electroactive organics: (a) n-type; (b) p-type; (c) ambipolar-type. A^- means anion of the electrolyte and Li^+ can be replaced by other alkali ions or organic cations. Reproduced with permission from [157a], Copyright (2013) Royal Society of Chemistry.

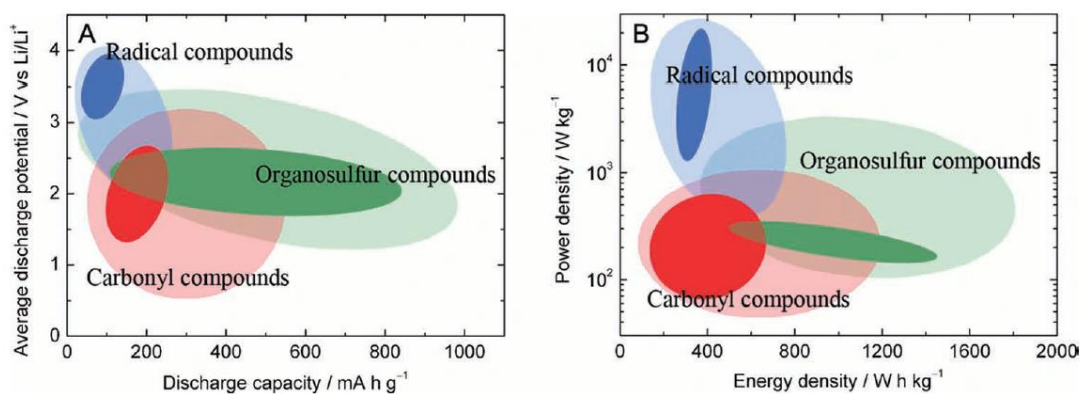
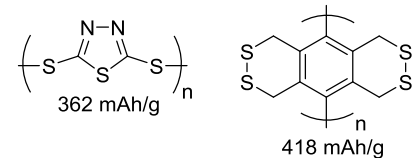
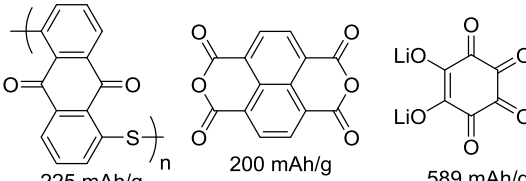
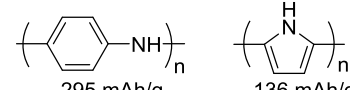
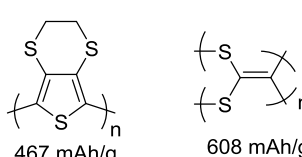
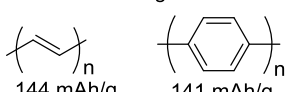
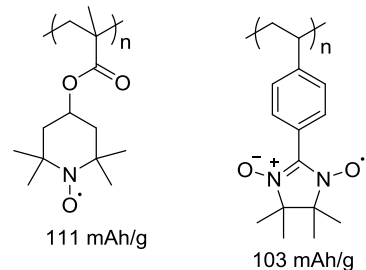


Figure 1.24 Graphical comparison of the cell performance of organosulfur (green), radical (blue), and carbonyl compounds (red) in the form of discharge potential vs capacity (a) and power density vs energy density (b). The regions marked with deep shades cover the most typical values reported in the literature, while those with light shades represent achievable values for the specific class of compounds. Reproduced with permission from [157b], Copyright (2012) John Wiley and Sons.

Table 1.1 List of different types of organic electrode materials and their redox mechanisms. Selective examples and their theoretical capacity are given. Reproduced with permission from [157a], Copyright (2013) Royal Society of Chemistry.

Type	Structure	Redox mechanism	Examples
n-type	Organodisulfide	$R-S-S-R \rightleftharpoons 2R-S^-$	
	Conjugated carbonyl	$R-C(=O)-R \rightleftharpoons R-C(O^-)-R$	
p-type	Conjugated amine	$R-NH-R \rightleftharpoons R-N^+-R$	
	Conjugated thioether	$R-S^+-R \rightleftharpoons R-S-R$	
bipolar-type	Conjugated hydrocarbon	$(R)^{x+} \rightleftharpoons (R) \rightleftharpoons (R)^{y-}$	
	Nitroxyl radical	$R-N^+=O \rightleftharpoons R-N\cdot \rightleftharpoons R-N^--O^-$	

For n-type organics, such as organodisulfide^[158] and conjugated carbonyl molecules,^[159] the electron transfer is between the neutral state (N) and the negatively charged state (N⁻) of a molecule (Figure 1.23a). Conjugated carbonyl molecules have been firstly studied as organic electrodes for batteries. Early in 1969, D. L. Williams et al. used dichloroisocyanuric acid as cathode in a primary lithium battery.^[160] Beside simple quinones (e.g. benzoquinone (BQ), naphthoquinone (NQ), anthraquinone (AQ)^[159a]), a lot of quinone derivatives, multi-carbonyl quinones, dianhydrides,^[153b] quinone polymers,^[159b] Li or Na salts of hydroxyl quinone^[159c,161] and conjugated dicarboxylates^[162] have been investigated. Typically, the electrochemistry of AQ molecules in solution shows a two-step reversible redox mechanism with a radical transition state. But in the LIBs, only one flat charge and discharge plateau at around 2.2 V,

which can be contributed to very unstable radical intermediate in solid state, has been found (Figure 1.25).^[159a] However, due to the solubility issues of the AQ, the cycling stability is not satisfactory. Compared to AQ, the thioether linked anthraquinones (PAQS) have shown a much better cycling stability and rate capability with 151 mAh g^{-1} at 2 C rate.^[159b] But the charge and discharge curve show a bigger slop resulting in a lower average discharge voltage. The poor electronic conductivity of PAQS is harmful to its electrochemical performance although conductive carbon was introduced in the electrode. However, *in situ* polymerization of the molecule for increasing its electronic conductivity would be an efficiency approach.

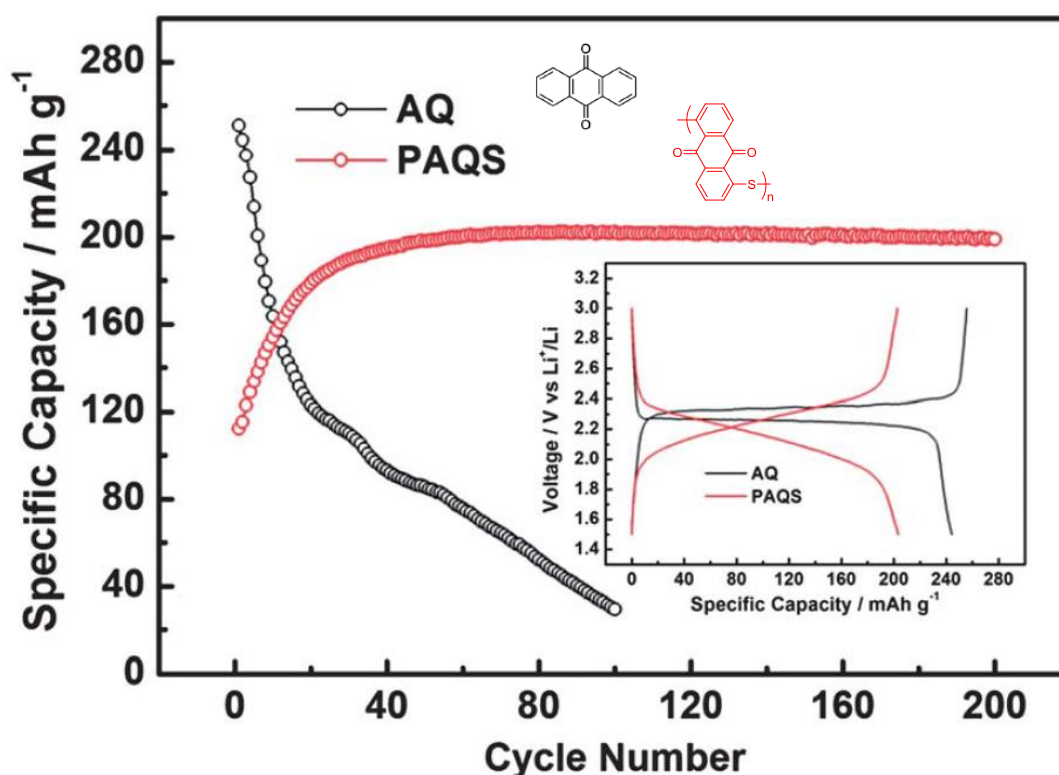


Figure 1.25 Comparison between the electrochemical performance of AQ and PAQS as cathode materials for LIBs. Reproduced with permission from [157a], Copyright (2013) Royal Society of Chemistry.

In p-type organics, such as conjugated amine^[163] and conjugated thioether molecules^[164], the reaction is between the neutral state (P) and the positively charged state (P⁺) (Figure 1.23b).

In ambipolar-type organics (B) (Figure 1.25c), such as conjugated hydrocarbon^[165] and nitroxyl radical molecules^[166], the reaction occurs either between the negatively charged state (B⁻) and the neutral state (B), or between the positively charged state (B⁺) and the neutral state (B), or even between the negatively charged state (B⁻) and the positively charged state (B⁺).

The nitroxide radical is a typical ambipolar-type organic battery material. It can either be oxidized to form the corresponding oxoammonium cation (p-type) or reduced to the aminoxy anion (n-type). As for electrode materials, the nitroxide is normally used in its polymer form.^[166d,167] The first nitroxyl radical polymer (PTMA) as cathode material of LIBs was reported in 2002 showing an average discharge potential of 3.5 V (vs Li/Li⁺) and good cycling stability and rate capability.^[166a-c]

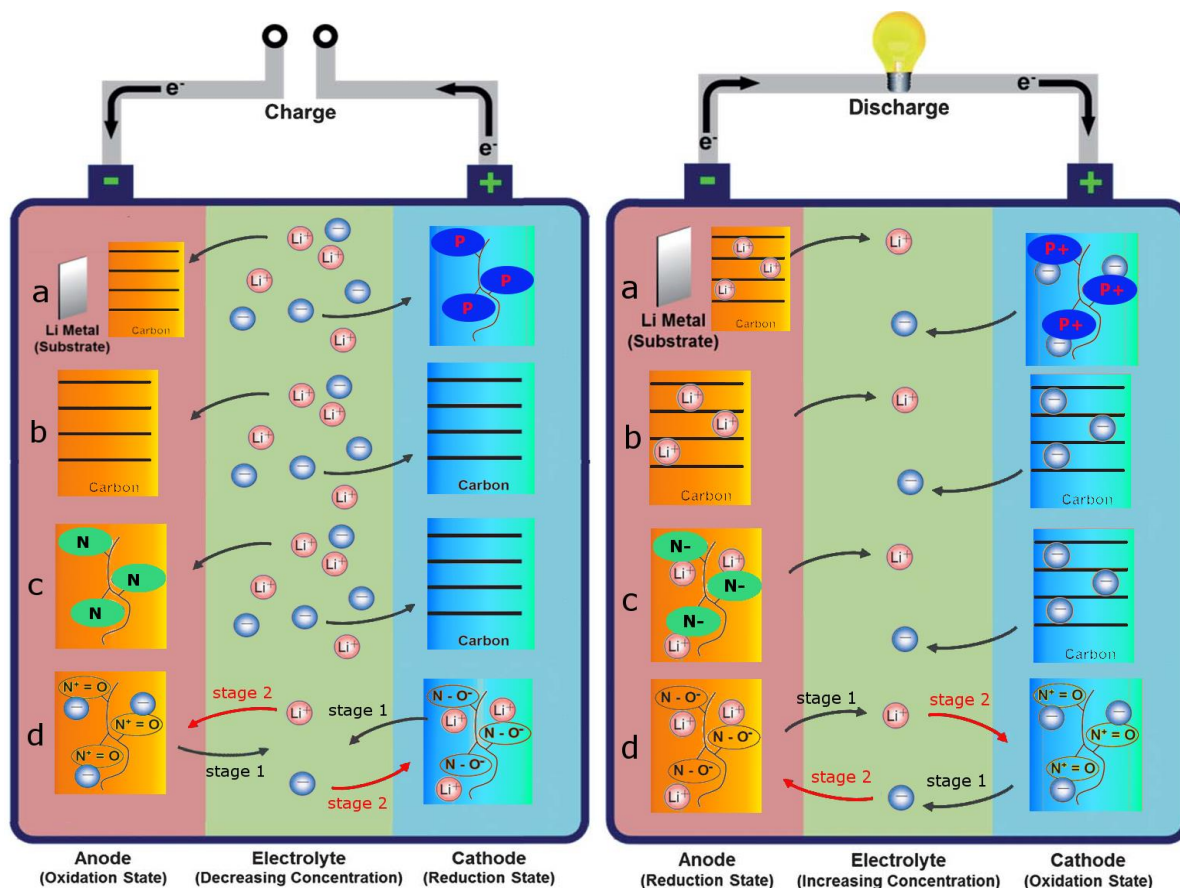


Figure 1.26 Schematic representations of four types of dual-ion batteries where the shuttle ions are both cations and anions. (a) p-type organic as cathode and Li metal or graphite as anode cell.^[168] (b) A symmetric dual ion cell with graphite as both cathode and anode.^[169] (c) An n-type organic as anode and graphite as cathode cell, LiA can be replaced by ionic liquid.^[170] (d) An all organic battery cell using nitroxide radical compounds as both cathode and anode.^[166d]

Interestingly, these nitroxide radical polymers can be used as both cathode and anode to form an all organic battery with symmetric configuration. In one example, poly[4-(nitronylnitroxyl)styrene] was applied as an active material using $(C_4H_9)_4N^+ClO_4^-$ in acetonitrile solvent as electrolyte.^[166d] In the charging process, anions were migrated to the cathode, whereas cations were transferred to the anode (Figure 1.26d). The cations and anions returned into the electrolyte during the discharging process. In addition, it can have further discharge stages resulting in the reversion of cathode and anode. Overall, the system delivered

a discharge voltage of 1.3 V and showed remarkably high rate capability and stable cycle performance.

Another example of an all-organic cell employing a porphyrinoid compound (dimesitylnorcorrole nickel(II) complex (NiNC)) as active material has been studied with LiPF_6 as an electrolyte.^[171] Four-electrons can be transferred between the B^{2+} and B^{2-} species. Based on this reaction mechanism, the all-organic battery also can be considered as an electrochemical pseudocapacitor if the reaction occurs in the interface of the active material.

When replacing the cathode and anode as graphite, the cations and anions can in principle be electrochemically intercalated into the cathode and/or anode and form graphite intercalation compounds. In the discharge process, both cations and anions are returned into the electrolyte. These batteries normally show high voltage and very high rate capability.

Compared to the limited number of cationic intercalation guests (Li^+ , Na^+), a variety of anions can be intercalated into the graphite, such as fluoride based species, (e.g. PF_6^- , AsF_6^- , BF_4^-), oxide based guests (SO_4^{2-} , NO_3^- , ClO_4^-), tetrachloride compounds such as AlCl_4^- ,^[172] and organic anions (such as bis(trifluoromethanesulfonyl) imide ($(\text{CF}_3\text{SO}_2)_2\text{N}^-$), tris(trifluoromethanesulfonyl) methide ($(\text{CF}_3\text{SO}_2)_3\text{C}^-$), trifluoroacetate (CF_3COO^-) and perfluorooctanesulfonate ($\text{C}_8\text{F}_{17}\text{SO}_3^-$)).^[169]

As a summary in Figure 1.26, these batteries discussed above can be classified to act as a dual-ion battery. Normally, during the charging procedure, the cations and anions will be moved to the anode and cathode respectively, and resulting in diluting the concentration of the electrolyte. During the discharging procedure, the cations and anions will be released from the electrodes. When the p-type organic materials work as cathode or the n-type organic materials works as anode, or in the case of ambipolar materials (such as graphite and bipolar organic materials), the dual-ion batteries can be formed.

Rechargeable batteries based on dual-ion shuttle would provide many opportunities to build novel sustainable energy storage devices. It could be a suitable candidate for bridging supercapacitors and batteries for the next generation energy storage.

2. Aim of the thesis

In the past decades, alkyne compounds have attracted much interest as extremely valuable building blocks in organic synthesis and material science. The aim of this thesis is to design and synthesize novel alkyne derivatives and to explore (i) new on-surface reactions and (ii) surface polymerization, or applications in (iii) molecular junctions and (iv) batteries.

1. Alkyne compounds have previously been introduced as powerful precursors to many on-surface reactions such as azide-alkyne cycloaddition, cyclotrimerization and homo-coupling. However, due to the high activity of alkyne compounds, several side reactions were observed upon thermal treatment on the surface. To increase the selectivity of the alkyne-alkyne C–C coupling remains a challenge. Here, we propose a linear alkyne precursor, and choose a vicinal surfaces Ag(877) as template to increase the chemoselectivity of the homo-coupling to obtain longer 1D conjugated polymer.

2. Graphdiyne (GDY), which combines sp^2 and sp -hybridized carbon atoms, has been proposed as a novel structural motif among the carbon allotropes. Presumable GDY materials have been tested in catalysis, Li-ion storage, solar cell, but the structure was not yet completely elucidated. The high chemical activity of the precursors results in insertion reactions and oxidations during the synthetic procedure leading to unknown structures. We introduce here a stable starting material hexakis[4-(ethynyl)phenyl]benzene aiming to obtain better control of the C–C bond-formation in GDY and to comprehend the reaction mechanisms.

3. The C–Au σ -bonds currently seem to be the best anchoring motif to achieve low-ohmic contacts between the molecular backbone and the metal electrodes. Here, we introduce a family of diethynyl-oligophenyls, which can directly form a C–Au bond to the Au leads by the *in situ* deprotonation of the acidic C–H proton of the alkynyl groups. This approach avoids the use of deprotecting agents or toxic leaving groups.

4. Organic batteries are considered to be one of the candidates for the next generation of energy storage. Porphyrins might be utilized as ambipolar organic electrode materials, in which the neutral molecule can either be oxidized or reduced. Considering the structural rigidity and electronic conductivity of a terminal alkyne group to exert on the electrochemical properties of the porphyrins, we design a new alkyne substituted porphyrin Cu complex aiming to investigate its electrochemical performance in an all-organic rechargeable battery. With this ambipolar electrode material, novel Li-ion free batteries can be designed. Fast charge and discharge ability and high cycling stability are expected in battery applications.

3. Alkyne derivatives for on-surface assembly and reactions

3.1 Synthesis of graphdiyne wires by surface templating

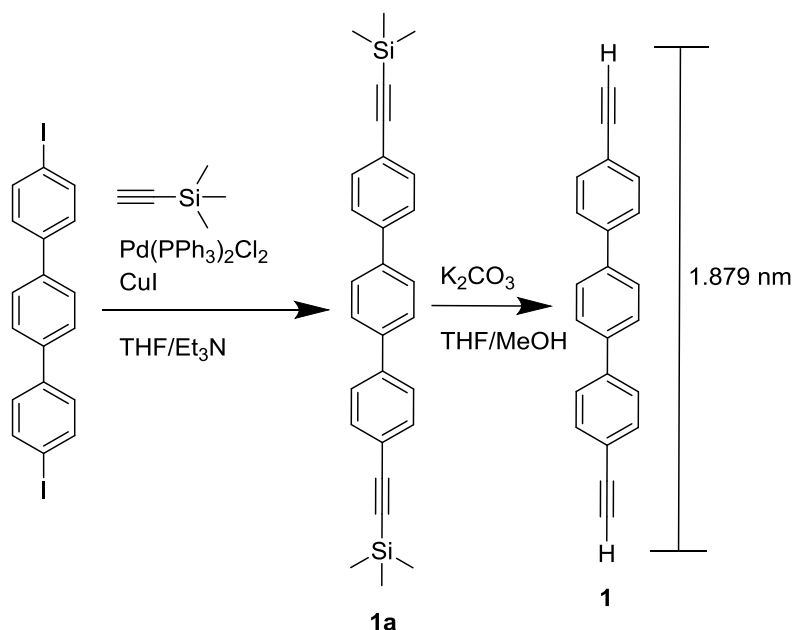
This chapter was adapted from the co-authored publication *Nano Lett.* **2014**, *14*, 1891-1897, entitled “Synthesis of extended graphdiyne wires by vicinal surface templating”, Copyright (2014) American Chemical Society.^[173] The presented results were obtained in collaboration with the group of Prof. Dr. J. V. Barth at the Technical University of Munich.

In the past decades, alkyne compounds containing *sp* carbon atoms have attracted great interest as valuable building blocks in organic synthesis and material science.^[1] Due to the high σ -character and electronegativity of the ethynyl carbons, the terminal alkyne group shows an increased acidity and higher reactivity than terminal alkane and alkene groups.^[174] Alkyne compounds have also been introduced to many on-surface reactions. Reactions such as azide-alkyne cycloaddition,^[107] cyclotrimerization^[20] and homo-coupling^[63b,64,99-101] have been investigated on Cu(111)^[99], Au(111)^[20,64,100] and Ag(111)^[63b,64,101], whereby a preference for cyclotrimerization and homo-coupling is exhibited on Au(111)^[20] and Ag(111),^[63b,101] respectively. However, on Cu(111) surface, a wider variety of reactions is observed^[99] and alkyne organometallic complexes are formed during the annealing procedure.^[95i,100-101] Thus, to achieve an alkyne C–C homo-coupling with high chemoselectivity remains challenging.

Due to the high activity of alkyne groups, the homo-coupling on surface is typically accompanied by side reactions upon the thermal treatment. Several approaches have been proposed and realized in order to avoid these side reactions, such as sterically hindered substitutions,^[64,101] organometallic intermediates^[100-101] and irradiation by UV light^[175], all aiming to obtain longer GDY wires and larger area of highly ordered 2D GDY nanosheets.

Inspired by the templating concepts developed in solution chemistry,^[176] we have notably introduced the vicinal surface Ag(877) to suppress the unwanted branching side reactions. Step edges have been employed in the past regarding their increased catalytic activity^[177] or to steer the assembly of 1D supramolecular wires.^[178] The employed linear ligands 4,4'-diethynyl-1,1':4',1''-terphenyl (**1**) prefers to align on the vicinal surface Ag(877) on the formed terraces. After annealing, a novel 1D poly(terphenylene-butadiynylene) was yielded through preferential regioselective homo-coupling of the precursors. The employed compound **1** was synthesized by a Sonogashira reaction as depicted in Scheme 3.1.1. The distance between the terminal hydrogens was obtained from DFT calculations to be 18.79 Å. The three phenyl rings act as a rigid backbone, while the two terminal alkynes form the active groups for the homo-coupling. Due to the high σ -character and hence electronegativity of the *sp* carbon atoms, the terminal H atoms show an increased acidity compared to those

connecting to sp^2 and sp^3 carbon atoms.^[174] This feature entails high reactivity of terminal alkyne compounds on surface-assisted homo-coupling.^[63b]



Scheme 3.1.1 The synthetic route for compound **1**; length refers to the distance between terminal hydrogen atoms.

The STM experiments were carried out in a home-built Besocke-type scanning tunneling microscope (STM) under liquid nitrogen temperature (~ 5 K) in UHV ($\sim 10^{-10}$ mbar) conditions. The samples were prepared *in situ* under the same conditions by evaporating the molecules with organic molecular beam epitaxy (OMBE) on pre-cleaned Ag(111) surfaces. The theoretical part of the study was performed by periodic density functional theory (DFT) calculations using the VASP code^[179] with the projected augmented wave method^[180], and the PBE exchange-correlation functional.^[181] The plane waves were expanded to a cutoff of 500 eV. Structural optimizations were performed until the forces acting on all atoms were smaller than 0.01 eV/Å.

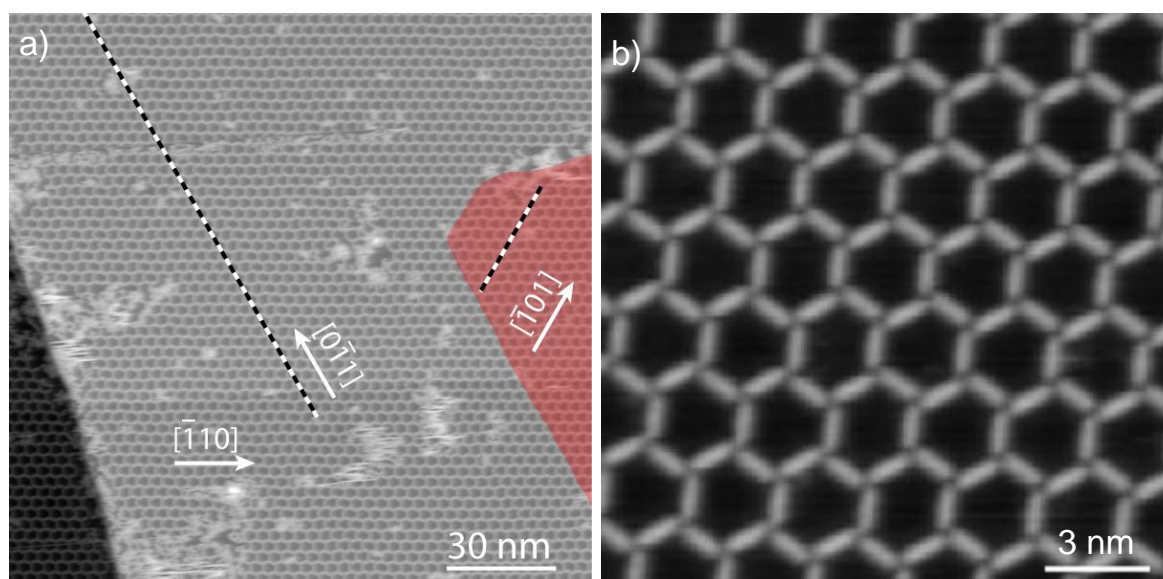


Figure 3.1.1 (a) STM image of a self-assembled **1** on Ag(111). Black-white dashed lines indicate the main-axis directions. (b) Zoom-in STM image of the honeycomb self-assembly. ($U_{\text{bias}} = -1.0$ V, $I_t = 0.03$ nA). The sample was measured by Yi-Qi Zhang.

1 was initially deposited onto the Ag(111) surface hold at a temperature of 250 K. Aggregation is mediated via terminal alkyne groups forming a 3-fold node through weak C–H $\cdots\pi$ interactions with neighboring units enclosing a 120° angle (Figure 3.1.1b). With one monolayer (ML) molecular coverage, although defects are present, the network is spread out continuously over large Ag(111) terraces; showing a large area of honeycomb pattern (Figure 3.1.1). After annealing at 400 K, linear homo-coupled oligomeric compounds (green circles in Figure 3.1.2a,b) are formed, but they represent a minority product (34.2% yield). The dominating products are the branched ones, where three (46.8%, red) or four (15.2%, blue) end groups merge, which can be attributed to cis/trans hydrogenations, multiple insertion reactions and/or possibly cyclotrimerisation of compound **1** (Figure 3.1.2b,c). More complex structures with five monomers (3.8%, yellow circles) are also observed. Considering the encountered wide variety of different mechanisms for polymerization reactions, the simple use of planar surfaces is obviously not ideal to fabricate either hydrocarbon molecular wires or 2D periodic lattices via acetylenic coupling. Strict chemoselectivity is required for the targeted linear reaction.

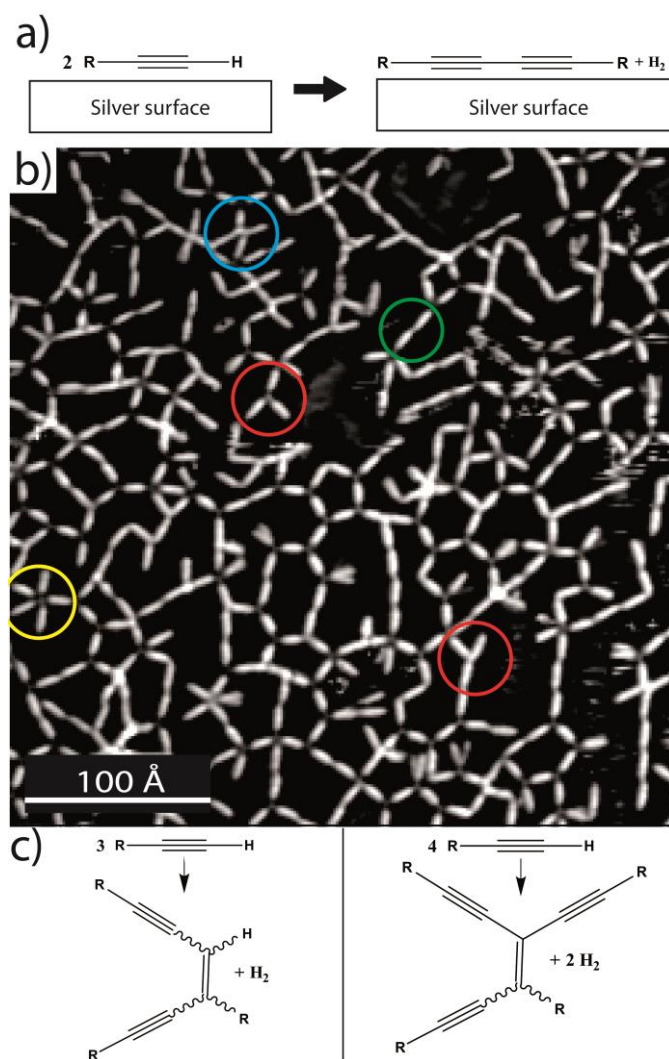


Figure 3.1.2 (a) Schematic representation of the targeted linear covalent homo-coupling reaction of the terminal acetylenic compounds with the Ag(111) surface as a catalyst. (b) STM image ($U_{\text{bias}} = -0.29 \text{ V}$, $I_t = 0.075 \text{ nA}$) of a polymerized, irregular porous network fabricated by annealing **1** on the Ag(111) substrate to 400 K. Reaction products resulting from covalent coupling of two, three, four or even five monomers are highlighted in green, red, blue, and yellow, respectively. (c) Examples of side reactions involving three and four reacting monomers. Reproduced with permission from [173], Copyright (2014) American Chemical Society. The sample was measured by Borja Cirera.

To direct the homo-coupling of alkynes chemoselectively to form linear butadiyne scaffolds, the terraces of the vicinal surface Ag(877) were used. The theoretical values for terrace width and step height of Ag(877) are $W = 36.6 \text{ \AA}$ (15 atomic rows along the $[11\bar{2}]$ direction forming the (100) microfacets) and $h = 2.35 \text{ \AA}$ respectively (Figure 3.1.3a). The real Ag(877) surface exhibits a distribution of terrace widths around the ideal value separated by monatomic steps (Figure 3.1.3b-f).

To identify the favorable adsorption sites of **1**, a small concentration of molecules was evaporated onto the Ag(877) template held at 186 K. The compound **1** binds preferably to the lower step edges parallelly (inset of Figure 3.1.3b shows two superimposed models). This step decoration persists at increased coverage, and not a single molecular unit deviates from the

preferred alignment (Figure 3.1.3c). The templating effect is ascribed to interactions between the rod-like molecules and the step-edge atoms.^[182] As shown in Figure 3.1.4a, the distance d between neighboring molecules is $22.9 \pm 1.8 \text{ \AA}$. This value varies appreciably as the 1D molecular density at the step depends sensitively on the surface coverage. The two nearby hydrogen atoms in terminal ethyne groups between neighboring molecules show a distance $4.11 \pm 1.8 \text{ \AA}$ due to the polarity of the C–H bond.^[183] Therefore, this arrangement is very suitable for subsequent polymerization.

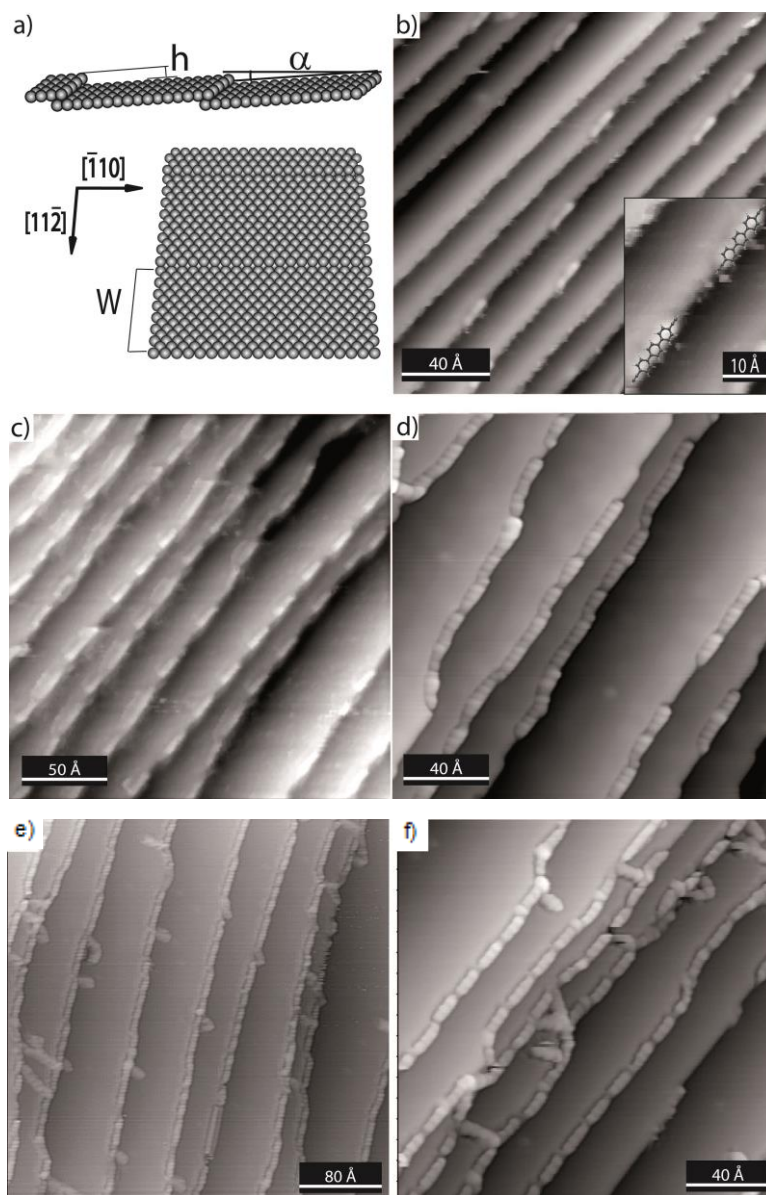


Figure 3.1.3 (a) Model of the ideal Ag(877) surface with a terrace width of $W = 36.6 \text{ \AA}$, step height $h = 2.35 \text{ \AA}$ and miscut angle $\alpha = 3.67^\circ$ with respect to the (111) plane. (b) STM image showing the preferential step-edge decoration upon exposure to small amounts of **1**; inset highlights two monomers with their models superimposed ($U_{\text{bias}} = -1.0 \text{ V}$, $I_t = 0.06 \text{ nA}$). (c) Regular alignment close to step-edge saturation at low temperature ($U_{\text{bias}} = -1.03 \text{ V}$, $I_t = 0.08 \text{ nA}$). (d) After annealing the sample to 450 K extended connected structures are present at the (100) microfacets, with sub-molecular features resolved ($U_{\text{bias}} = -1.08 \text{ V}$, $I_t = 0.07 \text{ nA}$). To emphasize step-edge features, the data are presented by subtracting an average plane of the entire image leading to a variable contrast of the terraces related to their widths. (e) Large-scale STM image of the sample after annealing more monomers ($U_{\text{bias}} = -1.1$

V, $I_t = 0.07$ nA). (f) High-quality STM image showing a small area with the typical appearance of the samples ($U_{\text{bias}} = -0.5$ V, $I_t = 0.12$ nA). Reproduced with permission from [173], Copyright (2014) American Chemical Society. The sample was measured by Borja Cirera.

In order to trigger the homo-coupling reaction between the terminal alkyne groups, we annealed a sample with the ideal pre-reaction ordering (similar to Figure 3.1.3c) to 450 K. Extended and connected chains along the step edges are discernible (as shown in Figure 3.1.3d-f). To prove that the formed bonds between the monomers are consistent with the covalent homo-coupling, we measured the distance d^* between neighboring monomers after annealing, giving a value of $d^* = 17.9 \pm 0.6$ Å (Figure 3.1.4b), which is significantly smaller than the d in the self-assembled 1D phase and smaller than the length of a single molecule **1** (Scheme 3.1.1). The experimental value $l_{b1-b3} = 8.4 \pm 0.6$ Å between the two benzene rings at both ends of one monomer is in good agreement with the theoretical value 8.56 Å (Figure 3.1.4b), indicating an intact structure of the molecular backbone. Considering these findings, the corrugation in the line profile can be interpreted as the three phenyl rings of **1**, connected by newly formed butadiynyl bridges, which corresponds to a terphenyl-butadiyne compound.

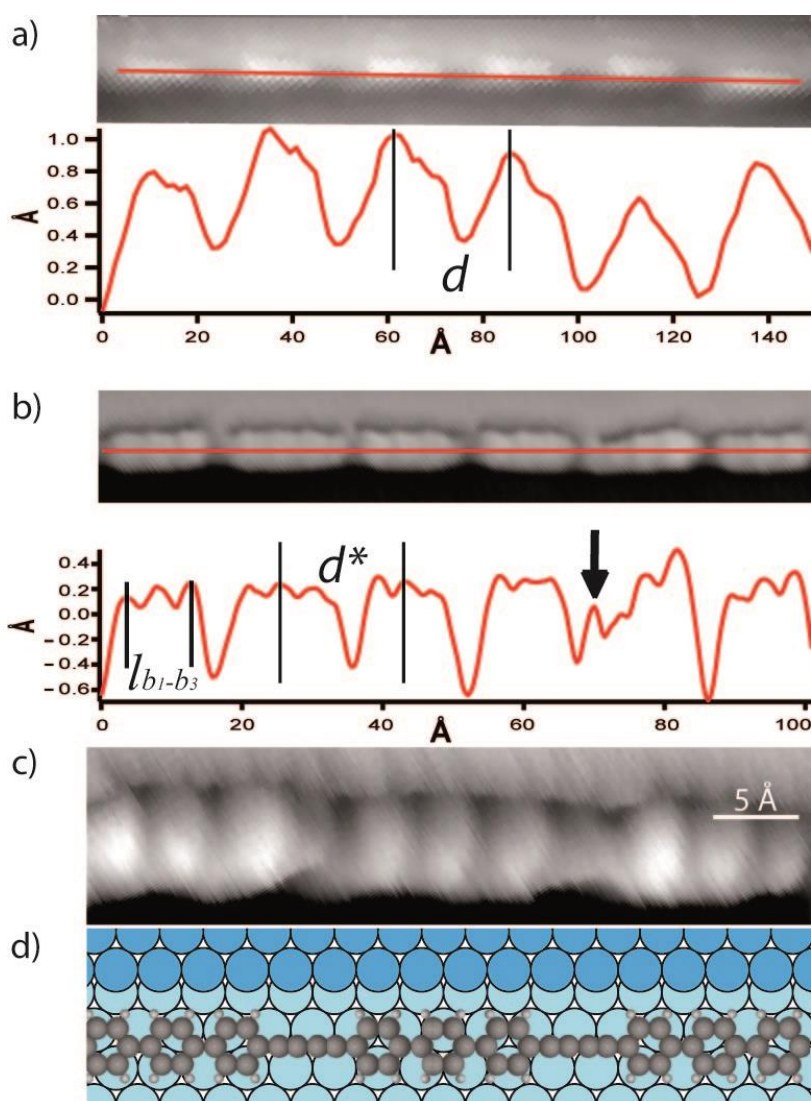


Figure 3.1.4 (a) STM image of six-membered molecular segment at a step edge in the low-temperature phase. The line profile (red) shows an intermolecular distance of $d = 22.9 \pm 1.8 \text{ \AA}$ ($U_{\text{bias}} = -1.03 \text{ V}$, $I_t = 0.08 \text{ nA}$). (b) STM image of six polymerized molecules ($U_{\text{bias}} = -0.5 \text{ V}$, $I_t = 0.12 \text{ nA}$). The distances between the center of two adjacent monomers and the external peaks in every trio are defined as d^* and l_{b1-b3} . The experimental line profile (red line) gives the values $d^* = 17.9 \pm 0.6 \text{ \AA}$ and $l_{b1-b3} = 8.4 \pm 0.6 \text{ \AA}$. (c) High-resolution STM image of a part of a terphenyl-butadiyne wire placed at the lower step-edge ($U_{\text{bias}} = -1.5 \text{ V}$, $I_t = 0.05 \text{ nA}$). (d) Model of the situation depicted in (c) with the chemical structure of the wire and the registry with the underlying Ag(877) substrate. Dark blue and light blue refer to the upper and lower terrace edge, respectively. (c) and (d) are of the same scale. Reproduced with permission from [173], Copyright (2014) American Chemical Society. The sample was measured by Borja Cirera.

To test the stability of the 1D GDY molecular wires, *in situ* manipulations by laterally displacing the STM tip in the constant current mode were carried out (Figure 3.1.5).^[184] The movement path of the tip was along the black arrow in Figure 3.1.5a. In this process, a segment of a polymer wire is strongly distorted, while keeping its topologic integrity (Figure 3.1.5b,c). As shown in Figure 3.1.5c, the eleven monomers form an almost closed circle after manipulation. The butadiyne groups exhibit an impressive flexibility, and the angles β enclosed by the long axes of two neighboring units (Figure 3.1.5c) cover a range from 25° to 40° .

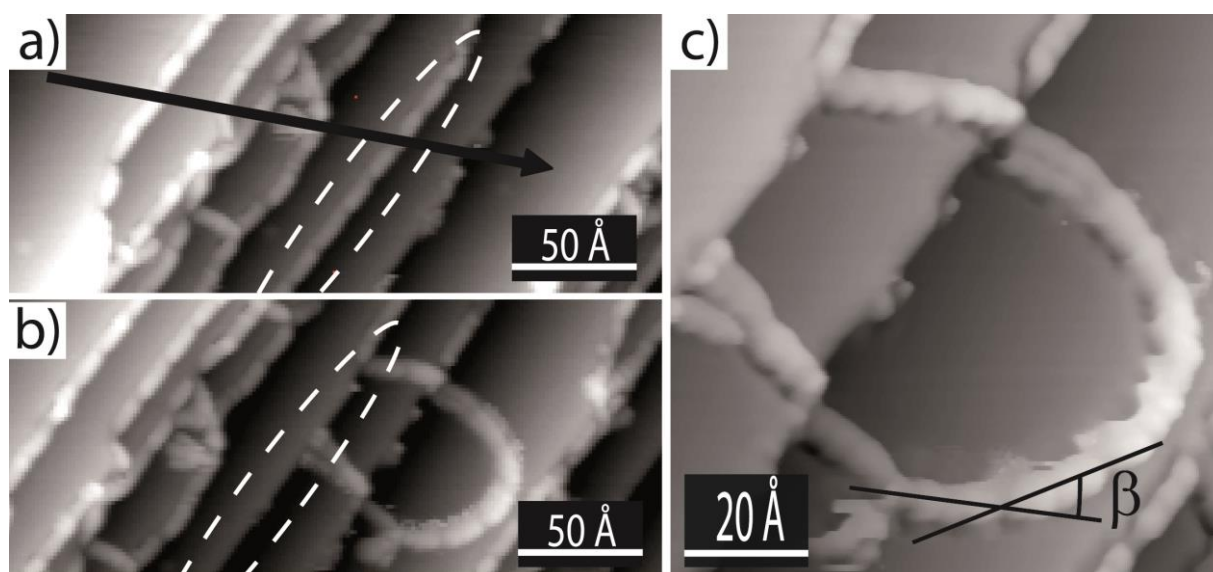


Figure 3.1.5 (a) Direct manipulation of a polyphenyl-butadiyne chain. ($U_{\text{bias}} = -0.98 \text{ V}$, $I_t = 0.1 \text{ nA}$). The black arrow indicates the path of the tip manipulation and the white dashed ellipse highlights the segment to be displaced. (b) Same area after performing the lateral manipulation (Parameters: $U_{\text{bias}} = 0.1 \text{ V}$, $I_t = 20 \text{ nA}$) using constant-current mode imaging ($U_{\text{bias}} = -0.98 \text{ V}$, $I_t = 0.1 \text{ nA}$). (c) Zoomed-in image of the detached segment of **1** polymer ($U_{\text{bias}} = -0.5 \text{ V}$, $I_t = 0.1 \text{ nA}$). Butadiyne bridges exhibit a significant flexibility, with an angle β between neighboring monomers in the range of 25° to 40° . Reproduced with permission from [173], Copyright (2014) American Chemical Society. The sample was measured by Borja Cirera.

For the investigation of the electronic properties of the 1D material, we used DFT calculations to compute the electronic band structure of an infinite defect-free 1D wire,

without any interaction with the substrate (Figure 3.1.6). The maxima of the occupied states and the minima of the unoccupied are both at $k_x = 0$, with a band gap value ca. 1.6 eV. Therefore, the ideal terphenylene-butadiynylene wire constitutes a direct band gap organic semiconductor.

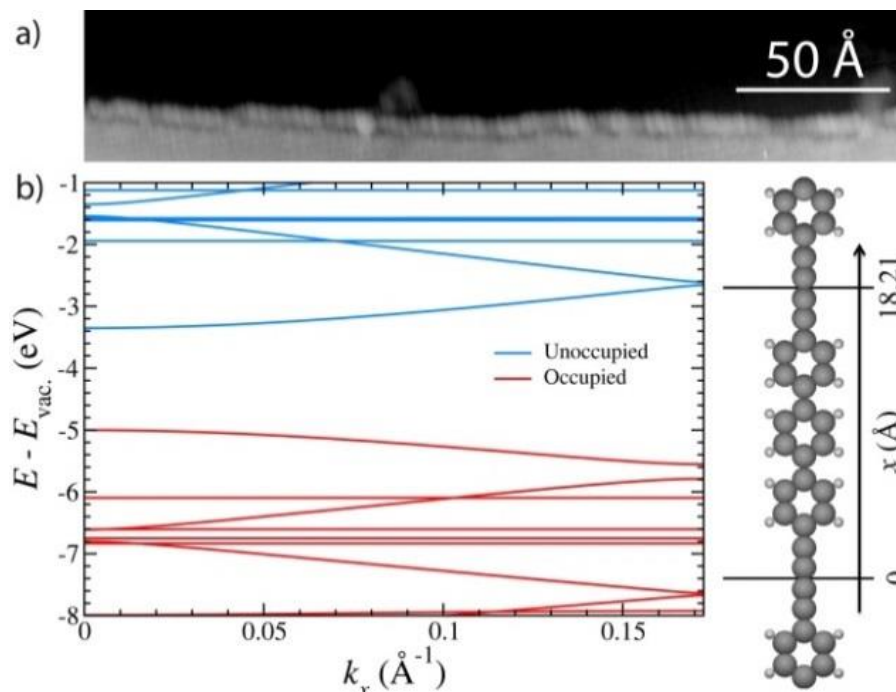


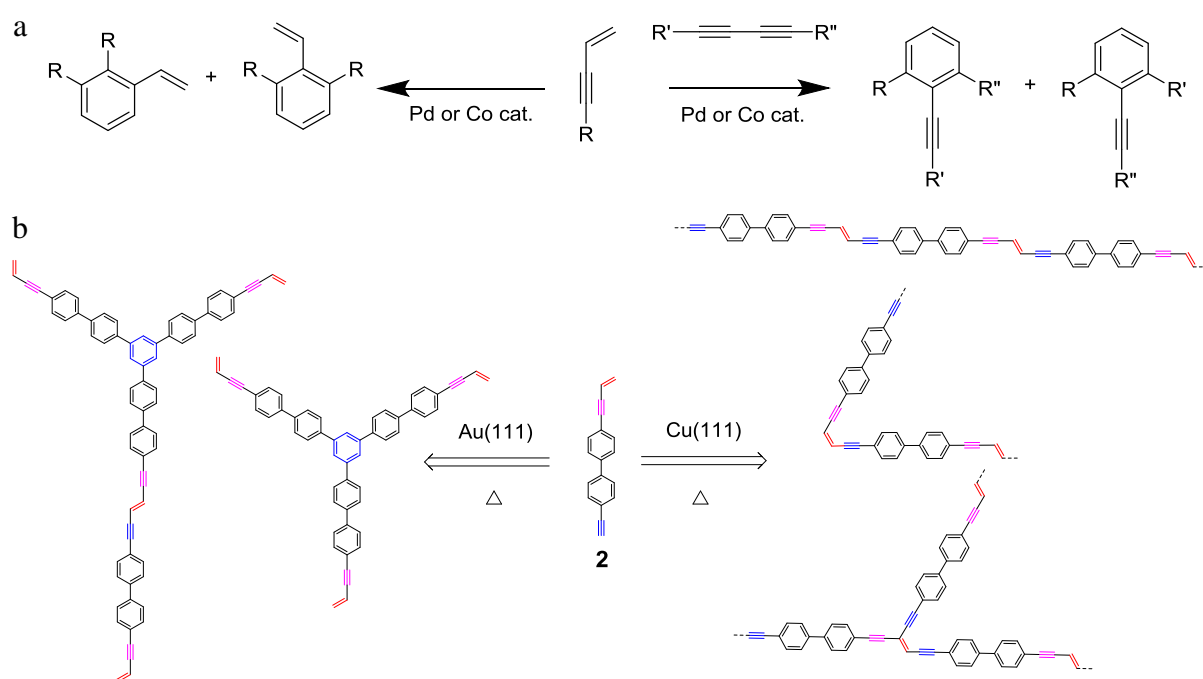
Figure 3.1.6 (a) STM image of a ca. 268 Å long polymer, by successfully covalently linking at least 15 monomers ($U_{\text{bias}} = -1.08$ V, $I_t = 0.07$ nA). (b) Electronic band structure (left) obtained from DFT calculations of an infinite 1D polymer (right) as a function of the wave vector k_x . Reproduced with permission from [173], Copyright (2014) American Chemical Society. The Calculation was carried out by Jonas Björk.

In conclusion, by confining the terminal alkyne precursor to step edges of a vicinal Ag(877) template, chemoselective homo-coupling of alkyne is preferred over branching side-reactions on the planar Ag(111) surface, yielding a novel atomically precise 1D extended GDY. DFT calculations show the new material is a 1D semiconductor with a prosperously simple band structure with the desirable small energy gap.

3.2 Polymerization of alkyne and enyne containing compounds on metal surfaces

The STM work of this chapter was carried out by myself in the group of Prof. Dr. J. V. Barth at the Technical University of Munich during the stay from March 2015 to August 2015.

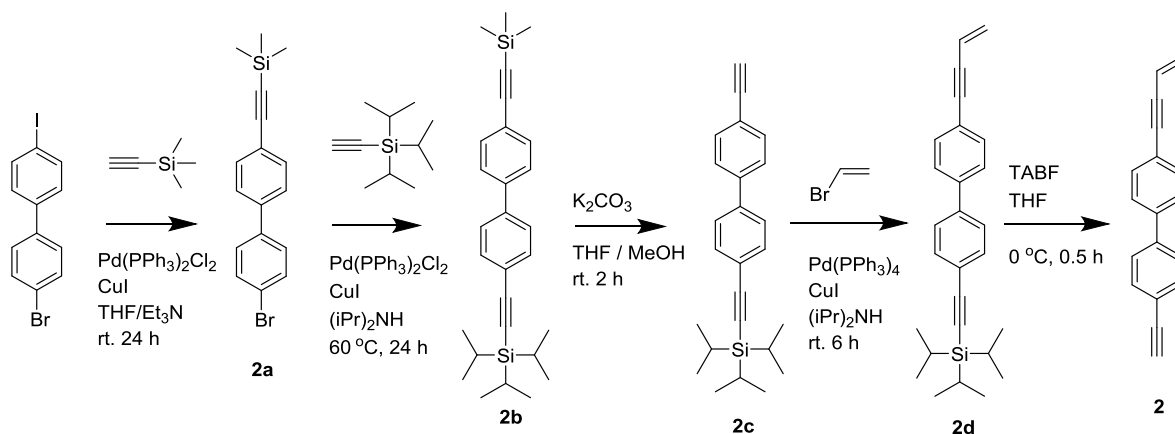
Compared to terminal alkyne compounds, terminal alkene molecules show lower reactivity. For example, terminal alkenes are normally not activated on Au(111) and Cu(111) surfaces. However they can be coupled to (*Z,Z*)-butadiene with high stereoselectivity on the Cu(110) surface.^[185] Almost all previously mentioned on-surface reactions involve C–C homo-coupling, however, the cross-coupling of alkyne (*sp* carbon) and alkene (*sp*² carbon) has not yet been studied under surface confinement. With this aim in mind, we have introduced both an alkyne and an enyne group into a biphenyl backbone rendering the compound 4-(but-3-en-1-ynyl)-4'-ethynyl-1,1'-biphenyl (**2**); considered to act as the precursor for on-surface cross-coupling reactions. Taking advantage of the different functional groups within the same molecule and their different degrees of activity on different substrates, our goal is to cross-couple *sp*² and *sp* carbons on surfaces.



Scheme 3.2.1 (a) The [4 + 2] Cross-Benzannulation reactions of enyne with alkynes in solution. (b) Possible on-surface reactions after annealing of **2**; blue color bonds are terminal alkyne groups; purple bonds are alkyne groups in enyne groups; red bonds are alkene groups. On Au(111) surface the main reaction is cyclotrimerization. On Cu(111) surface, the main reaction is cross-coupling.

In solution, the enyne compounds prefer to undergo [4 + 2] cycloadditions with an alkyne group (Scheme 3.2.1a),^[186] While on surfaces the enyne and the alkyne show a totally different reaction path (Scheme 3.2.1b). During the annealing, the main reaction observed is the cyclotrimerization of the alkyne on the Au(111) surface; while on the Cu(111) surface the main reaction consists in the cross-coupling of enyne group and alkyne group. The observed reactions of compound **2** would be an interesting model for the study of the different selectivity on surfaces for alkyne and alkene reactions.

The structure of the novel compound **2** is depicted in Scheme 3.2.1b. The compound is an asymmetrically substituted molecule with one 1,3-enyne group in 4 position and other alkyne group in the 4' position of the biphenyl backbone. Compound **2** was synthesized from 4-bromo-4'-iodo-1,1'-biphenyl by a stepwise procedure as shown in Scheme 3.2.2.



Scheme 3.2.2 Synthetic route of compound **2**.

TMS and TIPS protecting groups were introduced for the alkynylation of the arenes step by Sonogashira cross-coupling. This surprising behavior is attributed to the different activity of I and Br substituents in the starting material. Using the specific reactivity of the TMS and TIPS protective groups, after selective cleavage of TMS by $\text{K}_2\text{CO}_3/\text{MeOH}$, the vinyl bromide was used to cross-couple the terminal alkyne to form the enyne group. After cleavage of TIPS by TBAF, compound **2** could be isolated. The GC-MS (Figure 3.2.1) and NMR spectra confirmed that the final product is obtained with high purity.

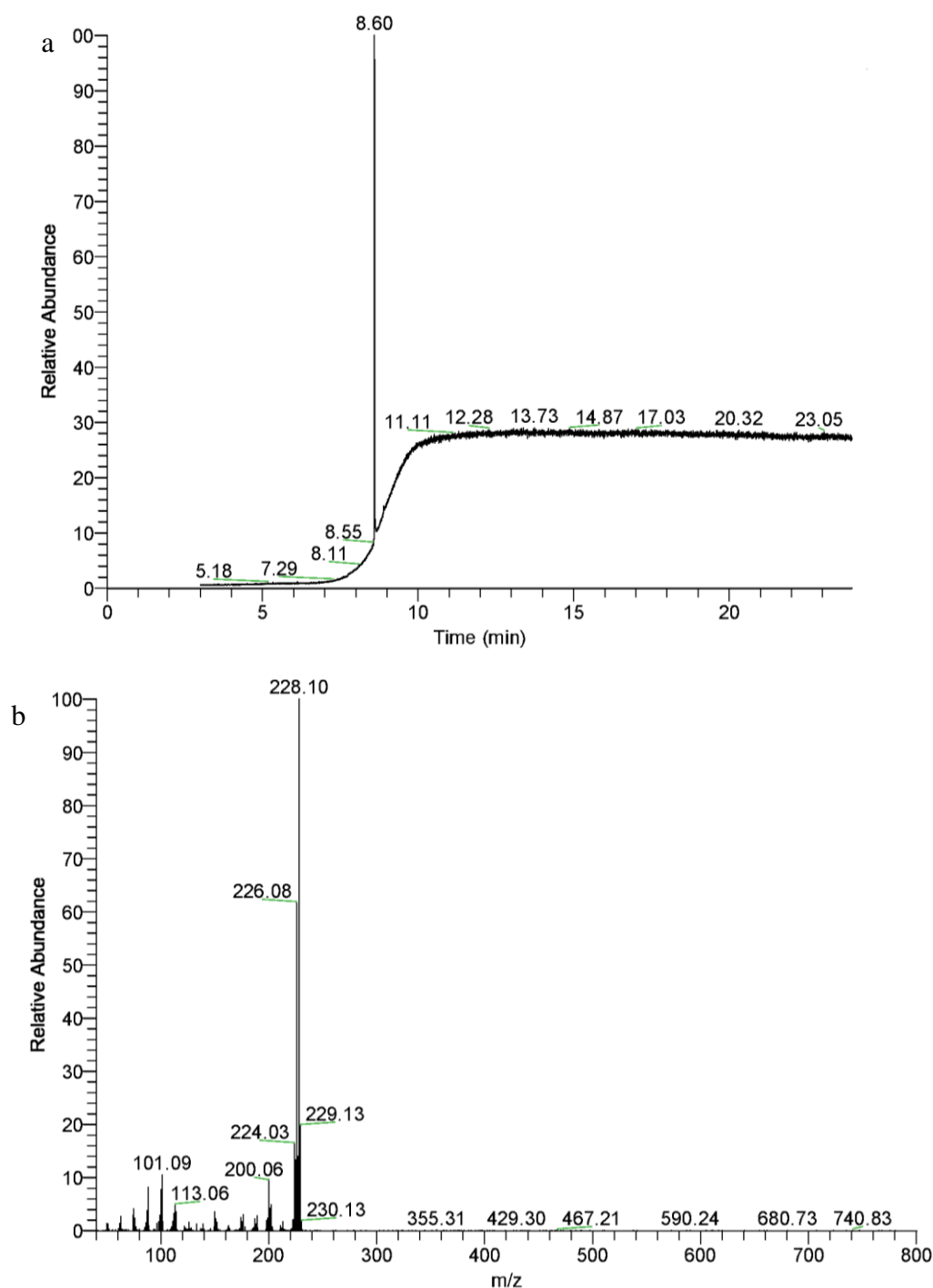


Figure 3.2.1 GC-MS of compound **2**. (a) GC spectrum of compound **2**. (b) EI-MS spectrum of compound **2** at the time 8.60 min.

STM experiments were carried out in a home-built Besocke-type ultrahigh-vacuum scanning tunneling microscope (UHV-STM) with a base pressure below 2×10^{-10} mbar. The Au(111) and Cu(111) single crystal surfaces were cleaned by repeated cycles of Ar^+ ion sputtering (10 min) and annealing at 600 and 400 °C, respectively. Molecules of compound **2** were deposited by organic molecular beam epitaxy (OMBE), at a crucible temperature of around 60 °C. Mass spectrometry (MS) was used to verify that the evaporated molecules were

intact. The samples were *in situ* transferred into the hosting chamber of the STM. All STM images were collected in the constant-current mode with an electrochemically etched tungsten tip at a stable temperature of 5.5 K. The Cu(111) substrate was atomically resolved at equilibrium temperatures to calibrate the data with the theoretical lattice parameters: interatomic distance $a = 2.556 \text{ \AA}$,^[187] two nearest row distance $d = 2.214 \text{ \AA}$,^[188] obtained with the correction factor 1.085 and 1.077 for x and y , respectively (Figure 3.2.2).

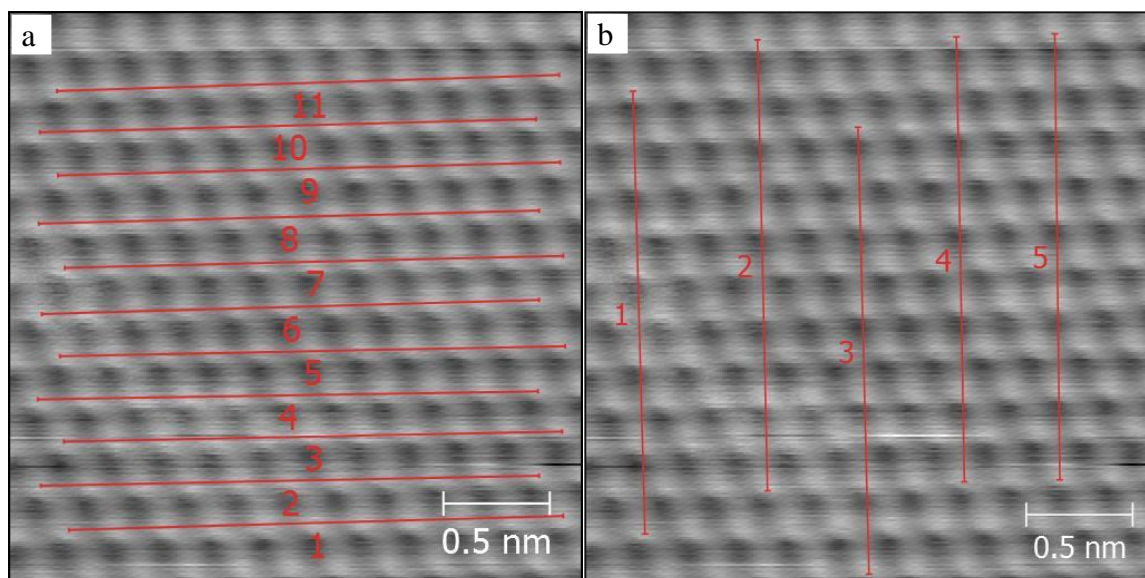


Figure 3.2.2 Cu(111) surface calibration at low temperature. Distance measurements for (a) a and (b) d . Scanning parameters: $U_{\text{bias}} = -0.07 \text{ mV}$, $I_t = 0.5 \text{ nA}$.

A coverage of 0.3 monolayers (ML) of **2** was deposited onto the Au(111) substrate, which was held at $0 \text{ }^\circ\text{C}$. As shown in Figure 3.2.3a, an individual molecule of **2** appears as a rod with a protrusion at one side (red arrows in Figure 3.2.3c). The protrusion can be ascribed to the enyne group. Besides individual molecules, the molecules also form self-assembled patterns, namely, windmill, triangle and square motifs. Upon deposition, the molecules preferentially occupy elbow sites. It can also be observed that some fuzzy features appear in the image, which indicate that the molecules are still mobile even at such low temperature (scanning temperature about 5 K). When more molecules being deposited, they begin to grow along fcc stripes irregularly, as shown in Figure 3.2.3b (0.8 ML).

Three kinds of molecular interactions lead the observed self-assembled patterns. The first phenomenon is the weak intermolecular $\text{C-H}\cdots\pi$ interaction between hydrogen atoms of the terminal alkyne groups and the π system of enyne group of the nearby compound **2** molecules. As a result, the triangle (red circles in Figure 3.2.3b, Figure 3.2.3c-i,d-i, 2%) and rectangle shaped (yellow circle in Figure 3.2.3b, Figure 3.2.3c-ii,d-ii, 1%) supramolecular nodes are assembled by three and four molecules, respectively.

Second, the main and strongest interaction is the intermolecular C–H \cdots π interaction between hydrogen atoms of the terminal alkyne groups and the π bond of terminal alkyne group of the nearby compound **2** molecules.^[189] Four-fold windmill-shaped nodes (yellow circles in Figure 3.2.3b, Figure 3.2.3c-iii,d-iii, 80%), five-fold (blue circles in Figure 3.2.3b, Figure 3.2.3c-iv,d-iv, 7%) and six-fold (purple circles in Figure 3.2.3b, Figure 3.2.3c-v,d-v, 5%) windmill-shaped nodes are formed. All supramolecular nodes show chiral geometry with *R* or *S* enantiomers (solid circles and dash circles for *R* and *S* respectively).^[190] Both enantiomorphs are expressed in two almost equivalent configurations.

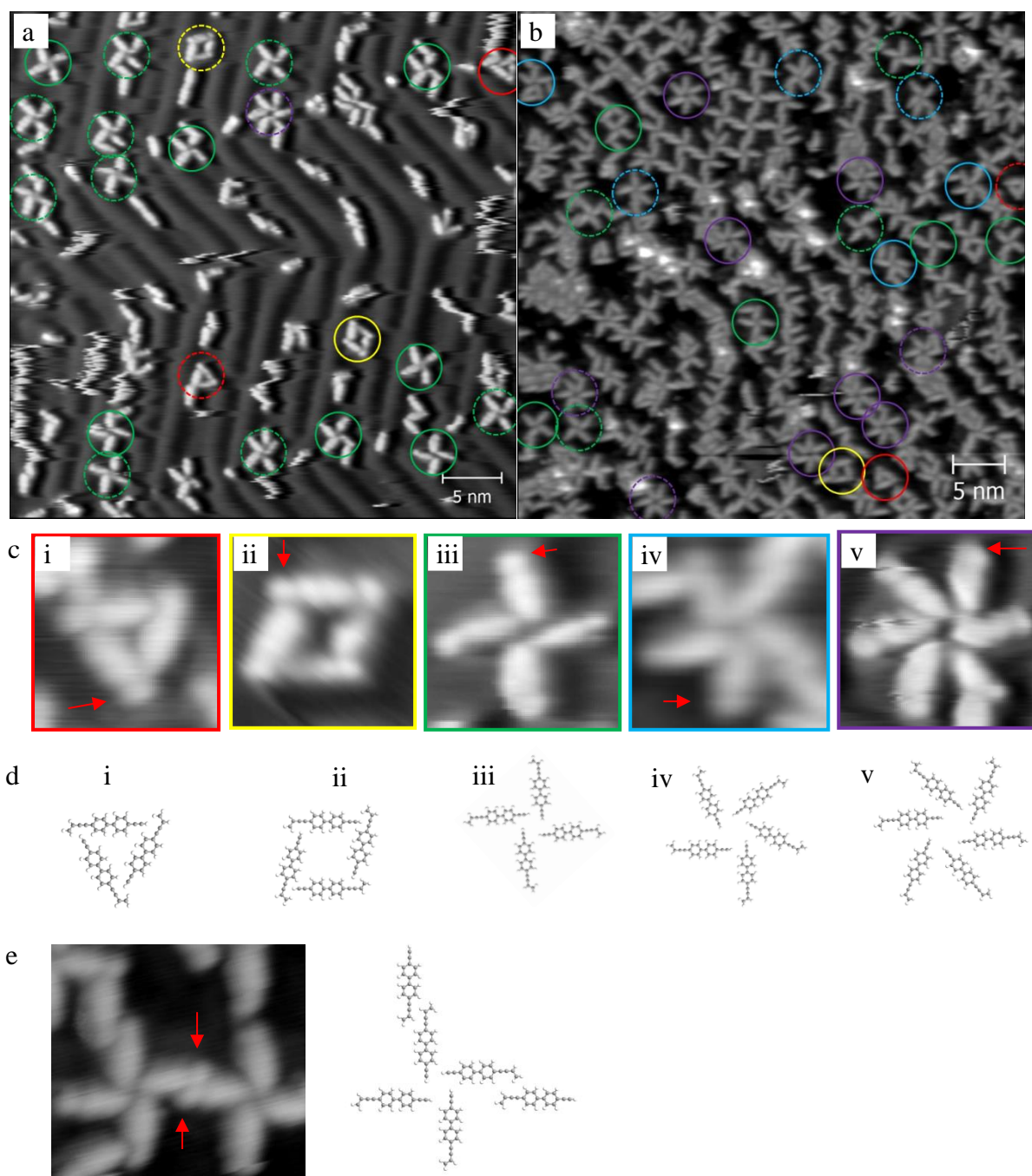


Figure 3.2.3 Initial deposition of compound **2** on Au(111) surface (0 °C) with about (a) 0.3 ML and (b) 0.8 ML coverage. Scanning parameters: $U_{\text{bias}} = -1$ V, $I_t = 0.1$ nA. (c) Magnified STM images of five kinds of isolated supramolecular nodes (i-v). Red arrows show the pro the enyne groups. (d) Five models of supramolecular nodes corresponding to (a,b,c). (e) One unit in 2D close-packing from four-fold windmill nodes.

The third interaction is the weak $\text{C-H}\cdots\pi$ interaction between two enyne groups (Figure 3.2.3e). Besides the irregular domains made from different nodes, there are also some regular closely-packed reticular four-fold assemblies, which are formed by the third interaction between the four-fold windmill-shaped nodes. When carefully analyzing the enantiomorphs of these domains which were formed by four-fold windmill-shaped node as a unit, we find out that these domains are 2D racemic crystals. The heterochiral bonding motifs are arranged as line-wise stacking phase (Figure 3.2.4a),^[191] the closest neighbors phase (Figure 3.2.4b),^[190c,192] and a mixed phase (Figure 3.2.4c).

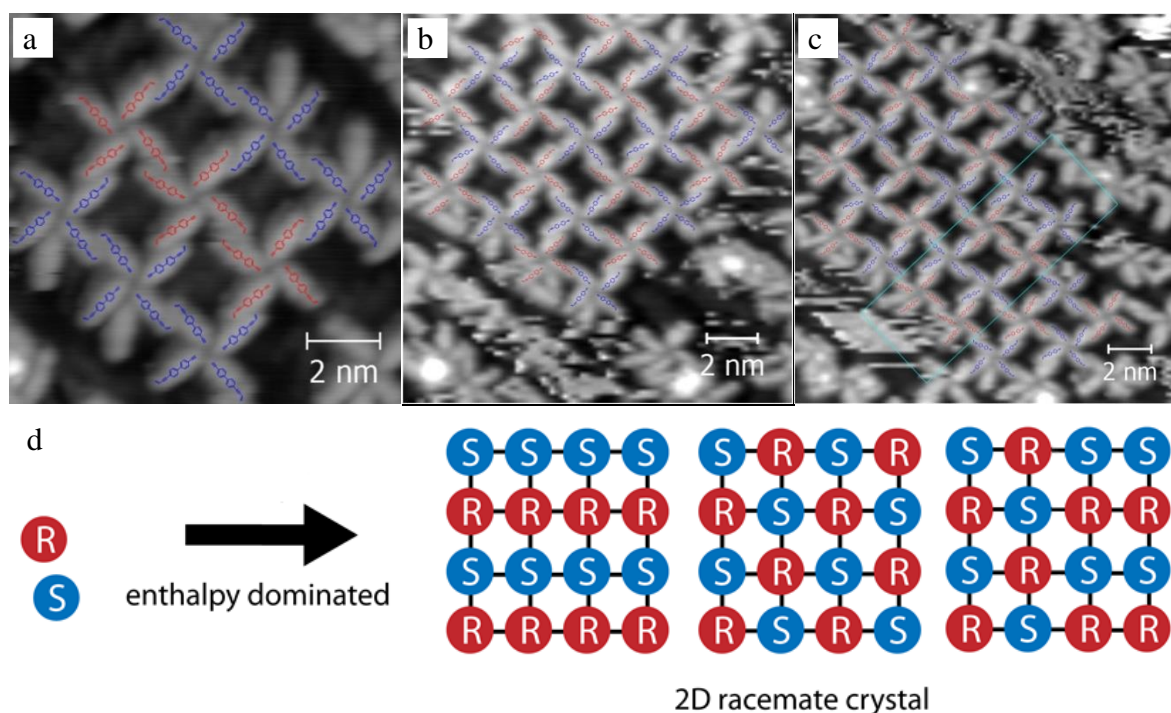


Figure 3.2.4 The STM images of three domains of supramolecular networks on Au(111) deposited when surface hold at 0 °C: (a) the closest neighbors phase, (b) following line-wise stacking phase, and (c) the mix phase with the green box highlighted the closest neighbors small domain. (d) The schematic representations of enthalpy dominated three kinds phase of 2D racemate crystal model.

After annealing the sample of compound **2** at 120 °C for 10 min, the majority of the compounds undergoes cyclotrimerization (blue cycles in Figure 3.2.5a) on isolated places on the surface. There is a protrusion in each terminal of the Y shape cyclotrimerization product (red arrows in Figure 3.2.5b) which proves that the cyclotrimerization occur between the alkyne groups not the enyne groups. Moreover, some tetramers (green cycles in Figure 3.2.5a)

also exist due to the reaction between the enyne group of the cyclotrimerization product with alkyne group of another compound **2** molecule. It can be seen that a small amount of monomers (blue arrows in Figure 3.2.5a) as well as of dimers (pink cycles in Figure 3.2.5a) molecules is present on the surface.

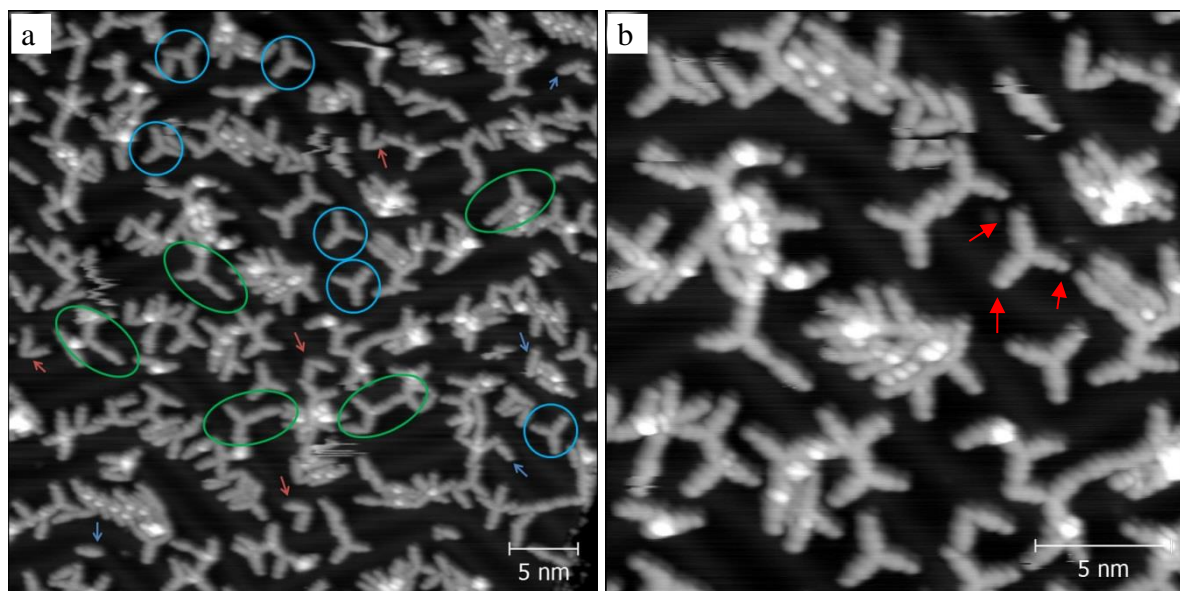


Figure 3.2.5 STM images of annealing products of **2** on Au(111) after 120 °C thermal treatment. Scanning parameters: $U_{\text{bias}} = -1$ V, $I_t = 0.1$ nA.

In order to trigger the further polymerization of the still unreacted molecules, we annealed the sample to 160 °C for 10 min. As shown in Figure 3.2.6, the molecular coverage decreases indicating that some molecules are desorbed from the substrate during this process. No further reaction occurs after applying the new conditions (Figure 3.2.6).

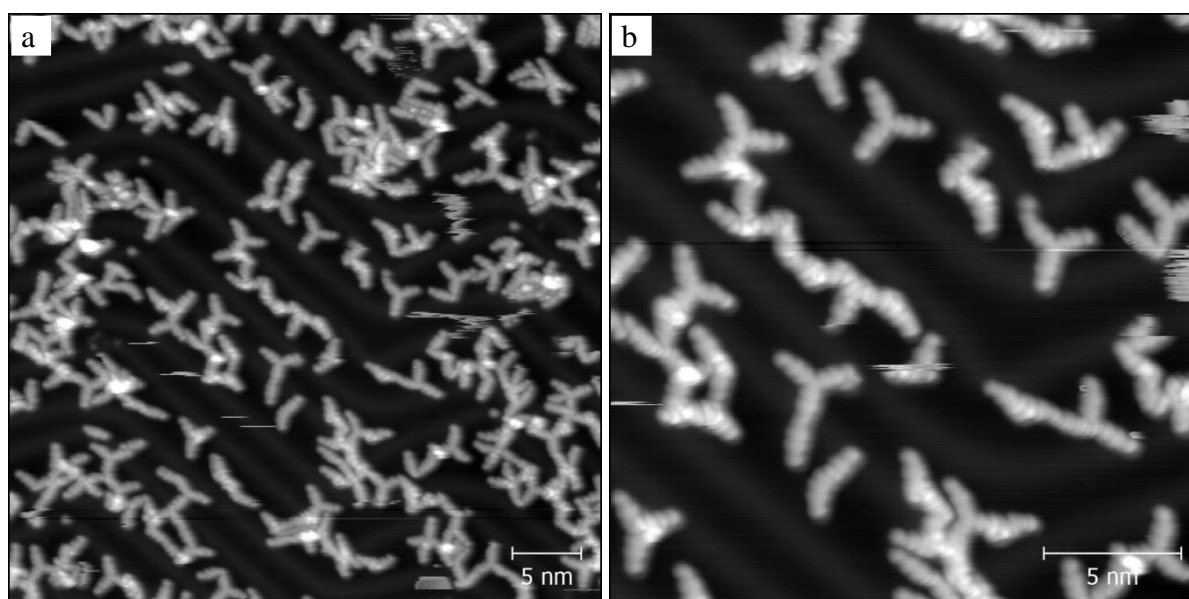


Figure 3.2.6 STM images of annealing products of **2** on Au(111) after 160 °C thermal treatment. Scanning parameters: $U_{\text{bias}} = -1$ V, $I_t = 0.1$ nA.

Due to the low activity of enyne group on Au(111), we changed to Cu(111), which has a higher catalytic surface. As a first approach, a 0.3 ML coverage of the compound **2** molecules was deposited onto the Cu(111) substrate, which was held at $-70\text{ }^{\circ}\text{C}$. As shown in Figure 3.2.7a, compound **2** molecules is isolatedly distribute and the molecules appear as a rod with a protrusion at one side as on Au(111) surface. The protrusion can be ascribed to the enyne group (red arrows in Figure 3.2.7b).

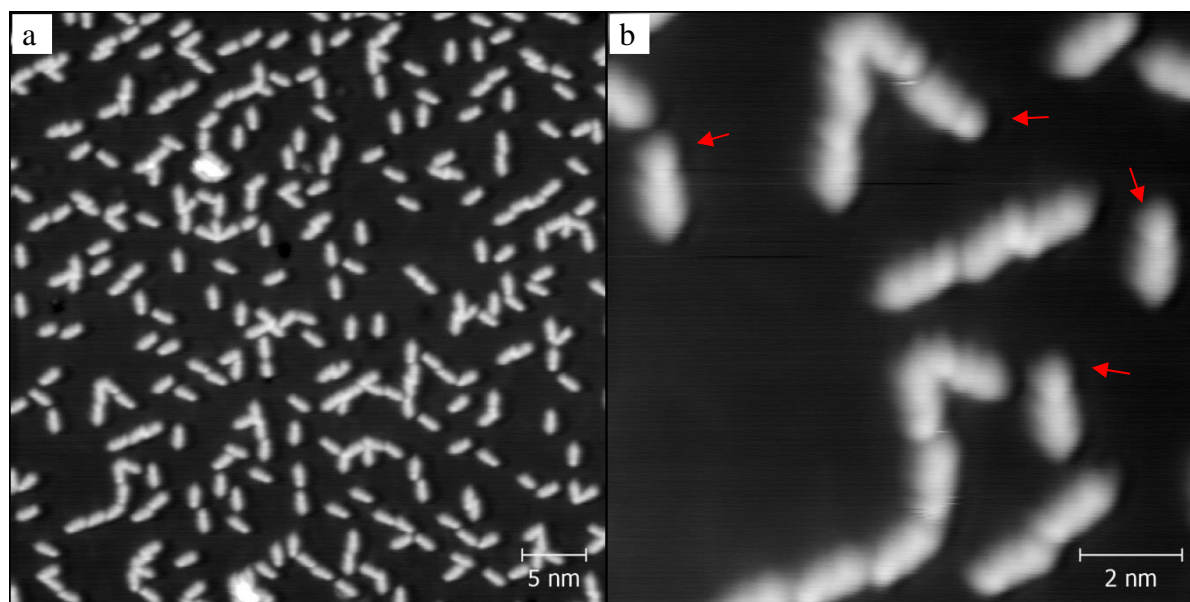


Figure 3.2.7 (a,b) STM images of the deposition of **2** molecules (0.3 ML) on Cu(111) as a substrate temperature of $-70\text{ }^{\circ}\text{C}$. Red arrows show the protrusion of the compound **2** molecule which ascribed to be the enyne group.

As shown in Figure 3.2.8a,b, after annealing at $90\text{ }^{\circ}\text{C}$, some linear chains appear, indicating that this thermal treatment triggers the formation of covalent bonds. Conversely, on Au(111) surface, the main reaction is the linear cross-coupling reaction of the enyne and alkyne groups of two compound **2** molecules. Some branched cross-coupling reactions also occur (Scheme 3.2.2) giving V and Y shape connected nodes and making the polymer extending to a disordered 2D covalent network. To further verify the reaction, we measured the distance of the repeating units (Figure 3.2.8b) which around $1.57 \pm 0.06\text{ nm}$. This measured distance is congruent with the distance of 1.587 nm of a model oligomer simulated by MP7 method through a MAPOC program (Figure 3.2.8e).

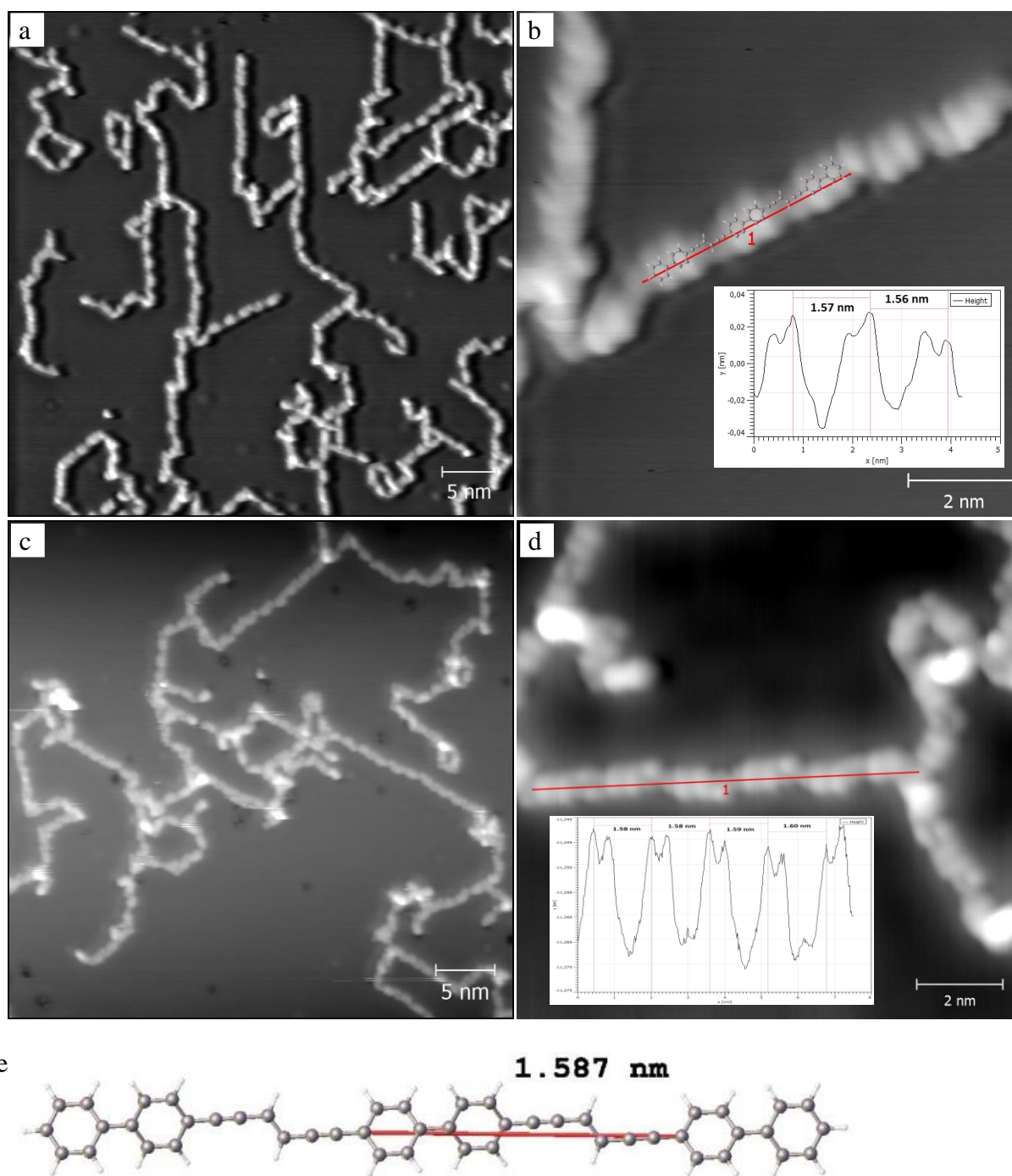


Figure 3.2.8 (a,b) Polymerization of **2** on Cu(111) surface after 90 °C annealing. Inset of (b) is the line-scan profile of the polymer marked by red line in (b). (c,d) Polymerization of **2** on Cu(111) surface after 160 °C annealing. Inset of (d) is the line-scan profile of the polymer shown in (d, red line). (e) A structure model calculated by MP7 through MOPAC program, where the distance is in good agreement with the result obtained from line-scan profiles of (b) and (d).

Furthermore, to achieve increased polymerization activity an annealing at 160 °C was carried out. The structure shown in Figure 3.2.8c,d displays one single polymer. Such a large polymer shows that the cross-coupling of alkyne and enyne groups is an effective reaction path for on surface polymerizations. Interestingly, we find out that there are always one or two bright spots along each alkyne-alkene linkage. The measurement of the repeating units

distance shows that each unit is perfect with a distance of 1.59 ± 0.06 nm; almost identical with the 90°C annealing product. We assume that some Cu atoms are pulled out of the surface and coordinate to the alkyne-alkene-alkyne linkage of the polymer. One bright spot corresponds to a single Cu atom (Figure 3.2.9).

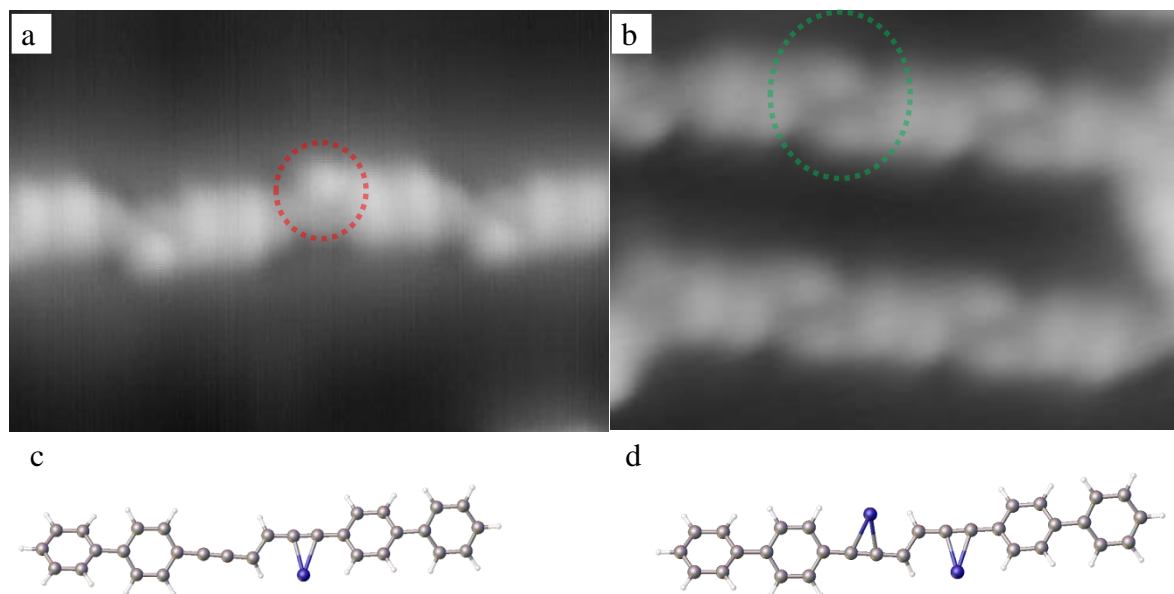


Figure 3.2.9 Magnified STM images of 1D chain of polymer with one (a, red cycle) or two (b, green cycle) bright spots appeared near the alkyne-alkene-alkyne linkage. (c,d) The possible metalorganic structures of the two kinds of polymer chain repeating units.

To investigate the effect of the coverage on the reactions, we deposited a high coverage (0.8 ML) of compound **2** molecules on the Cu(111) surface (Figure 3.2.10a). There is still not regular self-assembly. These may be attributed to the alkyne and enyne groups, which have strong interaction with the Cu(111) surface, blocking finally the self-assembly. After annealing at 160°C , the entire surface became one extended polymer through the cross-coupling reactions (Figure 3.2.10b,c,d). The figures also show similar reaction types as found as low coverage and the linear wires become shorter, which makes covalent network to express only a narrow porosity.

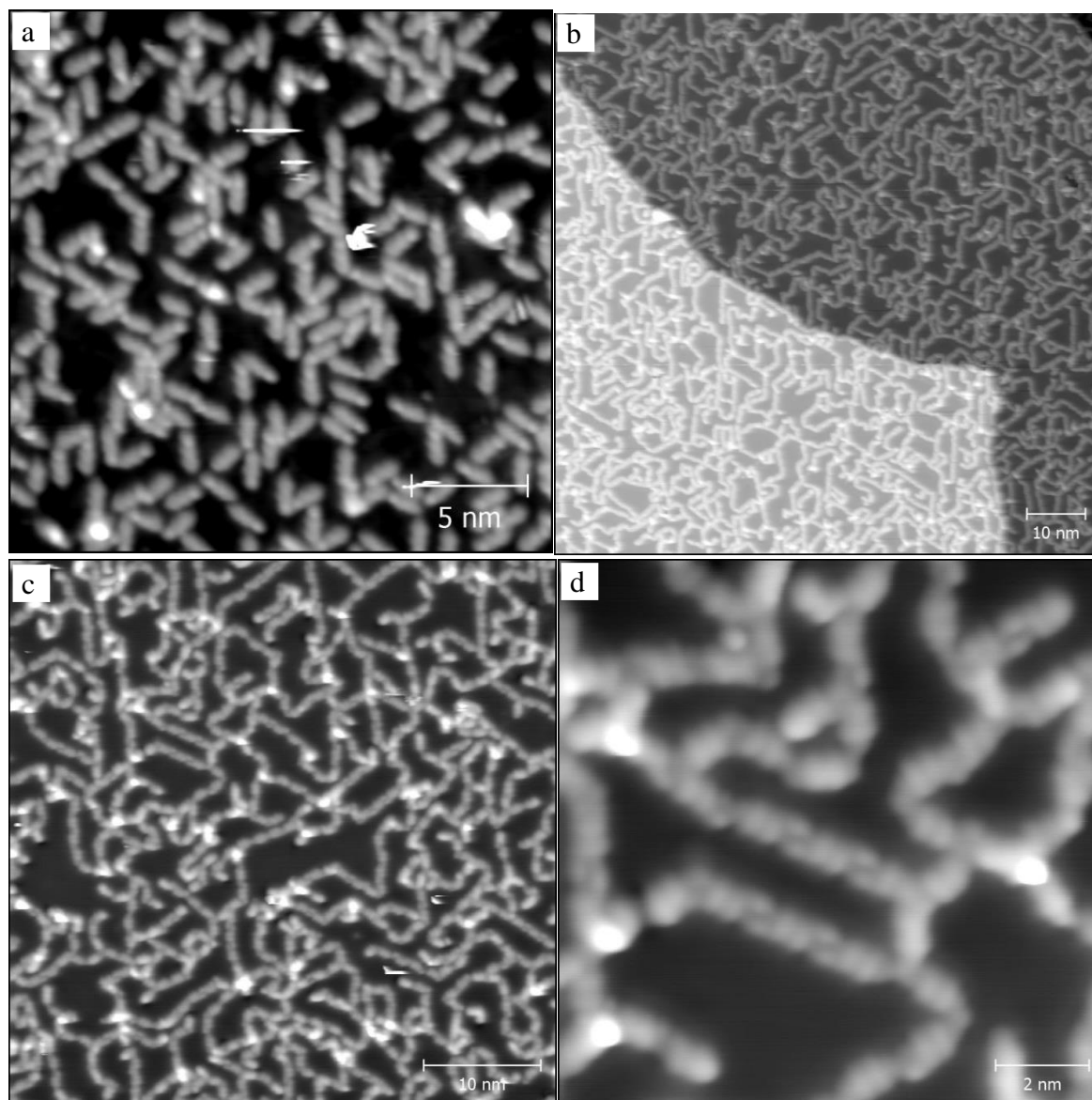


Figure 3.2.10 (a) STM images of the deposition of compound **2** molecules (0.8 ML) on Cu(111) with substrate temperature of -70 °C. (b,c,d) Polymerization of **2** on Cu(111) surface after 160 °C annealing.

In conclusion, the self-assembly and the reactions after annealing of enyne and alkyne groups containing compound **2** were investigated on the Au(111) and Cu(111) surfaces. On Au(111) surface, compound **2** can form windmill, triangle and square supramolecular nodes. The four-fold windmill-shaped nodes can further self-assemble to 2D racemate crystals with three kinds of phases: line-wise stacking phase, closest neighbors phase and mixed phase. During the annealing, the Au(111) surface does not achieve to activate the enyne group yielding as the mainly cyclotrimerization of alkyne. On the Cu(111) surface, the enyne groups can cross-couple very effectively with alkyne groups giving a 2D infinite covalent network. After annealing at 160 °C, the Cu atoms can coordinate to the alkyne-alkene-alkyne linkages to form the organometallic polymer chains. The work herein reports on the first alkyne/alkene

cross-coupling reaction on surfaces, which opens a new route towards the fabrication of covalent polymers on surfaces.

3.3 Alkynenitriles as ligand for surface 2D coordination network

This chapter was adapted from the publication *Beilstein J. Nanotechnol.* 2015, 6, 327-335, entitled “Synthesis, characterization, monolayer assembly and 2D lanthanide coordination of a linear terphenyl-di(propiolonitrile) linker on Ag(111)”, © 2015 Chen et al.^[193] All results were elaborated in close collaboration with the group of Prof. Dr. J. V. Barth at the Technical University of Munich.

During the last decade, supramolecular chemistry on surfaces has emerged as a versatile strategy to design surface-confined nanoarchitectures and has attracted strong interest because of its potential for novel materials and functional nanoscopic devices.^[89]

In parallel, rare-earth complexes have been employed in the design of materials with extraordinary magnetic properties,^[194] including single molecular magnets (SMMs),^[194b,195] which serve as pivotal subunits for modern developments in spintronic devices.^[196]

Combining these two recent developments, a 2D Ln-*p*-terphenyl-dicarbonitrile network showing five-vertex Archimedean surface tessellation was successfully synthesized on Ag(111) surface.^[95b,95g]

Terphenyl-4,4''-dicarbonitrile (NC-Ph₃-CN, **TDCN**), belonging to the class of polyphenyl-dicarbonitrile molecules NC-Ph_{*n*}-CN, has been intensively studied as a linker in molecular and metal coordination assemblies under 2D confinement.^[93,95b,197] With the goal to achieve increased coordination numbers (7-12) (typically for f-block elements in bulk chemistry^[95b,198]), we introduced the alkyne group between the phenyl group and the CN group and designed a novel terphenyl-4,4''-dipropiolonitrile (NC-C≡C-Ph₃-C≡C-CN, **3**) linker to reduce the steric repulsion induced by the α-C-H bonds at the terminal phenyl rings and the coordinating donor N-atom of the CN group. By incorporating the propiolonitrile groups into the terphenyl backbone, the distance between the coordination-active N-atom of the CN group and the adjacent phenyl ring bearing the α-C-H group in linker **3** is consequently increased from 2.58 Å (**TDCN**) to 5.14 Å (Figure 3.3.1).

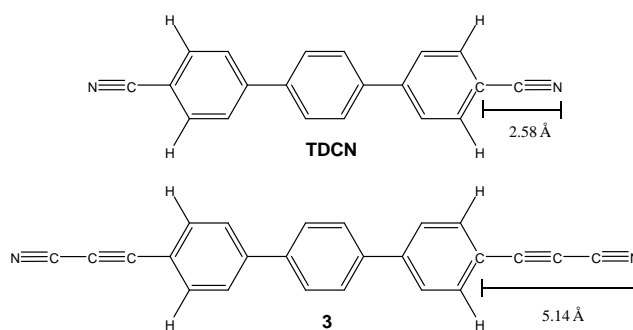
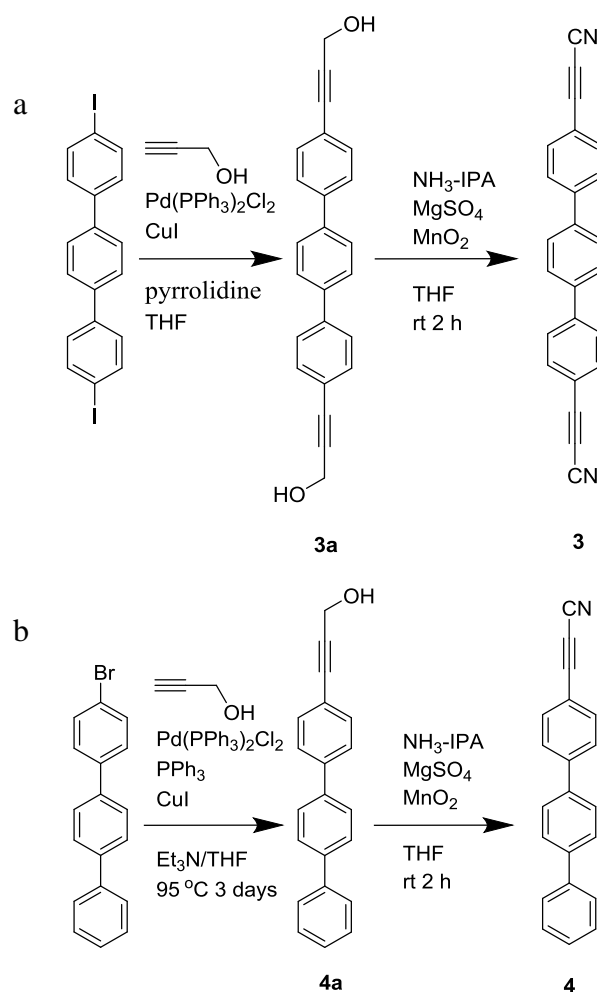


Figure 3.3.1 Representation of the structure of the molecular linkers: **TDCN** and compound **3** showing the increased distance of the coordinating carbonitrile from the sterically hindering α -C-H group at the phenyl ring.

The synthesis of **3** was accomplished in a stepwise manner. Firstly, the diiodoterphenyl was subjected to a cross-coupling reaction with propargyl alcohol in the presence of catalytic amounts of Pd(II) salts yielding the intermediary compound **3a**. This compound was subsequently reacted by a tandem manganese dioxide-mediated alcohol oxidation with *in situ* trapping of the resulting aldehydes with ammonia giving the final product **3** with an overall yield of 18% (Scheme 3.3.1a).^[199]



Scheme 3.3.1 Syntheses of compounds **3** (a) and **4** (b).

Additionally, a small amount of by-product identified as terphenyl-4-propiolonitrile (Ph₃-C≡C-C≡N, **4**) was separated and revealed to be a so far unreported decarboxylation reaction of the propiolonitrile group. The nature of this compound has been confirmed by its direct synthesis from 4-bromoterphenyl following the similar protocol of **3** (Scheme 3.3.1b). The structures of **3** and **4** were characterized by single crystal X-ray structure analysis.

Crystals of compound **3** suitable for single crystal X-ray diffraction were obtained by slow diffusion of hexane into a 1,4-dioxane solution of **3**. Compound **3** crystallizes in the monoclinic system with space group $P2_1/n$. The asymmetric unit consists of a half of crystallographically independent molecule of compound **3** (Figure 3.3.2). The twist angles between phenyl rings are 31° . The long axis of the molecule is distorted such that carbon atoms connecting the phenyl rings deviate from the straight line connecting the terminal nitrogen atoms. Similar distortions are quite common for molecules with aromatic rings connected in *para* position. Within the solid phase of compound **3**, the shortest C–H \cdots N \equiv C hydrogen bond distances amount to 2.89 Å and 2.70 Å (N \cdots H separation). The chain formation of NC–C \equiv C–Ph₃–C \equiv C–CN results from H bonding and π -stacking. The different layers stack in molecular columns oriented along the *b*-axis with identical arrangement of the individual moieties resulting in a π -stacking distance of 3.39 Å as can be seen in Figure 3.3.2b, typically appearing for π -stacking.

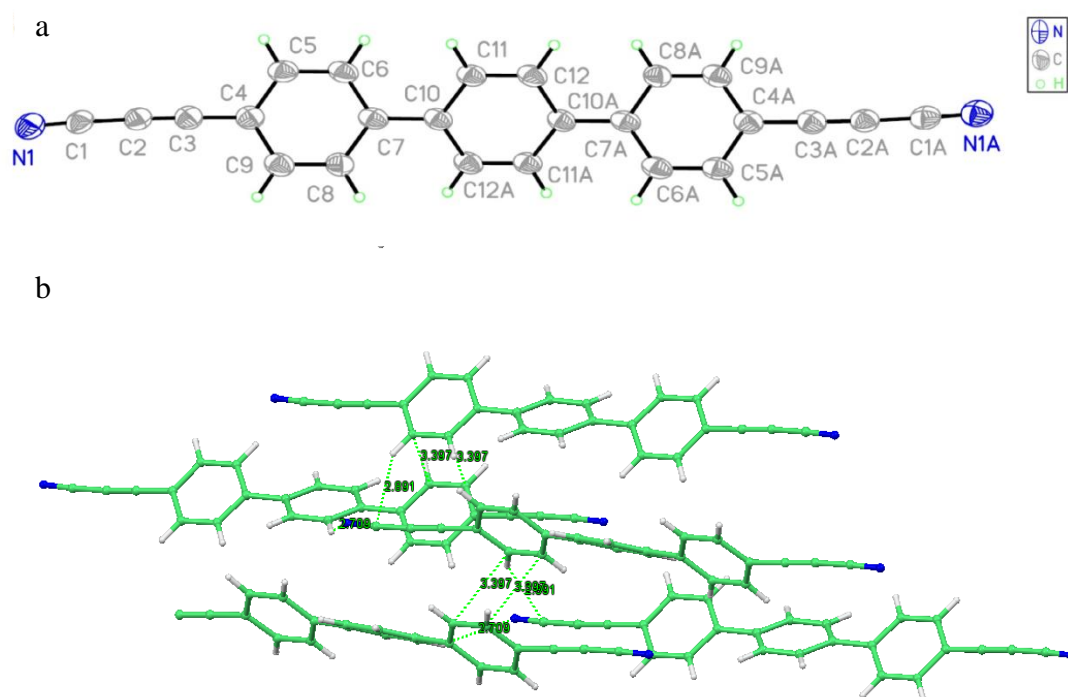


Figure 3.3.2 (a) ORTEP plot of compound **3** with ellipsoids drawn at 30% level of probability for all non-hydrogen atoms, indicating the numbering scheme. (b) The packing view of compound **3** demonstrating the parallel layers arrangement with H bonds of the N \cdots C–H. All distances are given in Å.

Crystals of compound **4** suitable for single crystal X-ray diffraction were grown by slow diffusion of hexane into a solution of **4** in the DCM. Compound **4** crystallizes in the triclinic system with space group $P\bar{1}$. The asymmetric unit consists of three crystallographically independent molecules of compound **4** (Figure 3.3.3). All three molecules exhibit a screw-like structures resulting from by a gradual rotation of the phenyl rings. In contrast to the ditopic

molecule **3**, the twist angles between phenyl rings A/B and B/C of one molecule in the unit cell of **4** are 33° and 10° respectively. The twist angles between phenyl rings in other two independent molecules are average of 35° (Figure 3.3.3a,b). Each nitrogen atom establishes two C–H \cdots N hydrogen bonds, one connecting to the neighbouring molecule within the layer (Figure 3.3.3c) with a N \cdots H separation of 2.56 Å and one connecting to a molecule of the next layer with the separation of 2.62 Å. As can be seen in Figure 3.3.3c, a layer-by-layer arrangement is present in the crystal phase too, but no direct stacking of identically oriented molecules as in the case of compound **3** takes place.

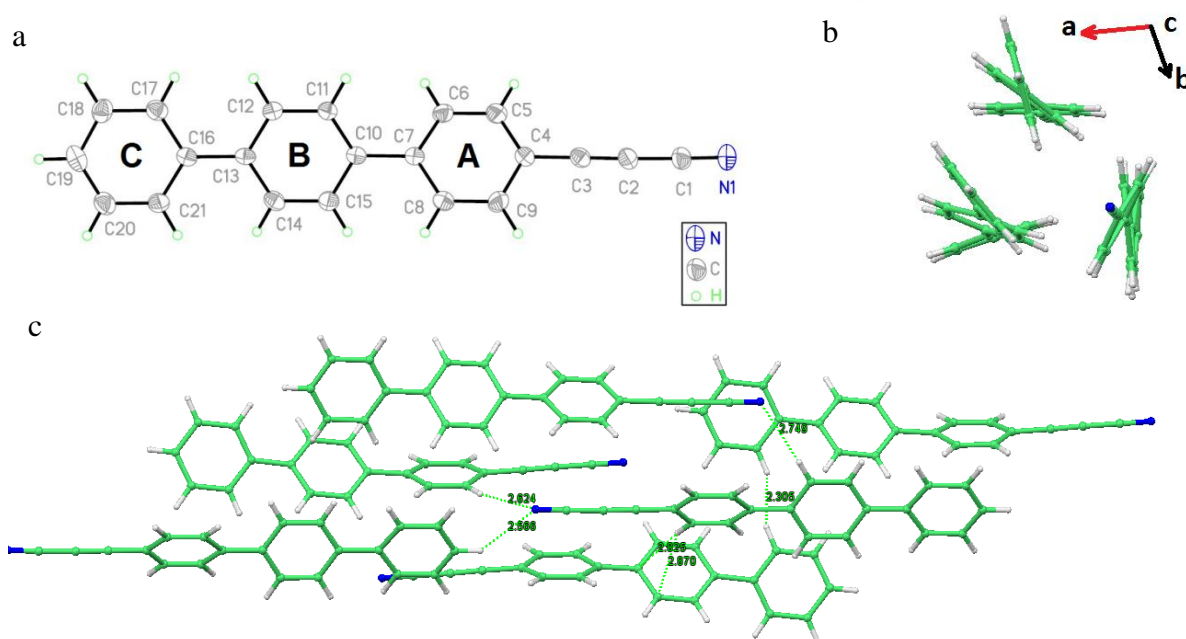


Figure 3.3.3 (a) ORTEP plot of compound **4** with ellipsoids drawn at 30% level of probability for all non-hydrogen atoms, indicating the numbering scheme. (b) 3D visualization of the molecular conformation in the asymmetric unit (view along direction *c*). (c) Molecules arrange in parallel layers. Propiolonitrile groups acquire an antiparallel ordering motif. Two H bonds of the N \cdots C–H type are present. All distances are given in Å.

The STM measurements were performed using a CreaTec low temperature STM (LT-STM). The base pressure of the UHV system was below 2×10^{-10} mbar. The Ag(111) substrate was prepared using standard cycles of Ar⁺ sputtering (800 eV) and subsequent annealing to 723 K for 10 min. All STM images were taken in constant-current mode with an electrochemically etched tungsten tip.

The supramolecular networks based on Gd-ligand coordination motifs were fabricated in a two-step process: Firstly, the compound **3** molecules were deposited by organic molecular beam epitaxy (OMBE) from a quartz crucible held at $T = 479$ K by OMBE onto a clean Ag(111) crystal hold at ~ 300 K. Subsequently, Gd atoms were sublimated by means of

electron beam evaporation from an outgassed Gd rod (99.9%, MaTecK GmbH, 52428 Juelich, Germany) onto the sample hold at ~ 300 K.

In recent years, we performed systematic studies on a series of polyphenylene-dicarbonitrile linkers ($\text{NC-Ph}_n\text{-CN}$, $n = 3-6$) on the Ag(111) surfaces demonstrating the controlled formation of highly-ordered monolayers.^[93,200] Increasing the number of phenyl rings results in either densely packed chevron patterns ($n = 3$), open rhombic networks ($n = 4$) or complex Kagomé lattices ($n = 5, 6$). Changing the stereochemical position of the coordinating -CN groups leads to higher order complexities with partially systemic behavior.^[201]

The new linker **3** was initially deposited onto Ag (111) surfaces hold at 300 K. Similar to **TDCN** (Figure 3.3.4a),^[93] the individual molecules of **3** appeared as rod-like protrusions showing a chevron arrangement but now exhibiting an additional Moiré pattern (Figure 3.3.4b). The Moiré pattern results from the superposition of the monolayer and substrate symmetries, rotated by an angle showing the very subtle balance between molecule-substrate and molecule-molecule interactions.

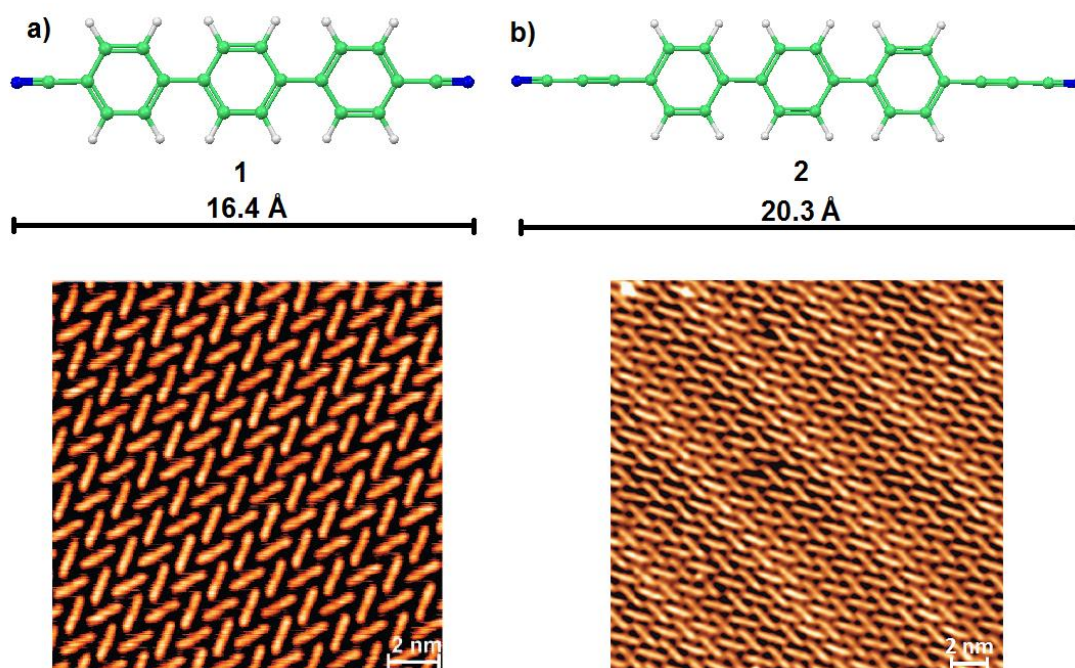


Figure 3.3.4 Comparison of the molecular self-assembled networks of **TDCN** and **3** on the Ag(111) surface. (a) Densely packed chevron layer formed by **TDCN**.^[202] (b) Densely packed chevron layer formed by the **3** species (Data measured at 6 K. Scanning parameters: $U_{\text{bias}} = 0.3$ V, $I = 0.05$ nA). The sample was measured by José I. Urgel.

Figure 3.3.5a shows the high-resolution STM topograph of **3** on Ag(111). The chevron pattern is formed by a proton acceptor-ring interaction between the propionitrile end groups and H-atoms of the phenyl rings from adjacent linkers. To better understand the interaction, a

model based on averaged bonding distances and angles between adjacent molecules whose structure was optimized in the gas phase is given in Figure 3.3.5b. The average phenylene-N distance is 0.26 ± 04 nm, which is slightly shorter than in the earlier reported **TDCN** network (0.33 ± 03 nm).^[93]

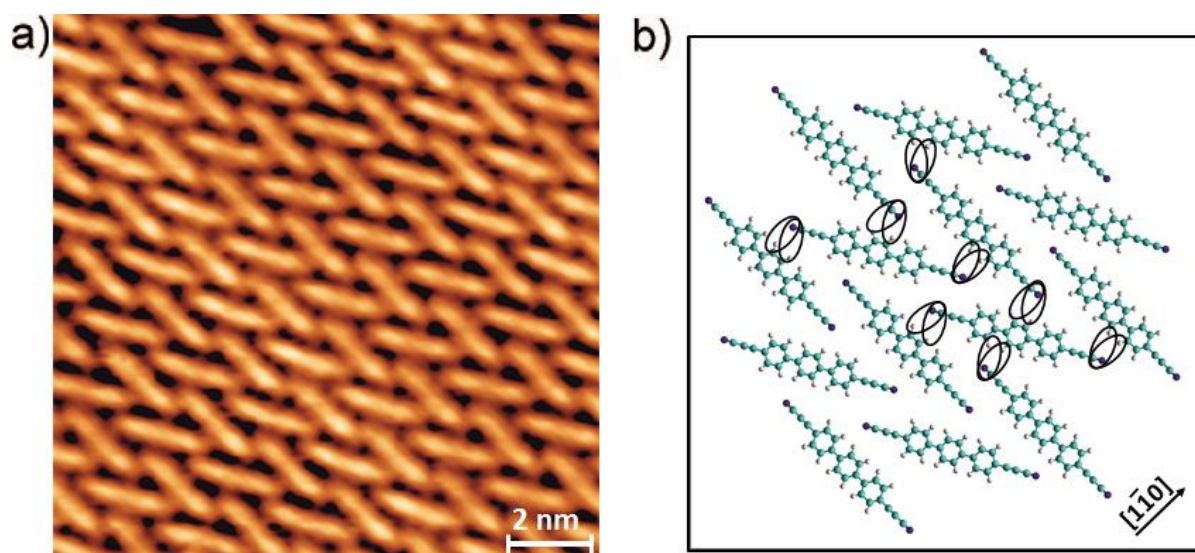


Figure 3.3.5 High-resolution STM image showing (a) the molecular packing in chevron layers mediated by the propionitrile end groups of **3** species (data measured at 6 K. Scanning parameters: $U_{\text{bias}} = 0.3$ V, $I = 0.05$ nA). (b) Corresponding model showing the interaction of adjacent groups. The sample was measured by José I. Urgel.

In previous work, regular metallo-supramolecular nanomeshes were obtained on Ag(111) surfaces from the exposure of $\text{NC-Ph}_n\text{-CN}$ ($n = 3, 4, 5, 6$) linkers to cobalt atoms,^[197a,201b,203] while the use of lanthanide atoms (Ce, Gd) yielded an Archimedean snub square tiling.^[95b,95g] The underlying driving force for the diversity in results is associated with the remarkable coordination reactivity of the carbonitrile groups, which is well known in bulk coordination chemistry.

To investigate the influence of the incorporation of propionitrile groups to the coordination number of lanthanide, Gd atoms provided from an electron beam source were co-deposited to the chevron pattern of linker **3** on Ag(111) hold at 300 K. In contrast to snub square tiling motif constituted of **TDCN** and Gd (Figure 3.3.6a),^[95b,95g] the co-evaporation of Gd atoms with **3** presented an irregular metal-organic pattern. Nodes with variable coordination motifs, including clustering, can be observed in STM topographs (Figure 3.3.6b). Consequently, no clear preference of one coordination motif with higher coordination number can be found. This provides an unintended route towards 2D, randomly reticulated coordination networks, which is in line with the usage of linear and nonlinear dicyanitrile linkers as recently reported.^[201b,201d]

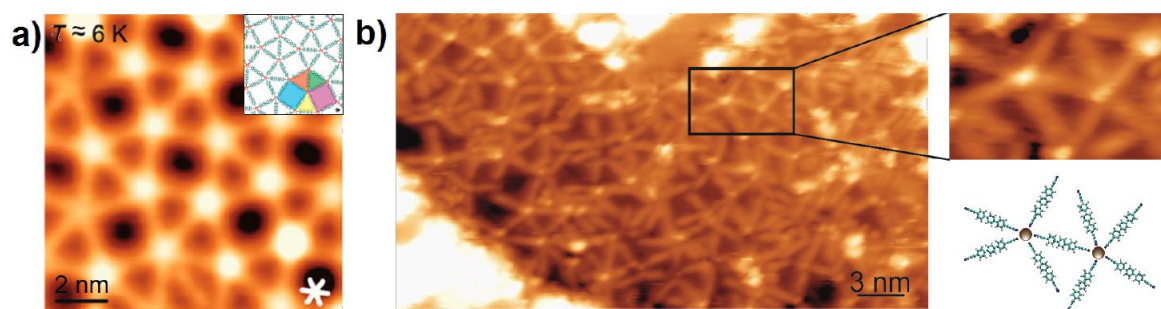


Figure 3.3.6 STM images of the lanthanide-directed assembly on Ag(111) for appreciable surface concentration (linker:Ln = 5:2). (a) Snub square tiling motif constituted of **TDCN** and Gd centers (atomistic model of the snub square Archimedean tessellation of the surface in insert), adapted from;^[95g] (b) irregular metal-organic network comprised of **3** molecules and Gd centers. In inset: model of one of the 5-fold **3**-Gd nonameric unit presented (Scanning parameters: $U_{\text{bias}} = 0.7$ V, $I = 0.1$ nA). The sample was measured by José I. Urgel.

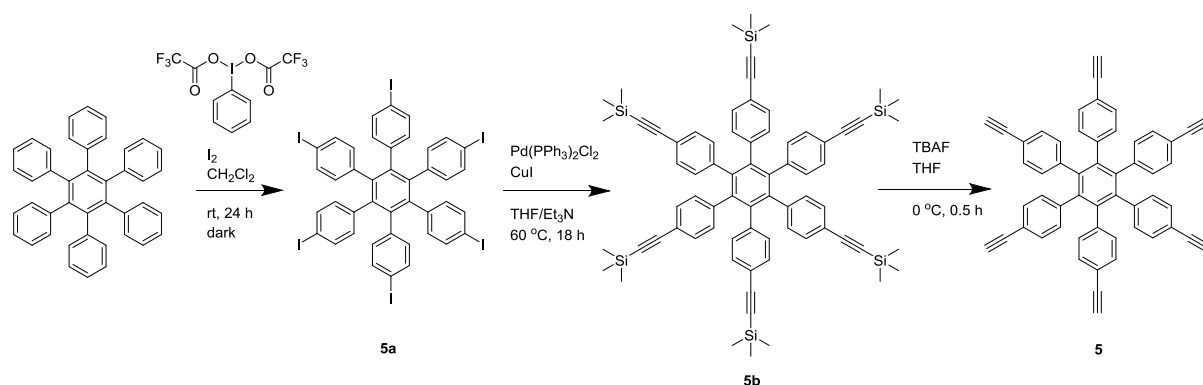
The Figure 3.3.6b shows an amplified image of a dinuclear five-fold coordination vertex unit with a chemical model below. Despite serious efforts, only surface-confined networks with limited length scales could be obtained. Obviously, the expression of regular metallo-supramolecular nanostructures or layers requires a careful balance of surface bonding, mobility and lateral interactions between metal centers and linkers.^[204] The reduced order may be attributed to the high reactivity of the $\text{-C}\equiv\text{C-}$ bonds in propiolonitrile groups. In bulk chemistry, it is well known that the activation of the acetylene group by noble metal substrates can occur.^[202,205] This was demonstrated by on-surface homo-coupling of alkynes on planar surfaces with a clear tendency towards branching side reactions.^[2c,63a,99,206] Although in the presented work we could not deduce any changes of the $\text{-C}\equiv\text{C-}$ bonds from the STM investigations, we attribute the hampering of the expression of a regular network to the presence of active $\text{-C}\equiv\text{C-}$ bonds close to the coordinating CN units.

In conclusion, we have designed and synthesized the novel organic compound terphenyl-4,4''-di(propiolonitrile) (**3**). The self-assembly of **3** on the Ag(111) surface showed a densely packed monolayer with chevron arrangement exhibiting a Moiré pattern. Gd-directed assembly resulted in an irregular metal-organic pattern with variable coordination motifs, but without any evidence of coordination numbers higher than five. We attribute the irregular property to the high reactivity of the $\text{-C}\equiv\text{C-}$ bonds in the propiolonitrile groups preventing the surface-confined molecular system from formation of regular metal-organic nanostructures or layers. Our results highlight the paramount importance of the nature of the coordinating end groups for the surface-confined lanthanide coordination chemistry in attempts to design molecular architectures incorporating the sophisticated properties of f-elements.^[207]

4. Synthesis of graphdiyne at the liquid-solid interface

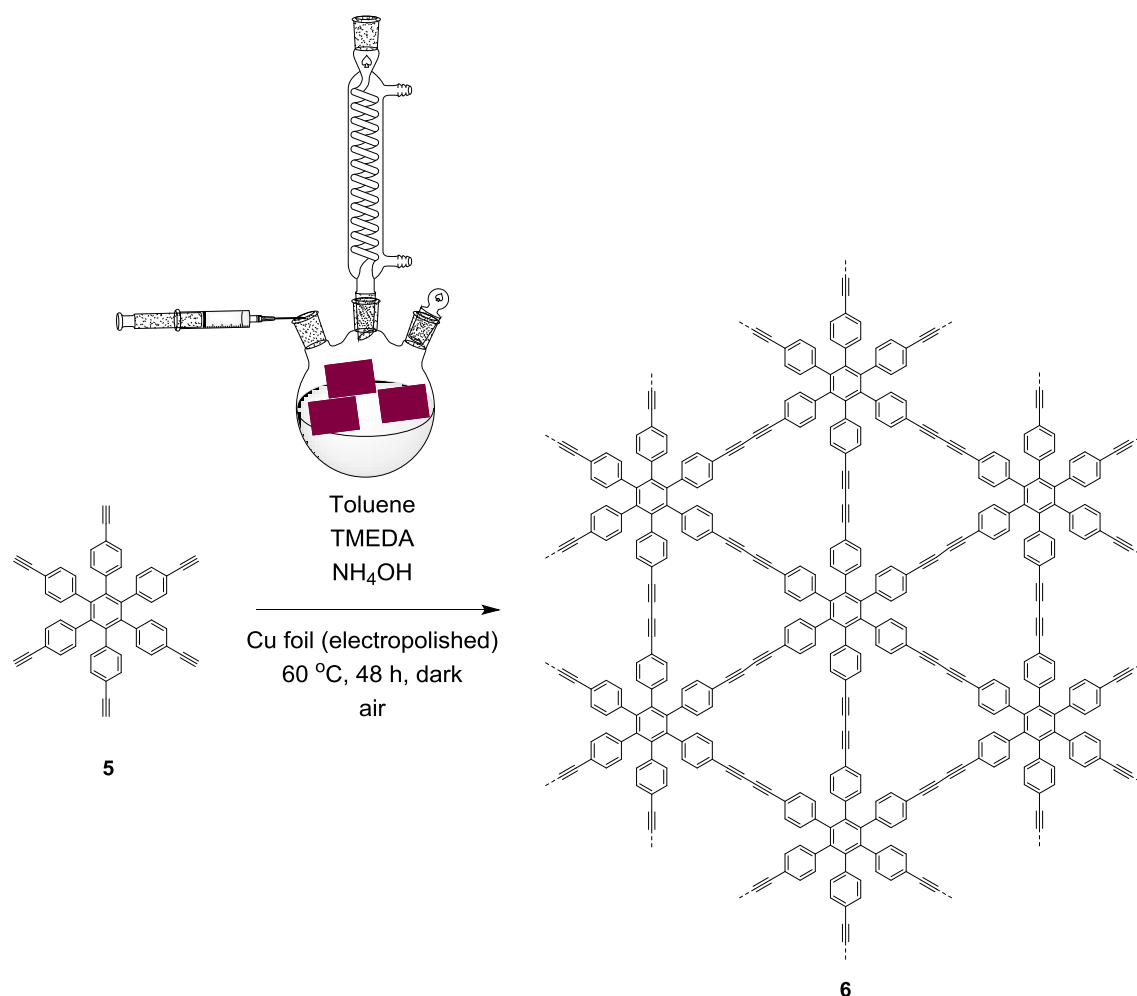
Graphyne (GY) and graphdiyne (GDY), combining sp^2 and sp hybridized carbon atoms, have been proposed as a novel structure of the carbon family.^[45a,45c] With directional anisotropy and nonequivalent Dirac points, GY and GDY are predicted to have a tunable band gap beyond graphene with a range from 0.46 to 1.22 eV.^[45a] These compounds are predicted to have highly interesting electronic properties. Also with their uniform pores, activated triple bonds, in some aspects, they will be more versatile than graphene. Recently, Li's group^[76] reported the first GDY synthesis which was carried out on Cu foil via a homo-coupling reaction using hexaethynylbenzene (HEB) in the presence of pyridine. These GDY films showed good 2D crystallinity and outstanding semiconducting properties. This GDY has been successfully applied in field emission,^[77] catalysis,^[74,78] Li ion storage,^[79] solar cell,^[80] oil water separation^[82] and sensor platform^[75,81].

However, the structure was not yet completely elucidated. The high chemical activity of the precursors HEB results in insertion reactions and oxidations during the synthetic procedure leading to unknown structures.^[76] Here, we introduce a stable starting material hexakis[4-(ethynyl)phenyl]benzene (**5**) aiming to obtain better control of the C–C bond-formation in GDY and to comprehend the reaction mechanisms.



Scheme 4.1 Synthetic route of monomer **5**.

The monomer **5** was synthesized according to the steps illustrated in Scheme 4.1. Hexakis(4-iodophenyl)benzene (**5a**) was synthesized from hexaphenylbenzene in the presence of [bis(trifluoroacetoxy)iodo]benzene and iodine in DCM.^[208] The intermediate hexakis[4-(trimethylsilylethynyl)phenyl]benzene (**5b**) was achieved by the Sonogashira reaction of compound **5a** with ethynyltrimethylsilane using $\text{Pd}(\text{PPh}_3)_2\text{Cl}_2/\text{CuI}$ as catalyst in a mixture of THF and trimethylamine.^[209] The monomer **5** was obtained by deprotection of the compound **5b** in presence of TBAF under an argon atmosphere at 0 °C for 0.5 h.^[209] The IR spectrum of the **5** showed the typical band at 3295 cm^{-1} ascribed to the C–H stretching vibration in $-\text{C}\equiv\text{C}-\text{H}$, whilst the band of 2108 cm^{-1} was the typical $\text{C}\equiv\text{C}$ stretching vibration.



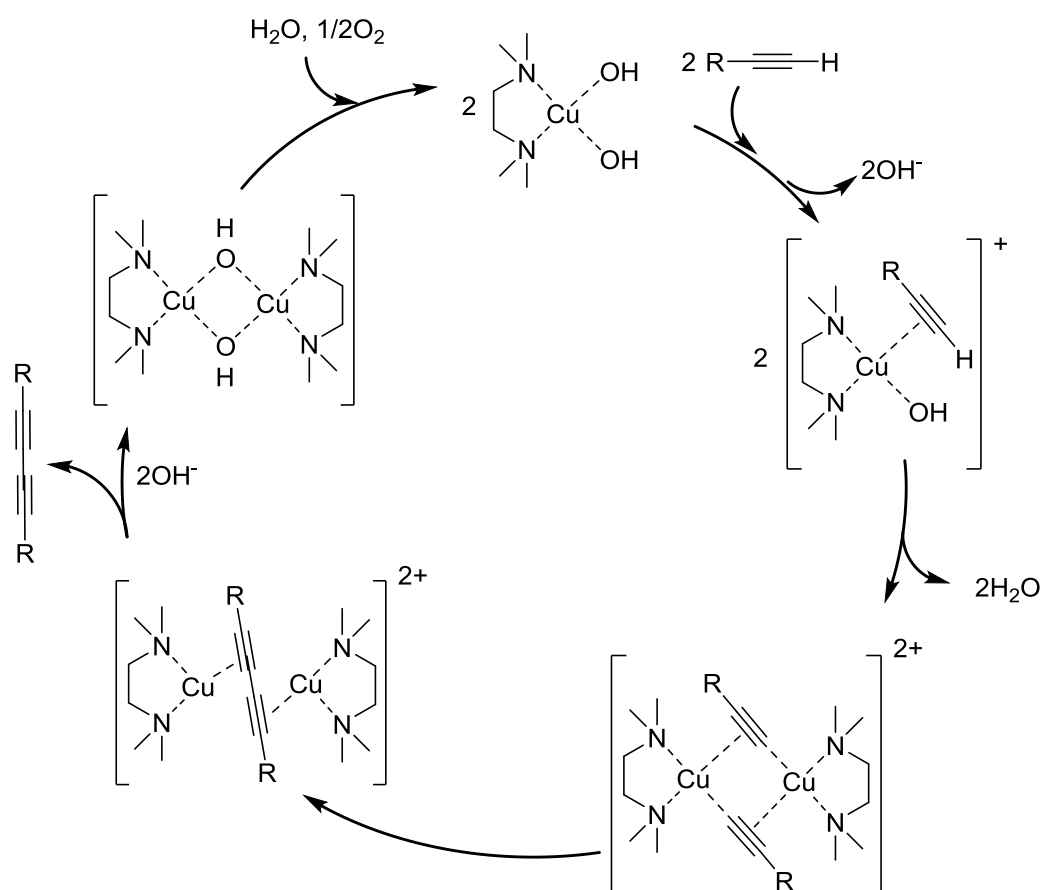
Scheme 4.2 Proposed synthetic route of GDY 6 from monomer 5.

In Glaser-Hay coupling serials reactions, the Cu salts, nitrogen ligands and solvent can affect the coupling efficiency.^[210] Several ligands have previously been investigated, such as ammonium hydroxide, pyridine, *N,N,N',N'*-tetramethylethylenediamine (TMEDA).^[60-61,65] The TMEDA is the most frequently used due to the good selectivity and yield.^[60] In 2010, the first GDY films were successfully synthesized by Li and co-workers on the Cu foil via a homo-coupling reaction using HEB in the presence of pyridine.^[76] In 2015, Zhang's group further modified the Glaser-Hay coupling reaction conditions which used an adjusted ratio of solvents: TMEDA, acetone and pyridine and firstly synthesized GDY nanowalls with thickness 15 nm and good crystallinity.^[77]

Based on this information, here, for the first time, we modified a new route of Glaser-Hay homo-coupling reaction to produce GDY nanofilms at the solid/liquid interface. As shown in Scheme 4.2, Cu foils were placed in the mixed solution of toluene (20 mL), TMEDA (5 mL) and ammonium hydroxide (0.3 mL); then a toluene solution of **5** was added dropwise by a syringe pump in 20 hours (See experimental section for details). Cu atom from the foil can be

easily converted to ions in the presence of a catalytic amount of base,^[45c] where a Glaser-Hay coupling reaction proceeds efficiently with the aid of TMEDA. Cu foil not only served as the catalyst for this reaction, but also was the substrate for the growth of GDY films. The well shape-controlled GDY **6** nanofilms grew perfectly on the whole surface of Cu foil. After dissolving the Cu foils in a 0.5 mol/L $(\text{NH}_4)_2\text{S}_2\text{O}_8$ solution or a 1 mol/L HCl solution, the intact films were washed with deionized water and methanol subsequently, giving clear and pale yellow GDY **6** nanofilms suspended in the methanol solution.

The proposed mechanism for this modified Glaser-Hay coupling reaction is shown in Scheme 4.3.^[66,211] The catalytic cycle starts with the π -coordination of phenylacetylene to the Cu^{II} -TMEDA complex. Then, two of these complexes form a dicopper-diacetylide complex. After cleaving the butadiyne product, a $[(\text{TMEDA})\text{Cu}(\text{OH})]_2$ dimer forms. In our reaction condition, the ammonia solution not only helps to dissolve Cu ions from Cu foil to the solution, but also helps to supply OH^- anions for the catalytic cycle.



Scheme 4.3 Proposed mechanism for modified Glaser-Hay coupling reaction.^[66,211]

The elementary composition and bonding structure of GDY **6** were systemically researched by energy-dispersive X-ray spectroscopy (EDX), Raman spectroscopy and IR spectroscopy.

After transferring the GDY **6** nanofilms to a silicon wafer, the EDX spectrum (Figure 4.1) of the GDY **6** nanofilms was measured. The results show that nanofilms were mainly composed of elemental carbon, as shown in Table 4.1. There is quite few elemental oxygen (O) originated from absorption of air in GDY **6**. The extra alkyne units between benzene rings increase the pore size of the network, which leads to air absorption in the pores of nanofilms. The terminal alkyne can also be oxidized resulting in the defects in the films.^[77]

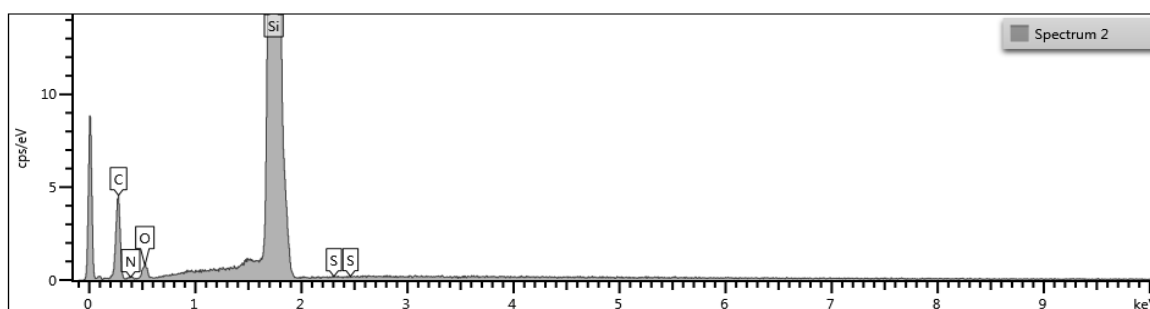


Figure 4.1 EDX spectrum of GDY **6** nanofilms on silicon wafer.

Table 4.1 Elemental atomic percentage of GDY **6** on silicon wafer obtained from EDX.

	Atomic %
C	69.79
N	2.83
O	3.58
Si	23.9
Total:	100

In addition, Raman spectroscopy as a powerful tool to detect $C\equiv C$ bonds was applied to analyze the produced films. The measurements were directly conducted in the GDY **6** nanofilms on the pretreated Cu foil. As shown in Figure 4.2, the Raman spectra exhibit three prominent peaks at 1350 cm^{-1} , 1604 cm^{-1} and 2212 cm^{-1} , respectively. The peak at 1350 cm^{-1} can be attributed to the breathing vibration of sp^2 carbon domains in aromatic rings (D band). The peak at 1604 cm^{-1} is attributed to the first-order scattering of the E_{2g} mode of in-phase stretching vibration of sp^2 carbon lattice in aromatic rings (G band).^[212] The peak at 2212 cm^{-1} corresponds to the vibration of conjugated butadiyne links ($-C\equiv C-C\equiv C-$).^[213] It has an obvious hypochromatic shift compared to the peak of the $C\equiv C$ bonds in the monomer **5** ($C\equiv C-H$) around 2110 cm^{-1} .^[57a] The good intensity of the butadiyne peak also shows that the

homo-coupling of monomers **5** are very effective. Our GDY **6** synthesized from stable starting material **5** shows a better linkage than the GDY synthesized from HEB.^[76]

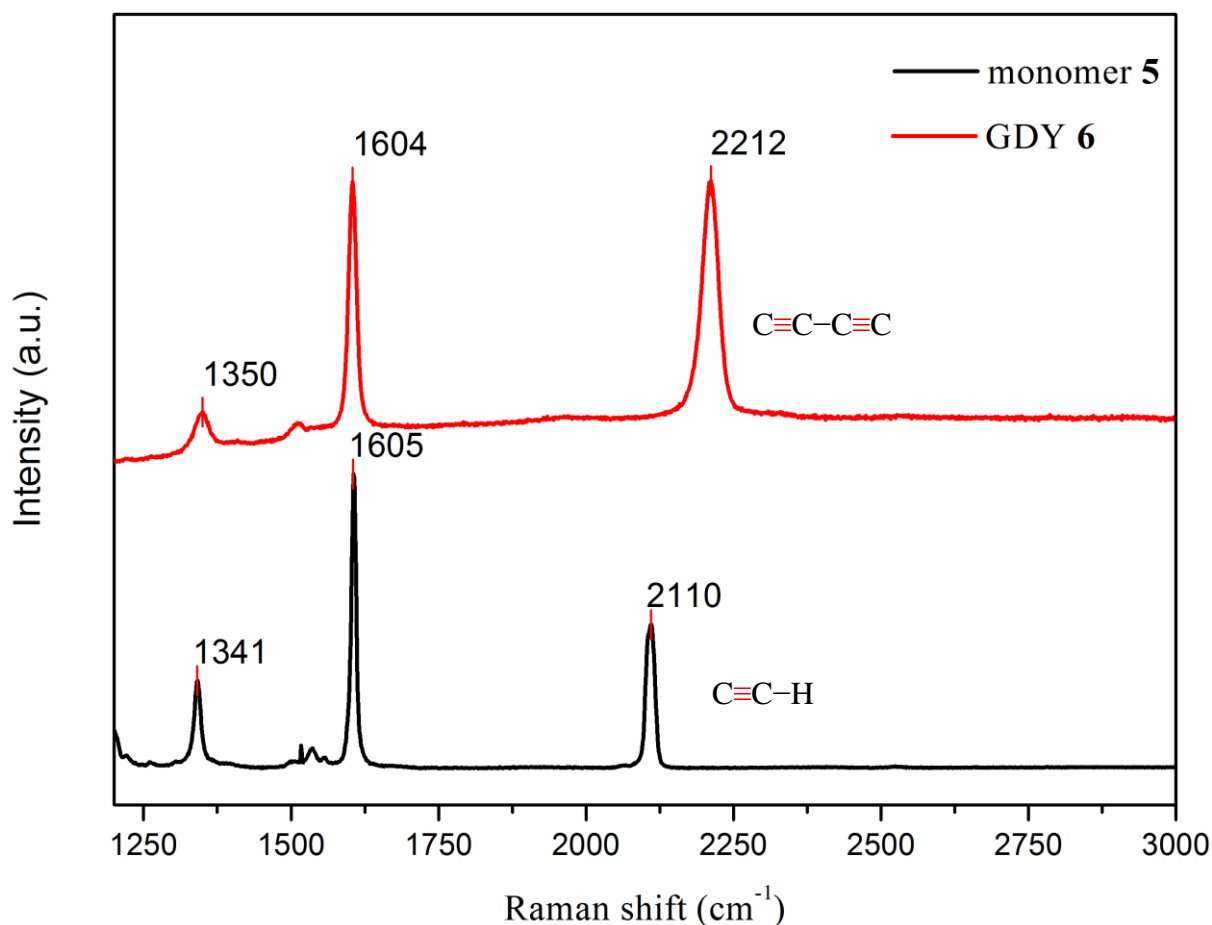


Figure 4.2 Raman spectra of monomer **5** and GDY **6**.

Furthermore, after transferring the GDY **6** nanofilms to Al foil, the IR spectra of the GDY **6** nanofilms were measured on a Bruker FTIR Tensor 37 via the attenuated total reflection (ATR) method. As shown in Figure 4.3, the results reveal that the band at 3293 cm^{-1} of monomer **5**, the typical C-H stretching vibration in $\text{C}\equiv\text{C}-\text{H}$, totally vanish in GDY **6**, which also proves the successful polymerization. In the range of $600\text{-}1600\text{ cm}^{-1}$, GDY **6** shows very similar peaks as monomer **5**; this reveals that the GDY **6** is really polymerized from monomers **5**, not from other impurities.

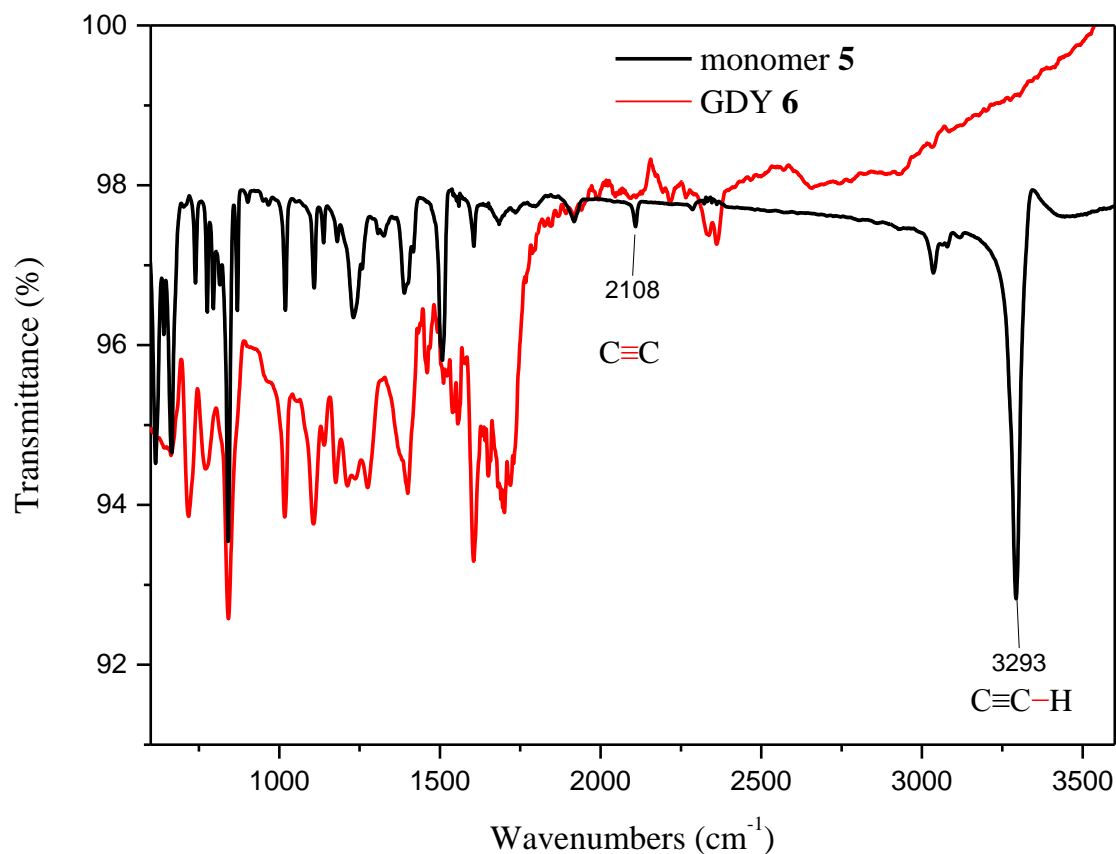


Figure 4.3 IR spectra of monomer **5** and GDY **6**.

To investigate the morphology of as-prepared GDY **6** nanofilms, optic microscopy (OM), scanning electron microscopy (SEM), atomic force microscopy (AFM) and transmission electron microscopy (TEM) were employed.

Figure 4.4 displays OM observation of as-obtained GDY **6**, verifying that the size of film is very large. Figure 4.5 shows the typical SEM images of exfoliated samples transferred on silicon wafer. The higher magnification image (Figure 4.5b) indicates the nanofilms are continuous and flat.

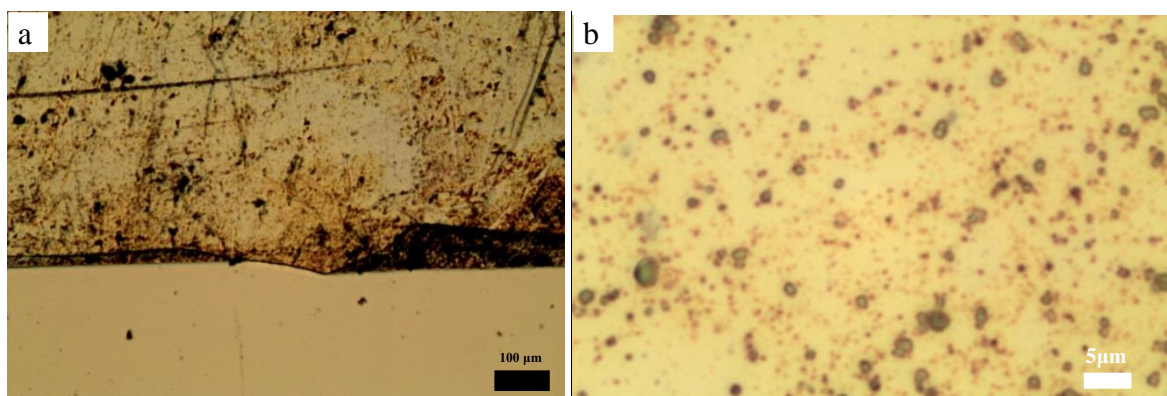


Figure 4.4 OM images of GDY **6**.

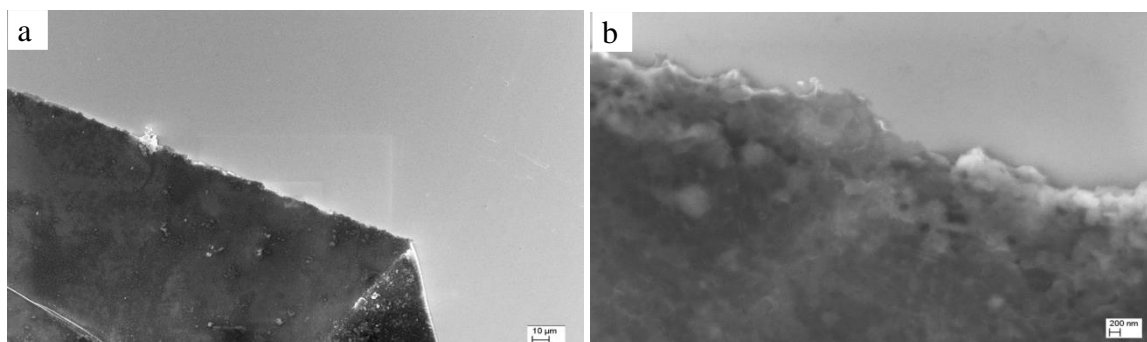


Figure 4.5 SEM images of exfoliated GDY **6** samples on silicon wafer. (a) Large-area and (b) higher magnification images.

Moreover, the thickness of exfoliated GDY **6** nanofilms transferred on silicon wafer was characterized by AFM. Figure 4.6 indicates the typical AFM images of GDY **6**. The cross-sectional views of the AFM image reveal that the average thickness of GDY **6** nanofilms is 117 nm which is much thinner than GDY synthesized from HEB.^[76]

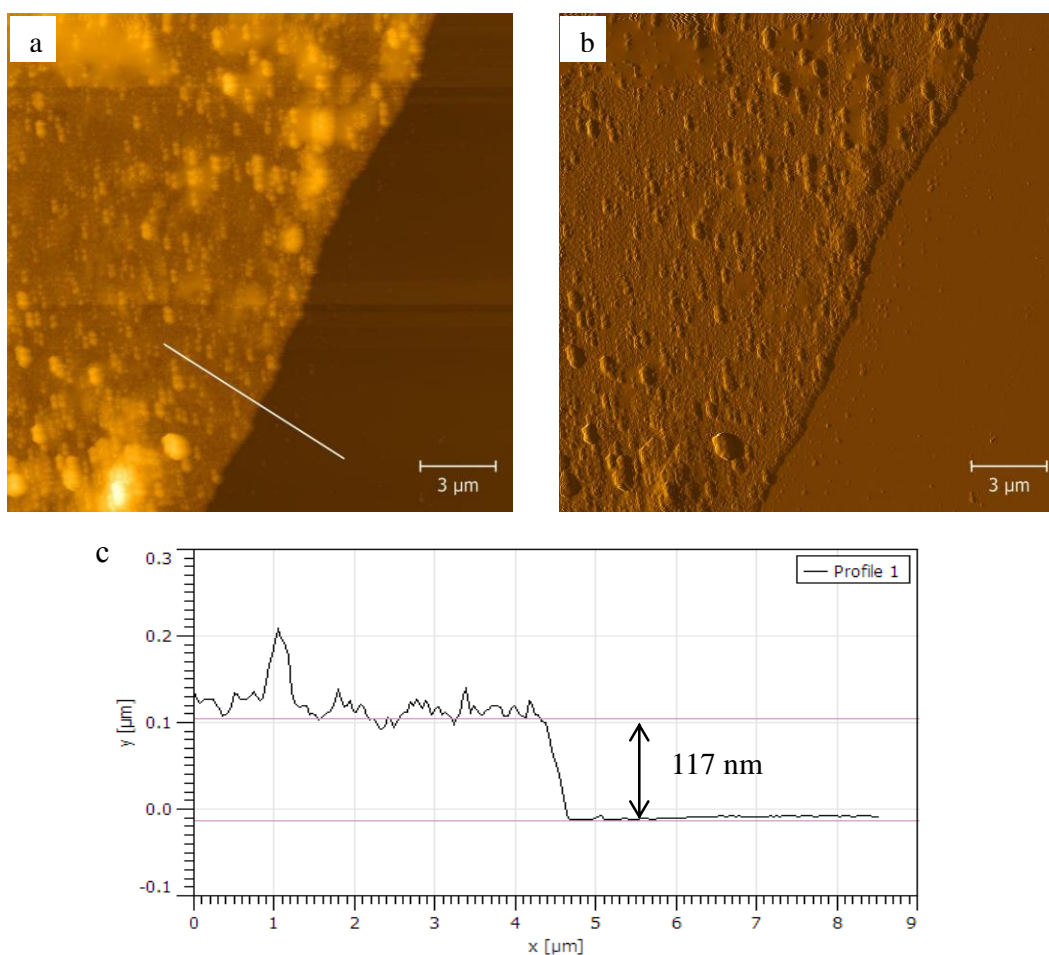


Figure 4.6 AFM images of GDY **6**. (a) The height, (b) the amplitude, (c) the height profile of GDY **6** taken along the white line in (a).

TEM images of GDY **6** nanofilms (Figure 4.7a,b,c) demonstrate that there are no defects and dislocations in the visible area of nanofilms. The high magnification TEM images (inset

of Figure 4.7a and Figure 4.7c) exhibit curved streaks with the lattice fringe of 0.37 nm at the edge regions of the films. This shows that the spacing value between carbon layers is around 0.37 nm,^[214] revealing that the GDY nanofilms grow in 2D manner on the copper foil. The value of the GDY film was larger than that of the graphene around 3.50 Å,^[215] and similar value to the GDY synthesized from HEB (0.365 nm).^[77] The selected area electron diffraction (SAED) pattern in Figure 4.7d shows the dotted ring pattern which suggests the good crystalline nature of GDY **6** nanofilms.

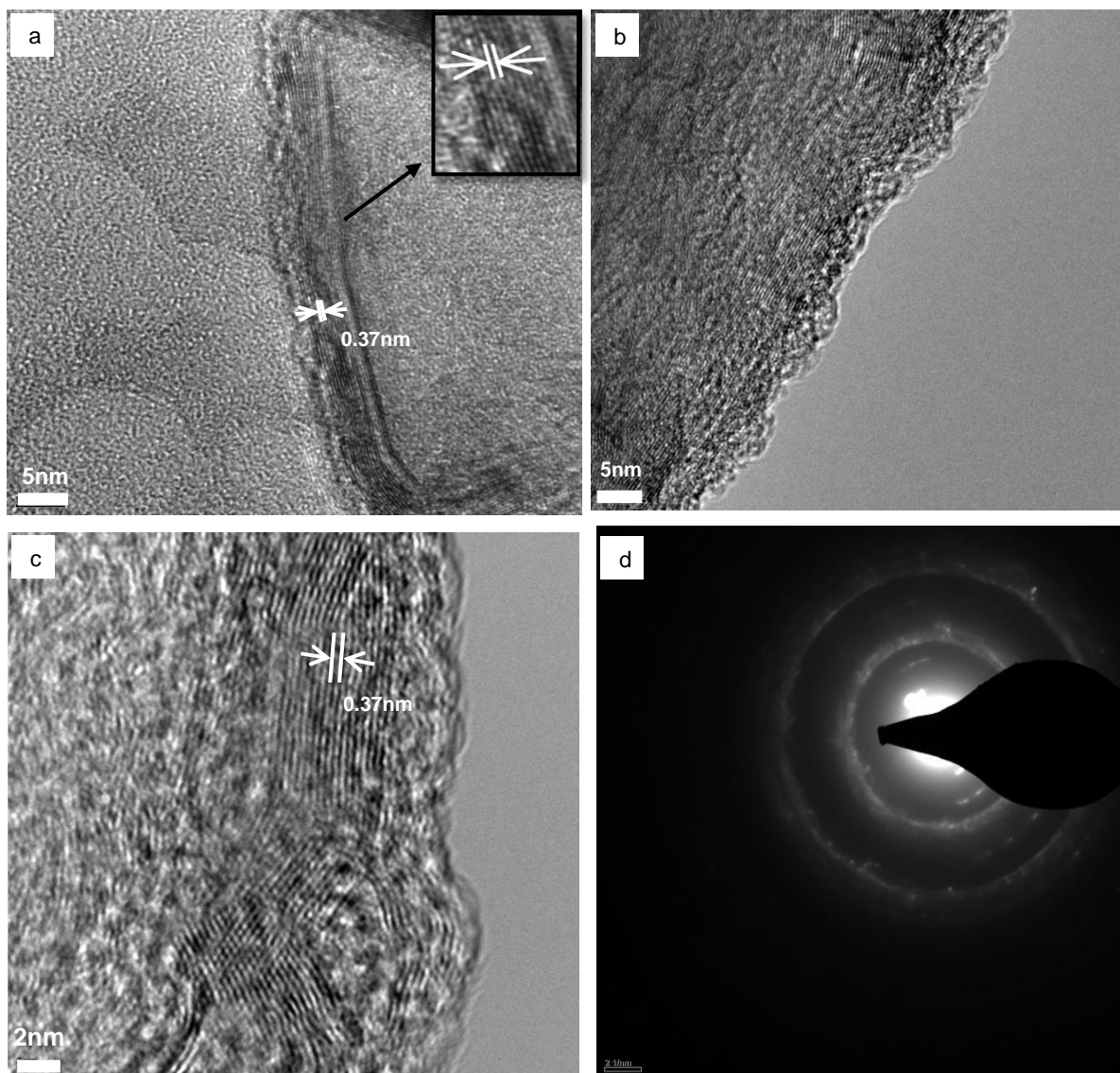


Figure 4.7 (a,b,c) TEM images and (d) related SAED pattern of GDY **6** nanofilms.

The devices for conductivity measurement derived from GDY **6** nanofilms were manufactured and measured at room temperature.^[216] The GDY **6** nanofilm was transferred onto Al foil which worked as bottom electrode, and conductive silver printing ink with thin Cu wire as top electrode.^[217] The *I-V* curve was measured by Electrochemical Instruments (Autolab) using the normal cyclic and linear sweep voltammetry mode in the range of voltage

between -0.300 V and $+0.300$ V with a step potential 0.01 V at a scan rate 0.2 V s $^{-1}$. The equilibration time was 5 s. The I - V curve behavior is highly linear, which indicates Ohmic behavior of GDY **6** nanofilm, and the slope of the line is 3.08×10^{-4} (Figure 4.8). The conductivity is 5.1×10^{-6} S m $^{-1}$ as calculated in the following equations, revealing that GDY **6** nanofilms show semiconducting properties.

$$R = V/I = 3.24 \text{ k}\Omega \quad (4.1)$$

$$R = \rho \times L/A \quad (4.2)$$

$$\sigma = 1/\rho = L / (A \times R) = 117 \text{ nm} / (7.0 \text{ mm}^2 \times 3.24 \text{ k}\Omega) = 5.1 \times 10^{-6} \text{ S m}^{-1} \quad (4.3)$$

R : resistance, ρ : resistivity, A : area, L : thickness, σ : conductivity.

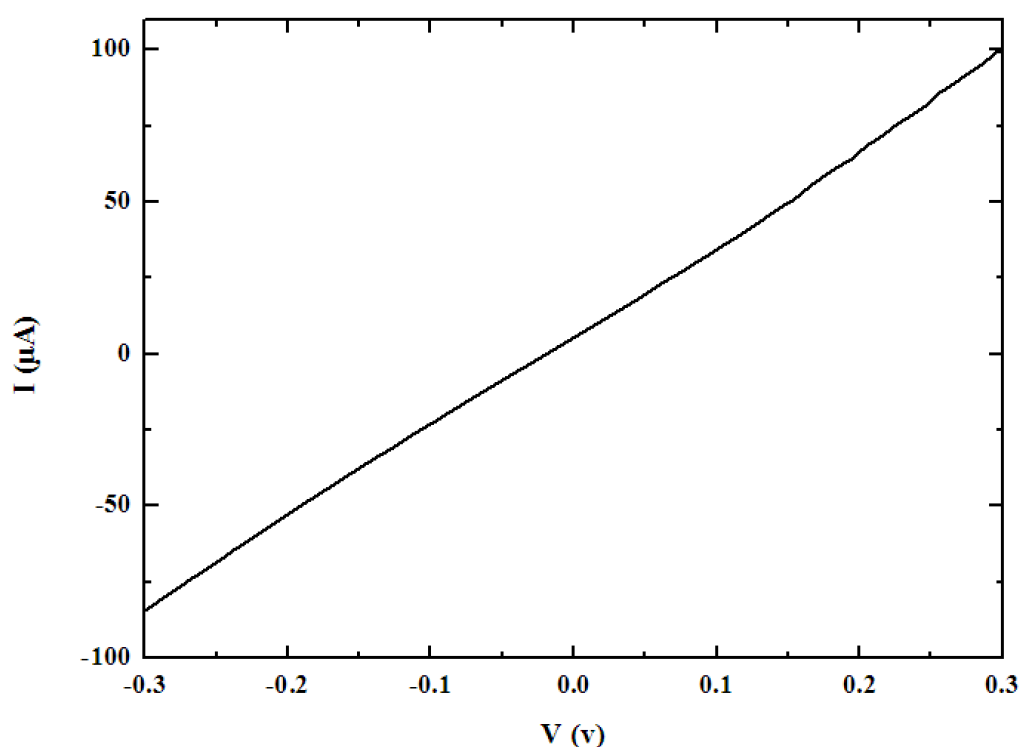


Figure 4.8 I - V curve of GDY **6**.

In summary, for the first time, a new route of a modified Glaser-Hay homo-coupling reaction of a stable alkyne compound hexakis[4-(ethynyl)phenyl]benzene was used to synthesize large area of GDY nanofilm on Cu foil. The vanishing 3293 cm $^{-1}$ peak of typical C–H stretching vibration in $-\text{C}\equiv\text{C}-\text{H}$ in IR spectra and hypochromatic shift of butadiyne peak to 2212 cm $^{-1}$ in Raman spectra show that the homo-coupling of alkynes is very effective. OM, SEM, AFM images show that this nanofilm is very flat. Especially, AFM images reveal that the average thickness of GDY nanofilms is 117 nm. The HR-TEM images exhibit curved streaks with the lattice fringe of 0.37 nm at the edge regions of the films. This shows that the spacing value between carbon layers is around 0.37 nm, revealing the GDY nanofilms grow

in 2D manner on the copper foil. It also shows good crystallinity. The device based on GDY nanofilms for measurement of electrical property was manufactured and showed a conductivity of $5.15 \times 10^{-6} \text{ S m}^{-1}$, indicating semiconducting properties. All the measurements showed that GDY **6** nanofilms were more stable and thinner, comparing to GDY films synthesized from HEB. As a result, we can expect that GDY **6** nanofilms will become a superb competitor among the different types of 2D carbon materials in the electrical nanodevices applications and other applications.

5. Alkyne derivatives for molecular junction applications

This chapter was adapted from co-authored publication *J. Am. Chem. Soc.* 2016, 138, 8465-8469, entitled “C–Au covalently bonded molecular junctions using nonprotected alkynyl anchoring groups”, Copyright (2016) American Chemical Society.^[218] The herein described results were elaborated in collaboration with the group of Prof. Dr. H. v. d. Zant at the University of Technology Delft.

The direct C–Au σ bonds currently seem to be an interesting anchoring motif to achieve low-ohmic contacts between the molecular backbone and the metal electrodes.^[115] The contact carbon can be classified following to the sp^3 , sp^2 and sp Carbon hybridizations. For instance, for sp^3 carbon, a conductance approaching $0.9 G_0$ was obtained for Au–C *p*-xylylene molecular junctions using SnMe_3 as leaving groups.^[129] For sp carbons a high conductance molecular junction exhibiting a σ -bond of sp -hybridized carbon on Au electrodes was formed by using TBAF as deprotecting agent to cleave the TMS end groups from the oligophenylene backbone.^[131,219]

Nevertheless, these reported approaches show also some important drawbacks. The SnMe_3 group requires rather toxic precursors as well as the need of TBAF to deprotect TMS group makes the handling of the MCBJ more complicated.

Here, The conductance of a family of diethynyl–oligophenyls (**OPAn**, $n = 1$, **OPA1**, 1,4-diethynylbenzene (**7**); $n = 2$, **OPA2**, 4,4'-diethynyl-1,1'-biphenyl (**8**); $n = 3$, **OPA3**, 4,4''-diethynyl-1,1':4',1''-terphenyl (**1**); $n = 4$, **OPA4**, 4,4'''-diethynyl-1,1':4',1'':4'',1'''-quaterphenyl (**9**)) with the alkynyl endgroup (R–C \equiv C–H) as an anchoring group (Figure 5.1a) is determined by the use of the mechanically controllable break junctions (MCBJs). The molecules bind to the gold electrodes through the sp -hybridized carbon atom at each side of the molecule without the need for deprotective agents or toxic leaving groups. The conductance values are of the same order of magnitude as found for similar molecules with sp - or sp^2 -hybridized Au–C bonds while being an order of magnitude lower than those reported using sp^3 Au–C hybridization.^[129]

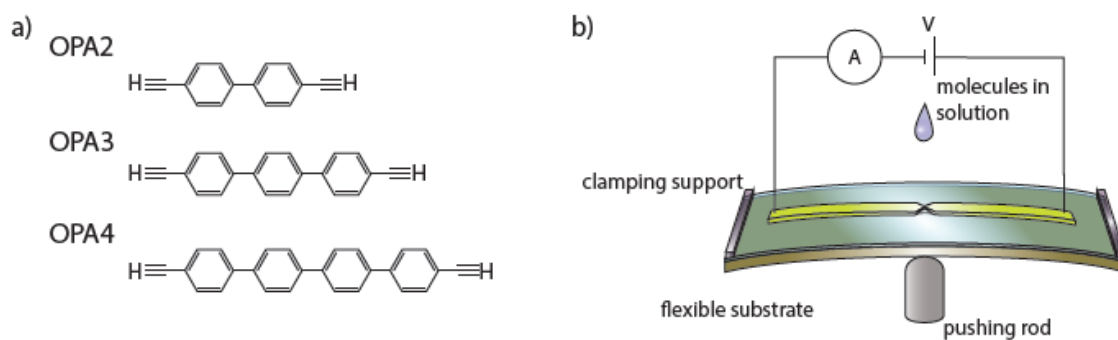
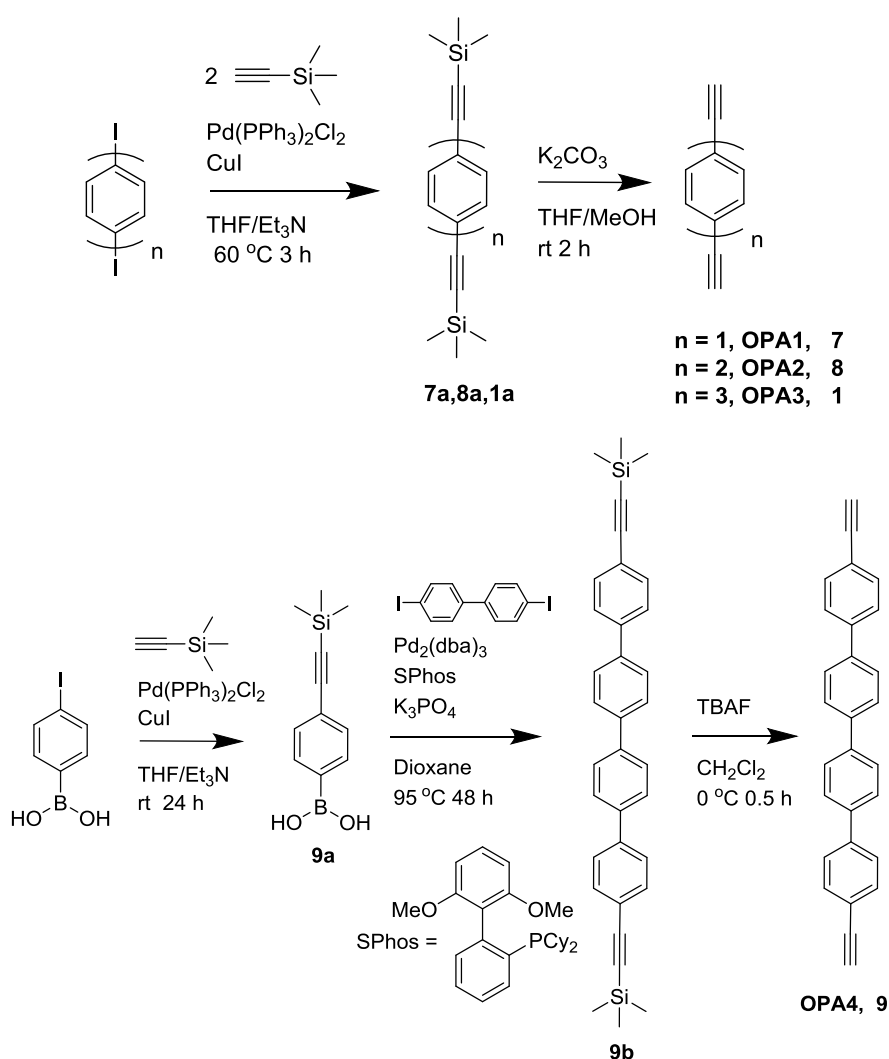


Figure 5.1 (a) Chemical structure of the molecules studied in this work. Phenylene hydrogen atoms are omitted. (b) Schematic representation of the MCBJ setup. Reproduced with permission from [218], Copyright (2016) American Chemical Society.

The syntheses of **OPA1** to **OPA3** are based on the Sonogashira reaction from diiodo-oligophenyl.^[220] Due to the low solubility of diiodo-quaterphenyl, the precursor (4,4''-bis(trimethylsilylethynyl)-1,1':4',1'':4'',1'''-quaterphenyl (**9b**)) of **OPA4** was synthesized through a Suzuki-Miyaura reaction of 4-(Trimethylsilylethynyl)phenylboronic acid (**9a**) with 4,4'-diiodobiphenyl.^[221]



Scheme 5.1 Synthetic routes of **OPAn** molecules: **7**, **8**, **1** and **9**.

Single-molecule conductance measurements were performed in a MCBJ set up.^[222] The devices consist of a phosphorus bronze flexible substrate coated with a polyimide insulation layer, on top of which a lithographically defined gold wire with a constriction is patterned. The narrower part of the wire is suspended by reactive ion etching of the polyimide. The substrate is then clamped at both ends and bent by the action of a pushing rod beneath the center of the substrate (Figure 5.1b) until the gold wire breaks leaving two atomically sharp electrodes separated by a nano-scale gap. The electrodes are fused and broken thousands of times at a rate of 10 nm s⁻¹. During this process, the conductance ($G = I/V$) is recorded using a logarithmic amplifier with a bias voltage of 0.1 V. During each breaking process the conductance is recorded as a function of the electrode displacement. Before the gold wire breaks, the conductance of the junction drops in a stepwise manner due to atomic rearrangements in the contact. When the metallic contact breaks, the conductance sharply drops below 1 G_0 , where G_0 is the conductance quantum ($G_0 = 2e^2h^{-1}$ with h the Planck's constant and e the charge of an electron). This sharp decrease in conductance is used to set the zero displacement of each trace. In the case that no molecule bridges the gap; the breaking traces show a featureless exponential conductance decrease, indicative of single-barrier tunneling. If a molecule contacts both electrodes, the conductance no longer follows this behavior. Instead, a slower conductance decay with plateau-like features is observed.

The 2D conductance vs displacement histograms were built from 2000 consecutive traces. To check the presence of spurious contaminants in the MCBJ devices, 1000 traces are first recorded on the bare Au devices before exposing them to the solvent with the molecules. Only if a clean junction was formed as indicated by clear single-barrier tunneling traces (Figure 5.3), the molecules are deposited by pipetting a 2 μ L drop of solution onto the sample. Subsequently, the solvent (dichloromethane) is let to evaporate. The molecules in this study consist of an n -phenylene backbone ($n = 2, 3, 4$) with alkynyl moieties at both sides (Figure 5.1a). Calibration of the electrode displacement is done using the length of single-gold atom chains obtained from the 1000 traces on bare junctions before molecular deposition.^[222-223]

As shown in figure 5.2, the conductance vs electrode displacement histograms of three oligo(pyhenylene ethynylene) molecules all show two characteristics. Firstly, the three diagrams all present the Au electrodes tunneling characteristic with an exponential conductance decay exhibiting between 0 and 0.5 nm and covering the conductance range from about $10^{-4} G_0$ to the noise level (marked with thin black lines). The second characteristic is a region where the molecular junction conductance decreases slower with stretching. **OPA3** shows this region between displacements ranging from 0 to 1 nm with a conductance around

$10^{-3} G_0$ (Figure 5.2b). This regime of **OPA4** is observed between 0 and 1.5 nm with a conductance around $10^{-4} G_0$ (Figure 5.2c). Noticeably, **OPA2** presents two of such regions: (i) a region shorter than 0.6 nm with a conductance around $10^{-3} G_0$, (ii) traces between 0.5 and 2.5 nm with conductance near $10^{-5} G_0$. It is interesting that most of the traces of **OPA2** to **OPA4** show slanted plateaus rather than flat ones as is usually seen in molecular wires.

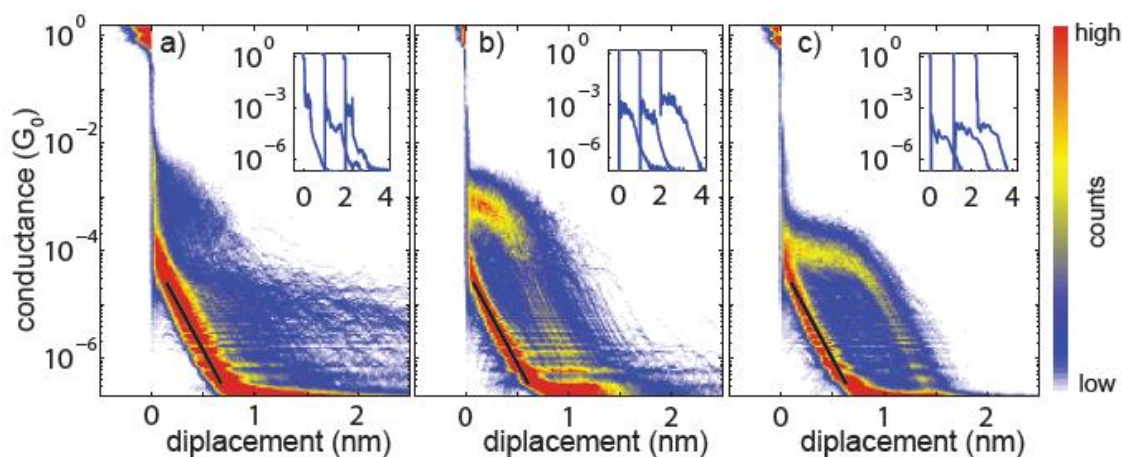


Figure 5.2 2D conductance vs electrode displacement histograms constructed from 2000 consecutive breaking traces measured at room temperature in air with a 0.1 V bias voltage applied and a ramp rate of 10 nm/s. Junctions exposed to a 28 μM molecule solution in dichloromethane for (a) **OPA2**, (b) **OPA3** and (c) **OPA4**. Insets show examples of individual conductance traces with plateau-like features assigned to the presence of a molecule; traces are offset in the displacement direction. Reproduced with permission from [218], Copyright (2016) American Chemical Society. Samples were measured by Ignacio José Olavarria-Contreras.

However, the **OPA1** molecule did not show clear conductance signatures during our measurements (Figure 5.3b). In reference ^[131] a similar single phenyl ring with an unprotected alkynyl anchoring group was measured, but no conductance was observed there either. However, the same backbone with a TMS protecting group (named **OPE1** here) showed molecular features.

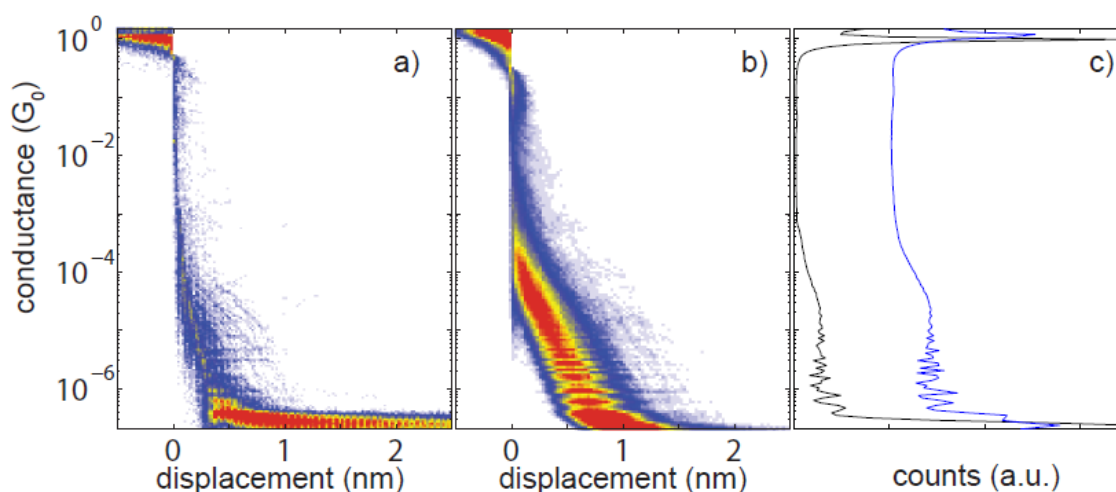


Figure 5.3 Conductance vs. electrode displacement 2D histograms of (a) a bare gold sample (1000 traces) and (b) **OPA1** molecule (2000 traces) in which no clear plateaus or regions of highly probable conductance can be identified. (c) Normalized 1D conductance histogram of gold (in black) and **OPA1** (blue); the curves are offset for clarity. For **OPA1** no features are visible in the 1D histogram, indicating a very low probability of junction formation. Reproduced with permission from [218], Copyright (2016) American Chemical Society. Samples were measured by Ignacio José Olavarria-Contreras.

1D conductance histograms of the **OPAn** molecules without any data selection is shown in Figure 5.4a. The most probable molecular conductance values for the three molecules were extracted by fitting a log-normal distribution to the conductance regions with molecular features (dotted lines in Figure 5.4a). For each molecule two samples were measured, and the values of the obtained conductance are summarized in Table 5.1. For **OPA2**, one high conductance and one low conductance are found. The highest one can be attributed to the molecular conductance of the molecule itself, whereas the lower value with plateau lengths exceeding the length of the molecule can be associated to the presence of dimers of the molecule^[131,224] or to π - π stacking of two molecules each attached to one electrode (Figure 5.5).^[225] To further understand this behavior, we have analyzed the time evolution of the conductance vs. displacement curves of **OPA2** to investigate whether the dimer formation occurs more frequently as times progresses (Figure 5.6). After 4 h of measurements, high and low-conductance traces are still present which indicates that time does effect the high and low conductance features. We have also tested the influence of different concentrations of **OPA2** on the conductance (Figure 5.7 and Table 5.2). It still shows the similar high and low-conductance features during different concentrations.

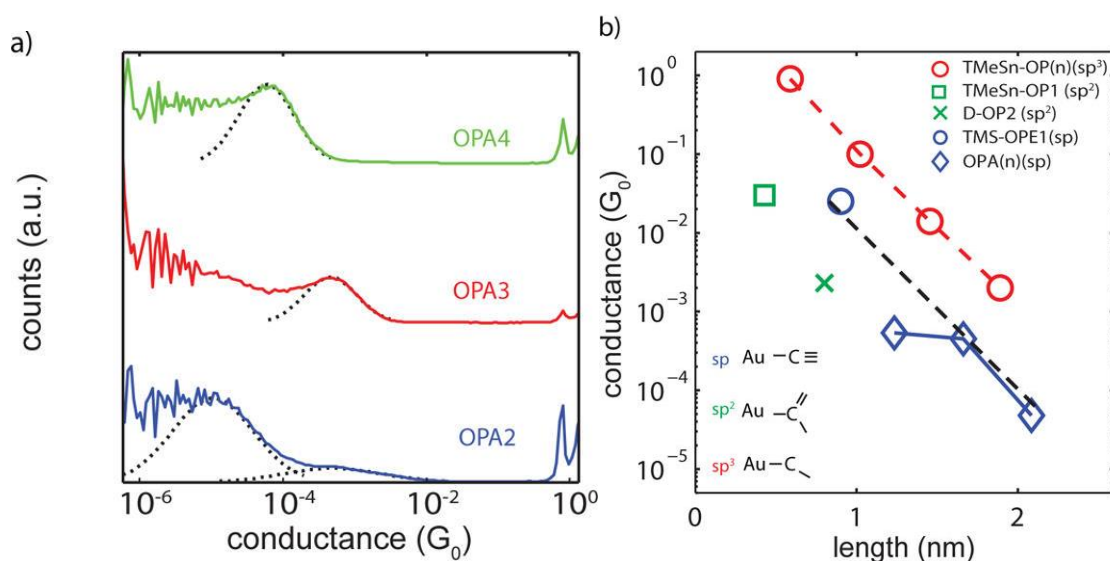


Figure 5.4 (a) 1D conductance histograms using a logarithmic binning (solid line) for **OPA2** (blue), **OPA3** (red), and **OPA4** (green). Dotted lines represent log-normal fittings around the regions of high counts in the histograms and are used to extract the most probable conductance value. (b) Conductance as a function of molecular length for **OPAn** (blue) compared with other molecules in the literature that

form direct C–Au bonds. Different families present different hybridization of the last carbon. Red open circles represent molecules with direct sp^3 C–Au bonding from ref ^[129]; the green square is a single benzene ring connected to gold through an sp^2 -hybridized carbon;^[128] the open blue circle corresponds to **OPE1** connected to gold via an sp -hybridized carbon from the series in ref ^[131]; the green \times is a diazonium terminated **OP2**, which is electrochemically deprotected and connected through an sp^2 -hybridized carbon that was studied in ref ^[130]. The black dashed line connects the **OPAn** series. Note that the structure of **OPE1** corresponds to the same structure as **OPA1** in this study when contacted to the gold electrodes. Reproduced with permission from [218], Copyright (2016) American Chemical Society. Data were analysed by Ignacio José Olavarria-Contreras.

Table 5.1 Most probable molecular conductance for the series of **OPAn** molecules extracted from the 1D conductance histograms. Reproduced with permission from [218], Copyright (2016) American Chemical Society.^a

compound	conductance (G_0)	
OPA2	6.6×10^{-4} , 1.0×10^{-5}	4.1×10^{-4} , 7.8×10^{-6}
OPA3	4.6×10^{-4}	4.4×10^{-4}
OPA4	5.7×10^{-5}	3.9×10^{-5}

^aThe first column contains the values obtained with a concentration of $28 \mu\text{M}$ and the values in the second column were obtained with a saturated concentration of molecules, meaning 4.95 mM for **OPA2**, 0.36 mM for **OPA3** and $28 \mu\text{M}$ for **OPA4**. The values plotted in Figure 5.4 are the average of the two measurements of each molecule. For **OPA2**, two values are listed; one at high conductance and one at low conductance.

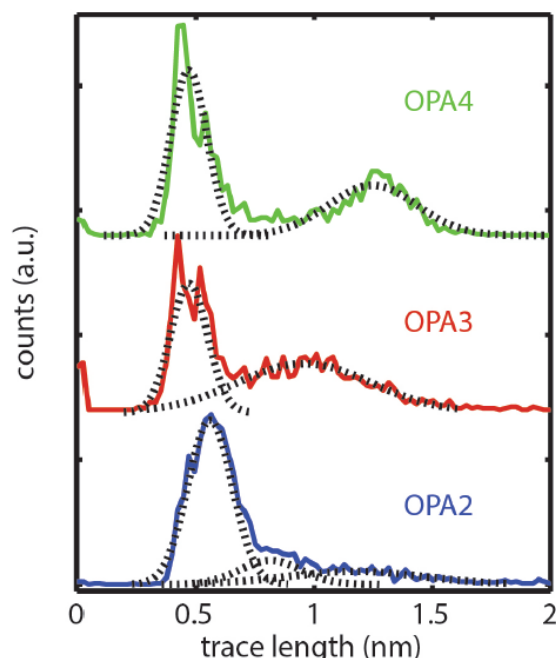


Figure 5.5 Trace-length histograms for **OPA2** (blue), **OPA3** (red) and **OPA4** (green). The black dashed lines correspond to Gaussian fits and can be related with two kind of traces; tunneling traces (in average 0.5 nm long) and molecular traces that scale with molecular length. The length of each trace is defined as the total displacement between the sharp drop below $1 G_0$ and the last point where the trace was above $1 \times 10^{-6} G_0$. Reproduced with permission from [218], Copyright (2016) American Chemical Society. Data were analysed by Ignacio José Olavarria-Contreras.

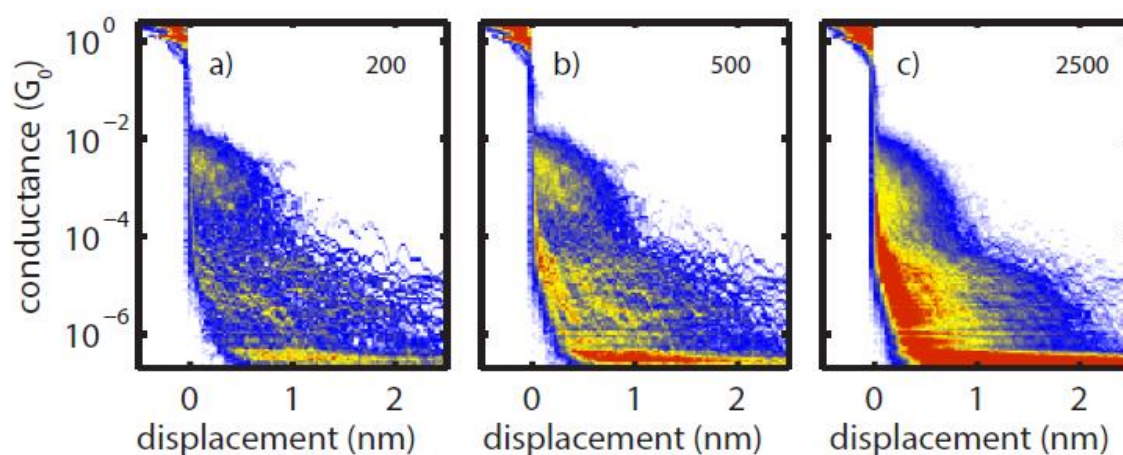


Figure 5.6 Conductance vs electrode displacement 2D histograms of **OPA2** considering the first (a) 200, (b) 500 and (c) 2500 traces. The measurements were carried out during 4 hours; the same regions of high counts can be observed in all of them. Reproduced with permission from [218], Copyright (2016) American Chemical Society. Samples were measured by Ignacio José Olavarria-Contreras.

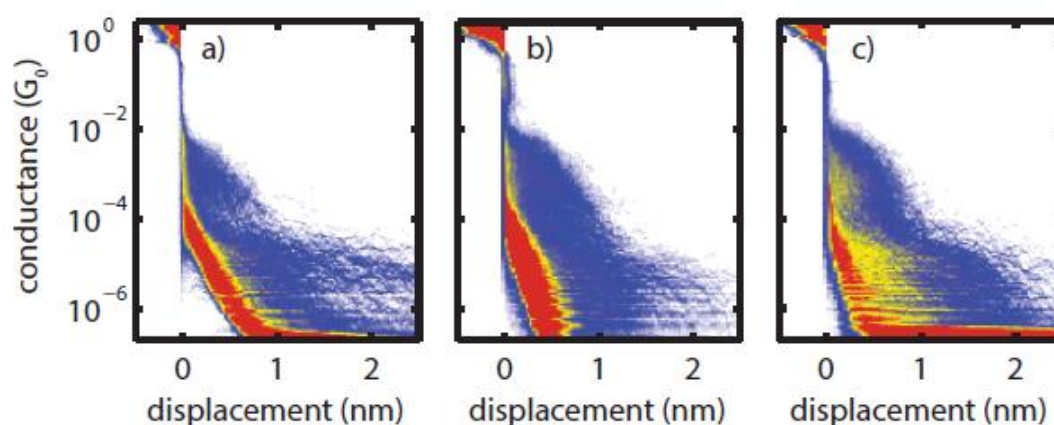


Figure 5.7 Conductance vs electrode displacement 2D histograms of **OPA2** for molecular concentration of (a) $28 \mu\text{M}$, (b) $280 \mu\text{M}$ and (c) 4.95 mM . The regions of high counts are very similar and the conductance values obtained from them are summarized in Table 5.2. Reproduced with permission from [218], Copyright (2016) American Chemical Society. Samples were measured by Ignacio José Olavarria-Contreras.

Table 5.2 Most probable molecular conductance for **OPA2** extracted from 1D conductance histograms obtained from experiments performed with different concentrations. Reproduced with permission from [218], Copyright (2016) American Chemical Society.

concentration	high conductance (G_0)	low conductance (G_0)
$28 \mu\text{M}$	6.6×10^{-4}	1.0×10^{-5}
$280 \mu\text{M}$	1.1×10^{-3}	6.4×10^{-6}
4.95 mM	4.1×10^{-4}	7.8×10^{-6}

The average nonexponential decay of conductance values for **OPAn** ($n = 2, 3, 4$) series are plotted with blue diamonds as a function of molecular length in Figure 5.4b. Interestingly, if we take the value of **OPE1** (deprotected from **TMS-OPE1**), which has the same structure as **OPA1** in reference ^[131] into account, the conductance values of **OPE1**, **OPA3** and **OPA4** (black dashed line in Figure 5.4b) show an exponential decay, with $\beta \approx 0.45 \text{ \AA}^{-1}$ which is similar to the exponential decay value of different anchoring groups with the same oligophenylene backbones.^[129,226] Notably, the conductance of **OPA2** has unexpected value which is approximately the same as **OPA3** deviating from the exponential decay line.

The odd behavior of the **OPA2** conductance may be associated to the freedom of phenyl rings. For example, a nonexponential decay of conductance has also been observed for oligothiophene molecules.^[227] In that case, it was attributed to that a 4-thiophene can rotate toward a more conjugated configuration, while the 3-thiophene cannot rotate. Another explanation is that this nonexponential decay may originate from the binding configuration. As reported in the literature ^[2a,228], alkynyl groups may change to sp^2 binding configuration to contact with gold; the smaller the molecule, the easier sp^2 binding configuration occur. When comparing the conductance value of sp^2 -hybridized **OP1** and diazonium terminated **OP2** data points (open square and the green \times , respectively) and **OPA2** from our study, we find that they show an exponential decay for sp^2 -hybridized anchoring carbon atoms, and they are in the same line which is parallel to the black (sp) and red (sp^3) lines (Figure 5.4b).

When comparing our data with other molecules that also form Au–C bonds to the leads, the conductance of molecules with oligophenylene backbone, which are connected via sp^3 -hybridized carbon atoms, is higher than the corresponding molecule connected by sp -hybridized carbon atoms. To better understand the trend, density functional theory (DFT) calculations were used to compute the molecular geometries and electronic structures of the **OPn** ($n = 2, 3, 4$) molecules with sp^3 hybridized anchoring carbon atoms deprotected from **SnMe3-OPn** molecules and the **OPAn** ($n = 2, 3, 4$) molecules with sp hybridized anchoring carbon atoms. These calculations were combined with the non-equilibrium Green's function (NEGF) formalism to obtain the transmissions; self-energies were corrected by using DFT + Σ method.^[229] By comparing the iso-surface of the highest occupied molecular orbital (HOMO) for **OP3** (Figure 5.8a) and **OPA3** (Figure 5.8b) with Au electrodes, we note that: (i) the amplitude of the wave functions around the linking gold is smaller in the case of sp hybridization; (ii) the main contribution of the gold to the wave function comes from the $5d$ orbital in the case of sp hybridization, while the $6s$ orbital of the gold in the case of the sp^3 -hybridized carbon.

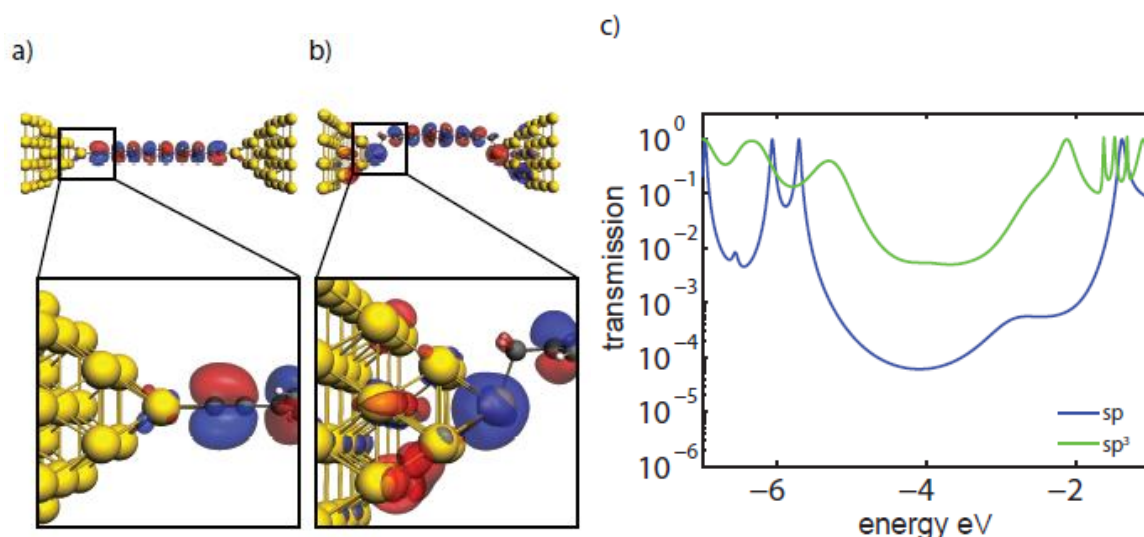


Figure 5.8 Diagram of the HOMO of a **OP3** attached to gold atoms through (a) sp - and (b) sp^3 -hybridized carbon. Zoom in images (lower panels) show the same orbitals near the Au–C interface. (c) Transmissions calculated using DFT+NEGF for the **OP3** molecule with sp - (blue line) and sp^3 -hybridized (green line) linking to the gold. Reproduced with permission from [218], Copyright (2016) American Chemical Society. The calculations were carried out by Mickael L. Perrin.

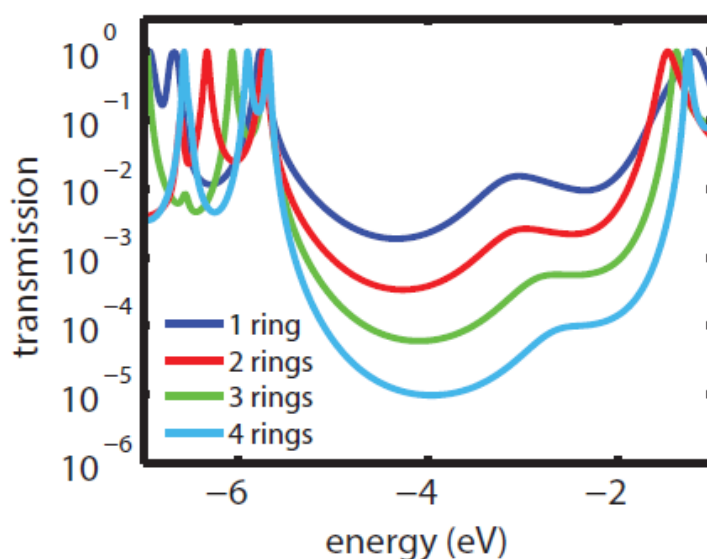


Figure 5.9 Transmission computed using NEGF-DFT for the four **OPAn** series reported in this study. The distances between consecutive transmissions are the same (in log scale) for level alignments between -5 and -2 eV. Reproduced with permission from [218], Copyright (2016) American Chemical Society. The calculations were carried out by Mickael L. Perrin.

The transmission functions of **OP3** and **OPA3** are displayed in Figure 5.8c. The shape of the resonance peaks of **OP3** (green line) is broader than **OPA3** (blue line) indicating that the sp^3 hybridized anchoring carbon atom has a higher coupling with the Au electrodes; in full agreement with the wave function overlap discussion earlier. The plot also shows that sp^3 hybridization gives a higher conductance due to the favorable coupling between the gold electrodes and the molecule conforming to the experimental results trend shown in Figure 5.4b. We also analyzed the dependence of the conductance on the molecular length and found

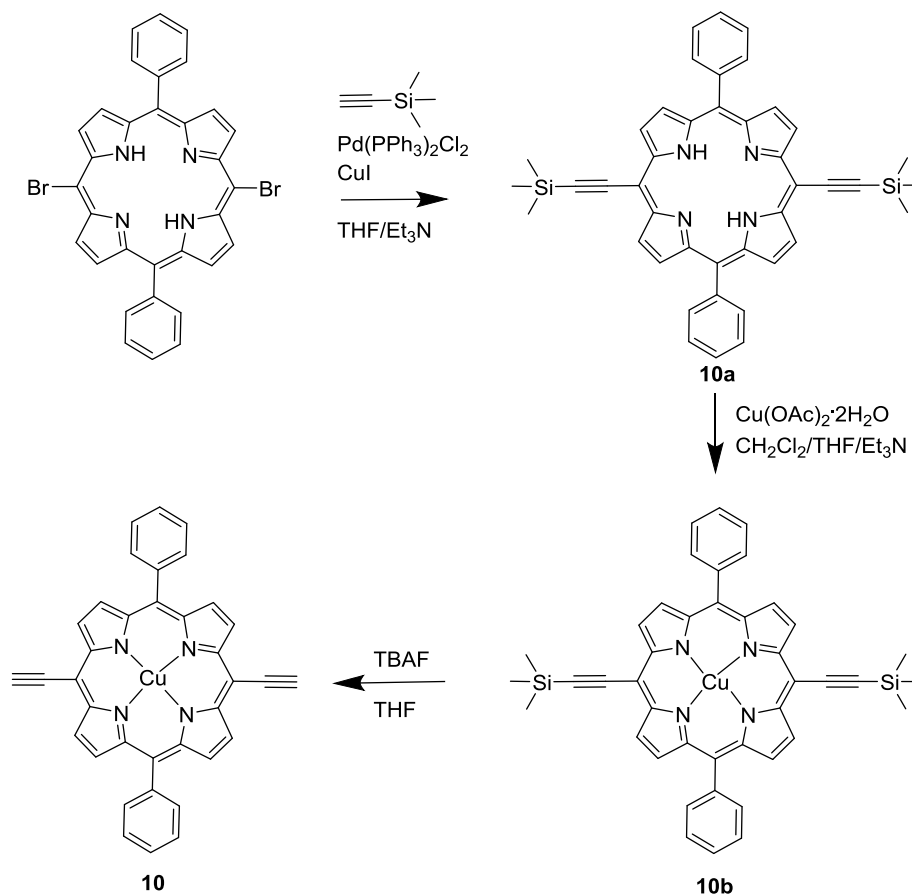
that the transmission function decays exponentially with molecular length for the *sp*-hybridized **OPAn** series (Figure 5.9). But the experimental value of **OPA2** does not fit the calculated result due to the possible reasons mentioned before.

In conclusion, we have demonstrated that terminal alkyne compound can directly bind to the gold electrodes through de-protonating *sp*-hybridized carbon atom to form a molecular junction. This method avoids the need of deprotective agents or toxic leaving groups. The conductance of **OPA3** and **OPA4** shows an exponential decay $\beta \approx 0.45 \text{ \AA}^{-1}$, which is similar to the value of *sp*³ C–Au junctions with the same molecular oligophenylene backbone. But the conductance of the molecules contact via the *sp*-hybridized carbon atom is lower than the previous ones reported using *sp*³ hybridization due to strong differences in the coupling of the conducting orbitals with the gold leads.

designed and synthesized a new porphyrin complex [5,15-bis(ethynyl)-10,20-diphenylporphinato]copper(II) (**CuDEPP**, **10**) and investigated its electrochemical performance for rechargeable batteries.

The **CuDEPP** compound was readily synthesized from commercially available 5,15-dibromo-10,20-diphenyl-21*H*,23*H*-porphyrin (Scheme 6.2). The crystals of the intermediate products 5,15-bis(trimethylsilanylethynyl)-10,20-diphenyl-21*H*,3*H*-porphyrin (**10a**) and [5,15-bis(trimethylsilylethynyl)-10,20-diphenylporphinato]copper(II) (**10b**) were crystallized by slowly evaporation of their solution in the hexane and dichloromethane mixture.

Compound **10a** crystallizes in the monoclinic system with space group $P2_1/n$, while **10b** crystallizes in the triclinic system with space group $P\bar{1}$. The asymmetric unit of **10a** consists of one crystallographically independent molecule of **10a** (Figure 6.1 and 6.2). The porphyrin ring is not in an exact plane. The angles of two phenyl rings with the porphyrin ring are 47.43° and 64.50° respectively. The asymmetric unit of **10b** consists of half a crystallographically independent molecule of **10b** (Figure 6.3 and 6.4). The porphyrin ring is in an exact plane. The angle of phenyl ring with the porphyrin ring is 67.34° . Interestingly, the alkyne group have a weak interaction with the Cu atom in the nearby molecule with distance C11–Cu1 of 3.515 \AA along the a axis (Figure 6.5).



Scheme 6.2 Synthetic route of **CuDEPP** (**10**).

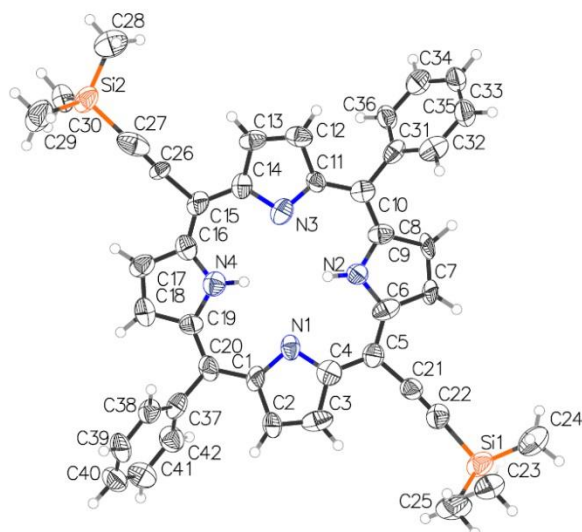


Figure 6.1 ORTEP plot of **10a** with ellipsoids drawn at 30% level of probability for all non-hydrogen atoms.

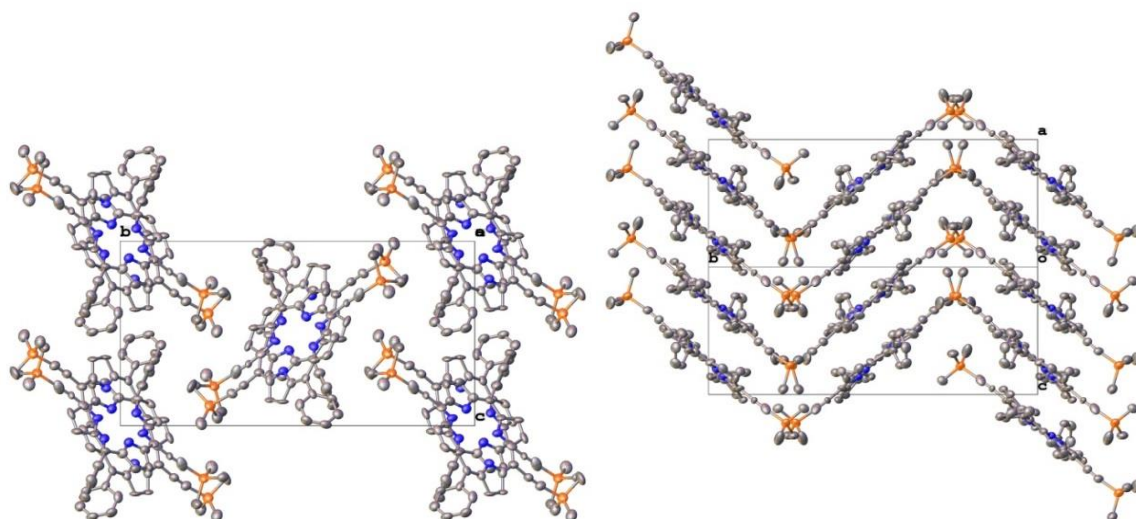


Figure 6.2 Crystal packing of **10a** viewed along the (100) and (101) directions. H atoms are omitted in the crystal structures.

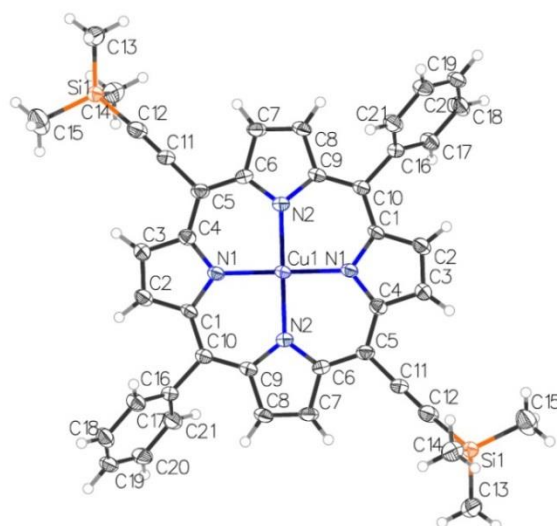


Figure 6.3 ORTEP plot of **10b** with ellipsoids drawn at 30% level of probability for all non-hydrogen atoms.

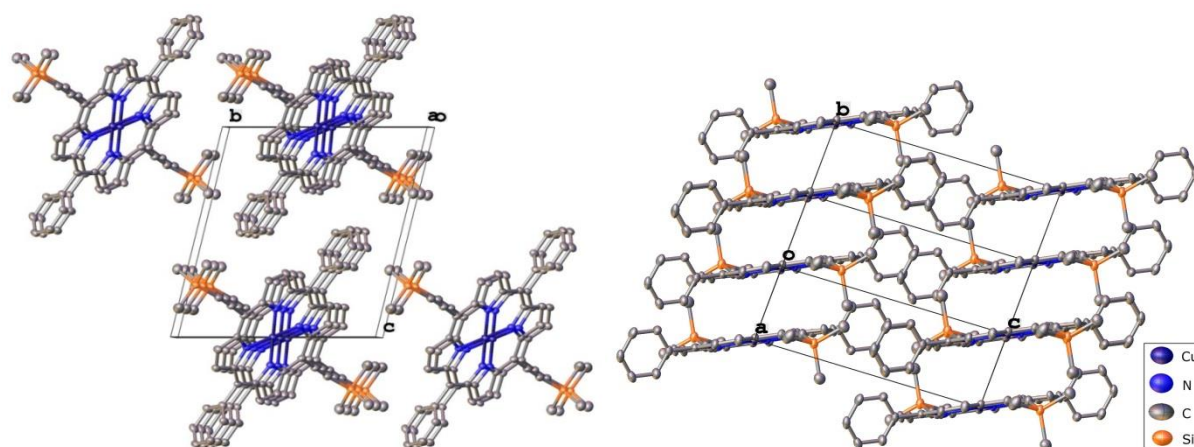


Figure 6.4 Crystal packing of **10b** viewed along the (100) and (1/2 0) directions. H atoms are omitted in the crystal structures.

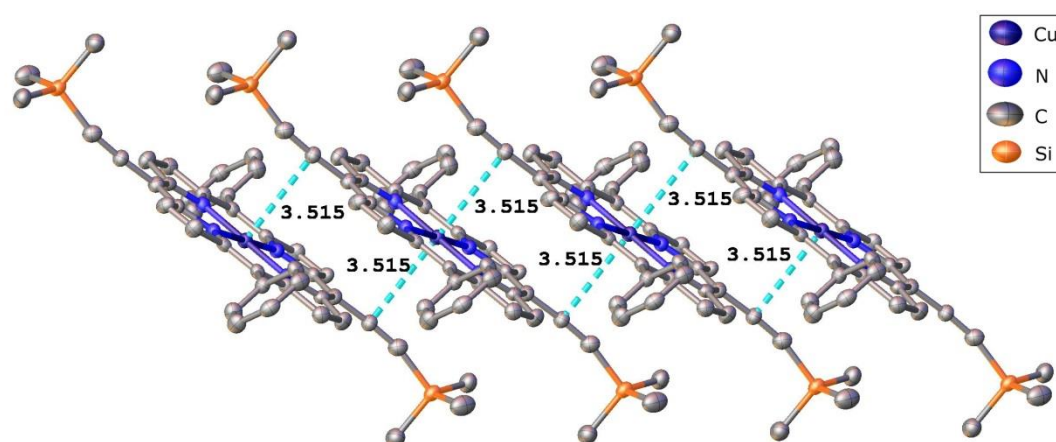


Figure 6.5 C≡C and Cu interactions along (100) direction in **10b**. H atoms are omitted in the crystal structures.

The **CuDEPP** was characterized by spectroscopic and microscopic methods. MALDI-ToF spectra show that the mass of **CuDEPP** fit well of the calculated value (Figure 6.6). The intensity of UV-vis of **CuDEPP** is lower than **10a** and **10b** due to the poor solubility of **CuDEPP** (Figure 6.7). This low solubility in organic solvents gives **CuDEPP** an advantage for Li battery application which reduces the loss of active material to electrolyte. Compared four Q-bands peaks of **10a**, **10b** and **CuDEPP** both has two Q-bands peaks in UV-vis spectra. The Soret band of **CuDEPP** blue shift a bit compared to **10b** (exact peaks number in synthesis part). Notably, the **CuDEPP** molecule is thermally stable up to 250 °C in air measured by the thermogravimetric-differential scanning calorimetric analysis (TGA-DSC) as shown in Figure 6.8. After heating up to 220 °C in air, the IR spectra of the **CuDEPP** still remain the same, which also reveals the high stability of **CuDEPP** (Figure 6.9). The SEM image shows that the **CuDEPP** complexes form smooth nanorods about 4 μm long and 200 – 400 nm in diameter (Figure 6.10).

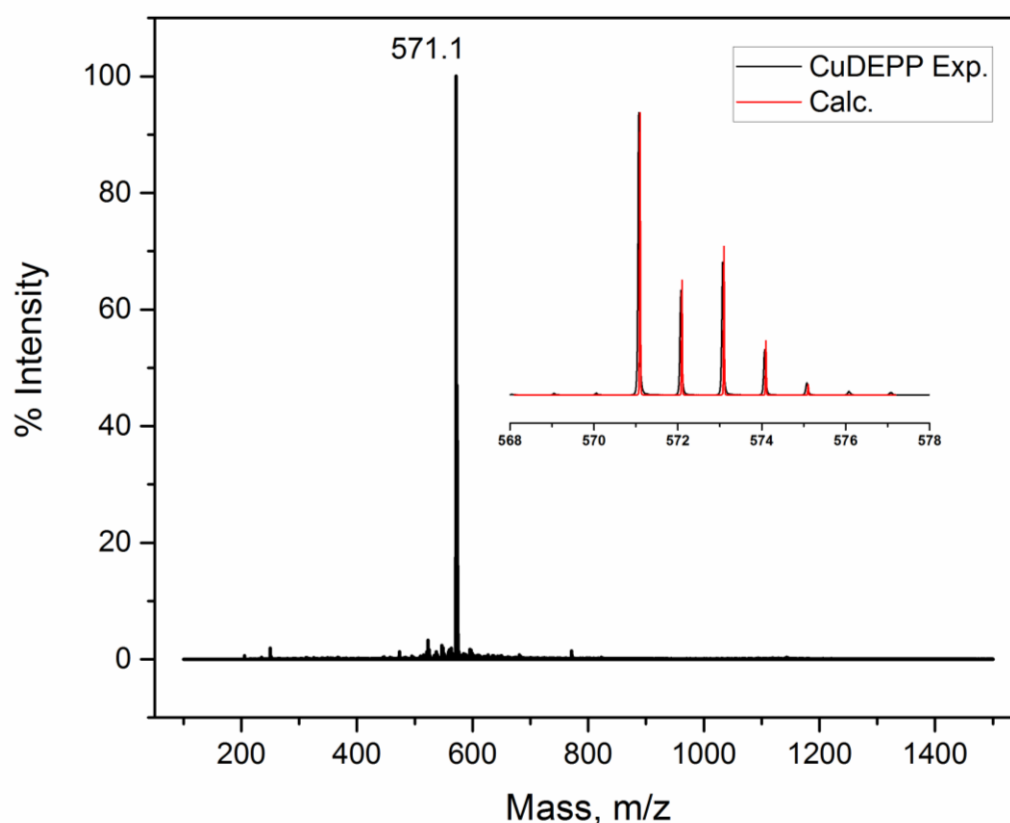


Figure 6.6 MALDI-ToF mass spectrum of **CuDEPP**.

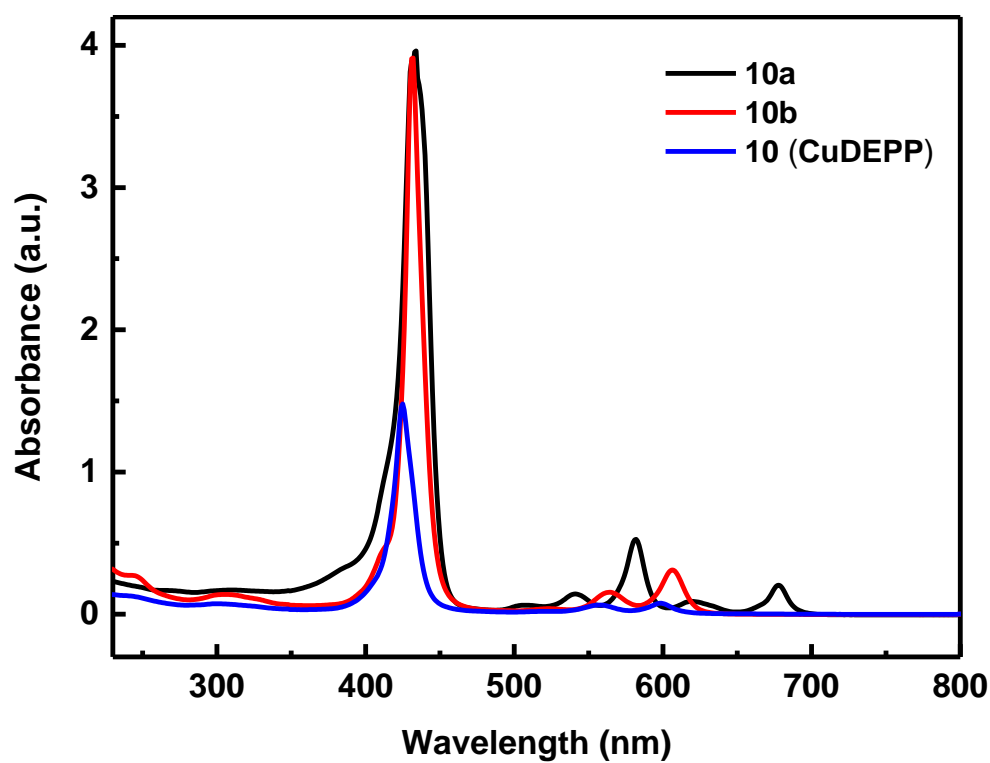


Figure 6.7 UV-vis spectra of compound CuDEPP, 10a and 10b.

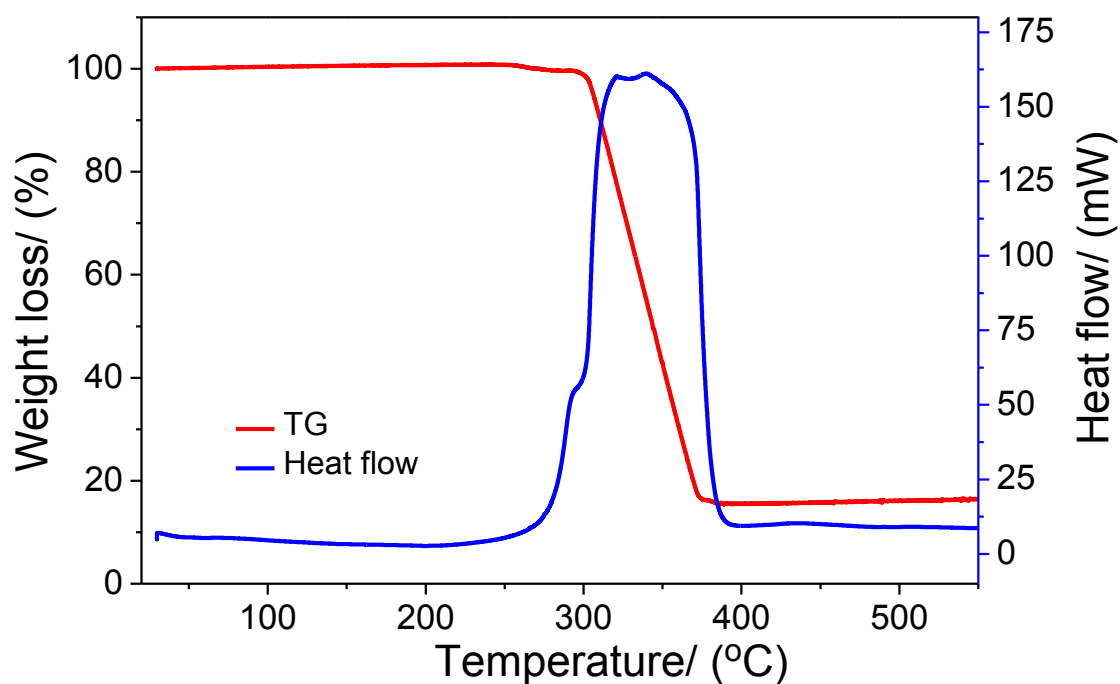


Figure 6.8 TGA-DSC profile of CuDEPP in air.

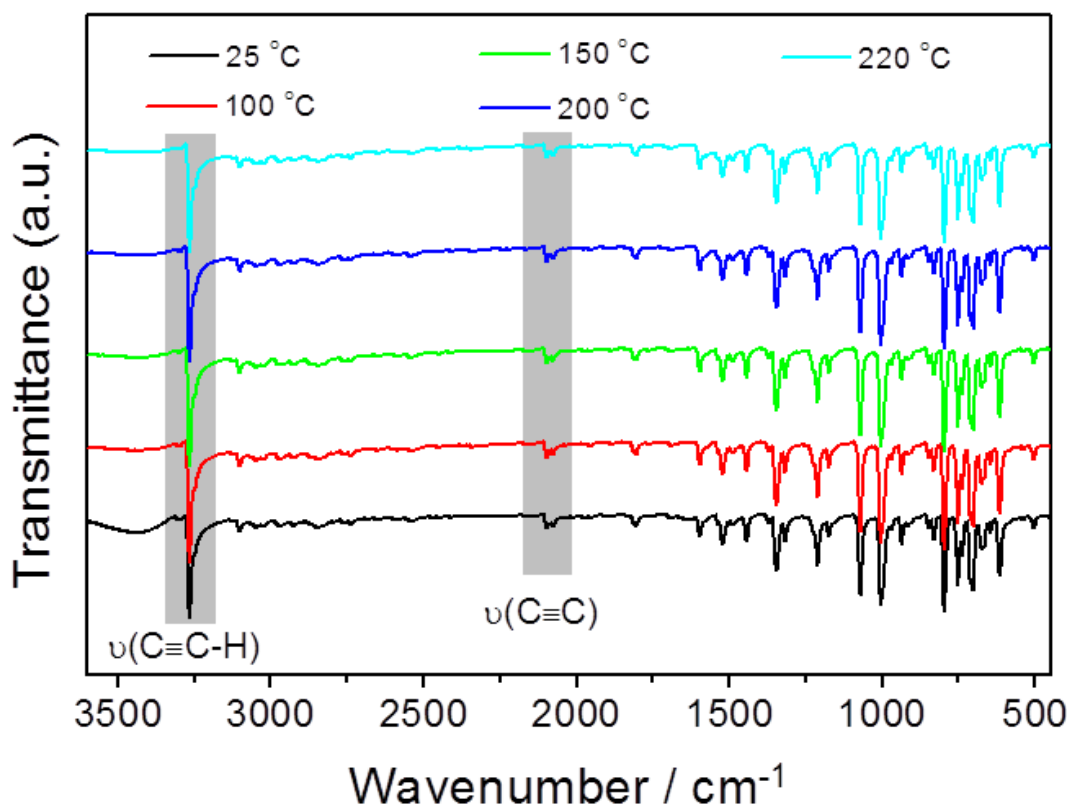


Figure 6.9 IR spectra of **CuDEPP** after heating at different temperatures.

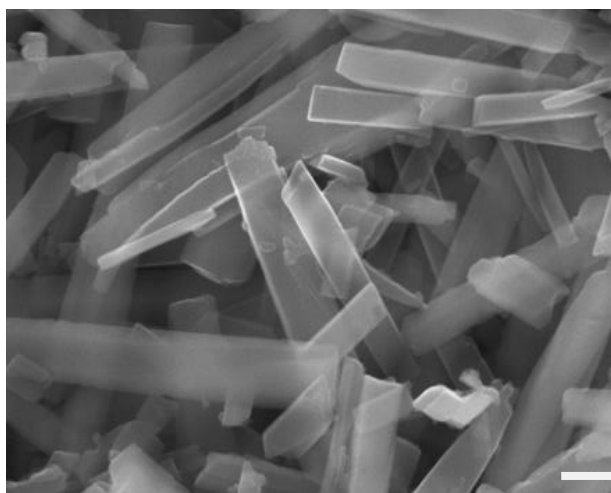


Figure 6.10 SEM image of **CuDEPP** (The white scale bar represents 300 nm).

The **CuDEPP** could not be recrystallized for crystallographic studies due to its poor solubility in organic solvents. The crystal structure of **CuDEPP** was finally determined by means of powder X-ray diffraction (PXRD) (Figure 6.11).

We chose Reflex module of Materials Studio software (Accelrys, Inc.) to determine the crystal structure of **CuDEPP** from experimental PXRD. Firstly, the Dicvol 91 method was used to index the peaks of experimental PXRD, giving the appropriate cell parameters an empty cell. Secondly, this cell was refined by using the Pawley method, and the suitable space

group was selected. Thirdly, a compound **CuDEPP** molecule taken suitable fragment from crystal structure of compound **10b**, was put in the empty cell, and set the freedom of the angle of porphyrin ring and phenyl rings for the optimization. Monte Carlo simulated annealing method was applied to solve the structure. The refinement procedure was performed using Rietveld refinement with refined parameters: background, scale factor, lattice parameters, atom positions and the global anisotropic temperature factor.

The **CuDEPP** and **10b** have very similar crystal structures in triclinic crystal system with space group $P\bar{1}$ (Figure 6.12). Similar to compound **10b**, the porphyrin ring is also in an exact plane, but the angle of phenyl ring with the porphyrin ring is 96.09° . Owing to the rigid planar structure and high π -conjugation, porphyrins and metalloporphyrins generally have intermolecular π - π interactions, resulting in the self-assembly of diverse nanocrystals.^[234] As shown in Figure 6.13 and 6.14, the packing structure of **CuDEPP** shows that the porphyrin rings stack parallel with offset center such that Cu sits between the $C\equiv C$ bonds of the neighboring porphyrins. The interplanar separation in π -stacked porphyrins in **CuDEPP** is about 3.240 \AA , which is smaller than that in **10b** due to the removal of the bulky TMS groups.

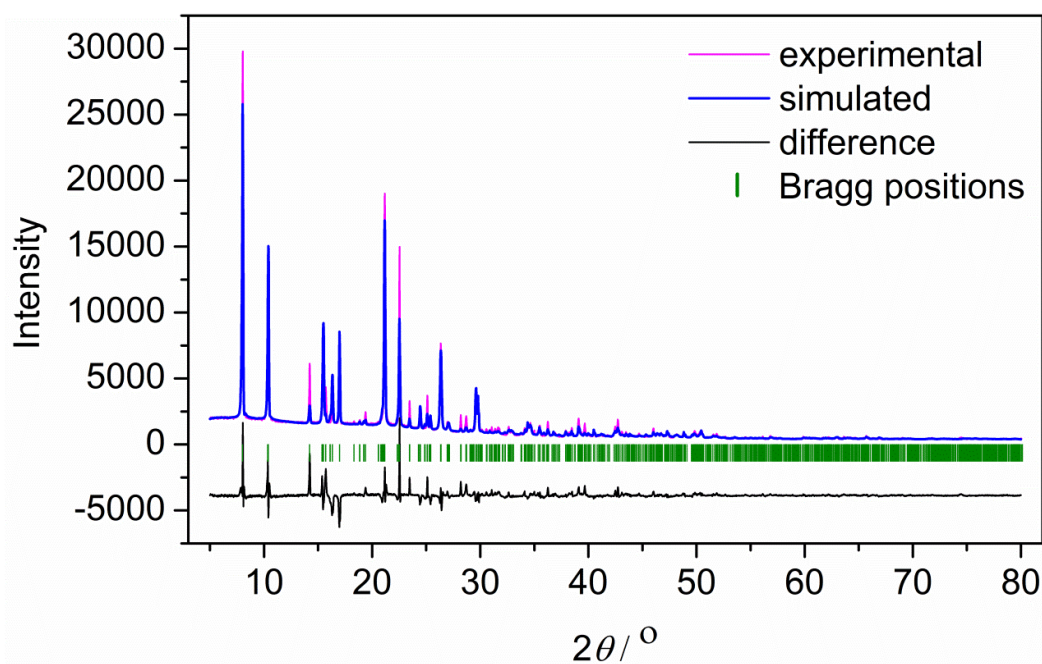


Figure 6.11 Comparison of the calculated and experimental PXRD patterns for **CuDEPP** after Rietveld refining.

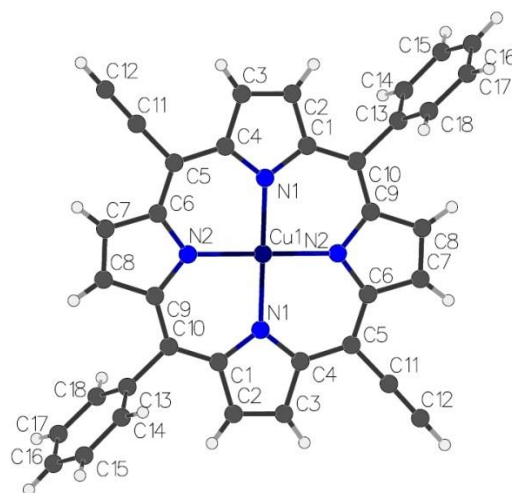


Figure 6.12 Molecular structure of **CuDEPP**.

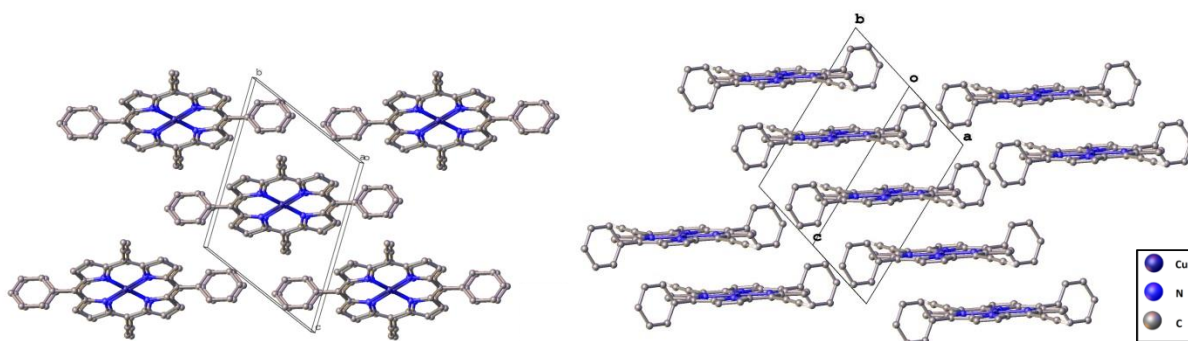


Figure 6.13 Crystal packing of **CuDEPP** viewed along the (100) and (110) directions. H atoms are omitted in the crystal structures.

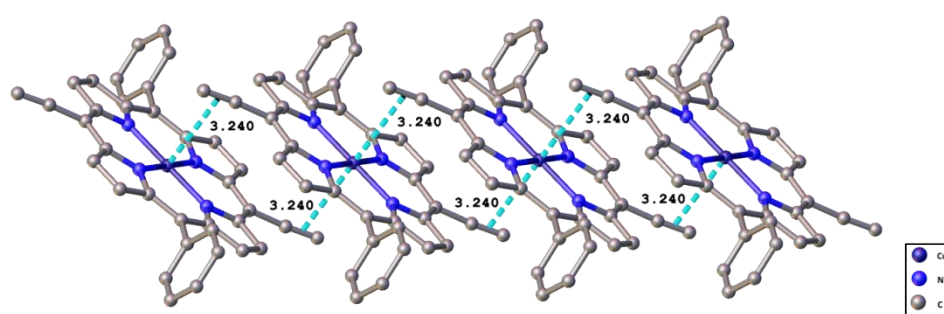


Figure 6.14 C≡C and Cu interactions along (100) direction in **CuDEPP**. H atoms are omitted in the crystal structures.

Due to its low solubility in the common organic solvents, a cyclic voltammetric (CV) analysis of the **CuDEPP** in solution could not be conducted. Based on the reported redox chemistry of the analogous compound **CuTPP**,^[235] we propose that the **CuDEPP** bearing 18 π -electron proceeds a reversible two-electron oxidation and a two-electron reduction, forming a dicationic species (CuDEPP^{2+} , 16 π -electron) and a dianionic species (CuDEPP^{2-} , 20 π -

electron), respectively, as shown in Scheme 6.1. The oxidation (reduction) of **CuDEPP** is likely via a radical cation $\text{CuDEPP}^{\bullet+}$ (anion $\text{CuDEPP}^{\bullet-}$) to CuDEPP^{2+} (CuDEPP^{2-}), respectively. These radical ions are normally recognized as instable species and are not illustrated in the scheme.

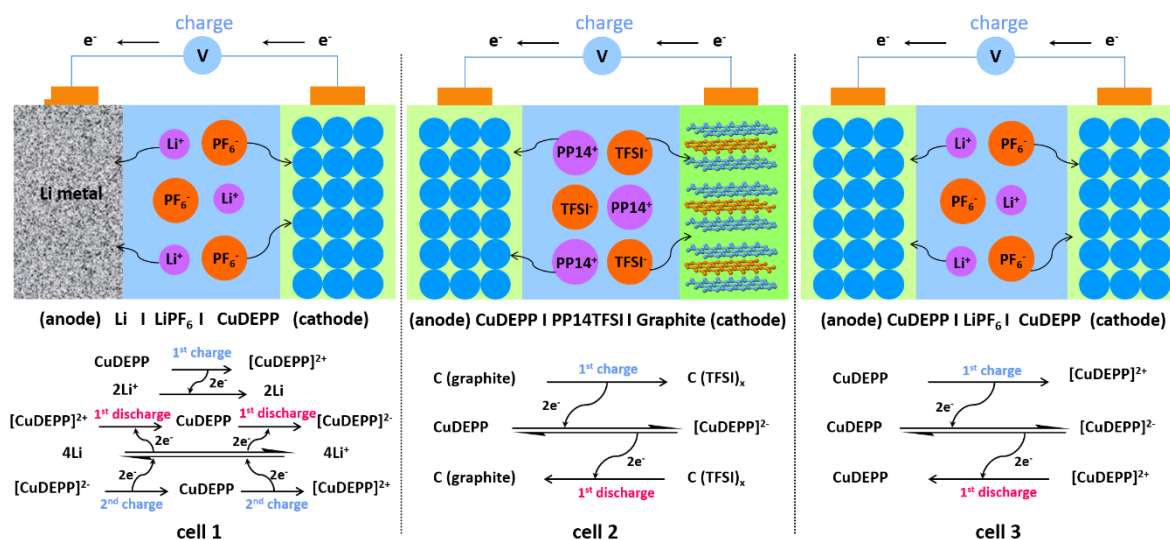


Figure 6.15 Illustration of three cell setups and the corresponding electron transfer processes.

To verify the intriguing reactivity as electron donor-acceptor and versatile redox chemistry of the **CuDEPP**, three different battery systems were designed according to the corresponding redox mechanisms as illustrated in Figure 6.15. In **cell 1** (Li/LiPF₆/CuDEPP), using a lithium foil anode, the **CuDEPP** served as a cathode in the LiPF₆ electrolyte solution. In **cell 2** (CuDEPP/PP₁₄TFSI/graphite), the **CuDEPP** served as an anode coupled with a graphite cathode in an anhydrous ionic liquids of 1-butyl-1-methylpiperidinium bis(trifluoromethylsulfonyl)imide (PP₁₄TFSI) as electrolyte. In **cell 3** (CuDEPP/LiPF₆/CuDEPP), **CuDEPP** served as both cathode and anode in the LiPF₆ electrolyte, resulting in an all-organic battery system. The **CuDEPP** electrode was typically prepared by mixing of the **CuDEPP** redox active material with carbon black and a polyvinylidene fluoride binder (PVDF).

Cell 1: CuDEPP as cathode in a Li-based cell.

To determine the working potential window for **cell 1**, we first recorded the CV in a wide voltage range from 4.5 to 0.05 V using **CuDEPP** material as working electrode and a Li foil as the counter and reference electrode. During the first anodic sweep, a distinct irreversible oxidative peak appears at 4.2 V as shown in Figure 6.16a, suggesting a side reaction between the electrode and electrolyte. We hypothesize that the first anodic peak at 4.2 V might be

attributed to the electrochemical oxidation induced reaction of the ethynyl groups in the **CuDEPP**, which is being further investigated and will be discussed later.

Nevertheless, the oxidation of the porphyrin core [CuDEPP] to [CuDEPP]²⁺ might also occur during the initial anodic scan (to differentiate from the original porphyrin compound **CuDEPP**, [CuDEPP] is denoted for the porphyrin core of the electrode material after the electrochemical oxidation process). The subsequent cathodic peaks at 3.61 V and 2.34 V might be correlated to the reduction reactions at the porphyrin core, e.g. [CuDEPP]²⁺ + 2e⁻ ↔ [CuDEPP] and [CuDEPP] + 2e⁻ ↔ [CuDEPP]²⁻, respectively. The lowest irreversible reductive signals at about 1.27 and 0.78 V are likely associated with the reduction of the center Cu(II) to Cu(I) or/and potential other side reactions. It is worth noting that the reduction of the center Cu(II) may influence the coordination chemistry of the porphyrin and Cu ion and thus change the redox properties of the porphyrin ring. This could be the reason for the absence of signals for the reduction reactions from [CuDEPP]²⁻ to [CuDEPP]²⁺ in the reverse anodic scan (Figure 6.16a). In contrast, the CV analysis in the voltage range of 4.5 to 1.8 V exhibits repetitive reversible reductive-oxidative couples at 2.22/2.95 V and 3.55/3.68 V after the first anodic sweeping (Figure 6.16b), which are assigned to the reversible redox reactions between the [CuDEPP]²⁺ to [CuDEPP]²⁻ as described above.

On the basis of the CV results, the voltage range of 4.5 – 1.8 V was utilized in the galvanostatic charge/discharge tests for **cell 1**. The flat voltage plateau at approximately 4 V in the initial charging process shown in Figure 6.16c is consistent with the distinct oxidation feature at 4.2 V exhibited in CV (Figure 6.16a,b). Highly reversible discharge and charge behavior is presented in the profiles after the first charging process. The discharge capacity of 182 mAh g⁻¹ in the 3rd cycle is close to the theoretical value of 187 mAh g⁻¹ based on four-electron redox reactions from the dication to dianion species of the molecule ([CuDEPP]²⁺ → [CuDEPP]²⁻, *vice versa* for the recharge process).

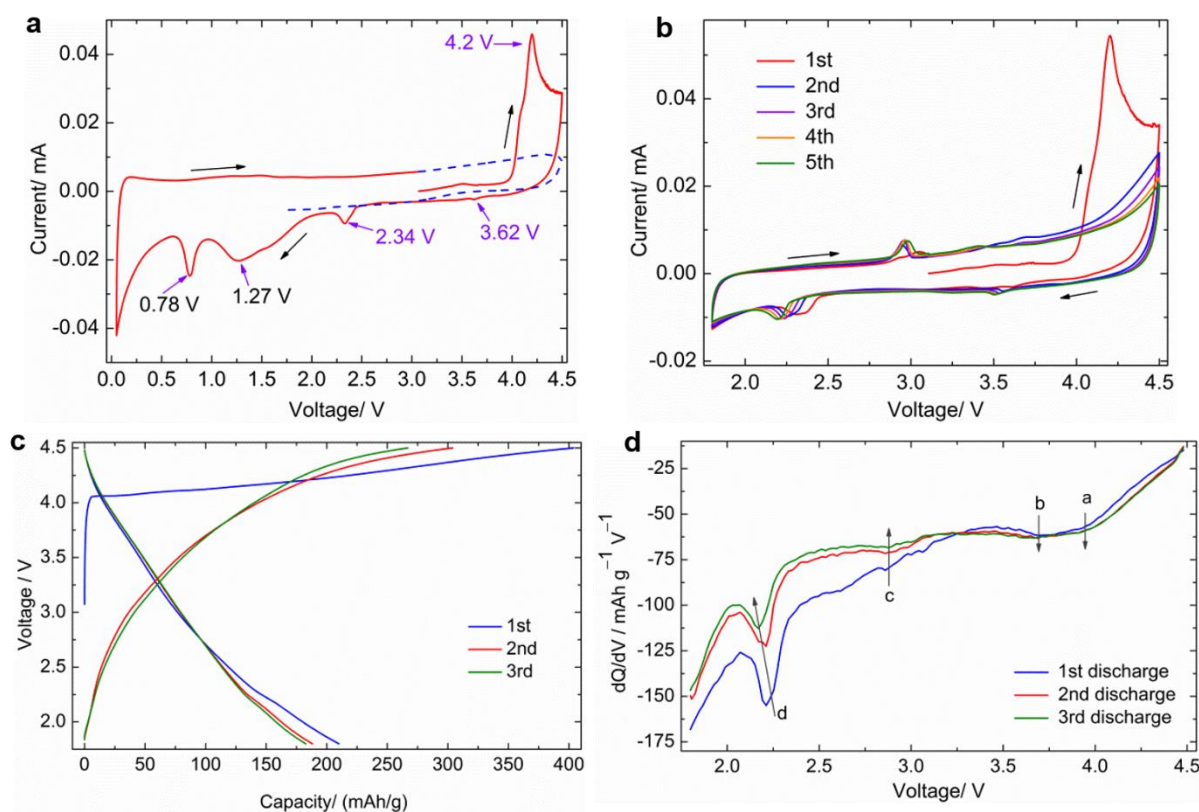


Figure 6.16 Cyclic voltammograms and charge/discharge profiles. (a) **Cell 1** in a voltage range of 4.5 – 0.05 V. (b) the initial five cycles in a voltage range of 4.5 – 1.8 V. The scan rate was 0.1 mV s^{-1} . (c) Initial charge and discharge curves in a voltage range of 4.5 – 1.8 V at 200 mA g^{-1} . (d) dQ/dV plot of the discharge curve in c.

No well-defined voltage plateaus were observed in charge/discharge profiles of **cell 1**, suggesting a fast electron transfer process through the instability of the intermediate species rather than a two-phase transition mechanism as in the conventional inorganic electrodes.^[236] In addition, the subtle discharge behaviors were indicated in the dQ/dV plots as shown in Figure 6.16d, in which four potential peaks at 3.94, 3.69, 2.88 and 2.2 V were revealed.

Interestingly, the discharge capacity gradually increased after 10 cycles and was maintained at approximately 186 mAh g^{-1} with a coulombic efficiency of 84% after the 20th cycle at a current density of 200 mA g^{-1} as shown in Figure 6.17a. This implies that the original **CuDEPP** electrode material was electrochemically modified in the initial cycles as was also observed in the CV measurements. The increased capacity can be attributed to the continued polymerization of the monomers remaining on the surface of the electrodes, due to enhanced electrolyte accessibility into the cathode materials upon cycling. The initial cycling process is obviously crucial for the superior battery performance and considered to be “self-conditioning” for the batteries. The cycling and rate performance of **cell 1** were further evaluated by applying increased current rates. Discharge capacities of 163, 143, 132, 125 mAh g^{-1} were retained at current densities of 1, 2, 4 and 6 A g^{-1} within a 100 cycles,

respectively (Figure 6.17a). The discharge capacities were mostly retrieved by tuning of the current rates from 10 to 1 A g⁻¹ during cycling, which demonstrates the high rate capability and reversible capacity of the [CuDEPP] electrode. The selected discharge curves of the [CuDEPP] electrode at different current rates are shown in Figure 6.17b, which presents slightly decreased potentials upon increasing the discharge rate and cycles. Remarkably, even at a high current density of 10 A g⁻¹ (53 C), the [CuDEPP] electrode still delivered a stable reversible discharge capacity of 115 mAh g⁻¹, which was achieved within 42 seconds with a coulombic efficiency of 99%. These values correspond to a specific energy density of 345 Wh kg⁻¹ and a specific power of 29 kW kg⁻¹. The outstanding cycling stability of the cell at an extremely high current density of 10 A g⁻¹ is also represented in the characteristic charge/discharge profiles, where no distinct change in the curves was observed (Figure 6.17c).

In addition to the rate tests, the long-term cycling performance of the **cell 1** at a high current density of 4 A g⁻¹ (21 C) was conducted. As shown in Figure 6.17d, the cell was operated for 20 cycles for a “self-conditioning” as described above. A maximal capacity of 150 mAh g⁻¹ was obtained in the 226th cycle and the capacity retention was approximately 85% for the first 2000 cycles and gradually decreased to 60% after 8000 cycles with a coulombic efficiency close to 100%. Accordingly, the electrode exhibited a specific energy density of 240 Wh kg⁻¹ at a power density of 11 kW kg⁻¹ for over 8000 cycles. The selected charge and discharge profiles of the cathode are shown in Figure 6.17e. Additional cyclic voltammograms were captured after cycling the cell for 2000 cycles. As shown in Figure 6.17f, a reversible and well-defined redox peak at approximately 3 V is visible at a sweeping rate of 10 mV s⁻¹, which is consistent with the average discharge/charge potential of 3 V (Figure 6.18).

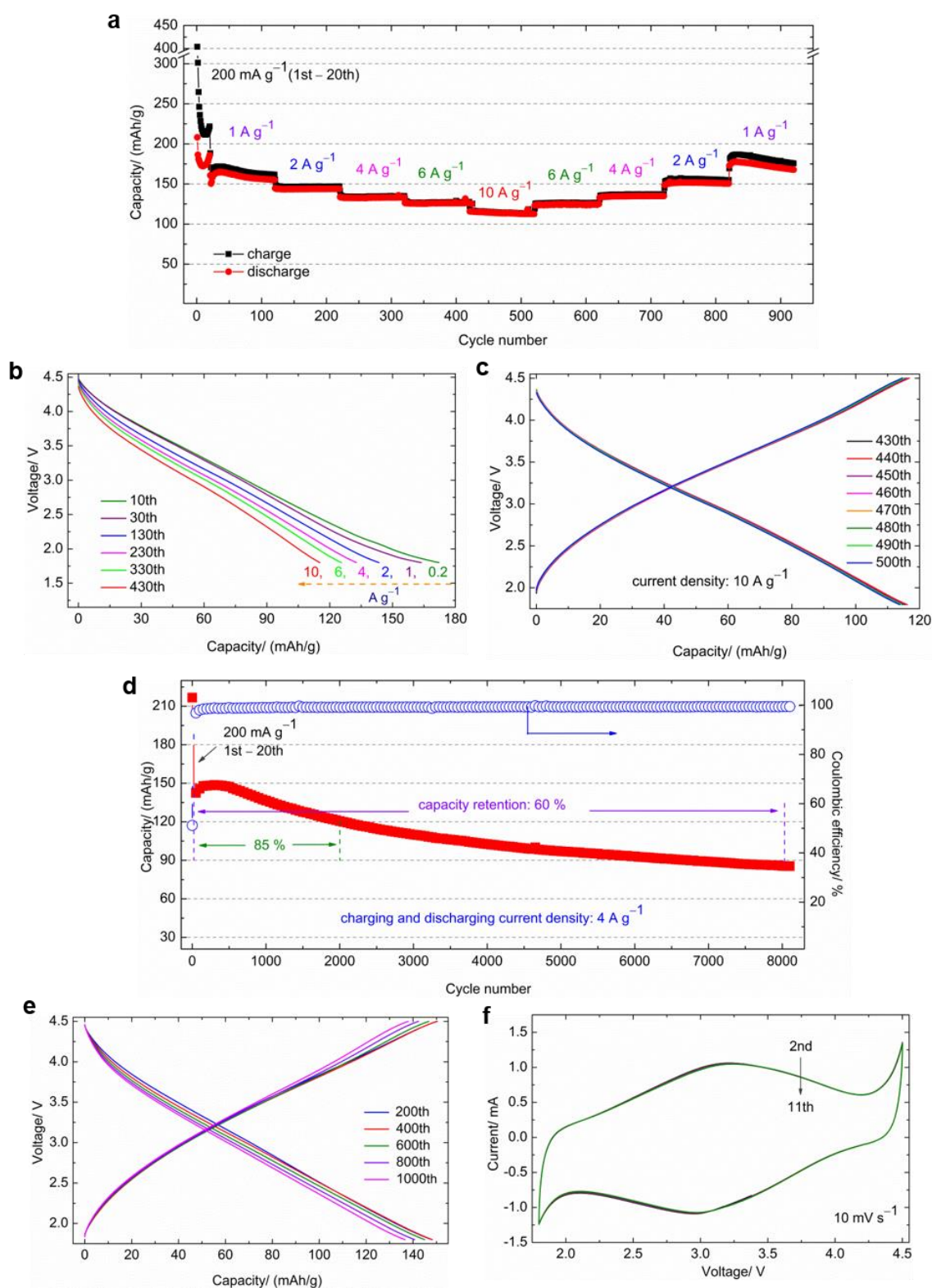


Figure 6.17 Electrochemical performance of the [CuDEPP] electrode. (a) Charge and discharge performance at different current rates. (b) Discharge curves at different current rates. (c) The selected charge/discharge profiles at a high current density of 10 A g^{-1} . (d) Long-term cycling performance. (e) Selected charge and discharge curves at a current density of 4 A g^{-1} . (f) CV curves after a battery test for 2000 cycles at a sweeping rate of 10 mV s^{-1} .

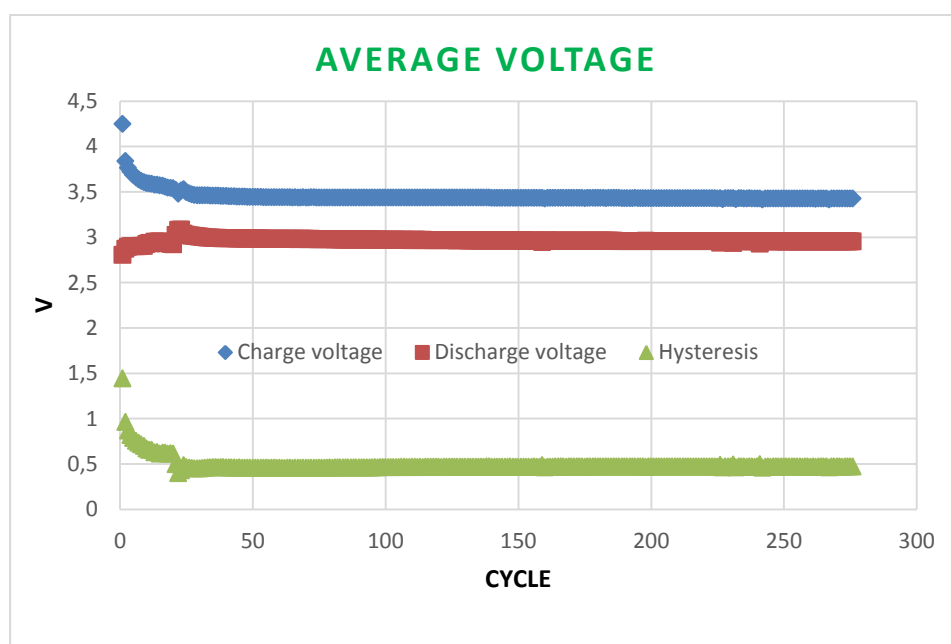


Figure 6.18 The average charge, discharge and hysteresis voltage of cell 1 during the battery testing. The charge and discharge current density was 0.2 A g^{-1} for the initial 20 cycles then at 4 A g^{-1} in the following cycles. The average discharge voltage was close to 3 V (vs Li/Li^+).

Electrochemical measurements of [5,10,15,20-tetraphenylporphinato]copper(II) (CuTPP)

The **CuTPP** electrode was prepared as the same procedure as for the **CuDEPP** electrode. The voltage range for the battery tests was $4.5 - 1.8 \text{ V}$ (vs Li/Li^+) (Figure 6.19). The theoretical capacity of the **CuTPP** electrode is 158 mAh g^{-1} based on four electrons transferring. The OCV of the cell was around 3.0 V . The first discharge capacity of 17 mAh g^{-1} was only obtained with a coulombic efficiency of 11.6%.

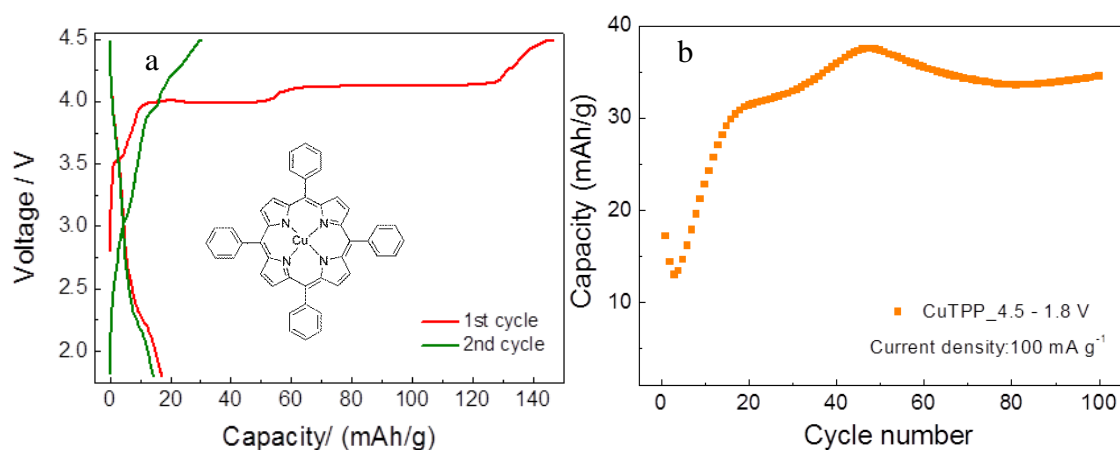


Figure 6.19 (a) the first and the second charge and discharge profiles of the **CuTPP** electrode. Inset of (a) shows the structure of the **CuTPP** molecule. (b) Cycling performance of the $\text{Li}/\text{LiPF}_6/\text{CuTPP}$ cell at a current density of 100 mA g^{-1} .

Mechanistic studies

To gain more insight into the mechanism of the beneficial “self-conditioning” process for **cell 1**, we carried out postmortem studies to learn about the chemical and structural change of the **CuDEPP** material after the initial cycles. It has been noticed that the cycled electrode material has an even lower solubility in organic solvents than the as-synthesized **CuDEPP**, which impeded the characterization of the reaction products associated with the initial electrochemical oxidation via mass spectrometry (MS). On the other hand, it also implies the chemical change of the cathode material by the electrochemical reactions. The morphology and crystallinity of the **CuDEPP** electrode material in the first cycles was analyzed by *ex-situ* SEM and XRD, respectively. The rod-like shape of **CuDEPP** material remained unchanged after 10 charge-discharge cycles (Figure 6.20a-d). However, the crystallinity was reduced after the 1st charge and further undermined at the discharged state as indicated by the XRD patterns (Figure 6.21). This can be ascribed to the decrease of long-range order of the crystals by the aforementioned the possible chemical change of the **CuDEPP** molecules and the progressive incorporation of the PF₆⁻ and Li⁺ anions into the lattice of the electrode material during the charge/discharge process.^[237] The insertion/de-insertion of PF₆⁻ in [CuDEPP] electrode was supported by the *ex-situ* IR spectroscopy, in which the signals at 838 cm⁻¹ and 556 cm⁻¹ for PF₆⁻ appear after charge and disappear after discharge, respectively (Figure 6.22b). This supports the redox mechanism for **cell 1** involving both anion (PF₆⁻) and cation (Li⁺) incorporation processes (Figure 6.15).

The IR band at 3264 cm⁻¹ associated with the characteristic stretching vibration of the *sp* C–H bonds of the ethynyl group (–C≡C–H) in **CuDEPP** vanished after the 1st charge (Figure 6.22a), providing clear evidence of a change in the ethynyl group induced by the anodic oxidation.

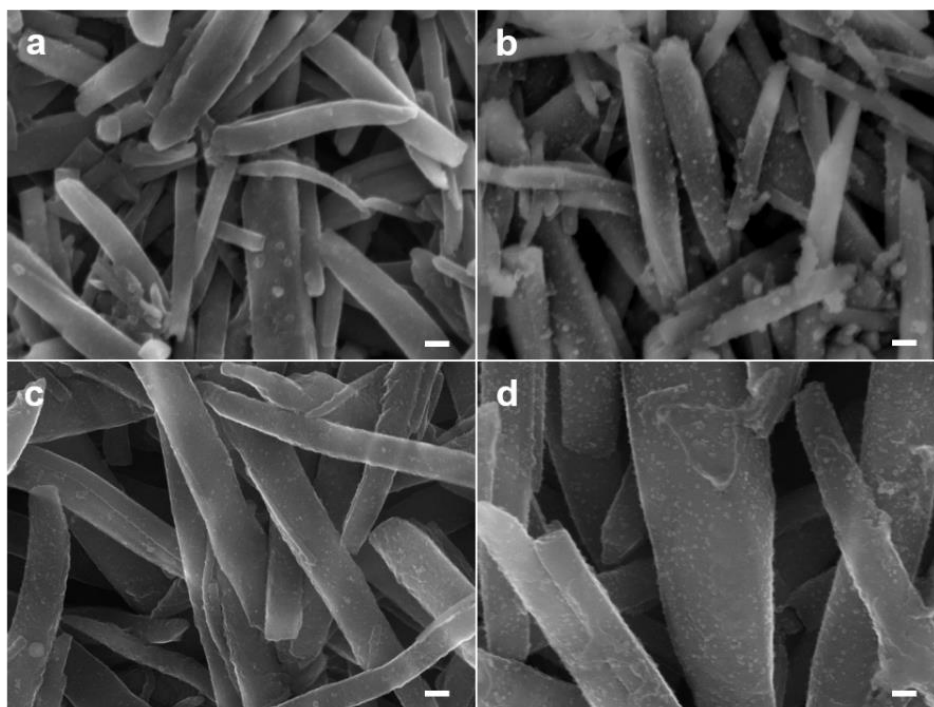


Figure 6.20 (a,b) SEM images of the 1st charged and discharged sample in **cell 1**, respectively. (c,d) SEM images of the sample charged and discharged in the 10th cycle, respectively. The scale bar represents 300 nm.

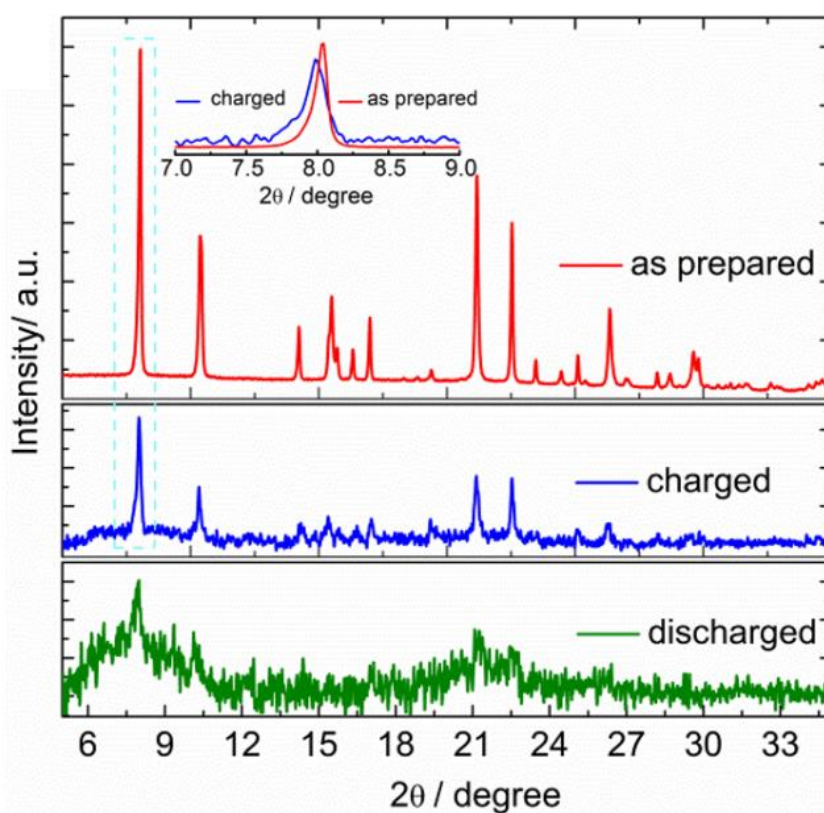


Figure 6.21 XRD patterns of the **CuDEPP** electrode as-prepared and after charge and discharge in the 1st cycle.

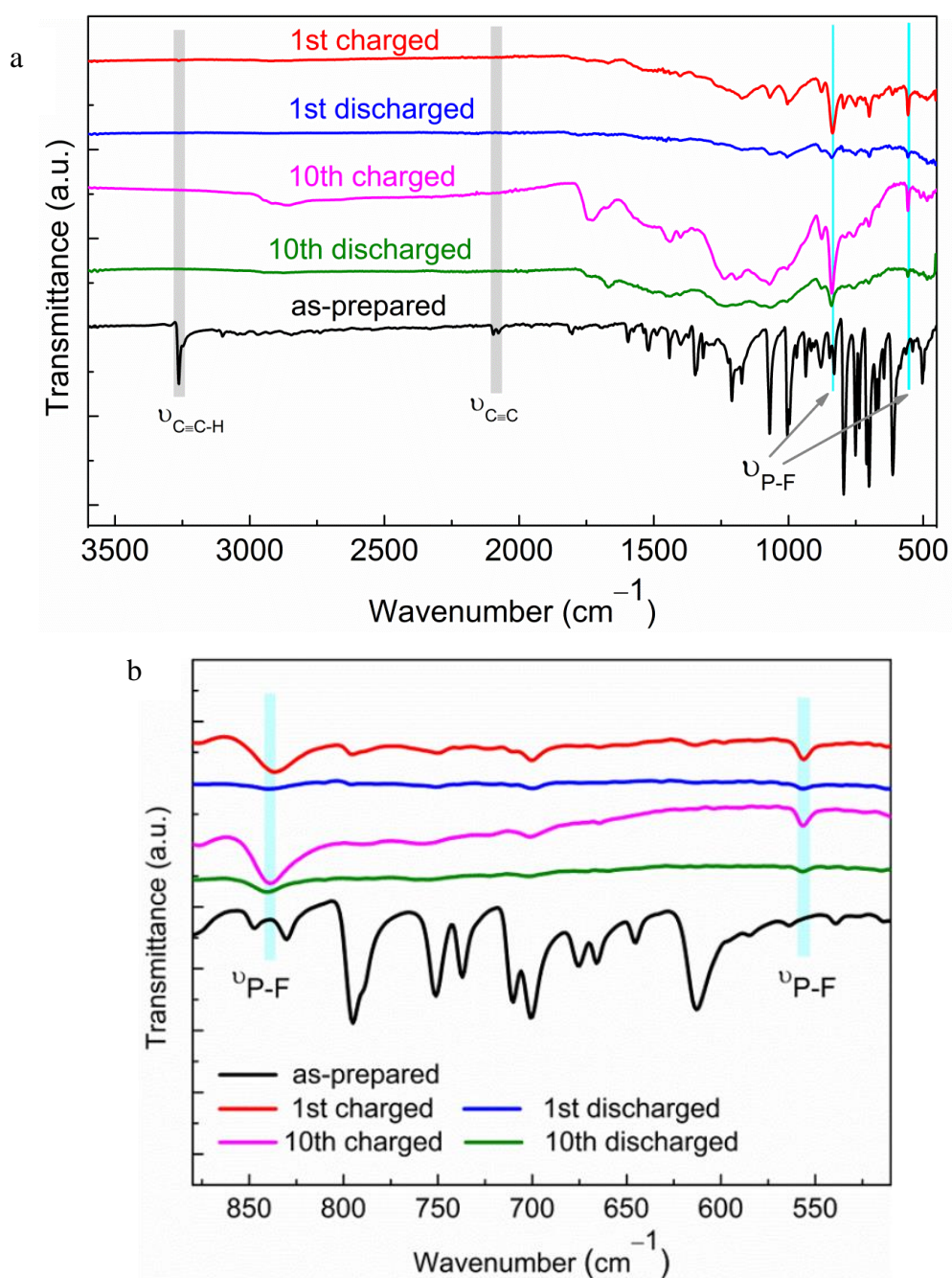


Figure 6.22 *Ex-situ* IR spectra of the **CuDEPP** electrode in the as-prepared, charged (4.5 V) and discharged state (1.8 V) in the 1st cycle and 10th cycle of **cell 1**. (b) The zoom-in image of (a).

Cell 2: CuDEPP/PP₁₄TFSI/graphite

To further explore the bipolar reactivity of the **CuDEPP** molecule, a Li-free rechargeable battery was configured by utilizing the **CuDEPP** as anode and graphite as cathode in the PP₁₄TFSI electrolyte (**cell 2** in Figure 6.15).

CV measurements were performed using graphite as the working electrode and the **CuDEPP** as a counter electrode in a PP₁₄TFSI electrolyte in a potential range of 4.0 – 0.0 V at various scan rates, as shown in Figure 6.23a. In the first anodic sweep at a scan rate of 5 mV s⁻¹, a pair of distinct oxidation/reduction peaks was observed at 3.51/3.14 V, which is

associated with the intercalation/de-intercalation of TFSI^- into/from the graphite electrode.^[169a,169c,170] Three additional reduction peaks at 2.57, 1.73 and 0.66 V in the first cathodic sweep indicate a multi-step electrochemical reaction correlated to a multi-stage de-intercalation of TFSI^- anions from the graphite cathode.^[169a,169c]

The galvanostatic charge-discharge tests for the $\text{CuDEPP}/\text{PP}_{14}\text{TFSI}/\text{graphite}$ cell were operated in a voltage range of 4.0 to 0.0 V at different current rates. An initial discharge capacity of 94 mAh g^{-1} was obtained, which is close to the theoretical value of the **CuDEPP** anode based on a two electrons transfer ($\text{CuDEPP} \rightarrow \text{CuDEPP}^{2-}$, 93.5 mAh g^{-1}). Good cycling reversibility and rate capability were demonstrated at current densities between 1 to 10 A g^{-1} as shown in Figure 6.23b. Notably, a reversible discharge capacity of 32 mAh g^{-1} was provided within 12 seconds at a current density of 10 A g^{-1} (106 C) with the Li-free cell, which corresponds to a high specific power of 14 kW kg^{-1} . The cycling performance of the **cell 2** was tested at a high current rate of 5 A g^{-1} (53 C) and a stable discharge capacity of 44 mAh g^{-1} was retained in 200 cycles (Figure 6.23c). The selected charge/discharge curves show an average cell potential around 2.0 V with a highly stable cyclability at a high current rate (Figure 6.23d).

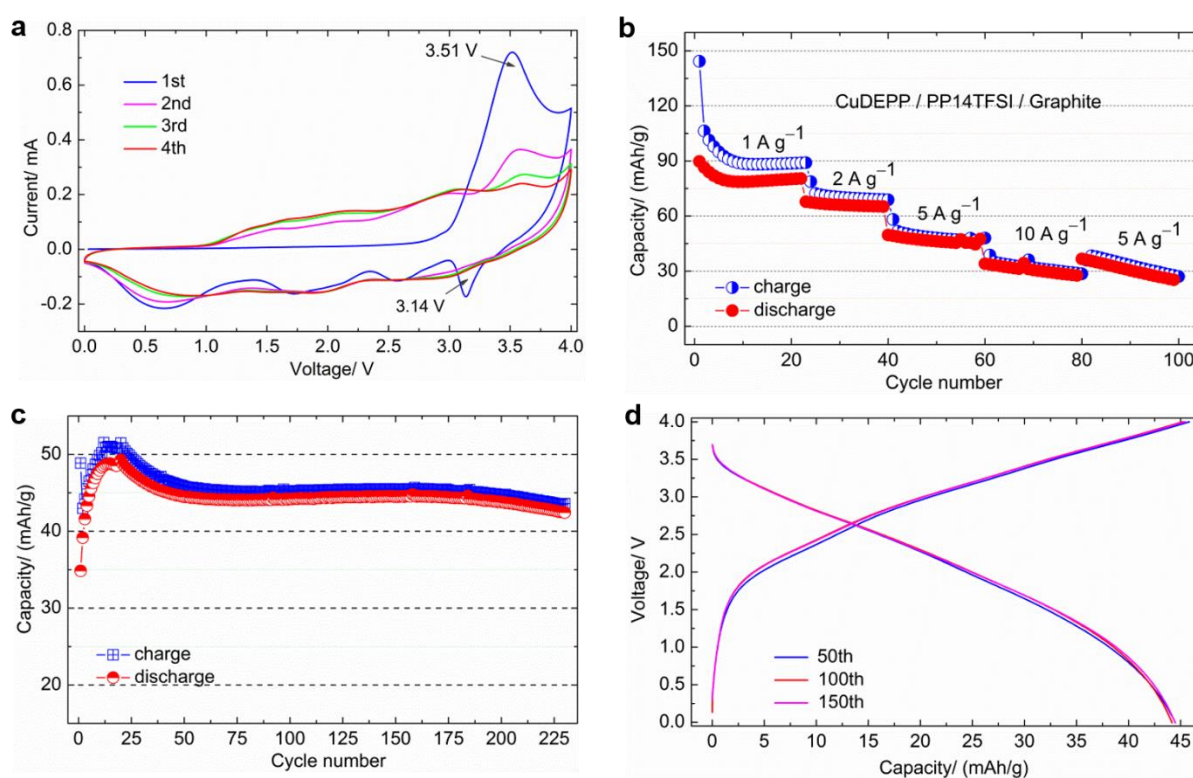


Figure 6.23 (a) Initial CV curves of the **cell 2** at a scanning rate of 5 mV s^{-1} . The sweeping voltage range was 4.0 – 0.0 V. (b) Rate performances. (c) Cycling performance at a current density of 5 A g^{-1} . (d) Selected charge/discharge profiles in (c).

The intercalation of TFSI⁻ anions into the graphite layers was verified by means of SEM, EDX and XRD. The charged/discharged graphite samples were prepared by initially charging the CuDEPP/PP₁₄TFSI/graphite cell to a cut-off voltage of 4 V and subsequently discharged to 0 V at a current rate of 200 mA g⁻¹. The SEM images and the corresponding EDX spectra of graphite cathode at various electrochemical states are shown in Figure 6.24. As shown in Figure 6.25b-f, the elemental maps reveal the uniform distribution of carbon (C), oxygen (O), fluorine (F), nitrogen (N) and sulfur (S) in graphite after charging and EDX confirms the presence of TFSI⁻ species at the graphite cathode. Moreover, XRD patterns in the charged graphite show that the characteristic of 002 diffraction peak ($2\theta = 26.4^\circ$) of graphite shifted to a low diffraction angle ($2\theta = 25.3^\circ$) due to the lattice expansion, and nearly returned to its original position ($2\theta = 26.3^\circ$) after discharge indicating a reversible intercalation/de-intercalation process of the TFSI⁻ anions in the graphite electrode (Figure 6.26).

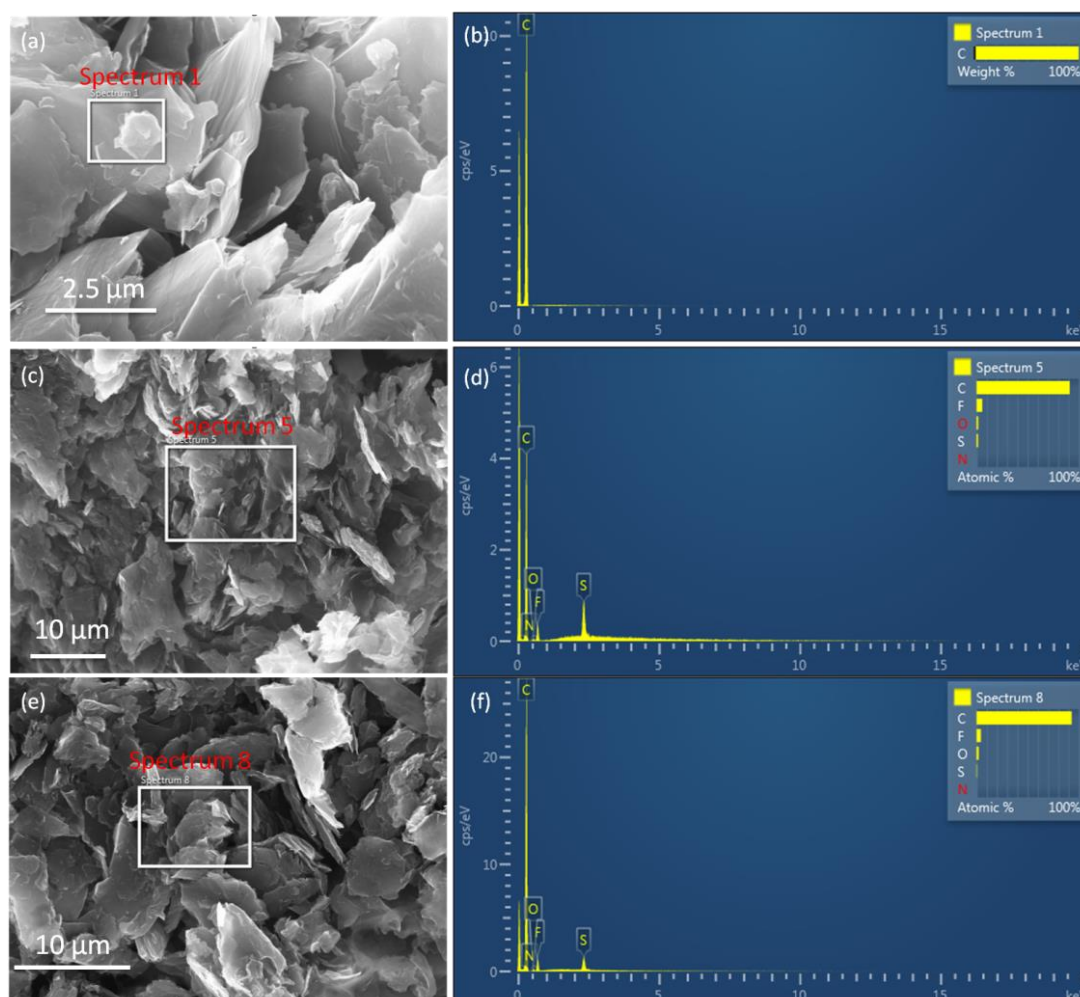


Figure 6.24 SEM images of graphite cathode of cell 2 and its corresponding EDX spectra: (a,b), as-prepared state, (c,d), charged state, and (e,f), discharged state.

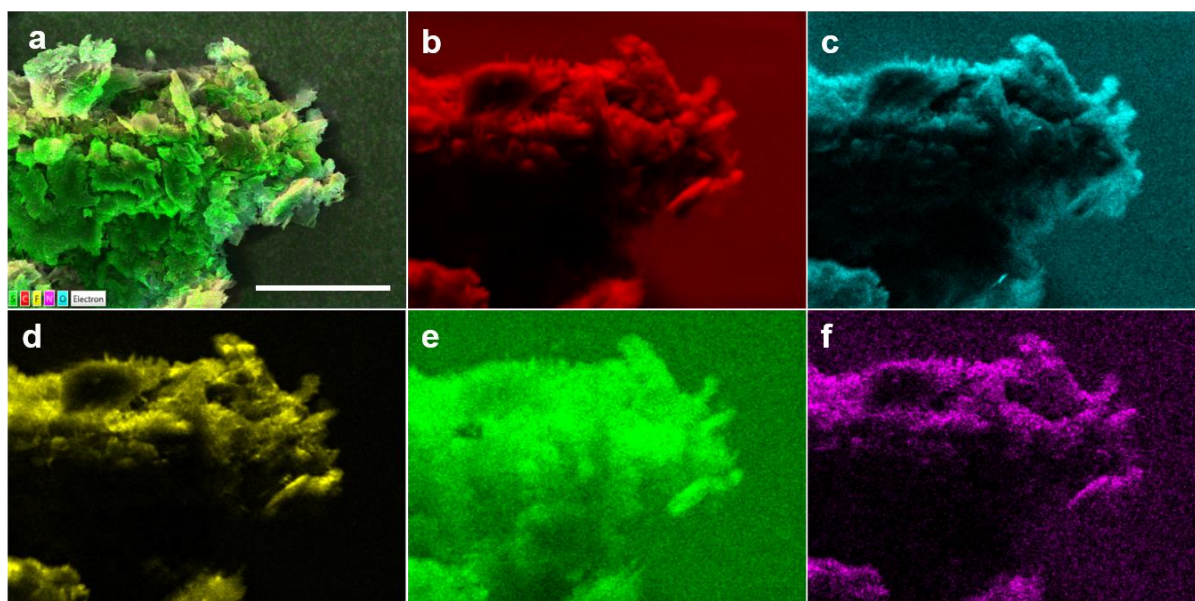


Figure 6.25 (a) SEM images of the charged graphite cathode in **cell 2**, and the scale bar represents 50 μm . (b-f) The corresponding element maps denoted as carbon, oxygen, fluorine, nitrogen and sulfur, respectively.

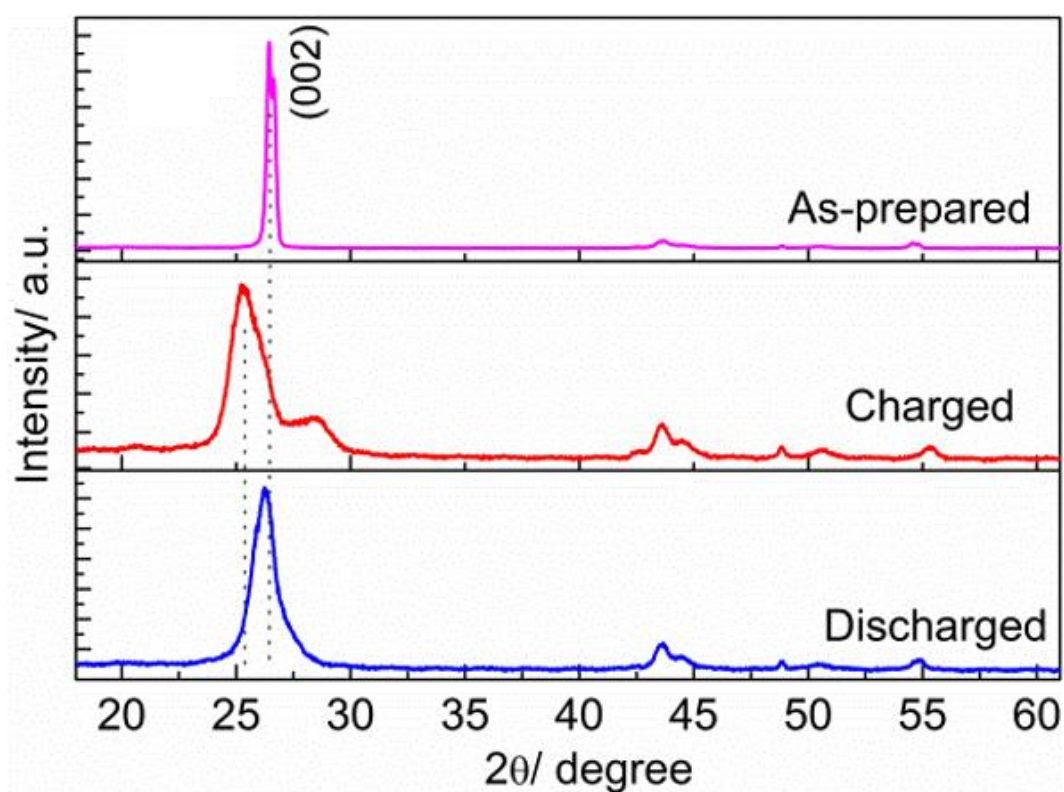


Figure 6.26 XRD patterns of the graphite cathode in the as-prepared, charged and discharged state in **cell 2**.

Cell 3: CuDEPP/LiPF₆/CuDEPP

The bipolar redox features of the **CuDEPP** molecules were further applied to a symmetric cell comprising the **CuDEPP** as both cathode and anode material in LiPF₆ electrolyte. The

working mechanism of such organic battery is schematically illustrated in Figure 6.15 (**cell 3**, CuDEPP/LiPF₆/CuDEPP). An initial capacity of 72 mAh g⁻¹ was achieved in a voltage range of 0.0 – 2.8 V corresponding to a two-electron redox process CuDEPP²⁺ → CuDEPP at the cathode and CuDEPP²⁻ → CuDEPP at the anode, respectively (shown in Figure 6.27a).

Based on the 4 electrons transfer process (CuDEPP²⁺ ↔ CuDEPP ↔ CuDEPP²⁻), the symmetric cell was also operated in a voltage range of 2.6 – (-1.8) V with high reversibility (Figure 6.27b), further proving the bipolar properties of the CuDEPP molecules although the capacity in the negative voltage range cannot be practically utilized.

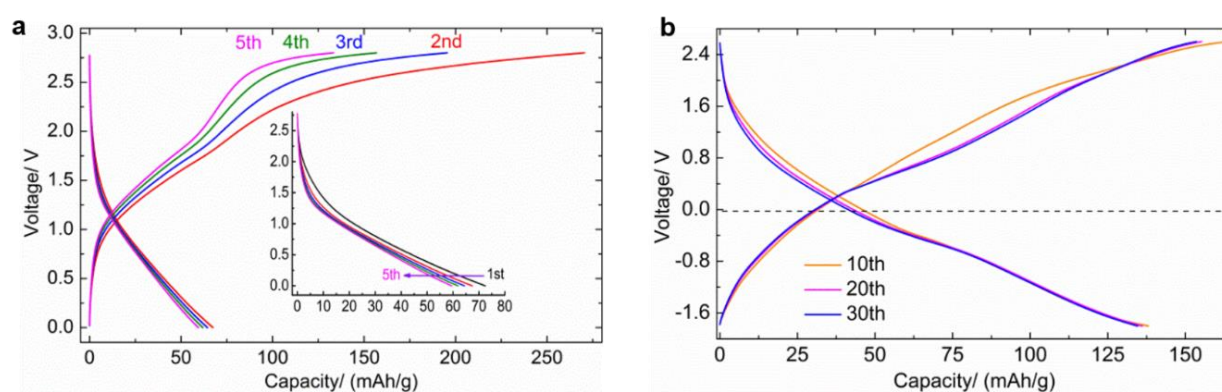


Figure 6.27 Charge/discharge profiles of the symmetric **cell 3**. (a) Selected charge-discharge curves of in the voltage range of 2.8 – 0.0 V at a current density of 200 mA g⁻¹, insert is the initial discharge curves. (b) Selected charge-discharge curves at 2.6 – (-1.8) V at a current rate of 200 mA g⁻¹.

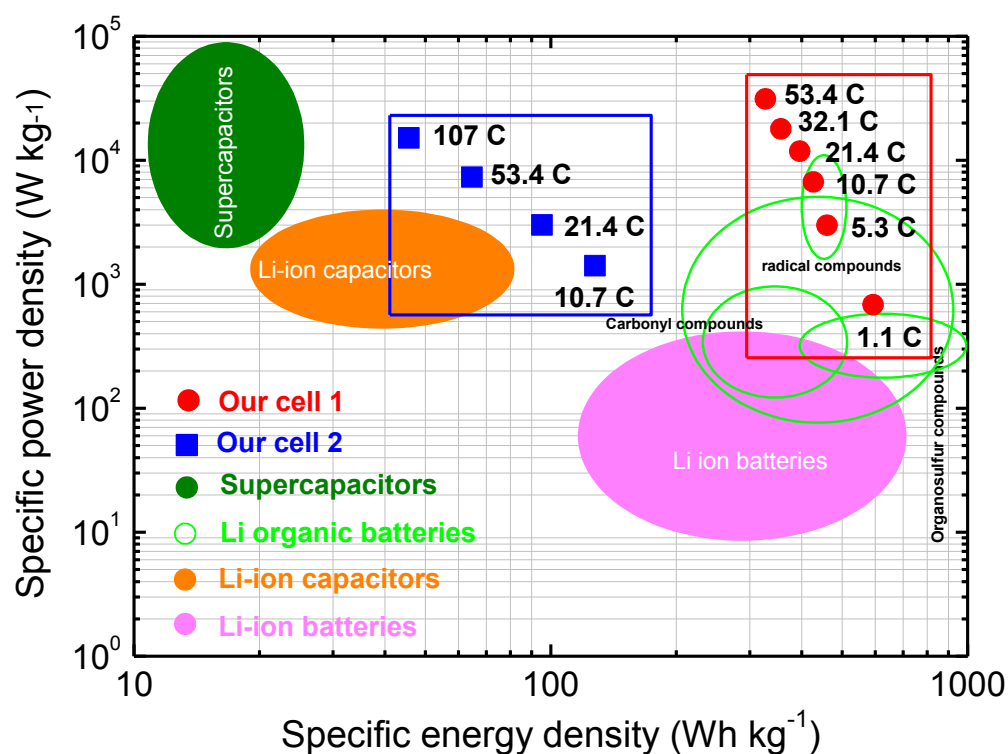


Figure 6.28 Ragone plots of the energy density and power density for various energy storage systems.

In conclusion, the porphyrin complex **CuDEPP** is a novel bipolar redox material capable of playing different roles in diverse rechargeable battery configurations. Three different cell setups were proposed and investigated. First, a Li/LiPF₆/CuDEPP cell delivered an initial discharge capacity of 210 mAh g⁻¹ and the capacity retention of approximately 85% and 60% was maintained within 2000 and 8000 cycles respectively and at a high current density of 4 A g⁻¹, thereby demonstrating excellent cyclability. Notably, a stable reversible discharge capacity of 115 mAh g⁻¹ was achieved at a current of 10 A g⁻¹ within 42 seconds, offering energy density of 345 Wh kg⁻¹ at a high specific power of 29 kW kg⁻¹. Second, **CuDEPP** served as an anode-active material in a Li free CuDEPP/PP₁₄TFSI/graphite cell, in which a discharge capacity of 94 mAh g⁻¹ was obtained at a current density of 1 A g⁻¹ and good cyclability and rate capability were demonstrated. The reversible intercalation of the TFSI⁻ anion into (from) the graphite cathode was indicated by *ex-situ* XRD and EDX spectroscopy. Finally, in an all-organic symmetric configuration, the bipolar redox reactivity of **CuDEPP** electrode enabled a four-electron transfer.

In comparison with the conventional energy storage devices currently, the cells with the **CuDEPP** electrode developed in this investigation demonstrated promising performance as shown in Figure 6.28. In contrast to the slow lithium insertion process in Li-ion batteries, higher rate capability can be achieved with the **CuDEPP** electrode. In particular, the observed specific power density of the **CuDEPP** electrode was close to that of the supercapacitors without sacrificing its high specific energy density (same order of magnitude as Li-ion battery). Therefore, the energy storage device using **CuDEPP** as electrode-active material would bridge the gap between the batteries and the supercapacitors.

Sample preparation

Commercial graphite material (Sigma-Aldrich) was dried at 200 °C for 12 h under vacuum. The ionic liquid of 1-butyl-1-methylpiperidinium bis(trifluoromethylsulfonyl)imide (PP₁₄TFSI, 99%, IoLiTech GmbH) was dried at 85 °C for 72 h under vacuum.

Electrochemical measurements

The electrolyte containing 1 M lithium hexafluorophosphate (LiPF₆) in ethylene carbonate (EC): dimethyl carbonate (DMC): propylene carbonate (PC) (EC : DMC : PC = 1 : 3 : 1 by volume ratio) was used for the Li/LiPF₆/CuDEPP and CuDEPP/LiPF₆/CuDEPP cells. The ionic liquid PP₁₄TFSI was utilized as the electrolyte for the CuDEPP/PP₁₄TFSI/graphite cell.

All the experiments were performed using a 2032 coin-type cell (Hohsen Corp., Japan) in an argon-filled glove box with a concentration of water and oxygen less than 0.1 ppm. Glass fiber filters (GF/D, Whatman) were used as separator in all cells. The **CuDEPP** electrode was

prepared by grinding a mixture of 50 wt% of **CuDEPP** active material, 40 wt% of carbon black (Sigma-Aldrich) and 10 wt% of poly(vinylidene difluoride) (PVDF) with N-methylpyrrolidone (NMP) as solvent. The graphite electrode was composed of 90 wt% of graphite and 10 wt% of PVDF. The working electrodes were made by casting the slurry on a stainless steel current collector (16 mm) and dried at 100 °C. The mass loading of **CuDEPP** electrode and graphite electrode were about 1.0 and 3.0 mg cm⁻², respectively.

Li/LiPF₆/CuTPP cell: The electrode was prepared by grinding a mixture of 50 wt% of **CuTPP** (Sigma-Aldrich), 40 wt% of carbon black (Sigma-Aldrich) and 10 wt% of poly(vinylidene difluoride) (PVDF) using N-methylpyrrolidone (NMP) as solvent. The obtained slurry was then spread on a stainless steel (16 mm) current collector and dried at 100 °C for over night. The mass loading of the active material **CuTPP** was about 1.0 mg cm⁻². Using Li foil as an anode and 1 M lithium hexafluorophosphate (LiPF₆) in ethylene carbonate (EC): dimethyl carbonate (DMC): propylene carbonate (PC) (1 : 3 : 1 in vol.), the electrochemical performance of **CuTPP** electrode was tested with a 2032 coin-type cell in an argon-filled glove box.

Charge and discharge measurements were performed with an Arbin BT2000 battery system at 25 °C. Cyclic voltammetry (CV) data was collected using a Biologic VMP-3 electrochemical workstation. For the *ex-situ* XRD, SEM, IR characterization of working electrodes, coin cells were disassembled in the glove box. The electrodes were rinsed gently in DMC to remove the residual electrolyte and then dried at 80 °C under vacuum.

7. Experimental part

7.1 Materials and equipment

THF and Et₃N were dried over sodium and CaH₂ respectively, then distilled and stored under argon. Commercially available chemicals were used as received. Thin-layer chromatography was performed on aluminum plates precoated with Merck 5735 silica gel 60 F₂₅₄. Column chromatography was performed with Merck silica gel 60 (230-400 mesh).

¹H NMR and ¹³C NMR spectra were recorded on a Bruker DRX 500 spectrometer; chemical shifts are given in ppm, referenced to residual proton resonances of the solvents.

Electro ionization mass spectrometry (EI-MS) data were got in a Thermo Scientific TRACE 1300 GC with ISQ System.

Electro spray ionization mass spectrometry (ESI-MS) was acquired with a Bruker micrOTOF-Q II spectrometry.

Matrix-assisted laser desorption/ionization time-of-flight (MALDI-ToF) mass data were acquired with a Voyager-DE PRO Bio spectrometry work station without additional matrix compound.

Infrared spectra were measured in KBr pellets (MAGNA FTIR 750, Nicolet) in the 4000-400 cm⁻¹ region. IR spectra of **GDY 6** nanofilms on Al foil were obtained on a Bruker FTIR Tensor 37 via the attenuated total reflection method (ATR).

Raman spectra were recorded on a Renishaw inVia Raman Microscope using a 532 nm argon ion laser.

Elemental analyses were carried out in a Vario Micro Cube.

UV-vis spectra of the samples were obtained on an UV-vis spectrophotometer (Cary 500 Scan). The photocatalytic degradation of the MB dye was monitored by measuring the real-time UV-vis spectra of the catalytic systems using a Cary 500 Scan spectrometer.

Powder X-ray diffraction (XRD) patterns were recorded in transmission geometry using a STOE STADI-P diffractometer (operated at 40 kV, 40 mA).

Thermogravimetric differential scanning calorimetry (TGA-DSC) measurements were conducted by a SETARAM SENSYS Evo thermal analyzer under air flow (20 mL min⁻¹) with a heating rate of 5 °C min⁻¹.

Scanning electron microscopy (SEM) measurements were carried out using a ZEISS LEO Gemini 1530 system.

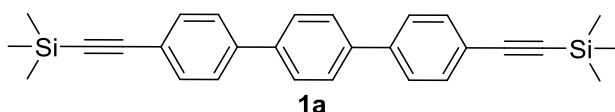
Energy dispersive X-ray spectroscopy (EDX) was measured with an Oxford Instruments X-act energy dispersive spectrometer that was attached to the ZEISS LEO Gemini 1530 system.

Atomic force microscopy (AFM) measurements were conducted using MultiMode™ SPM system.

Transmission electron microscopy (TEM) measurements were performed using an aberration-corrected (image) FEI Titan 80-300 operated at 300 kV acceleration voltage, equipped with a Gatan US1000 CCD camera and a Gatan Tridem 863 energy filter. To prepare TEM samples, 10 μL of GDY **6** nanofilms suspended in methanol solution was dropped on a carbon coated Cu grid.

7.2 Syntheses of the compounds

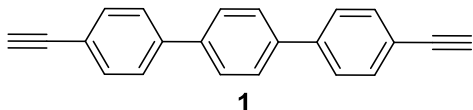
4,4''-bis(trimethylsilylethynyl)-1,1':4',1''-terphenyl (**1a**)^[221]



4,4''-Diiodo-1,1':4',1''-terphenyl (1.446 g, 3 mmol), Pd(PPh₃)₂Cl₂ (0.105 g, 0.15 mmol), CuI (0.030 g, 0.15 mmol) and ethynyltrimethylsilane (0.91 mL, 6.6 mmol) were added into the mixture of THF (60 mL) and triethylamine (30 mL) under an argon atmosphere. The reaction mixture was heat up at 60 °C for 3 hours, and then the solution was poured into 150 mL water and extracted by DCM. Solvents were removed in vacuum and the residue was purified by column chromatography on silica gel (hexane:DCM = 8:1) affording light yellow crystalline solid of target product **1a** (1.134 g, yield 89%).

¹H NMR (500 MHz, CDCl₃) δ/ppm 7.70 (s, 4H), 7.59 (q, *J* = 8.46, 8.46, 8.45 Hz, 8H), 0.30 (s, 18H). ¹³C NMR (126 MHz, CDCl₃) δ/ppm 140.46, 139.92, 132.48, 127.45, 126.74, 122.21, 105.00, 95.09, 0.02.

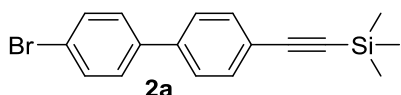
4,4''-diethynyl-1,1':4',1''-terphenyl (**1**)^[220b]



Compound **1a** (1.134 g, 2.69 mmol) and K₂CO₃ (1.467 g) were added into the mixture of 60 mL THF and 15 mL methanol under an argon atmosphere at room temperature, and stirred for 2 h. The reaction mixture was poured into 150 mL water and then extracted by DCM; solvents were removed in vacuum and the residue was purified by column chromatography on silica gel (hexane:DCM = 5:1). After further recrystallization from ethyl acetate, a pale-creamy crystalline product **1** (0.662 g, yield 88%) was obtained.

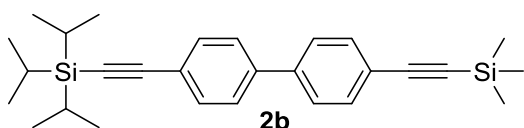
¹H NMR (500 MHz, CDCl₃) δ/ppm 7.70 (s, 4H), 7.66-7.59 (m, 8H), 3.17 (s, 2H). ¹³C NMR (126 MHz, CDCl₃) δ/ppm 140.85, 139.58, 132.66, 127.52, 126.89, 121.20, 83.51, 77.95.

IR (KBr, cm⁻¹): 3444, 3283 (C-H), 2104 (C≡C), 1911, 1487, 1400, 1263, 1149, 1113, 1001, 817, 659, 640, 623, 519. MALDI-ToF calculated for C₂₂H₁₄: [M]⁺, *m/z*, 278.1; found: 278.1. Elemental analysis calculated (%) for C₂₂H₁₄: C 94.93, H 5.07; found: C 94.35, H 5.08.

4-trimethylsilylethynyl-4'-bromo-1,1'-biphenyl (2a)^[238]

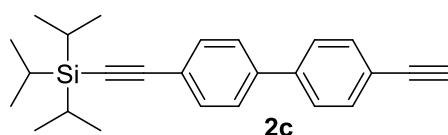
4-Bromo-4'-iodo-1,1'-biphenyl (0.718 g, 2 mmol), Pd(PPh₃)₂Cl₂ (0.070 g, 0.1 mmol), CuI (0.040 g, 0.2 mmol) and ethynyltrimethylsilane (0.3 mL, 2.1 mmol) were added into the mixture of THF (20 mL) and triethylamine (15 mL) under an argon atmosphere. The reaction mixture was stirred at room temperature for 24 hours, and then the solution was poured into 150 mL water and extracted by DCM. Solvents were removed in vacuum and the residue was purified by column chromatography on silica gel (hexane:DCM = 10:1) affording white solid of target product **2a** (0.417 g, yield 63%).

¹H NMR (500 MHz, CDCl₃) δ/ppm 7.59 (d, *J* = 8.46 Hz, 2H), 7.56 (d, *J* = 8.34 Hz, 2H), 7.52 (d, *J* = 8.34 Hz, 2H), 7.47 (d, *J* = 8.47 Hz, 2H), 0.30 (s, 9H). ¹³C NMR (126 MHz, CDCl₃) δ/ppm 139.90, 139.22, 132.53, 131.98, 128.61, 126.67, 122.47, 121.98, 104.76, 95.28, 0.01.

4-triisopropylsilylethynyl-4'-trimethylsilylethynyl-1,1'-biphenyl (2b)^[239]

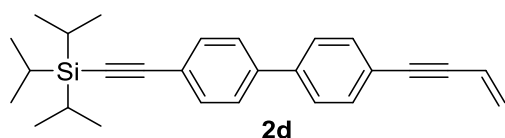
Compound **2a** (0.329 g, 1 mmol) Pd(PPh₃)₂Cl₂ (0.035 g, 0.05 mmol), CuI (0.020 g, 0.1 mmol) and ethynyltriisopropylsilane (0.3 mL, 1.2 mmol) were added into 15 mL diisopropylamine under an argon atmosphere. The reaction mixture was heat up at 60 °C for 24 hours, and then the solution was poured into 150 mL water and extracted by DCM. Solvents were removed in vacuum and the residue was purified by column chromatography on silica gel (hexane:DCM = 10:1) affording white solid of target product **2b** (0.385 g, yield 89%).

¹H NMR (500 MHz, CDCl₃) δ/ppm 7.54-7.56 (m, 8H), 1.17 (s, 21H), 0.29 (s, 9H). ¹³C NMR (126 MHz, CDCl₃) δ/ppm 140.30, 140.07, 132.53, 132.46, 131.97, 128.60, 126.74, 126.66, 122.86, 122.39, 106.81, 104.85, 95.21, 91.69, 18.70, 11.34, -0.01.

4-triisopropylsilylethynyl-4'-ethynyl-1,1'-biphenyl (2c)^[239]

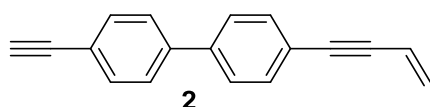
Compound **2b** (0.385 g, 0.89 mmol) and K_2CO_3 (0.414 g, 3 mmol) were added into the mixture of 15 mL THF and 5 mL methanol under an argon atmosphere at room temperature, and stirred at room temperature for 2 h. The reaction mixture was poured into 100 mL water and then extracted by DCM; solvents were removed in vacuum and the residue was purified by column chromatography on silica gel (hexane:DCM = 10:1) affording white powder of compound **2c** (0.253 g, yield 78%).

1H NMR (500 MHz, $CDCl_3$) δ /ppm 7.54-7.60 (m, 8H), 3.16 (s, 1H) 1.17 (s, 21H). ^{13}C NMR (126 MHz, $CDCl_3$) δ /ppm 140.00, 140.73, 132.63, 132.56, 126.89, 126.79, 122.97, 121.34, 106.76, 91.77, 83.44, 78.02, 18.70, 11.34.

4-(but-3-en-1-ynyl)-4'-triisopropylsilylethynyl-1,1'-biphenyl (2d)^[186c]

$Pd(PPh_3)_4$ (0.014 g, 0.012 mmol), CuI (0.008 g, 0.04 mmol) were added into 15 mL diisopropylamine under an argon atmosphere and cooled to 0 °C. Then compound **2c** (0.215 g, 0.6 mmol) and 1 mol/L vinyl bromide in tetrahydrofuran (0.84 mL, 0.84 mmol) were added to the mixture. The reaction mixture was stirred at room temperature for 6 hours, and then the solution was poured into 150 mL water and extracted by DCM. Solvents were removed in vacuum and the residue was purified by column chromatography on silica gel (hexane:DCM = 5:1) affording white solid of target product **2d** (0.144 g, yield 62%).

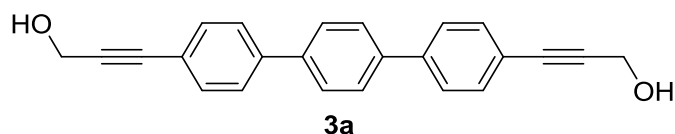
1H NMR (500 MHz, $CDCl_3$) δ /ppm 7.62-7.51 (m, 8H), 6.07 (dd, $J = 17.52, 11.17$ Hz, 1H), 5.79 (dd, $J = 17.53, 1.97$ Hz, 1H), 5.60 (dd, $J = 11.18, 1.75$ Hz, 1H), 1.17 (s, 1H). ^{13}C NMR (126 MHz, $CDCl_3$) δ /ppm 140.14, 140.08, 132.56, 132.08, 128.59, 126.88, 126.73, 122.86, 122.42, 117.19, 106.82, 91.70, 89.80, 89.04, 18.71, 11.35.

4-(but-3-en-1-ynyl)-4'-ethynyl-1,1'-biphenyl (2)

Compound **2d** (0.144 g, 0.37 mmol) was deprotected in 15 mL THF in presence of TBAF (0.252 g, 0.8 mmol, TBAF = tetrabutylammonium fluoride) under an argon atmosphere at 0 °C for 0.5 h. Then the solution was poured into 150 mL water and extracted by DCM. Solvents were removed in vacuum and the residue was purified by column chromatography on silica gel (hexane:DCM = 5:1) affording white solid of target product **2** (0.060 g, yield 71%).

¹H NMR (500 MHz, CDCl₃) δ/ppm 7.62-7.51 (m, 8H), 6.07 (dd, *J* = 17.53, 11.18 Hz, 1H), 5.79 (dd, *J* = 17.53, 2.00 Hz, 1H), 5.60 (dd, *J* = 11.18, 2.00 Hz, 1H), 3.17 (s, 1H). ¹³C NMR (126 MHz, CDCl₃) δ/ppm 140.64, 139.96, 132.65, 132.10, 127.14, 126.92, 126.87, 122.56, 121.37, 117.17, 89.74, 89.11, 83.44, 78.07.

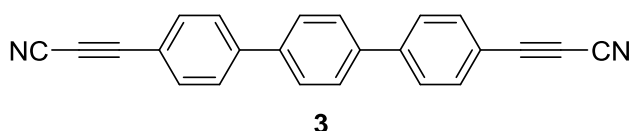
IR (KBr, cm⁻¹): 3287, 3271, 3036, 3008, 2924, 2853, 2216, 2184, 2106, 1918, 1659, 1603, 1490, 1394, 1253, 1111, 1004, 967, 923, 859, 825, 676, 660, 630, 566, 540. ESI-MS calculated for C₁₈H₁₂: [M]⁺, *m/z*, 228.09; found: 228.10.

3,3'-([1,1':4',1''-terphenyl]-4,4''-diyl)bis(prop-2-yn-1-ol) (3a)

Under an argon atmosphere 4,4''-diiodo-1,1':4',1''-terphenyl (192 mg, 1.0 mmol), prop-2-yn-1-ol (140 mg, 2.5 mmol), Pd(PPh₃)₂Cl₂ (40 mg), CuI (20 mg) were added to a mixture of 10 mL pyrrolidine and 10 ml THF and heated at 60 °C for 36 h. Hexane (50 mL) was added, and the residue was filtered off and dissolved in THF. The solution was chromatographed on silica gel using dichloromethane: ethyl acetate = 5:1 as eluent with a short column affording 240 mg of **3a** as yellow solid (yield 71%).

¹H NMR (500 MHz, DMSO-d₆): δ/ppm 4.34 (d, *J* = 5.96 Hz, 4H), 5.37 (t, *J* = 5.96, 5.96 Hz, 2H), 7.54 (d, *J* = 8.37 Hz, 4H), 7.77 (d, *J* = 8.39 Hz, 4H), 7.82 (s, 4H). ¹³C NMR (126 MHz, DMSO-d₆): δ/ppm 139.21, 138.43, 131.88, 127.20, 126.74, 121.62, 90.79, 83.39, 49.48.

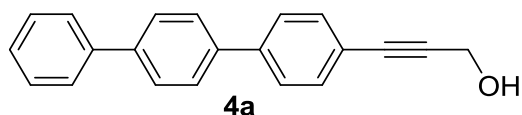
IR (KBr, cm⁻¹): 3383, 2924, 2184(C≡C), 1600, 1489, 1399, 1358, 1262, 1028, 1002, 952, 817, 516. MALDI-ToF calculated for C₂₄H₁₈O₂: [M]⁺, *m/z*, 338.1; found: 338.0.

3,3'-([1,1':4',1''-terphenyl]-4,4''-diyl)dipropiolonitrile (3**)**^[199]

A 2 M solution of ammonia in 2-propanol (1.8 mL, 3.2 mmol) and anhydrous magnesium sulfate (1.5 g, 12.8 mmol) were added to a stirred solution of compound **3a** (203 mg, 0.6 mmol) in THF (20 mL). Then activated manganese dioxide (1.1 g, 12.8 mmol) was added. The resulting mixture was stirred at room temperature for 2 hours and then diluted with dichloromethane (20 mL). The mixture was filtered through Celite, and washed well with dichloromethane and the combined filtrates were concentrated in a vacuum. The residue was purified by column chromatography on silica gel (hexane: dichloromethane = 2:1) affording 51 mg (26%) of **3** as light yellow solid.

¹H NMR (500 MHz, CDCl₃) δ /ppm 7.69-7.75 (m, 12H). ¹³C NMR (126 MHz, CDCl₃) δ /ppm 143.69, 139.46, 134.11, 127.85, 127.41, 116.60, 105.54, 82.86, 63.95.

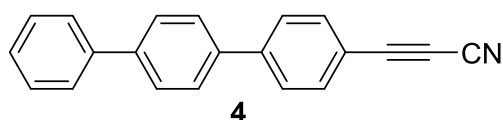
IR (KBr, cm⁻¹): 3446, 2260(C≡N), 2141(C≡C), 1598, 1486, 1396, 1271, 1187, 1003, 867, 819, 724, 523. MALDI-ToF calculated for C₂₄H₁₂N₂: [M]⁺, m/z, 328.1; found: 328.1. Elemental analysis calculated (%) for C₂₄H₁₂N₂: C 87.79, H 3.68, N 8.53; found: C 87.63, H 3.45, N 8.81.

3-([1,1':4',1''-terphenyl]-4-yl)prop-2-yn-1-ol (4a**)**

4-Bromo-1,1':4',1''-terphenyl (412 mg, 1.5 mmol), prop-2-yn-1-ol (126 mg, 2.25 mmol), Pd(PPh₃)₂Cl₂ (50 mg), CuI (30 mg), PPh₃ (40 mg) were added to a mixture of 30 mL triethylamine and 15 mL THF and heated under reflux for 10 h under an argon atmosphere [49]. Hexane (50 mL) was added, and the residue was filtered off and dissolved in dichloromethane. The solution was chromatographed on silica gel (hexane: dichloromethane = 1:1) affording 120 mg of **4a** as white needle crystals (yield 28%).

¹H NMR (500 MHz, CDCl₃): δ /ppm 4.56 (d, 2H), 7.36-7.74 (m, 13H). ¹³C NMR (126 MHz, CDCl₃): δ /ppm 140.75, 140.58, 140.54, 139.12, 132.20, 128.87, 127.61, 127.49, 127.39, 127.06, 126.89, 121.49, 87.90, 85.66, 51.79.

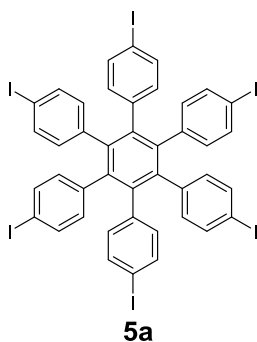
IR (KBr, cm⁻¹): 3430, 2924, 2184(C≡C), 1485, 1401, 1027, 953, 826, 764, 730, 691, 419. MALDI-ToF calculated for C₂₁H₁₆O: [M]⁺, m/z, 284.1; found: 284.0.

3-([1,1':4',1''-terphenyl]-4-yl)propionitrile (4)^[199]

A 2 M solution of ammonia in 2-propanol (0.8 mL, 1.6 mmol) and anhydrous magnesium sulfate (0.768 g, 6.4 mmol) were added to a stirred solution of compound **4a** (114 mg, 0.4 mmol) in THF (20 mL). Then activated manganese dioxide (557 mg, 6.4 mmol) was added. The resulting mixture was stirred at room temperature for 2 hours and then diluted with dichloromethane (20 mL). The mixture was filtered through Celite, washed well with dichloromethane and the combined filtrates were concentrated in a vacuum. The residue was purified by column chromatography on silica gel (hexane: dichloromethane = 2:1) affording light yellow solid compound **4** (37 mg, 33%).

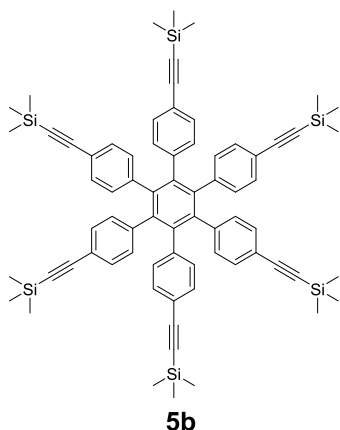
¹H NMR (500 MHz, CDCl₃): δ /ppm 7.41 (t, $J = 7.38, 7.38$ Hz, 1H), 7.50 (t, $J = 7.64, 7.64$ Hz, 2H), 7.64-7.74 (m, 10H). ¹³C NMR (126 MHz, CDCl₃): δ /ppm 144.19, 141.44, 140.25, 138.16, 134.06, 128.93, 127.79, 127.72, 127.56, 127.34, 127.08, 116.16, 105.61, 83.11, 63.79.

IR (KBr, cm⁻¹): 3446, 2263(C≡N), 2143(C≡C), 1599, 1483, 1395, 1004, 825, 767, 734, 698, 544. MALDI-ToF calculated for C₂₁H₁₃N: [M]⁺, m/z, 279.1; found: 279.0. Elemental analysis calculated (%) for C₂₁H₁₃N: C 90.29, H 4.69, N 5.01; found: C 90.24, H 4.91, N 5.07.

hexakis(4-iodophenyl)benzene (5a)^[208]

Hexaphenylbenzene (0.214 g, 0.4 mmol), [bis(trifluoroacetoxy)iodo]benzene (1.075 g, 2.5 mmol) and iodine (0.635 g, 2.5 mmol) were added into the 25 mL dry DCM under an argon atmosphere. The reaction mixture was stirred at room temperature for 24 hours at dark. Then the solution was poured into 100 mL Na₂SO₃ aqueous solution and extracted by DCM. After solvents were removed in vacuum, the residue was further recrystallized from the mixture of DCM and hexane, affording white solid of target product **5a** (0.435 g, yield 84%).

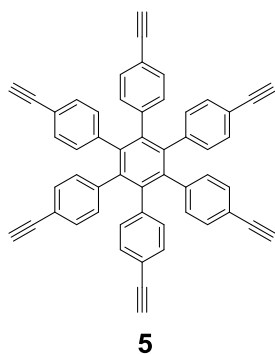
¹H NMR (500 MHz, CDCl₃) δ /ppm 7.27 (d, $J = 8.33$ Hz, 12H), 6.49 (d, $J = 8.33$ Hz, 12H). ¹³C NMR (126 MHz, CDCl₃) δ /ppm 139.49, 138.99, 136.35, 132.81, 91.98.

hexakis[4-(trimethylsilylethynyl)phenyl]benzene (5b)^[240]

Compound **5a** (0.258 g, 0.2 mmol), ethynyltrimethylsilane (0.21 mL, 1.5 mmol), Pd(PPh₃)₂Cl₂ (0.014 g, 0.02 mmol) and CuI (0.008 g, 0.04 mmol) were added into the mixture of THF (15 mL) and triethylamine (15 mL) under an argon atmosphere. The mixture was stirred at 60 °C for 18 hours. Then the solution was poured into 150 mL ammonium chloride aqueous solution and extracted by DCM. Solvents were removed in vacuum and the residue was purified by column chromatography on silica gel (hexane:DCM = 4:1) affording white product of **5b** (0.150 g, yield 67%).

¹H NMR (500 MHz, CDCl₃) δ/ppm 7.00 (d, *J* = 8.23 Hz, 12H), 6.70 (d, *J* = 8.23 Hz, 12H), 0.23 (s, 54H). ¹³C NMR (126 MHz, CDCl₃) δ/ppm 140.10, 139.81, 130.92, 130.82, 120.34, 105.24, 94.12, -0.07.

IR (KBr, cm⁻¹): 2959, 2899, 2157(C≡C), 1507, 1409, 1250, 1223, 1020, 867, 841, 760, 700, 630, 569. MALDI-ToF calculated for C₇₂H₇₈Si₆: [M]⁺, *m/z*, 1110.5; found: 1110.4. Elemental analysis calculated (%) for C₇₂H₇₈Si₆: C 77.77, H 7.07; found: C 77.70, H 7.25.

hexakis[4-(ethynyl)phenyl]benzene (5)^[240]

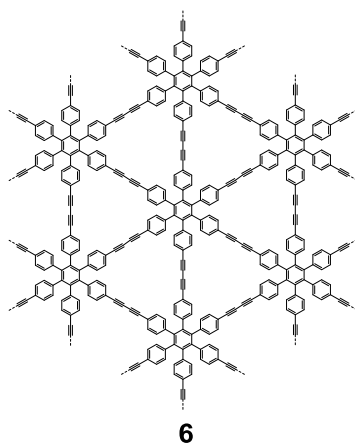
Compound **5b** (0.111 g, 0.1 mmol) was deprotected in 50 mL THF in presence of TBAF (0.378 g, 1.2 mmol) under an argon atmosphere at room temperature for 0.5 h. The reaction mixture was poured into 100 mL water and then extracted by DCM. Solvents were evaporated

under reduced pressure and the residue was purified by column chromatography on silica gel (hexane:DCM = 3:1) affording white product of **5** (0.062 g, yield 91%).

^1H NMR (500 MHz, CDCl_3) δ /ppm 7.05 (d, $J = 8.12$ Hz, 12H), 6.74 (d, $J = 8.14$ Hz, 12H), 3.00 (s, 6H). ^{13}C NMR (126 MHz, CDCl_3) δ /ppm 140.30, 139.84, 131.06, 130.99, 119.51, 83.58, 77.25.

IR (KBr, cm^{-1}): 3293(CC-H), 3035, 2108($\text{C}\equiv\text{C}$), 1917, 1684, 1605, 1507, 1389, 1231, 1137, 1108, 1019, 869, 841, 795, 776, 739, 666, 641, 615, 555, 527. MALDI-ToF calculated for $\text{C}_{54}\text{H}_{30}$: $[\text{M}]^-$, m/z , 677.2; found: 677.1. Elemental analysis calculated (%) for $\text{C}_{72}\text{H}_{78}\text{Si}_6$: C 95.55, H 4.45; found: C 95.08, H 4.60.

Graphdiyne **6**

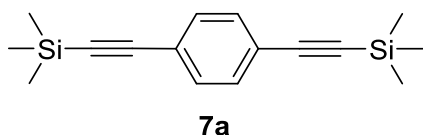


Electropolishing of Cu foils: 0.025 mm thick Cu foil (3×5 cm, annealed, uncoated, 99.8%, Alfa Aesar,) used as an anode, was electropolished in a homemade electrochemistry cell with a large stainless steel plate as the cathode; the electropolishing solution contained 200 mL of water, 100 mL of ethanol, 20 mL of isopropyl alcohol, 100 mL of orthophosphoric acid, and 2 g of urea. Supported by an alligator clip, the Cu foil was placed into the solution. A laboratory power supply (EA-PS 3032-10 B) was used to supply constant voltage/current, and a voltage in 4.0 V was applied for 2 min (current was around 2.4 A). After electropolishing, the Cu foil was rinsed with deionized water, further washed with ethanol, and then blow-dried.

The treated Cu foils were added to the mixture of 20 mL toluene, 5 mL TMEDA and 0.3 mL ammonium hydroxide (NH_3 is 30% mass fraction in water) in a flask. 2 mg **5** was dissolved with 10 ml toluene. After 1 min ultrasonication, the solution was added slowly in 20 hours (0.5 mL/h) into the mixed solution mentioned above. Then the mixture was stirred under an ambient atmosphere at 60 °C for 2 days at dark. After reaction, GDY nanofilms **6** were successfully grown on the surface of Cu foils through a homo-coupling reaction. Finally

the Cu foils were washed with methanol and DCM to remove the Cu salts, unreacted monomer and oligomer. After dissolve the Cu foils in 0.5 mol/L $(\text{NH}_4)_2\text{S}_2\text{O}_8$ solution or 1 mol/L HCl solution, the intact films were transferred deionized water and methanol sequently, giving clear a bit yellow GDY nanofilms **6**.

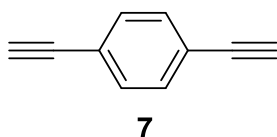
1,4-bis(trimethylsilylethynyl)benzene (7a)^[220a]



1,4-Diiodobenzene (0.330 g, 1 mmol), $\text{Pd}(\text{PPh}_3)_2\text{Cl}_2$ (0.035 g, 0.05 mmol), CuI (0.010 g, 0.05 mmol) and ethynyltrimethylsilane (0.3 mL, 2.2 mmol) were added into the mixture of THF (20 mL) and triethylamine (10 mL) under an argon atmosphere. The reaction mixture was heat up at 60 °C for 3 hours, and then the solution was poured into 150 mL water and extracted by DCM. Solvents were removed in vacuum and the residue was purified by column chromatography on silica gel (hexane:DCM = 8:1) affording light yellow crystalline solid of target product of **7a** (0.257 g, yield 95%).

^1H NMR (500 MHz, CDCl_3) δ /ppm 7.41 (s, 4H), 0.27 (s, 18H). ^{13}C NMR (126 MHz, CDCl_3) δ /ppm 131.76, 123.14, 104.56, 96.32, -0.08.

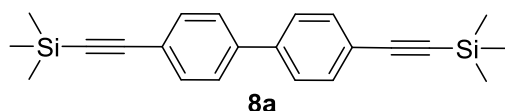
1,4-diethynylbenzene (7)^[220a]



Compound **7a** (0.150 g, 0.55 mmol) and K_2CO_3 (0.300 g) were added into the mixture of 20 mL THF and 5 mL methanol under an argon atmosphere at room temperature, and stirred for 2 h. The reaction mixture was poured into 100 mL water and then extracted by DCM; solvents were removed in vacuum and the residue was purified by column chromatography on silica gel (hexane:DCM = 5:1) affording white powder of compound **7** (0.049 g, yield 71%).

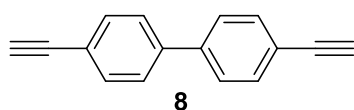
^1H NMR (500 MHz, CDCl_3) δ /ppm 7.46 (s, 4H), 3.19 (s, 2H). ^{13}C NMR (126 MHz, CDCl_3) δ /ppm 132.03, 122.56, 83.03, 79.09.

IR (KBr, cm^{-1}): 3453, 3264 (C–H), 2104 (C≡C), 1919, 1792, 1672, 1495, 1404, 1369, 1254, 1105, 1016, 964, 835, 707, 676, 640, 621, 547, 494. EI-MS calculated for C_{10}H_6 : $[\text{M}]^+$, m/z, 126.05; found: 126.06. Elemental analysis calculated (%) for C_{10}H_6 : C 95.21, H 4.79; found: C 94.99, H 4.89.

4,4'-bis(trimethylsilylethynyl)biphenyl (8a)^[220a]

Following the same synthetic procedure of **7a**, from 4,4'-diiodobiphenyl (0.406 g, 1 mmol) a white solid as target product **8a** (0.342 g, yield 99%) was obtained.

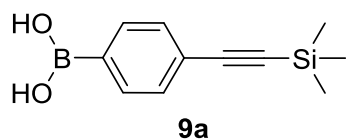
¹H NMR (500 MHz, CDCl₃) δ/ppm 7.55 (s, 8H), 0.29 (s, 18H). ¹³C NMR (126 MHz, CDCl₃) δ/ppm 140.20, 132.46, 126.74, 122.42, 104.84, 95.24, -0.01.

4,4'-diethynyl-1,1'-biphenyl (8)^[220a]

Following the same synthetic procedure of **7**, from **8a** (0.173 g, 0.5 mmol) a white solid of **8** (0.067 g, yield 66%) was obtained.

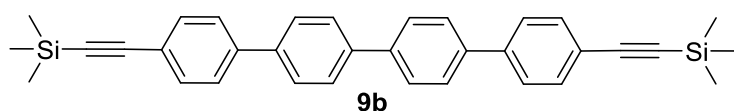
¹H NMR (500 MHz, CDCl₃) δ/ppm 7.59 (q, *J* = 8.45, 8.44, 8.44 Hz, 8H), 3.18 (s, 2H). ¹³C NMR (126 MHz, CDCl₃) δ/ppm 140.55, 132.67, 126.93, 121.51, 83.41, 78.14.

IR (KBr, cm⁻¹): 3465, 3273 (C-H), 2106 (C≡C), 1918, 1603, 1488, 1393, 1251, 1107, 1003, 968, 857, 825, 678, 658, 647, 632, 565, 546, 513, 440. MALDI-ToF calculated for C₁₆H₁₀: [M]⁺, *m/z*, 202.1; found: 202.0. Elemental analysis calculated (%) for C₁₆H₁₀: C 95.02, H 4.98; found: C 94.83, H 4.87.

4-(trimethylsilylethynyl)phenylboronic acid (9a)^[241]

4-Iodophenylboronic acid (2.48 g, 10 mmol), Pd(PPh₃)₂Cl₂ (0.350 g, 0.5 mmol), CuI (0.191 g, 1 mmol) and ethynyltrimethylsilane (1.45 mL, 10.5 mmol) were added into the mixture of THF (50 mL) and triethylamine (50 mL) under an argon atmosphere. The reaction mixture was stirred at room temperature for 24 hours, and then the solution was dried under vacuum. The residue was purified by flash column chromatography on silica gel (hexane:DCM = 1:1) affording light gray solid of target product **9a** (1.55 g, yield 70%).

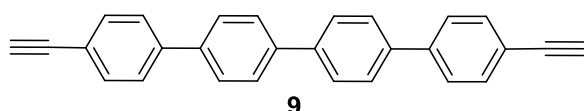
¹H NMR (500 MHz, CDCl₃) δ/ppm 8.17 (d, *J* = 8.14 Hz, 2H), 7.61 (d, *J* = 8.14 Hz, 2H), 0.31 (s, 9H). ¹³C NMR (126 MHz, CDCl₃) δ/ppm 135.36, 133.26, 131.42, 127.39, 104.93, 96.76, -0.06.

4,4'''-bis(trimethylsilylethynyl)-1,1':4',1'':4'',1'''-quaterphenyl (9b)^[221]

Compound **9a** (0.526 g, 2.4 mmol), 4,4'-diiodobiphenyl (0.406 g, 1 mmol), Pd₂(dba)₃ (0.092 g, 0.1 mmol, dba = (1*E*,4*E*)-1,5-diphenyl-1,4-pentadien-3-one), SPhos (0.082 g, 0.2 mmol, SPhos = 2-dicyclohexylphosphino-2',6'-dimethoxybiphenyl) and K₃PO₄ (2.123 g, 10 mmol) were added into 100 ml dioxane under an argon atmosphere. The reaction mixture was heat up at 90 °C for 48 hours, and then the solution was poured into 150 mL water. The solid formed was collected by filtration and washed by methanol, acetone and hexane sequentially. The solid was further recrystallized from DCM and hexane, affording light yellow solid of target product **9b** (0.160 g, yield 32%).

¹H NMR (500 MHz, CDCl₃) δ/ppm 7.73 (q, *J* = 8.43, 8.43, 8.42 Hz, 8H), 7.60 (dd, *J* = 21.59, 8.35 Hz, 8H), 0.30 (s, 18H). ¹³C NMR (126 MHz, CDCl₃) δ/ppm 140.55, 139.81, 139.36, 132.48, 127.46, 126.73, 122.15, 104.96, 95.05, 0.01.

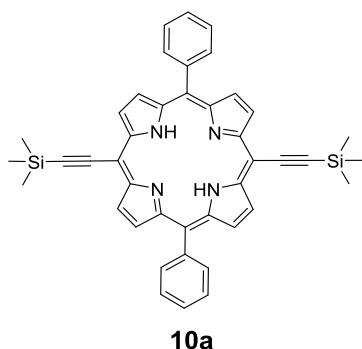
IR (KBr, cm⁻¹): 3034, 2957, 2899, 2157(C≡C), 1486, 1401, 1252, 1002, 865, 845, 814, 759, 725, 642, 515. MALDI-ToF calculated for C₃₄H₃₄Si₂: [M]⁺, *m/z*, 498.2; found: 498.2. Elemental analysis calculated (%) for C₃₄H₃₄Si₂: C 81.87, H 6.87; found: C 81.72, H 6.89.

4,4'''-diethynyl-1,1':4',1'':4'',1'''-quaterphenyl (9)

Compound **9b** (0.101 g, 0.25 mmol) was deprotected in 50 mL DCM in presence of TBAF (0.315 g, 1 mmol) under an argon atmosphere at 0 °C for 0.5 h. The reaction mixture was poured into 100 mL water and then extracted by DCM. Solvents were evaporated under reduced pressure and the residue was washed from methanol, and recrystallized by chlorobenzene affording light gray solid of **9** (0.066 g, yield 74%).

¹H NMR (500 MHz, CDCl₃) δ/ppm 7.63 (q, *J* = 8.05, 8.05, 8.03 Hz, 8H), 7.74 (dd, *J* = 20.85, 8.08 Hz, 8H), 3.17 (s, 2H).

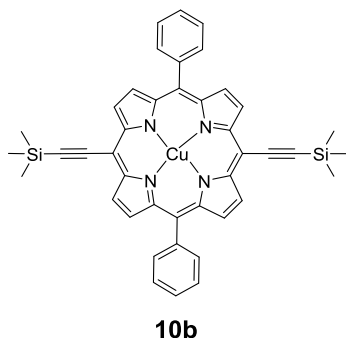
IR (KBr, cm⁻¹) 3445, 3284 (C-H), 2107 (C≡C), 1917, 1673, 1485, 1400, 1266, 1115, 1000, 843, 814, 729, 658, 639, 623, 555, 507. MALDI-ToF calculated for C₂₈H₁₈: [M]⁺, *m/z*, 354.1; found: 354.1. Elemental analysis calculated (%) for C₁₀H₆: C 94.88, H 5.12; found: C 94.34, H 5.06.

5,15-bis(trimethylsilanylethynyl)-10,20-diphenyl-21*H*,23*H*-porphyrin (10a)

5,15-Dibromo-10,20-diphenyl-21*H*,23*H*-porphyrin (0.620 g, 1 mmol), Pd(PPh₃)₂Cl₂ (0.035 g, 0.05 mmol), CuI (0.010 g, 0.05 mmol) and ethynyltrimethylsilane (0.206 g, 2.2 mmol) were added into the mixture of THF (35 mL) and triethylamine (15 mL) under an argon atmosphere. The reaction mixture was stirred at room temperature for 12 hours, and then the solution was poured into 150 mL water and extracted by DCM (3 × 50 mL). Solvents were removed in vacuum and the residue was purified by column chromatography on silica gel (hexane: DCM = 1:1) affording brown purple solid of **10a** (0.344 g, yield 52%).

¹H NMR (500 MHz, CDCl₃) δ ppm 9.63 (d, *J* = 4.68 Hz, 4H, pyrrole-*H*), 8.85 (d, *J* = 4.65 Hz, 4H), 8.20 (d, *J* = 6.14 Hz, 4H), 7.94-7.73 (m, 6H), 0.63 (s, 18H), -2.16 (s, 2H). ¹³C NMR (126 MHz, CDCl₃) δ ppm 141.35, 134.55, 128.01, 126.94, 121.81, 106.87, 102.75, 100.88, 0.336.

UV-vis (DCM, nm): 434, 508, 541, 582, 678. IR (KBr cm⁻¹): 3428, 3319, 2956, 2924(Si(C-H₃)₃), 2853, 2141(C≡C), 1597, 1558, 1441, 1467, 1441, 1398, 1337, 1247, 1194, 1138, 1069, 1002, 974, 964, 844, 797, 704, 657, 418. ESI-ToF calculated for C₄₂H₃₉N₄Si₂: [M+H]⁺, 655.3; Found: *m/z* 655.2.

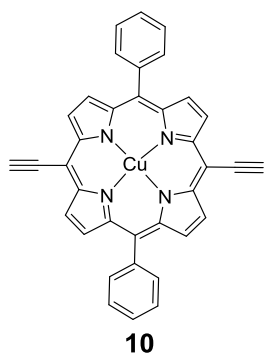
[5,15-bis(trimethylsilylethynyl)-10,20-diphenylporphinato]copper(II) (10b)

Cu(OAc)₂·H₂O (0.400 g, 2 mmol) was added to a solution of **10a** (0.332 g, 0.6 mmol) in a mixture of 50 mL THF, 50 mL DCM and 5 mL Et₃N. The reaction was stirred at room

temperature for 12 hours, then poured into 150 mL water and extracted by DCM (3×50 mL). The DCM solution was concentrated under reduced pressure and the residue was passed through a short column chromatography on silica gel (hexane:DCM = 1:1). After removed solvents, a dark purple solid **10b** (0.343 g, 80%) was obtained.

UV-vis (DCM, nm): 432, 564, 606. IR (KBr cm^{-1}): 2917($\text{Si}(\text{C}-\text{H}_3)_3$), 2849, 2134($\text{C}\equiv\text{C}$), 1523, 1462, 1443, 1344, 1246, 1209, 1166, 1067, 1004, 993, 840, 794, 755, 706, 666, 620, 566. ESI-ToF calculated for $\text{C}_{42}\text{H}_{36}\text{N}_4\text{Si}_2$: $[\text{M}]^+$, 715.2; Found: m/z 715.2.

[5,15-bis(ethynyl)-10,20-diphenylporphinato]copper(II) (**10**)



10b (0.322 g, 0.45 mmol) was dissolved in THF (50 mL) under an argon atmosphere at 0 °C. Then tetrabutylammonium fluoride (0.252 g, 0.8 mmol) was added. After 30 min, the reaction was poured into 50 mL MeOH. The precipitate was filtered and washed by 100 mL MeOH. The product was collected to yield a dark purple solid **10** (0.244 g, 95%).

UV-vis (DCM, nm): 425, 558, 598. IR (KBr cm^{-1}): 3264 (C-H), 2096 ($\text{C}\equiv\text{C}$), 1596, 1521, 1443, 1347, 1211, 1174, 1070, 1004, 936, 796, 751, 737, 711, 701, 676, 666, 646, 614, 503. MALDI-ToF calculated for $\text{C}_{36}\text{H}_{20}\text{N}_4\text{Cu}$: $[\text{M}]^-$, 571.1; Found: m/z 571.1.

7.3 Crystal structures

General considerations

Single crystal X-ray diffraction data of compounds **3**, **4**, **10a**, **10b** and **10** were collected on a STOE IPDS II diffractometer with graphite monochromated Mo-K α radiation (0.71073 Å) at 180 K. Data were corrected for Lorentz and polarization effects. Interframe Scaling was done with the implemented program LANA. The structures were solved by direct methods (SHELX-1997).^[242] Refinement was performed with anisotropic temperature factors for all non-hydrogen atoms. Molecular diagrams were prepared using PLATON, DIAMOND and Olex 2^[243].

3,3'-([1,1':4',1''-terphenyl]-4,4''-diyl)dipropionitrile (3)**Table 7.3.1** Crystal data and structure refinement for **3**.

Compound	3
Empirical formula	C ₂₄ H ₁₂ N ₂
Formula weight	328.36
Temperature/K	180.15
$\lambda/\text{\AA}$	0.71073
Crystal system	monoclinic
Space group	<i>P</i> 2 ₁ / <i>n</i>
<i>a</i> /\AA	9.9017(17)
<i>b</i> /\AA	8.3916(18)
<i>c</i> /\AA	10.6222(19)
$\alpha/^\circ$	90
$\beta/^\circ$	110.809(13)
$\gamma/^\circ$	90
Volume/\AA ³	825.0(3)
<i>Z</i>	2
ρ_{calc} mg/mm ³	1.322
μ/mm^{-1}	0.078
<i>F</i> (000)	340.0
Crystal size/mm ³	0.32 × 0.1 × 0.08
2 θ range for data collection/ $^\circ$	6.356 to 51.458
Reflections collected	3271
Independent reflections	1537 [<i>R</i> _{int} = 0.1376, <i>R</i> _{sigma} = 0.1148]
Data/restraints/parameters	1537/0/119
Goodness-of-fit on <i>F</i> ²	0.926
Final <i>R</i> indexes [<i>I</i> ≥ 2 σ (<i>I</i>)]	<i>R</i> ₁ = 0.0791, <i>wR</i> ₂ = 0.1947
Final <i>R</i> indexes [all data]	<i>R</i> ₁ = 0.1448, <i>wR</i> ₂ = 0.2349
CCDC number	1026443

Table 7.3.2 Selected bond lengths (Å) in compound **3**.

N1- C1	1.161(5)	C7- C8	1.401(5)
C1- C2	1.365(6)	C7- C10	1.471(5)
C2- C3	1.189(5)	C8- C9	1.369(5)
C3- C4	1.427(6)	C10-C11	1.391(5)
C4- C5	1.401(5)	C10-C12 ¹	1.402(5)
C4- C9	1.399(5)	C11-C12	1.368(5)
C5- C6	1.375(5)	C12-C10 ¹	1.402(5)
C6- C7	1.392(5)		

3-([1,1':4',1''-terphenyl]-4-yl)propionitrile (4)**Table 7.3.3** Crystal data and structure refinement for **4**.

Compound	4
Empirical formula	C ₂₁ H ₁₃ N
Formula weight	279.32
Temperature/K	180.15
$\lambda/\text{\AA}$	0.71073
Crystal system	triclinic
Space group	$P\bar{1}$
$a/\text{\AA}$	9.816(2)
$b/\text{\AA}$	12.229(2)
$c/\text{\AA}$	19.558(4)
$\alpha/^\circ$	98.36(3)
$\beta/^\circ$	101.77(3)
$\gamma/^\circ$	102.50(3)
Volume/ \AA^3	2199.0(9)
Z	6
$\rho_{\text{calc}} \text{ mg/mm}^3$	1.266
μ/mm^{-1}	0.073
$F(000)$	876.0
Crystal size/ mm^3	0.43 × 0.39 × 0.06

2θ range for data collection/ $^{\circ}$	4.342 to 51.158
Reflections collected	15902
Independent reflections	8004 [$R_{\text{int}} = 0.0950$, $R_{\text{sigma}} = 0.1090$]
Data/restraints/parameters	8004/0/595
Goodness-of-fit on F^2	0.995
Final R indexes [$I \geq 2\sigma(I)$]	$R_1 = 0.0923$, $wR_2 = 0.2641$
Final R indexes [all data]	$R_1 = 0.1533$, $wR_2 = 0.3006$
CCDC number	1006987

Table 7.3.4 Selected bond lengths (\AA) in compound **4**.

Atom	Atom	Length/ \AA	Atom	Atom	Length/ \AA
N1	C1	1.144(6)	C10	C15	1.394(6)
C1	C2	1.362(6)	C11	C12	1.378(6)
C2	C3	1.203(6)	C12	C13	1.382(6)
C3	C4	1.413(6)	C13	C14	1.378(6)
C4	C5	1.369(6)	C13	C16	1.484(5)
C4	C9	1.389(6)	C14	C15	1.393(6)
C5	C6	1.373(6)	C16	C17	1.395(6)
C6	C7	1.384(5)	C16	C21	1.383(6)
C7	C8	1.390(6)	C17	C18	1.386(6)
C7	C10	1.483(5)	C18	C19	1.380(7)
C8	C9	1.375(6)	C19	C20	1.342(7)
C10	C11	1.365(6)	C20	C21	1.378(6)

5,15-bis(trimethylsilanylethynyl)-10,20-diphenyl-21H,23H-porphyrin (10a)**Table 7.3.5** Crystal data and structure refinement for **10a**.

Compound	10a
Empirical formula	$\text{C}_{42}\text{H}_{38}\text{N}_4\text{Si}_2$
Formula weight	654.94
Temperature/K	180.15
Crystal system	monoclinic

Space group	$P2_1/n$
$a/\text{\AA}$	11.314(2)
$b/\text{\AA}$	24.647(5)
$c/\text{\AA}$	13.214(2)
$\alpha/^\circ$	90
$\beta/^\circ$	104.231(13)
$\gamma/^\circ$	90
Volume/ \AA^3	3571.9(12)
Z	4
$\rho_{\text{calc}}/\text{g/cm}^3$	1.218
μ/mm^{-1}	0.135
$F(000)$	1384.0
Crystal size/ mm^3	$0.38 \times 0.17 \times 0.02$
Radiation	Mo $K\alpha$ ($\lambda = 0.71073$)
2θ range for data collection/ $^\circ$	3.304 to 48.902
Reflections collected	15831
Independent reflections	5746 [$R_{\text{int}} = 0.3601$, $R_{\text{sigma}} = 0.4935$]
Data/restraints/parameters	5746/0/440
Goodness-of-fit on F^2	0.769
Final R indexes [$I \geq 2\sigma(I)$]	$R_1 = 0.0906$, $wR_2 = 0.1307$
Final R indexes [all data]	$R_1 = 0.3289$, $wR_2 = 0.2010$

Table 7.3.6 Bond Lengths for 10a.

Atom		Atom		Length/ \AA		Atom		Atom		Length/ \AA	
Si1	C22	1.883(12)	C10	C11	1.415(14)						
Si1	C23	1.868(10)	C10	C31	1.492(14)						
Si1	C24	1.876(13)	C11	C12	1.459(13)						
Si1	C25	1.860(11)	C12	C13	1.361(15)						
Si2	C27	1.919(14)	C13	C14	1.433(13)						
Si2	C28	1.849(12)	C14	C15	1.413(15)						

Si2	C29	1.867(12)	C15	C16	1.367(14)
Si2	C30	1.833(10)	C15	C26	1.480(13)
N1	C1	1.372(13)	C16	C17	1.426(15)
N1	C4	1.362(13)	C17	C18	1.362(13)
N2	C6	1.355(11)	C18	C19	1.429(14)
N2	C9	1.370(13)	C19	C20	1.401(13)
N3	C11	1.350(13)	C20	C37	1.460(15)
N3	C14	1.400(12)	C21	C22	1.121(12)
N4	C16	1.356(12)	C26	C27	1.101(13)
N4	C19	1.385(13)	C31	C32	1.413(14)
C1	C2	1.457(13)	C31	C36	1.387(13)
C1	C20	1.411(14)	C32	C33	1.407(15)
C2	C3	1.327(14)	C33	C34	1.365(14)
C3	C4	1.460(14)	C34	C35	1.350(14)
C4	C5	1.395(15)	C35	C36	1.392(15)
C5	C6	1.405(14)	C37	C38	1.422(14)
C5	C21	1.498(15)	C37	C42	1.374(14)
C6	C7	1.417(14)	C38	C39	1.369(14)
C7	C8	1.365(13)	C39	C40	1.358(15)
C8	C9	1.440(13)	C40	C41	1.387(15)
C9	C10	1.378(13)	C41	C42	1.384(15)

[5,15-bis(trimethylsilylethynl)-10,20-diphenylporphinato]copper(II) (10b)**Table 7.3.7** Crystal data and structure refinement for **10b**.

Compound	10b
Empirical formula	C ₄₂ H ₃₆ N ₄ Si ₂ Cu
Formula weight/g·mol ⁻¹	716.47
Temperature/K	180.15
Crystal system	triclinic
Space group	<i>P</i> $\bar{1}$
<i>a</i> /Å	6.0685(5)
<i>b</i> /Å	11.9579(10)
<i>c</i> /Å	12.7655(10)
α /°	76.138(6)
β /°	81.136(7)
γ /°	84.850(7)
Volume/Å ³	887.28(13)
<i>Z</i>	1
ρ_{calc} g/cm ³	1.341
μ /mm ⁻¹	0.719
<i>F</i> (000)	373.0
Crystal size/mm ³	0.36 × 0.06 × 0.02
Radiation	Mo K α (λ = 0.71073)
2 θ range for data collection/°	4.24 to 51.3
Reflections collected	7326
Independent reflections	3312 [<i>R</i> _{int} = 0.0869, <i>R</i> _{sigma} = 0.1001]
Independent reflections with <i>I</i> ≥ 2 σ (<i>I</i>)	2237
Data/restraints/parameters	3312/0/226
Goodness-of-fit on <i>F</i> ²	0.998
Final <i>R</i> indexes [<i>I</i> ≥ 2 σ (<i>I</i>)]	<i>R</i> ₁ = 0.0543, <i>wR</i> ₂ = 0.1121
Final <i>R</i> indexes [all data]	<i>R</i> ₁ = 0.0943, <i>wR</i> ₂ = 0.1280
CCDC number	1506859

Table 7.3.8 Bond Lengths for **10b**.

Atom		Atom Length/Å	Atom		Atom Length/Å
Cu1	N1 ¹	2.001(3)	C4	C5	1.408(5)
Cu1	N1	2.001(3)	C5	C6	1.392(5)
Cu1	N2	1.996(3)	C5	C11	1.434(6)
Cu1	N2 ¹	1.996(3)	C6	C7	1.430(5)
Si1	C12	1.830(4)	C7	C8	1.345(6)
Si1	C13	1.846(5)	C8	C9	1.437(5)
Si1	C14	1.857(5)	C9	C10	1.389(5)
Si1	C15	1.847(5)	C10	C1 ¹	1.390(5)
N1	C1	1.383(5)	C10	C16	1.509(5)
N1	C4	1.369(5)	C11	C12	1.218(6)
N2	C6	1.364(5)	C16	C17	1.385(6)
N2	C9	1.381(5)	C16	C21	1.375(6)
C1	C2	1.429(5)	C17	C18	1.391(6)
C1	C10 ¹	1.390(5)	C18	C19	1.371(6)
C2	C3	1.344(6)	C19	C20	1.376(6)
C3	C4	1.433(5)	C20	C21	1.394(6)

¹-X,1-Y,2-Z

[5,15-bis(ethynyl)-10,20-diphenylporphinato]copper(II) (10)**Table 7.3.9** Crystal data and Rietveld refinement for **10**.

Compound	10
Empirical formula	C ₃₆ H ₂₀ CuN ₄
Formula weight	572.14
Crystal system	triclinic
Space group	<i>P</i> $\bar{1}$
<i>a</i> /Å	6.287(3)
<i>b</i> /Å	9.289(5)
<i>c</i> /Å	11.877(7)
α /°	111.908(6)
β /°	87.901(5)
γ /°	82.867(5)
Volume/Å ³	635.911
<i>Z</i>	1
2 θ range used for refinement/°	5 to 80
<i>R</i> _p /%	8.24
<i>R</i> _{wp} /%	12.51

Table 7.3.10 Fractional atomic coordinates of **10**.

Atom	<i>x</i>	<i>y</i>	<i>z</i>
Cu1	1	0.5	0.5
N1	0.78422	0.63427	0.63927
N2	0.84152	0.31817	0.47302
C1	0.7792	0.79123	0.71116
C2	0.59274	0.84522	0.79659
C3	0.48673	0.7228	0.78
C4	0.60671	0.59203	0.68193
C5	0.545	0.44162	0.63373
C6	0.65714	0.31536	0.53588
C7	0.58665	0.16548	0.48587

C8	0.7285	0.07628	0.39018
C9	0.88907	0.17027	0.38215
C10	1.06848	0.11632	0.29783
C11	0.34563	0.42158	0.68431
C12	0.16943	0.41112	0.72436
C13	1.09742	-0.05265	0.20981
C14	1.2373	-0.16591	0.23044
C15	1.2679	-0.32069	0.14733
C16	1.16222	-0.3609	0.04344
C17	1.02254	-0.25046	0.02094
C18	0.99594	-0.09491	0.10304
H2	0.55103	0.94915	0.85476
H3	0.35789	0.72301	0.82452
H7	0.46381	0.13456	0.51444
H8	0.72329	-0.02906	0.33773
H12	0.03211	0.40297	0.75557
H14	1.31108	-0.13838	0.30013
H15	1.35993	-0.39682	0.16222
H16	1.18528	-0.46415	-0.01254
H17	0.94697	-0.27921	-0.04805
H18	0.90887	-0.01843	0.0859

8. Summary

In this thesis, ten novel alkyne derivatives were designed and synthesized and their applications in surface-assembly and C–C coupling reactions, molecular junctions and battery designs were explored. The compounds **2**, **3**, **4**, **6**, **9** and **10** were not published before.

Compounds **1**, **2** and **3** were employed in surface C–C coupling reactions and in metal-directed self-assembly on surfaces. Using the vicinal surfaces Ag(877) as template the chemoselectivity of the C–C homo-coupling of **1** was improved and 1D extended-GDY wires with lengths reaching 30 nm were obtained after annealing at 400 K. DFT calculation showed that the 1D polymer exhibits a band gap of 1.6 eV. Taking advantage of the fact that alkyne and alkene groups show different activities on Au(111) and Cu(111) surfaces, we successfully cross-coupled them in compound **2** and obtained 2D infinite covalent network. After annealing at 160 °C, the Cu atoms coordinated to the alkyne-alkene-alkyne moieties to form organometallic polymer chains. After depositing Gd atoms to the chevron arrangement of an organic monolayer of compound **3** on Ag(111), an irregular metal-organic monolayer with variable coordination motifs including clustering was observed.

For the first time, we synthesized large area graphdiynes (GDY **6**) with thicknesses of around 117 nm on Cu foils by the modified Glaser-Hay homo-coupling of compound **5**. IR, Raman, and TEM results showed that the homo-coupling of **5** to 2D butadiyne-linked GDY **6** was very efficient. The produced nanofilms showed a conductivity of $5.15 \times 10^{-6} \text{ S m}^{-1}$, indicating semiconductor properties.

Compound **1**, **7**, **8** and **9** were used to determine the single molecule conductance by the MCBJ technique. The molecules anchored to the gold leads through their terminal *sp*-hybridized carbon atom. The conductance of **1** and **9** showed an exponential decay $\beta \approx 0.45 \text{ \AA}^{-1}$ which was similar to the value of *sp*³ C–Au junctions with the same molecular oligophenylene backbone. But the conductance of the molecules contacted via the *sp*-hybridized carbon atom was lower than the previous ones reported using *sp*³ hybridization due to strong differences in the coupling of the conducting orbitals with the gold leads.

Finally, a novel alkyne-substituted porphyrin compound **10** (**CuDEPP**) was investigated in view of its electrochemical performance as electrode in rechargeable batteries. Three different cell designs were proposed and investigated in detail. First, a Li/LiPF₆/CuDEPP cell delivering an initial discharge capacity of 210 mAh g⁻¹ and high capacity retention of approximately 85% and 60% was preserved during 2000 and 8000 cycles, respectively, with a high current density of 4 A g⁻¹. Notably, a stable reversible discharge capacity of 115 mAh g⁻¹ was achieved at a current of 10 A g⁻¹ within 42 seconds, offering an energy density of 345

Wh kg⁻¹ at a high specific power of 29 kW kg⁻¹. Secondly, **CuDEPP** served as an anode-active material in a Li-free CuDEPP/PP₁₄TFSI/graphite cell, in which a discharge capacity of 94 mAh g⁻¹ was measured at a current density of 1 A g⁻¹. The reversible intercalation of the TFSI⁻ anion into (from) the graphite cathode was indicated by *ex-situ* XRD and EDX spectroscopy. Moreover, in an all-organic symmetric configuration, the ambipolar redox reactivity of **CuDEPP** electrode enabled a four-electron transfer. Therefore, the energy storage device using **CuDEPP** as electrode-active material will eventually bridge in future the gap between the batteries and the supercapacitors.

9. References

- [1] a) P. J. Stang, F. Diederich, *Modern Acetylene Chemistry*, Wiley-VCH: Weinheim, **1995**; b) F. Diederich, P. J. Stang, R. R. Tykwinski, *Acetylene Chemistry*, Wiley-VCH: Weinheim, **2004**.
- [2] a) P. Maity, S. Takano, S. Yamazoe, T. Wakabayashi, T. Tsukuda, *J. Am. Chem. Soc.* **2013**, *135*, 9450-9457; b) Y.-Q. Zhang, J. Björk, P. Weber, R. Hellwig, K. Diller, A. C. Papageorgiou, S. C. Oh, S. Fischer, F. Allegretti, S. Klyatskaya, M. Ruben, J. V. Barth, F. Klappenberger, *J. Phys. Chem. C* **2015**, *119*, 9669-9679; c) N. Kepčija, Y.-Q. Zhang, M. Kleinschrodt, J. Björk, S. Klyatskaya, F. Klappenberger, M. Ruben, J. V. Barth, *J. Phys. Chem. C* **2013**, *117*, 3987-3995.
- [3] K. N. Campbell, B. K. Campbell, *Org. Synth.* **1950**, *30*, 72-74.
- [4] a) P. Fritsch, *Liebigs Ann. Chem.* **1894**, *279*, 319-323; b) W. P. Buttenberg, *Liebigs Ann. Chem.* **1894**, *279*, 324-337; c) H. Wiechell, *Liebigs Ann. Chem.* **1894**, *279*, 337-344.
- [5] a) E. J. Corey, P. L. Fuchs, *Tetrahedron Lett.* **1972**, *13*, 3769-3772; b) T. Gibtner, F. Hampel, J.-P. Gisselbrecht, A. Hirsch, *Chem. Eur. J.* **2002**, *8*, 408-432.
- [6] a) E. Quesada, R. J. K. Taylor, *Tetrahedron Lett.* **2005**, *46*, 6473-6476; b) D. Seyferth, R. S. Marmor, P. Hilbert, *J. Org. Chem.* **1971**, *36*, 1379-1386; c) J. C. Gilbert, U. Weerasooriya, *J. Org. Chem.* **1982**, *47*, 1837-1845.
- [7] I. Omae, *Appl. Organomet. Chem.* **2008**, *22*, 149-166.
- [8] a) A. J. Chalk, R. A. Jerussi, *Tetrahedron Lett.* **1972**, *13*, 61-62; b) J. R. Leto, M. F. Leto, *J. Am. Chem. Soc.* **1961**, *83*, 2944-2951.
- [9] P. M. Maitlis, *J. Organomet. Chem.* **1980**, *200*, 161-176.
- [10] T. C. Wen, C. C. Chang, Y. D. Chuang, C. P. Cheng, J. P. Chiu, C. T. Chang, *J. Am. Chem. Soc.* **1981**, *103*, 4576-4578.
- [11] J. E. Hill, G. Balaich, P. E. Fanwick, I. P. Rothwell, *Organometallics* **1993**, *12*, 2911-2924.
- [12] J. B. Hartung, S. F. Pedersen, *Organometallics* **1990**, *9*, 1414-1417.
- [13] M. Tsutsui, H. Zeiss, *J. Am. Chem. Soc.* **1959**, *81*, 6090-6091.
- [14] J. Moulijn, *J. Catal.* **1972**, *25*, 434-436.
- [15] K. Ferré, L. Toupet, V. Guerchais, *Organometallics* **2002**, *21*, 2578-2580.
- [16] K. Hashizume, Y. Mizobe, M. Hidai, *Organometallics* **1995**, *14*, 5367-5376.
- [17] Y. Iwashita, F. Tamura, *Bull. Chem. Soc. Jpn.* **1970**, *43*, 1517-1520.
- [18] J. P. Collman, J. W. Kang, W. F. Little, M. F. Sullivan, *Inorg. Chem.* **1968**, *7*, 1298-1303.
- [19] H. Dietl, H. Reinheimer, J. Moffat, P. M. Maitlis, *J. Am. Chem. Soc.* **1970**, *92*, 2276-2285.
- [20] a) J. Liu, P. Ruffieux, X. L. Feng, K. Müllen, R. Fasel, *Chem. Commun.* **2014**, *50*, 11200-11203; b) H. Zhou, J. Liu, S. Du, L. Zhang, G. Li, Y. Zhang, B. Z. Tang, H.-J. Gao, *J. Am. Chem. Soc.* **2014**, *136*, 5567-5570.
- [21] a) P. L. Pauson, I. U. Khand, *Ann. N. Y. Acad. Sci.* **1977**, *295*, 2-14; b) J. Blanco-Urgoiti, L. Anorbe, L. Perez-Serrano, G. Dominguez, J. Perez-Castells, *Chem. Soc. Rev.* **2004**, *33*, 32-42.
- [22] a) C. Lecture, *Proc. Chem. Soc.* **1961**, 357-396; b) H. C. Kolb, M. G. Finn, K. B. Sharpless, *Angew. Chem., Int. Ed.* **2001**, *40*, 2004-2021.
- [23] a) W. Diltthey, G. Hurtig, *Ber. Dtsch. Chem. Ges.* **1934**, *67*, 2004-2007; b) M. A. Ogliaruso, M. G. Romanelli, E. I. Becker, *Chem. Rev.* **1965**, *65*, 261-367; c) C. D. Simpson, J. D. Brand, A. J. Berresheim, L. Przybilla, H. J. Räder, K. Müllen, *Chem. Eur. J.* **2002**, *8*, 1424-1429; d) T. J. Skalski, B. Britton, T. J. Peckham, S. Holdcroft, *J. Am. Chem. Soc.* **2015**, *137*, 12223-12226.

- [24] J. Liu, J. W. Lam, B. Z. Tang, *Chem. Rev.* **2009**, *109*, 5799-5867.
- [25] R. Chinchilla, C. Najera, *Chem. Rev.* **2007**, *107*, 874-922.
- [26] K. Sonogashira, Y. Tohda, N. Hagihara, *Tetrahedron Lett.* **1975**, *16*, 4467-4470.
- [27] a) R. Chinchilla, C. Najera, *Chem. Soc. Rev.* **2011**, *40*, 5084-5121; b) E. Negishi, L. Anastasia, *Chem. Rev.* **2003**, *103*, 1979-2017.
- [28] F. B. Sviridenko, D. V. Stass, T. V. Kobzeva, E. V. Tretyakov, S. V. Klyatskaya, E. V. Mshvidobadze, S. F. Vasilevsky, Y. N. Molin, *J. Am. Chem. Soc.* **2004**, *126*, 2807-2819.
- [29] M. Schilz, H. Plenio, *J. Org. Chem.* **2012**, *77*, 2798-2807.
- [30] P. G. M. Wuts, *Protection for the Alkyne -CH*, John Wiley & Sons, Inc, **2014**.
- [31] S. Lopez, F. Fernandez-Trillo, P. Midon, L. Castedo, C. Saa, *J. Org. Chem.* **2006**, *71*, 2802-2810.
- [32] S. Höger, K. Bonrad, *J. Org. Chem.* **2000**, *65*, 2243-2245.
- [33] K. L. Chandra, S. Zhang, C. B. Gorman, *Tetrahedron* **2007**, *63*, 7120-7132.
- [34] H.-Y. Chao, W. Lu, Y. Li, M. C. W. Chan, C.-M. Che, K.-K. Cheung, N. Zhu, *J. Am. Chem. Soc.* **2002**, *124*, 14696-14706.
- [35] H. B. Fyfe, M. Mlekuz, D. Zargarian, N. J. Taylor, T. B. Marder, *J. Chem. Soc., Chem. Commun.* **1991**, 188-190.
- [36] S. K. Hurst, M. P. Cifuentes, A. M. McDonagh, M. G. Humphrey, M. Samoc, B. Luther-Davies, I. Asselberghs, A. Persoons, *J. Organomet. Chem.* **2002**, *642*, 259-267.
- [37] C. Bianchini, M. Peruzzini, A. Vacca, F. Zanobini, *Organometallics* **1991**, *10*, 3697-3707.
- [38] a) H. Lang, A. del Villar, G. Rheinwald, *J. Organomet. Chem.* **1999**, *587*, 284-289; b) C. J. Adams, S. L. James, *Chem. Commun.* **1997**, 2155-2156; c) D. Qiu, Q. Zhao, H. Wang, Y. Feng, X. Bao, Y. Guo, Q. Huang, *Inorg. Chim. Acta* **2012**, *392*, 261-267.
- [39] H. W. Kroto, J. R. Heath, S. C. O'Brien, R. F. Curl, R. E. Smalley, *Nature* **1985**, *318*, 162-163.
- [40] S. Iijima, *Nature* **1991**, *354*, 56-58.
- [41] K. S. Novoselov, A. K. Geim, S. V. Morozov, D. Jiang, Y. Zhang, S. V. Dubonos, I. V. Grigorieva, A. A. Firsov, *Science* **2004**, *306*, 666-669.
- [42] a) G. H. Hoorn, *Recl. Trav. Chim. Pays-Bas* **2010**, *7*, 341-341; b) L. Shi, P. Rohringer, K. Suenaga, Y. Niimi, J. Kotakoski, J. C. Meyer, H. Peterlik, M. Wanko, S. Cahangirov, A. Rubio, Z. J. Lapin, L. Novotny, P. Ayala, T. Pichler, *Nat. Mater.* **2016**, *15*, 634-639.
- [43] R. H. Baughman, H. Eckhardt, M. Kertesz, *J. Chem. Phys.* **1987**, *87*, 6687-6699.
- [44] M. M. Haley, S. C. Brand, J. J. Pak, *Angew. Chem., Int. Ed.* **1997**, *36*, 836-838.
- [45] a) A. L. Ivanovskii, *Prog. Solid State Chem.* **2013**, *41*, 1-19; b) Q. Peng, A. K. Dearden, J. Crean, L. Han, S. Liu, X. Wen, S. De, *Nanotechnol. Sci. Appl.* **2014**, *7*, 1-29; c) Y. Li, L. Xu, H. Liu, Y. Li, *Chem. Soc. Rev.* **2014**, *43*, 2572-2586.
- [46] a) G. Luo, X. Qian, H. Liu, R. Qin, J. Zhou, L. Li, Z. Gao, E. Wang, W.-N. Mei, J. Lu, Y. Li, S. Nagase, *Phys. Rev. B* **2011**, *84*, 075439; b) M. Long, L. Tang, D. Wang, Y. Li, Z. Shuai, *ACS Nano* **2011**, *5*, 2593-2600; c) K. Srinivasu, S. K. Ghosh, *J. Phys. Chem. C* **2012**, *116*, 5951-5956; d) J. Kang, J. Li, F. Wu, S.-S. Li, J.-B. Xia, *J. Phys. Chem. C* **2011**, *115*, 20466-20470.
- [47] J. Wang, S. Zhang, J. Zhou, R. Liu, R. Du, H. Xu, Z. Liu, J. Zhang, Z. Liu, *Phys. Chem. Chem. Phys.* **2014**, *16*, 11303-11309.
- [48] a) Y. Pei, *Physica B* **2012**, *407*, 4436-4439; b) D. B. Brommer, M. J. Buehler, *J. Appl. Mech.* **2013**, *80*, 040908; c) Y. Yang, X. Xu, *Comput. Mater. Sci* **2012**, *61*, 83-88; d) S. W. Cranford, D. B. Brommer, M. J. Buehler, *Nanoscale* **2012**, *4*, 7797-7809; e) Q. Yue, S. Chang, J. Kang, S. Qin, J. Li, *J. Phys. Chem. C* **2013**, *117*, 14804-14811; f) M.

- Becton, L. Zhang, X. Wang, *Phys. Chem. Chem. Phys.* **2014**, *16*, 18233-18240; g) R. E. Roman, S. W. Cranford, *Adv. Eng. Mater.* **2014**, *16*, 862-871.
- [49] S. Jalili, F. Houshmand, J. Schofield, *Appl. Phys. A* **2015**, *119*, 571-579.
- [50] Y. Pan, Y. Wang, L. Wang, H. Zhong, R. Quhe, Z. Ni, M. Ye, W. N. Mei, J. Shi, W. Guo, J. Yang, J. Lu, *Nanoscale* **2015**, *7*, 2116-2127.
- [51] J. Gong, Y. Tang, P. Yang, *J. Mol. Struct.* **2014**, *1064*, 32-36.
- [52] a) C. Sun, D. J. Searles, *J. Phys. Chem. C* **2012**, *116*, 26222-26226; b) B. Jang, J. Koo, M. Park, H. Lee, J. Nam, Y. Kwon, H. Lee, *Appl. Phys. Lett.* **2013**, *103*, 263904; c) H. Zhang, Y. Xia, H. Bu, X. Wang, M. Zhang, Y. Luo, M. Zhao, *J. Appl. Phys.* **2013**, *113*, 044309; d) A. Mohajeri, A. Shahsavari, *Comput. Mater. Sci* **2016**, *115*, 51-59; e) Z. Xu, X. Lv, J. Li, J. Chen, Q. Liu, *RSC Adv.* **2016**, *6*, 25594-25600.
- [53] a) Y. Jiao, A. Du, M. Hankel, Z. Zhu, V. Rudolph, S. C. Smith, *Chem. Commun.* **2011**, *47*, 11843-11845; b) S. W. Cranford, M. J. Buehler, *Nanoscale* **2012**, *4*, 4587-4593; c) H. Zhang, X. He, M. Zhao, M. Zhang, L. Zhao, X. Feng, Y. Luo, *J. Phys. Chem. C* **2012**, *116*, 16634-16638; d) H. Zhang, X. Zhao, M. Zhang, Y. Luo, G. Li, M. Zhao, *J. Phys. D: Appl. Phys.* **2013**, *46*, 495307; e) M. Bartolomei, E. Carmona-Novillo, M. I. Hernández, J. Campos-Martínez, F. Pirani, G. Giorgi, *J. Phys. Chem. C* **2014**, *118*, 29966-29972; f) M. Bartolomei, E. Carmona-Novillo, M. I. Hernandez, J. Campos-Martinez, F. Pirani, G. Giorgi, K. Yamashita, *J. Phys. Chem. Lett.* **2014**, *5*, 751-755; g) Y. Jiao, A. Du, S. C. Smith, Z. Zhu, S. Z. Qiao, *J. Mater. Chem. A* **2015**, *3*, 6767-6771; h) X. Tan, L. Kou, H. A. Tahini, S. C. Smith, *Mol. Simul.* **2015**, *42*, 573-579.
- [54] a) J. Kou, X. Zhou, Y. Chen, H. Lu, F. Wu, J. Fan, *J. Chem. Phys.* **2013**, *139*, 064705; b) M. Xue, H. Qiu, W. Guo, *Nanotechnology* **2013**, *24*, 505720; c) C. Zhu, H. Li, X. C. Zeng, E. G. Wang, S. Meng, *Sci. Rep.* **2013**, *3*, 03163; d) J. Kou, X. Zhou, H. Lu, F. Wu, J. Fan, *Nanoscale* **2014**, *6*, 1865-1870.
- [55] a) Y. Liu, *Acta Chim. Sinica* **2013**, *71*, 260-264; b) Z.-Z. Lin, *Carbon* **2015**, *86*, 301-309; c) B. K. Das, D. Sen, K. K. Chattopadhyay, *Phys. Chem. Chem. Phys.* **2016**, *18*, 2949-2958; d) Z. Lu, S. Li, P. Lv, C. He, D. Ma, Z. Yang, *Appl. Surf. Sci.* **2016**, *360*, 1-7.
- [56] X. Chen, P. Gao, L. Guo, S. Zhang, *Sci. Rep.* **2015**, *5*, 16720.
- [57] a) M. M. Haley, *Pure Appl. Chem.* **2008**, *80*, 519-532; b) F. Diederich, M. Kivala, *Adv. Mater.* **2010**, *22*, 803-812.
- [58] F. Klappenberger, Y. Q. Zhang, J. Bjork, S. Klyatskaya, M. Ruben, J. V. Barth, *Acc. Chem. Res.* **2015**, *48*, 2140-2150.
- [59] C. Glaser, *Ber. Dtsch. Chem. Ges.* **1869**, *2*, 422-424.
- [60] A. S. Hay, *J. Org. Chem.* **1962**, *27*, 3320-3321.
- [61] I. D. Campbell, G. Eglinton, *Org. Synth.* **1965**, *45*, 39-42.
- [62] I. J. S. Fairlamb, P. S. Bäuerlein, L. R. Marrison, J. M. Dickinson, *Chem. Commun.* **2003**, 632-633.
- [63] a) N. Kepčija, M. Kleinschrodt, K. Diller, S. Fischer, A. C. Papageorgiou, F. Allegretti, J. Bjork, S. Klyatskaya, F. Klappenberger, M. Ruben, J. V. Barth, *Nat. Commun.* **2012**, *3*, 1286; b) Y.-Q. Zhang, N. Kepčija, M. Kleinschrodt, K. Diller, S. Fischer, A. C. Papageorgiou, F. Allegretti, J. Björk, S. Klyatskaya, F. Klappenberger, M. Ruben, J. V. Barth, *Nat. Commun.* **2012**, *3*, 1286.
- [64] H. Y. Gao, H. Wagner, D. Zhong, J. H. Franke, A. Studer, H. Fuchs, *Angew. Chem., Int. Ed.* **2013**, *52*, 4024-4028.
- [65] F. Bohlmann, H. Schönowsky, E. Inhoffen, G. Grau, *Chem. Ber.* **1964**, *97*, 794-800.
- [66] M. H. Vilhelmsen, J. Jensen, C. G. Tortzen, M. B. Nielsen, *Eur. J. Org. Chem.* **2013**, *2013*, 701-711.
- [67] M. Altmann, U. H. F. Bunz, *Macromol. Rapid Commun.* **1994**, *15*, 785-789.

- [68] a) M. Kijima, I. Kinoshita, T. Hattori, H. Shirakawa, *Synth. Met.* **1999**, *100*, 61-69; b) M. Kijima, H. Tanimoto, H. Shirakawa, *Synth. Met.* **2001**, *119*, 353-354; c) M. Kijima, H. Tanimoto, H. Shirakawa, A. Oya, T. T. Liang, Y. Yamada, *Carbon* **2001**, *39*, 297-300; d) I. Kinoshita, M. Kijima, H. Shirakawa, *Synth. Met.* **2001**, *119*, 187-188; e) I. Kinoshita, M. Kijima, H. Shirakawa, *Mol. Cryst. Liq. Cryst. Sci. Technol., Sect. A* **2001**, *365*, 237-245; f) S. Abe, Y. Nagasaki, M. Kijima, *Synth. Met.* **2003**, *135-136*, 123-124; g) M. Kijima, S. Matsumoto, I. Kinoshita, *Synth. Met.* **2003**, *135-136*, 391-392; h) I. Kinoshita, M. Kijima, K. Yoshikawa, Y. Mishima, N. Sasaki, *Synth. Met.* **2003**, *137*, 1059-1060; i) M. Kijima, T. Oda, T. Yamazaki, Y. Tazaki, J. Nakamura, *Chem. Lett.* **2006**, *35*, 844-845; j) M. Kijima, H. Tanimoto, K. Takakura, D. Fujiya, Y. Ayuta, K. Matsuishi, *Carbon* **2007**, *45*, 594-601.
- [69] V. E. Williams, T. M. Swager, *J. Polym. Sci., Part A: Polym. Chem.* **2000**, *38*, 4669-4676.
- [70] a) H. L. Anderson, S. J. Martin, D. D. C. Bradley, *Angew. Chem., Int. Ed.* **1994**, *33*, 655-657; b) T. E. O. Screen, K. B. Lawton, G. S. Wilson, N. Dolney, R. Ispasoiu, T. Goodson Iii, S. J. Martin, D. D. C. Bradley, H. L. Anderson, *J. Mater. Chem.* **2001**, *11*, 312-320; c) T. E. O. Screen, J. R. G. Thorne, R. G. Denning, D. G. Bucknall, H. L. Anderson, *J. Mater. Chem.* **2003**, *13*, 2796-2808; d) F. C. Grozema, C. Houarner-Rassin, P. Prins, L. D. Siebbeles, H. L. Anderson, *J. Am. Chem. Soc.* **2007**, *129*, 13370-13371; e) A. Saywell, J. K. Sprafke, L. J. Esdaile, A. J. Britton, A. Rienzo, H. L. Anderson, J. N. O'Shea, P. H. Beton, *Angew. Chem., Int. Ed.* **2010**, *49*, 9136-9139.
- [71] M. Häussler, R. Zheng, J. W. Y. Lam, H. Tong, H. Dong, B. Z. Tang, *J. Phys. Chem. B* **2004**, *108*, 10645-10650.
- [72] J. X. Jiang, F. Su, H. Niu, C. D. Wood, N. L. Campbell, Y. Z. Khimyak, A. I. Cooper, *Chem. Commun.* **2008**, 486-488.
- [73] A. C. Uptmoor, J. Freudenberg, S. T. Schwabel, F. Paulus, F. Rominger, F. Hinkel, U. H. Bunz, *Angew. Chem., Int. Ed.* **2015**, *54*, 14673-14676.
- [74] I. Hijazi, T. Bourgeteau, R. Cornut, A. Morozan, A. Filoramo, J. Leroy, V. Derycke, B. Joussetme, S. Campidelli, *J. Am. Chem. Soc.* **2014**, *136*, 6348-6354.
- [75] K. Wu, J. Guo, C. Wang, *Chem. Commun.* **2014**, *50*, 695-697.
- [76] G. Li, Y. Li, H. Liu, Y. Guo, Y. Li, D. Zhu, *Chem. Commun.* **2010**, *46*, 3256-3258.
- [77] J. Zhou, X. Gao, R. Liu, Z. Xie, J. Yang, S. Zhang, G. Zhang, H. Liu, Y. Li, J. Zhang, Z. Liu, *J. Am. Chem. Soc.* **2015**, *137*, 7596-7599.
- [78] a) X. Zhang, M. Zhu, P. Chen, Y. Li, H. Liu, Y. Li, M. Liu, *Phys. Chem. Chem. Phys.* **2015**, *17*, 1217-1225; b) N. Yang, Y. Liu, H. Wen, Z. Tang, H. Zhao, Y. Li, D. Wang, *ACS Nano* **2013**, *7*, 1504-1512; c) S. Wang, L. Yi, J. E. Halpert, X. Lai, Y. Liu, H. Cao, R. Yu, D. Wang, Y. Li, *Small* **2012**, *8*, 265-271; d) S. Thangavel, K. Krishnamoorthy, V. Krishnaswamy, N. Raju, S. J. Kim, G. Venugopal, *J. Phys. Chem. C* **2015**, *119*, 22057-22065; e) H. Qi, P. Yu, Y. Wang, G. Han, H. Liu, Y. Yi, Y. Li, L. Mao, *J. Am. Chem. Soc.* **2015**, *137*, 5260-5263; f) J. Li, X. Gao, B. Liu, Q. Feng, X. B. Li, M. Y. Huang, Z. Liu, J. Zhang, C. H. Tung, L. Z. Wu, *J. Am. Chem. Soc.* **2016**, *138*, 3954-3957.
- [79] a) S. Zhang, H. Du, J. He, C. Huang, H. Liu, G. Cui, Y. Li, *ACS Appl. Mater. Interfaces* **2016**, *8*, 8467-8473; b) C. S. Huang, S. L. Zhang, H. B. Liu, Y. J. Li, G. T. Cui, Y. L. Li, *Nano Energy* **2015**, *11*, 481-489; c) S. Zhang, H. Liu, C. Huang, G. Cui, Y. Li, *Chem. Commun.* **2015**, *51*, 1834-1837.
- [80] a) H. Ren, H. Shao, L. Zhang, D. Guo, Q. Jin, R. Yu, L. Wang, Y. Li, Y. Wang, H. Zhao, D. Wang, *Adv. Energy Mater.* **2015**, *5*, 1500296; b) C. Kuang, G. Tang, T. Jiu, H. Yang, H. Liu, B. Li, W. Luo, X. Li, W. Zhang, F. Lu, J. Fang, Y. Li, *Nano Lett.* **2015**, *15*, 2756-2762; c) J. Xiao, J. Shi, H. Liu, Y. Xu, S. Lv, Y. Luo, D. Li, Q. Meng,

- Y. Li, *Adv. Energy Mater.* **2015**, *5*, 1401943; d) H. Du, Z. Deng, Z. Lü, Y. Yin, L. Yu, H. Wu, Z. Chen, Y. Zou, Y. Wang, H. Liu, Y. Li, *Synth. Met.* **2011**, *161*, 2055-2057.
- [81] C. Wang, P. Yu, S. Guo, L. Mao, H. Liu, Y. Li, *Chem. Commun.* **2016**, *52*, 5629-5632.
- [82] X. Gao, J. Zhou, R. Du, Z. Xie, S. Deng, R. Liu, Z. Liu, J. Zhang, *Adv. Mater.* **2016**, *28*, 168-173.
- [83] I. Giaever, *Phys. Rev. Lett.* **1960**, *5*, 147-148.
- [84] G. Binnig, H. Rohrer, *IBM J. Res. Dev.* **2000**, *44*, 279-293.
- [85] J. Tersoff, D. R. Hamann, *Phys. Rev. B* **1985**, *31*, 805-813.
- [86] G. Doyen, D. Drakova, J. V. Barth, R. Schuster, T. Gritsch, R. J. Behm, G. Ertl, *Phys. Rev. B* **1993**, *48*, 1738-1749.
- [87] a) V. Madhavan, *Science* **1998**, *280*, 567-569; b) H. C. Manoharan, C. P. Lutz, D. M. Eigler, *Nature* **2000**, *403*, 512-515; c) P. Wahl, L. Diekhoner, G. Wittich, L. Vitali, M. A. Schneider, K. Kern, *Phys. Rev. Lett.* **2005**, *95*, 166601; d) A. Zhao, Q. Li, L. Chen, H. Xiang, W. Wang, S. Pan, B. Wang, X. Xiao, J. Yang, J. G. Hou, Q. Zhu, *Science* **2005**, *309*, 1542-1544; e) V. Iancu, A. Deshpande, S. W. Hla, *Nano Lett.* **2006**, *6*, 820-823; f) V. Iancu, A. Deshpande, S. W. Hla, *Phys. Rev. Lett.* **2006**, *97*, 266603; g) N. Neel, J. Kroger, L. Limot, K. Palotas, W. A. Hofer, R. Berndt, *Phys. Rev. Lett.* **2007**, *98*, 016801; h) I. Fernandez-Torrente, K. J. Franke, J. I. Pascual, *Phys. Rev. Lett.* **2008**, *101*, 217203; i) A. Zhao, Z. Hu, B. Wang, X. Xiao, J. Yang, J. G. Hou, *J. Chem. Phys.* **2008**, *128*, 234705; j) U. G. Perera, H. J. Kulik, V. Iancu, L. G. Dias da Silva, S. E. Ulloa, N. Marzari, S. W. Hla, *Phys. Rev. Lett.* **2010**, *105*, 106601; k) T. Komeda, H. Isshiki, J. Liu, Y. F. Zhang, N. Lorente, K. Katoh, B. K. Breedlove, M. Yamashita, *Nat. Commun.* **2011**, *2*, 217; l) J. Liu, H. Isshiki, K. Katoh, T. Morita, B. K. Breedlove, M. Yamashita, T. Komeda, *J. Am. Chem. Soc.* **2013**, *135*, 651-658.
- [88] a) T. Miyamachi, T. Schuh, T. Markl, C. Bresch, T. Balashov, A. Stohr, C. Karlewski, S. Andre, M. Marthaler, M. Hoffmann, M. Geilhufe, S. Ostanin, W. Hergert, I. Mertig, G. Schon, A. Ernst, W. Wulfhekel, *Nature* **2013**, *503*, 242-246; b) J. J. Li, M. L. Bai, Z. B. Chen, X. S. Zhou, Z. Shi, M. Zhang, S. Y. Ding, S. M. Hou, W. Schwarzacher, R. J. Nichols, B. W. Mao, *J. Am. Chem. Soc.* **2015**, *137*, 5923-5929.
- [89] S. Stepanow, N. Lin, J. V. Barth, *J. Phys.: Condens. Matter* **2008**, *20*, 184002.
- [90] J. Bjork, F. Hanke, *Chem. Eur. J.* **2014**, *20*, 928-934.
- [91] a) N. A. Wasio, R. C. Quardokus, R. P. Forrest, C. S. Lent, S. A. Corcelli, J. A. Christie, K. W. Henderson, S. A. Kandel, *Nature* **2014**, *507*, 86-89; b) L. Kampschulte, M. Lackinger, A. K. Maier, R. S. Kishore, S. Griessl, M. Schmittel, W. M. Heckl, *J. Phys. Chem. B* **2006**, *110*, 10829-10836; c) Y. Ye, W. Sun, Y. Wang, X. Shao, X. Xu, F. Cheng, J. Li, K. Wu, *J. Phys. Chem. C* **2007**, *111*, 10138-10141.
- [92] a) H. Kong, C. Zhang, L. Xie, L. Wang, W. Xu, *Angew. Chem., Int. Ed.* **2016**, *55*, 7157-7160; b) J. Li, S. Wiegold, M. A. Oner, P. Simon, M. V. Hauf, E. Margapoti, J. A. Garrido, F. Esch, C. A. Palma, J. V. Barth, *Nano Lett.* **2014**, *14*, 4486-4492; c) A. G. Slater, L. M. Perdigao, P. H. Beton, N. R. Champness, *Acc. Chem. Res.* **2014**, *47*, 3417-3427; d) C. Zhang, L. Xie, L. Wang, H. Kong, Q. Tan, W. Xu, *J. Am. Chem. Soc.* **2015**, *137*, 11795-11800.
- [93] U. Schlickum, R. Decker, F. Klappenberger, G. Zoppellaro, S. Klyatskaya, W. Auwärter, S. Neppel, K. Kern, H. Brune, M. Ruben, J. V. Barth, *J. Am. Chem. Soc.* **2008**, *130*, 11778-11782.
- [94] a) W. Auwärter, A. Weber-Bargioni, S. Brink, A. Riemann, A. Schiffrin, M. Ruben, J. V. Barth, *ChemPhysChem* **2007**, *8*, 250-254; b) Z. Shi, N. Lin, *ChemPhysChem* **2010**, *11*, 97-100.
- [95] a) A. Della Pia, M. Riello, J. Lawrence, D. Stassen, T. S. Jones, D. Bonifazi, A. De Vita, G. Costantini, *Chem. Eur. J.* **2016**, *22*, 8105-8112; b) D. Ecija, J. I. Urgel, A. C. Papageorgiou, S. Joshi, W. Auwärter, A. P. Seitsonen, S. Klyatskaya, M. Ruben, S.

- Fischer, S. Vijayaraghavan, J. Reichert, J. V. Barth, *Proc. Natl. Acad. Sci. U. S. A.* **2013**, *110*, 6678-6681; c) S. Fabris, S. Stepanow, N. Lin, P. Gambardella, A. Dmitriev, J. Honolka, S. Baroni, K. Kern, *Nano Lett.* **2011**, *11*, 5414-5420; d) P. Gambardella, S. Stepanow, A. Dmitriev, J. Honolka, F. M. F. De Groot, M. Lingenfelder, S. Sen Gupta, D. D. Sarma, P. Bencok, S. Stanesco, S. Clair, S. Pons, N. Lin, A. P. Seitsonen, H. Brune, J. V. Barth, K. Kern, *Nat. Mater.* **2009**, *8*, 189-193; e) T. Lin, G. Kuang, X. S. Shang, P. N. Liu, N. Lin, *Chem. Commun.* **2014**, *50*, 15327-15329; f) J. I. Urgel, B. Cirera, Y. Wang, W. Auwärter, R. Otero, J. M. Gallego, M. Alcami, S. Klyatskaya, M. Ruben, F. Martin, R. Miranda, D. Ecija, J. V. Barth, *Small* **2015**, *11*, 6358-6364; g) J. I. Urgel, D. Ecija, W. Auwärter, A. C. Papageorgiou, A. P. Seitsonen, S. Vijayaraghavan, S. Joshi, S. Fischer, J. Reichert, J. V. Barth, *J. Phys. Chem. C* **2014**, *118*, 12908-12915; h) J. I. Urgel, D. Ecija, G. Lyu, R. Zhang, C. A. Palma, W. Auwärter, N. Lin, J. V. Barth, *Nat. Chem.* **2016**, *8*, 657-662; i) P. B. Weber, R. Hellwig, T. Paintner, M. Lattelais, M. Paszkiewicz, P. Casado Aguilar, P. S. Deimel, Y. Guo, Y. Q. Zhang, F. Allegretti, A. C. Papageorgiou, J. Reichert, S. Klyatskaya, M. Ruben, J. V. Barth, M. L. Bocquet, F. Klappenberger, *Angew. Chem., Int. Ed.* **2016**, *55*, 5754-5759; j) B. Wurster, D. Grumelli, D. Hotger, R. Gutzler, K. Kern, *J. Am. Chem. Soc.* **2016**, *138*, 3623-3626.
- [96] a) M. Bieri, M. T. Nguyen, O. Groning, J. M. Cai, M. Treier, K. Ait-Mansour, P. Ruffieux, C. A. Pignedoli, D. Passerone, M. Kastler, K. Müllen, R. Fasel, *J. Am. Chem. Soc.* **2010**, *132*, 16669-16676; b) M. O. Blunt, J. C. Russell, N. R. Champness, P. H. Beton, *Chem. Commun.* **2010**, *46*, 7157-7159; c) J. Eichhorn, T. Strunskus, A. Rastgoo-Lahrood, D. Samanta, M. Schmittel, M. Lackinger, *Chem. Commun.* **2014**, *50*, 7680-7682; d) Q. Fan, C. Wang, Y. Han, J. Zhu, W. Hieringer, J. Kuttner, G. Hilt, J. M. Gottfried, *Angew. Chem., Int. Ed.* **2013**, *52*, 4668-4672; e) L. Grill, M. Dyer, L. Lafferentz, M. Persson, M. V. Peters, S. Hecht, *Nat. Nanotechnol.* **2007**, *2*, 687-691; f) S.-W. Hla, L. Bartels, G. Meyer, K.-H. Rieder, *Phys. Rev. Lett.* **2000**, *85*, 2777-2780; g) L. Lafferentz, F. Ample, H. Yu, S. Hecht, C. Joachim, L. Grill, *Science* **2009**, *323*, 1193-1197; h) T. Lin, X. S. Shang, J. Adisoejoso, P. N. Liu, N. Lin, *J. Am. Chem. Soc.* **2013**, *135*, 3576-3582.
- [97] a) J. Cai, C. A. Pignedoli, L. Talirz, P. Ruffieux, H. Sode, L. Liang, V. Meunier, R. Berger, R. Li, X. Feng, K. Müllen, R. Fasel, *Nat. Nanotechnol.* **2014**, *9*, 896-900; b) J. Cai, P. Ruffieux, R. Jaafar, M. Bieri, T. Braun, S. Blankenburg, M. Muoth, A. P. Seitsonen, M. Saleh, X. Feng, K. Müllen, R. Fasel, *Nature* **2010**, *466*, 470-473; c) P. Ruffieux, S. Wang, B. Yang, C. Sanchez-Sanchez, J. Liu, T. Dienel, L. Talirz, P. Shinde, C. A. Pignedoli, D. Passerone, T. Dumsclaff, X. Feng, K. Müllen, R. Fasel, *Nature* **2016**, *531*, 489-492.
- [98] M. Matena, T. Riehm, M. Stöhr, T. A. Jung, L. H. Gade, *Angew. Chem., Int. Ed.* **2008**, *47*, 2414-2417.
- [99] J. Eichhorn, W. M. Heckl, M. Lackinger, *Chem. Commun.* **2013**, *49*, 2900-2902.
- [100] Q. Sun, L. Cai, H. Ma, C. Yuan, W. Xu, *ACS Nano* **2016**, *10*, 7023-7030.
- [101] J. Liu, Q. Chen, L. Xiao, J. Shang, X. Zhou, Y. Zhang, Y. Wang, X. Shao, J. Li, W. Chen, G. Q. Xu, H. Tang, D. Zhao, K. Wu, *ACS Nano* **2015**, *9*, 6305-6314.
- [102] a) Q. Sun, C. Zhang, Z. W. Li, H. H. Kong, Q. G. Tan, A. G. Hu, W. Xu, *J. Am. Chem. Soc.* **2013**, *135*, 8448-8451; b) A. Riss, S. Wickenburg, P. Gorman, L. Z. Tan, H. Z. Tsai, D. G. de Oteyza, Y. C. Chen, A. J. Bradley, M. M. Ugeda, G. Etkin, S. G. Louie, F. R. Fischer, M. F. Crommie, *Nano Lett.* **2014**, *14*, 2251-2255.
- [103] a) S. Weigelt, C. Bombis, C. Busse, M. M. Knudsen, K. V. Gothelf, E. Lægsgaard, F. Besenbacher, T. R. Linderoth, *ACS Nano* **2008**, *2*, 651-660; b) S. Weigelt, C. Busse, C. Bombis, M. M. Knudsen, K. V. Gothelf, E. Lægsgaard, F. Besenbacher, T. R. Linderoth, *Angew. Chem., Int. Ed.* **2008**, *47*, 4406-4410; c) X.-H. Liu, C.-Z. Guan, S.-

- Y. Ding, W. Wang, H.-J. Yan, D. Wang, L.-J. Wan, *J. Am. Chem. Soc.* **2013**, *135*, 10470-10474; d) S. Weigelt, C. Busse, C. Bombis, M. M. Knudsen, K. V. Gothelf, T. Strunskus, C. Wöll, M. Dahlbom, B. Hammer, E. Lægsgaard, F. Besenbacher, T. R. Linderoth, *Angew. Chem., Int. Ed.* **2007**, *46*, 9227-9230.
- [104] a) J. F. Dienstmaier, A. M. Gigler, A. J. Goetz, P. Knochel, T. Bein, A. Lyapin, S. Reichlmaier, W. M. Heckl, M. Lackinger, *ACS Nano* **2011**, *5*, 9737-9745; b) S. Schlögl, T. Sirtl, J. Eichhorn, W. M. Heckl, M. Lackinger, *Chem. Commun.* **2011**, *47*, 12355-12357; c) J. F. Dienstmaier, D. D. Medina, M. Dogru, P. Knochel, T. Bein, W. M. Heckl, M. Lackinger, *ACS Nano* **2012**, *6*, 7234-7242; d) T. Faury, S. Clair, M. Abel, F. Dumur, D. Gimes, L. Porte, *J. Phys. Chem. C* **2012**, *116*, 4819-4823; e) C. Z. Guan, D. Wang, L. J. Wan, *Chem. Commun.* **2012**, *48*, 2943-2945.
- [105] a) M. Treier, N. V. Richardson, R. Fasel, *J. Am. Chem. Soc.* **2008**, *130*, 14054-14055; b) C. H. Schmitz, J. Ikonov, M. Sokolowski, *J. Phys. Chem. C* **2009**, *113*, 11984-11987; c) M. Treier, R. Fasel, N. R. Champness, S. Argent, N. V. Richardson, *Phys. Chem. Chem. Phys.* **2009**, *11*, 1209-1214; d) C. H. Schmitz, J. Ikonov, M. Sokolowski, *J. Phys. Chem. C* **2011**, *115*, 7270-7278.
- [106] B. Yang, J. Björk, H. Lin, X. Zhang, H. Zhang, Y. Li, J. Fan, Q. Li, L. Chi, *J. Am. Chem. Soc.* **2015**, *137*, 4904-4907.
- [107] a) O. D. Arado, H. Mönig, H. Wagner, J.-H. Franke, G. Langewisch, P. A. Held, A. Studer, H. Fuchs, *ACS Nano* **2013**, *7*, 8509-8515; b) F. Bebensee, C. Bombis, S.-R. Vadapoo, J. R. Cramer, F. Besenbacher, K. V. Gothelf, T. R. Linderoth, *J. Am. Chem. Soc.* **2013**, *135*, 2136-2139.
- [108] S. Boz, M. Stohr, U. Soydaner, M. Mayor, *Angew. Chem., Int. Ed.* **2009**, *48*, 3179-3183.
- [109] D. Xiang, X. Wang, C. Jia, T. Lee, X. Guo, *Chem. Rev.* **2016**, *116*, 4318-4440.
- [110] M. A. Reed, C. Zhou, C. J. Muller, T. P. Burgin, J. M. Tour, *Science* **1997**, *278*, 252-254.
- [111] C. Huang, A. V. Rudnev, W. Hong, T. Wandlowski, *Chem. Soc. Rev.* **2015**, *44*, 889-901.
- [112] H. Ohnishi, Y. Kondo, K. Takayanagi, *Nature* **1998**, *395*, 780-783.
- [113] V. Kaliginedi, P. Moreno-Garcia, H. Valkenier, W. Hong, V. M. Garcia-Suarez, P. Buitter, J. L. Otten, J. C. Hummelen, C. J. Lambert, T. Wandlowski, *J. Am. Chem. Soc.* **2012**, *134*, 5262-5275.
- [114] C. Jia, X. Guo, *Chem. Soc. Rev.* **2013**, *42*, 5642-5660.
- [115] F. Schwarz, E. Lortscher, *J. Phys. Condens. Matter.* **2014**, *26*, 474201.
- [116] M. L. Perrin, C. J. Verzijl, C. A. Martin, A. J. Shaikh, R. Eelkema, J. H. van Esch, J. M. van Ruitenbeek, J. M. Thijssen, H. S. van der Zant, D. Dulic, *Nat. Nanotechnol.* **2013**, *8*, 282-287.
- [117] a) S. Wagner, F. Kisslinger, S. Ballmann, F. Schramm, R. Chandrasekar, T. Bodenstein, O. Fuhr, D. Secker, K. Fink, M. Ruben, H. B. Weber, *Nat. Nanotechnol.* **2013**, *8*, 575-579; b) W. Hong, H. Valkenier, G. Meszaros, D. Z. Manrique, A. Mishchenko, A. Putz, P. M. Garcia, C. J. Lambert, J. C. Hummelen, T. Wandlowski, *Beilstein J. Nanotechnol.* **2011**, *2*, 699-713.
- [118] Y. Xing, T. H. Park, R. Venkatramani, S. Keinan, D. N. Beratan, M. J. Therien, E. Borguet, *J. Am. Chem. Soc.* **2010**, *132*, 7946-7956.
- [119] F. von Wrochem, D. Gao, F. Scholz, H. G. Nothofer, G. Nelles, J. M. Wessels, *Nat. Nanotechnol.* **2010**, *5*, 618-624.
- [120] P. Moreno-Garcia, M. Gulcur, D. Z. Manrique, T. Pope, W. Hong, V. Kaliginedi, C. Huang, A. S. Batsanov, M. R. Bryce, C. Lambert, T. Wandlowski, *J. Am. Chem. Soc.* **2013**, *135*, 12228-12240.
- [121] C. H. Ko, M. J. Huang, M. D. Fu, C. H. Chen, *J. Am. Chem. Soc.* **2010**, *132*, 756-764.

- [122] Y. S. Park, A. C. Whalley, M. Kamenetska, M. L. Steigerwald, M. S. Hybertsen, C. Nuckolls, L. Venkataraman, *J. Am. Chem. Soc.* **2007**, *129*, 15768-15769.
- [123] A. Mishchenko, L. A. Zotti, D. Vonlanthen, M. Burkle, F. Pauly, J. C. Cuevas, M. Mayor, T. Wandlowski, *J. Am. Chem. Soc.* **2011**, *133*, 184-187.
- [124] R. Parameswaran, J. R. Widawsky, H. Vázquez, Y. S. Park, B. M. Boardman, C. Nuckolls, M. L. Steigerwald, M. S. Hybertsen, L. Venkataraman, *J. Phys. Chem. Lett.* **2010**, *1*, 2114-2119.
- [125] F. Chen, X. Li, J. Hihath, Z. Huang, N. Tao, *J. Am. Chem. Soc.* **2006**, *128*, 15874-15881.
- [126] B. Kim, J. M. Beebe, Y. Jun, X. Y. Zhu, C. D. Frisbie, *J. Am. Chem. Soc.* **2006**, *128*, 4970-4971.
- [127] a) C. A. Martin, D. Ding, J. K. Sorensen, T. Bjornholm, J. M. van Ruitenbeek, H. S. van der Zant, *J. Am. Chem. Soc.* **2008**, *130*, 13198-13199; b) S. T. Schneebeli, M. Kamenetska, Z. Cheng, R. Skouta, R. A. Friesner, L. Venkataraman, R. Breslow, *J. Am. Chem. Soc.* **2011**, *133*, 2136-2139.
- [128] Z. L. Cheng, R. Skouta, H. Vazquez, J. R. Widawsky, S. Schneebeli, W. Chen, M. S. Hybertsen, R. Breslow, L. Venkataraman, *Nat. Nanotechnol.* **2011**, *6*, 353-357.
- [129] W. Chen, J. R. Widawsky, H. Vazquez, S. T. Schneebeli, M. S. Hybertsen, R. Breslow, L. Venkataraman, *J. Am. Chem. Soc.* **2011**, *133*, 17160-17163.
- [130] T. Hines, I. Diez-Perez, H. Nakamura, T. Shimazaki, Y. Asai, N. Tao, *J. Am. Chem. Soc.* **2013**, *135*, 3319-3322.
- [131] W. Hong, H. Li, S. X. Liu, Y. Fu, J. Li, V. Kaliginedi, S. Decurtins, T. Wandlowski, *J. Am. Chem. Soc.* **2012**, *134*, 19425-19431.
- [132] a) J. Hihath, N. Tao, *Semicond. Sci. Technol.* **2014**, *29*, 054007; b) N. J. Tao, *Nat. Nanotechnol.* **2006**, *1*, 173-181.
- [133] B. Gotsmann, H. Riel, E. Lörtscher, *Phys. Rev. B* **2011**, *84*, 205408.
- [134] Q. Lu, K. Liu, H. Zhang, Z. Du, X. Wang, F. Wang, *ACS Nano* **2009**, *3*, 3861-3868.
- [135] a) S. Wu, M. T. Gonzalez, R. Huber, S. Grunder, M. Mayor, C. Schonenberger, M. Calame, *Nat. Nanotechnol.* **2008**, *3*, 569-574; b) R. Huber, M. T. Gonzalez, S. Wu, M. Langer, S. Grunder, V. Horhoiu, M. Mayor, M. R. Bryce, C. Wang, R. Jitchati, C. Schonenberger, M. Calame, *J. Am. Chem. Soc.* **2008**, *130*, 1080-1084.
- [136] a) R. Yamada, H. Kumazawa, T. Noutoshi, S. Tanaka, H. Tada, *Nano Lett.* **2008**, *8*, 1237-1240; b) L. Luo, A. Benameur, P. Brignou, S. H. Choi, S. Rigaut, C. D. Frisbie, *J. Phys. Chem. C* **2011**, *115*, 19955-19961.
- [137] S. Ho Choi, B. Kim, C. D. Frisbie, *Science* **2008**, *320*, 1482-1486.
- [138] a) J. M. Tarascon, M. Armand, *Nature* **2001**, *414*, 359-367; b) M. Armand, J. M. Tarascon, *Nature* **2008**, *451*, 652-657.
- [139] R. M. Dell, *Solid State Ionics* **2000**, *134*, 139-158.
- [140] P. G. Bruce, *Solid State Ionics* **2008**, *179*, 752-760.
- [141] a) M. A. Kiani, M. F. Mousavi, M. S. Rahmanifar, *Int. J. Electrochem. Sci.* **2011**, *6*, 2581-2595; b) T. Ohzuku, A. Ueda, *J. Electrochem. Soc.* **1994**, *141*, 2972-2977.
- [142] J. M. Tarascon, *J. Electrochem. Soc.* **1991**, *138*, 2864-2868.
- [143] a) C. Delacourt, L. Laffont, R. Bouchet, C. Wurm, J.-B. Leriche, M. Morcrette, J.-M. Tarascon, C. Masquelier, *J. Electrochem. Soc.* **2005**, *152*, 913-921; b) S. Shi, C. Ouyang, Z. Xiong, L. Liu, Z. Wang, H. Li, D.-s. Wang, L. Chen, X. Huang, *Phys. Rev. B* **2005**, *71*, 1-6.
- [144] a) P. G. Bruce, S. A. Freunberger, L. J. Hardwick, J. M. Tarascon, *Nat. Mater.* **2012**, *11*, 19-29; b) X. L. Ji, L. F. Nazar, *J. Mater. Chem.* **2010**, *20*, 9821-9826.
- [145] J. Xu, S. Dou, H. Liu, L. Dai, *Nano Energy* **2013**, *2*, 439-442.
- [146] a) Y. P. Wu, E. Rahm, R. Holze, *J. Power Sources* **2003**, *114*, 228-236; b) E. Peled, *J. Electrochem. Soc.* **1996**, *143*, 4-7.

- [147] B. J. Landi, M. J. Ganter, C. D. Cress, R. A. DiLeo, R. P. Raffaele, *Energy Environ. Sci.* **2009**, *2*, 638-654.
- [148] C. Kim, K. S. Yang, M. Kojima, K. Yoshida, Y. J. Kim, Y. A. Kim, M. Endo, *Adv. Funct. Mater.* **2006**, *16*, 2393-2397.
- [149] J. Hou, Y. Shao, M. W. Ellis, R. B. Moore, B. Yi, *Phys. Chem. Chem. Phys.* **2011**, *13*, 15384-15402.
- [150] H. Zhou, S. Zhu, M. Hibino, I. Honma, M. Ichihara, *Adv. Mater.* **2003**, *15*, 2107-2111.
- [151] a) F. Zou, X. Hu, Z. Li, L. Qie, C. Hu, R. Zeng, Y. Jiang, Y. Huang, *Adv. Mater.* **2014**, *26*, 6622-6628; b) Z. Zhang, H. Yoshikawa, K. Awaga, *J. Am. Chem. Soc.* **2014**, *136*, 16112-16115; c) R. Wu, D. P. Wang, X. Rui, B. Liu, K. Zhou, A. W. Law, Q. Yan, J. Wei, Z. Chen, *Adv. Mater.* **2015**, *27*, 3038-3044; d) M. Wang, H. Yang, X. Zhou, W. Shi, Z. Zhou, P. Cheng, *Chem. Commun.* **2016**, *52*, 717-720; e) S.-L. Li, Q. Xu, *Energy Environ. Sci.* **2013**, *6*, 1656-1683; f) M. L. Aubrey, J. R. Long, *J. Am. Chem. Soc.* **2015**, *137*, 13594-13602.
- [152] a) A. S. Nagelberg, W. L. Worrell, *J. Solid State Chem.* **1979**, *29*, 345-354; b) Y. Cao, L. Xiao, W. Wang, D. Choi, Z. Nie, J. Yu, L. V. Saraf, Z. Yang, J. Liu, *Adv. Mater.* **2011**, *23*, 3155-3160.
- [153] a) Z. Jian, W. Luo, X. Ji, *J. Am. Chem. Soc.* **2015**, *137*, 11566-11569; b) Y. Chen, W. Luo, M. Carter, L. Zhou, J. Dai, K. Fu, S. Lacey, T. Li, J. Wan, X. Han, Y. Bao, L. Hu, *Nano Energy* **2015**, *18*, 205-211.
- [154] a) A. L. Lipson, B. Pan, S. H. Lapidus, C. Liao, J. T. Vaughey, B. J. Ingram, *Chem. Mater.* **2015**, *27*, 8442-8447; b) A. Ponrouch, C. Frontera, F. Barde, M. R. Palacin, *Nat. Mater.* **2016**, *15*, 169-172.
- [155] a) C. Kim, P. J. Phillips, B. Key, T. Yi, D. Nordlund, Y. S. Yu, R. D. Bayliss, S. D. Han, M. He, Z. Zhang, A. K. Burrell, R. F. Klie, J. Cabana, *Adv. Mater.* **2015**, *27*, 3377-3384; b) Z. Zhao-Karger, X. Zhao, D. Wang, T. Diemant, R. J. Behm, M. Fichtner, *Adv. Energy Mater.* **2015**, *5*, 1401155.
- [156] M. C. Lin, M. Gong, B. Lu, Y. Wu, D. Y. Wang, M. Guan, M. Angell, C. Chen, J. Yang, B. J. Hwang, H. Dai, *Nature* **2015**, *520*, 325-328.
- [157] a) Z. Song, H. Zhou, *Energy Environ. Sci.* **2013**, *6*, 2280-2301; b) Y. Liang, Z. Tao, J. Chen, *Adv. Energy Mater.* **2012**, *2*, 742-769.
- [158] a) K. Naoi, *J. Electrochem. Soc.* **1997**, *144*, 173-175; b) S.-R. Deng, L.-B. Kong, G.-Q. Hu, T. Wu, D. Li, Y.-H. Zhou, Z.-Y. Li, *Electrochim. Acta* **2006**, *51*, 2589-2593.
- [159] a) Z. Lei, W. Wei-kun, W. An-bang, Y. Zhong-bao, C. Shi, Y. Yu-sheng, *J. Electrochem. Soc.* **2011**, *158*, 991-996; b) Z. Song, H. Zhan, Y. Zhou, *Chem. Commun.* **2009**, 448-450; c) H. Chen, M. Armand, G. Demailly, F. Dolhem, P. Poizot, J. M. Tarascon, *ChemSusChem* **2008**, *1*, 348-355.
- [160] D. L. Williams, J. J. Byrne, J. S. Driscoll, *J. Electrochem. Soc.* **1969**, *116*, 2-4.
- [161] X. Wu, S. Jin, Z. Zhang, L. Jiang, L. Mu, Y. S. Hu, H. Li, X. Chen, M. Armand, L. Chen, X. Huang, *Sci. Adv.* **2015**, *1*, 1500330.
- [162] a) M. Armand, S. Grugeon, H. Vezin, S. Laruelle, P. Ribiere, P. Poizot, J. M. Tarascon, *Nat. Mater.* **2009**, *8*, 120-125; b) S. Wang, L. Wang, Z. Zhu, Z. Hu, Q. Zhao, J. Chen, *Angew. Chem., Int. Ed.* **2014**, *53*, 5892-5896.
- [163] a) A. G. MacDiarmid, L. S. Yang, W. S. Huang, B. D. Humphrey, *Synth. Met.* **1987**, *18*, 393-398; b) M. Zhou, J. Qian, X. Ai, H. Yang, *Adv. Mater.* **2011**, *23*, 4913-4917.
- [164] a) L. Zhan, Z. Song, J. Zhang, J. Tang, H. Zhan, Y. Zhou, C. Zhan, *Electrochim. Acta* **2008**, *53*, 8319-8323; b) L. Zhan, Z. Song, N. Shan, J. Zhang, J. Tang, H. Zhan, Y. Zhou, Z. Li, C. Zhan, *J. Power Sources* **2009**, *193*, 859-863.
- [165] a) P. J. Nigrey, *J. Electrochem. Soc.* **1982**, *129*, 1271; b) L. M. Zhu, A. W. Lei, Y. L. Cao, X. P. Ai, H. X. Yang, *Chem. Commun.* **2013**, *49*, 567-569.

- [166] a) K. Nakahara, S. Iwasa, M. Satoh, Y. Morioka, J. Iriyama, M. Suguro, E. Hasegawa, *Chem. Phys. Lett.* **2002**, 359, 351-354; b) M. Suguro, S. Iwasa, Y. Kusachi, Y. Morioka, K. Nakahara, *Macromol. Rapid Commun.* **2007**, 28, 1929-1933; c) K. Nakahara, K. Oyaizu, H. Nishide, *Chem. Lett.* **2011**, 40, 222-227; d) T. Suga, S. Sugita, H. Ohshiro, K. Oyaizu, H. Nishide, *Adv. Mater.* **2011**, 23, 751-754.
- [167] a) F. Xu, H. Xu, X. Chen, D. Wu, Y. Wu, H. Liu, C. Gu, R. Fu, D. Jiang, *Angew. Chem., Int. Ed.* **2015**, 54, 6814-6818; b) Z. Li, G. Ma, R. Ge, F. Qin, X. Dong, W. Meng, T. Liu, J. Tong, F. Jiang, Y. Zhou, K. Li, X. Min, K. Huo, Y. Zhou, *Angew. Chem., Int. Ed.* **2016**, 55, 979-982.
- [168] H. Nishide, Suga, T, *Electrochem. Soc. Interface* **2005**, 32-36.
- [169] a) S. Rothermel, P. Meister, G. Schmuelling, O. Fromm, H.-W. Meyer, S. Nowak, M. Winter, T. Placke, *Energy Environ. Sci.* **2014**, 7, 3412-3423; b) T. Placke, O. Fromm, S. F. Lux, P. Bieker, S. Rothermel, H.-W. Meyer, S. Passerini, M. Winter, *J. Electrochem. Soc.* **2012**, 159, 1755-1765; c) T. Placke, S. Rothermel, O. Fromm, P. Meister, S. F. Lux, J. Huesker, H.-W. Meyer, M. Winter, *J. Electrochem. Soc.* **2013**, 160, 1979-1991.
- [170] H. Maruyama, H. Nakano, M. Nakamoto, A. Sekiguchi, *Angew. Chem., Int. Ed.* **2014**, 53, 1324-1328.
- [171] J. Y. Shin, T. Yamada, H. Yoshikawa, K. Awaga, H. Shinokubo, *Angew. Chem., Int. Ed.* **2014**, 53, 3096-3101.
- [172] a) M. Noel, R. Santhanam, *J. Power Sources* **1998**, 72, 53-65; b) T. Placke, G. Schmuelling, R. Kloepsch, P. Meister, O. Fromm, P. Hilbig, H.-W. Meyer, M. Winter, *Z. Anorg. Allg. Chem.* **2014**, 640, 1996-2006; c) P. Meister, V. Siozios, J. Reiter, S. Klamor, S. Rothermel, O. Fromm, H.-W. Meyer, M. Winter, T. Placke, *Electrochim. Acta* **2014**, 130, 625-633.
- [173] J. B. Goodenough, K. Mizushima, Google Patents, **1981**.
- [174] G. N. Patwari, P. Venuvanalingam, M. Kołaski, *Chem. Phys.* **2013**, 415, 150-155.
- [175] H.-Y. Gao, D. Zhong, H. Mönig, H. Wagner, P.-A. Held, A. Timmer, A. Studer, H. Fuchs, *J. Phys. Chem. C* **2014**, 118, 6272-6277.
- [176] a) S. Anderson, H. L. Anderson, J. K. M. Sanders, *Acc. Chem. Res.* **1993**, 26, 469-475; b) L. Fang, S. Basu, C. H. Sue, A. C. Fahrenbach, J. F. Stoddart, *J. Am. Chem. Soc.* **2011**, 133, 396-399; c) M. C. O'Sullivan, J. K. Sprafke, D. V. Kondratuk, C. Rinfray, T. D. W. Claridge, A. Saywell, M. O. Blunt, J. N. O'Shea, P. H. Beton, M. Malfois, H. L. Anderson, *Nature* **2011**, 469, 72-75.
- [177] a) T. Zambelli, J. Wintterlin, J. Trost, G. Ertl, *Science* **1996**, 273, 1688-1690; b) A. Saywell, J. Schwarz, S. Hecht, L. Grill, *Angew. Chem., Int. Ed.* **2012**, 51, 5096-5100.
- [178] M. E. Cañas-Ventura, W. Xiao, D. Wasserfallen, K. Müllen, H. Brune, J. V. Barth, R. Fasel, *Angew. Chem. Int. Ed.* **2007**, 46, 1814-1818.
- [179] G. Kresse, J. Furthmüller, *Phys. Rev. B* **1996**, 54, 11169-11186.
- [180] P. E. Blöchl, *Phys. Rev. B* **1994**, 50, 17953-17979.
- [181] J. P. Perdew, K. Burke, M. Ernzerhof, *Phys. Rev. Lett.* **1996**, 77, 3865-3868.
- [182] M. Vladimirova, M. Stengel, A. De Vita, A. Baldereschi, M. Böhringer, K. Morgenstern, R. Berndt, W. D. Schneider, *Europhys. Lett.* **2001**, 56, 254-260.
- [183] D. Philp, J. M. A. Robinson, *J. Chem. Soc., Perkin Trans. 2* **1998**, 1643-1650.
- [184] D. Heim, D. Écija, K. Seufert, W. Auwärter, C. Aurisicchio, C. Fabbro, D. Bonifazi, J. V. Barth, *J. Am. Chem. Soc.* **2010**, 132, 6783-6790.
- [185] Q. Sun, L. Cai, Y. Ding, L. Xie, C. Zhang, Q. Tan, W. Xu, *Angew. Chem., Int. Ed.* **2015**, 54, 4549-4552.
- [186] a) V. Gevorgyan, K. Tando, N. Uchiyama, Y. Yamamoto, *J. Org. Chem.* **1998**, 63, 7022-7025; b) M. Rubina, M. Conley, V. Gevorgyan, *J. Am. Chem. Soc.* **2006**, 128,

- 5818-5827; c) F. Punner, G. Hilt, *Chem. Commun.* **2012**, 48, 3617-3619; d) P. Rose, C. C. Garcia, F. Punner, K. Harms, G. Hilt, *J. Org. Chem.* **2015**, 80, 7311-7316.
- [187] M. Wilms, P. Broekmann, C. Stuhlmann, K. Wandelt, *Surf. Sci.* **1998**, 416, 121-140.
- [188] S. Nakanishi, T. Horiguchi, *Jpn. J. Appl. Phys.* **1981**, 20, 214-216.
- [189] N. Kepčija, Y.-Q. Zhang, M. Kleinschrodt, J. Björk, S. Klyatskaya, F. Klappenberger, M. Ruben, J. V. Barth, *J. Phys. Chem. C* **2013**, 117, 3987-3995.
- [190] a) F. Vidal, E. Delvigne, S. Stepanow, N. Lin, J. V. Barth, K. Kern, *J. Am. Chem. Soc.* **2005**, 127, 10101-10106; b) M. Forster, M. S. Dyer, M. Persson, R. Raval, *Angew. Chem., Int. Ed.* **2010**, 49, 2344-2348; c) N. Abdurakhmanova, A. Floris, T. C. Tseng, A. Comisso, S. Stepanow, A. De Vita, K. Kern, *Nat. Commun.* **2012**, 3, 940.
- [191] a) R. Cortes, A. Mascaraque, P. Schmidt-Weber, H. Dil, T. U. Kampen, K. Horn, *Nano Lett.* **2008**, 8, 4162-4167; b) J. B. Lin, Z. X. Guo, J. Plas, D. B. Amabilino, S. De Feyter, A. P. H. J. Schenning, *Chem. Commun.* **2013**, 49, 9320-9322; c) J. Seibel, M. Parschau, K.-H. Ernst, *J. Am. Chem. Soc.* **2015**, 137, 7970-7973; d) M. Böhringer, W.-D. Schneider, R. Berndt, *Angew. Chem., Int. Ed.* **2000**, 39, 792-795.
- [192] F. Vidal, E. Delvigne, S. Stepanow, N. Lin, J. V. Barth, K. Kern, *J. Am. Chem. Soc.* **2005**, 127, 10101-10106.
- [193] Z. Chen, S. Klyatskaya, J. I. Urgel, D. Ecija, O. Fuhr, W. Auwärter, J. V. Barth, M. Ruben, *Beilstein J. Nanotechnol.* **2015**, 6, 327-335.
- [194] a) S. Cotton, *Electronic and Magnetic Properties of the Lanthanides*, John Wiley & Sons: Chichester, United Kingdom, **2006**; b) J. D. Rinehart, J. R. Long, *Chem. Sci.* **2011**, 2, 2078.
- [195] L. Bogani, W. Wernsdorfer, *Nat. Mater.* **2008**, 7, 179-186.
- [196] a) M. Urdampilleta, S. Klyatskaya, J. P. Cleuziou, M. Ruben, W. Wernsdorfer, *Nat. Mater.* **2011**, 10, 502-506; b) S. Sanvito, *Nat. Mater.* **2011**, 10, 484-485; c) R. Vincent, S. Klyatskaya, M. Ruben, W. Wernsdorfer, F. Balestro, *Nature* **2012**, 488, 357-360; d) S. Thiele, F. Balestro, R. Ballou, S. Klyatskaya, M. Ruben, W. Wernsdorfer, *Science* **2014**, 344, 1135-1138; e) M. Urdampilleta, N. V. Nguyen, J. P. Cleuziou, S. Klyatskaya, M. Ruben, W. Wernsdorfer, *Int. J. Mol. Sci.* **2011**, 12, 6656-6667; f) M. Ganzhorn, S. Klyatskaya, M. Ruben, W. Wernsdorfer, *ACS Nano* **2013**, 7, 6225-6236; g) M. Lopes, A. Candini, M. Urdampilleta, A. Reserbat-Plantey, V. Bellini, S. Klyatskaya, L. Marty, M. Ruben, M. Affronte, W. Wernsdorfer, N. Bendiab, *ACS Nano* **2010**, 4, 7531-7537; h) A. Candini, S. Klyatskaya, M. Ruben, W. Wernsdorfer, M. Affronte, *Nano Lett.* **2011**, 11, 2634-2639.
- [197] a) U. Schlickum, R. Decker, F. Klappenberger, G. Zoppellaro, S. Klyatskaya, M. Ruben, I. Silanes, A. Arnau, K. Kern, H. Brune, J. V. Barth, *Nano Lett.* **2007**, 7, 3813-3817; b) S. Klyatskaya, F. Klappenberger, U. Schlickum, D. Kühne, M. Marschall, J. Reichert, R. Decker, W. Krenner, G. Zoppellaro, H. Brune, J. V. Barth, M. Ruben, *Adv. Funct. Mater.* **2011**, 21, 1230-1240.
- [198] a) J. C. Bunzli, *Acc. Chem. Res.* **2006**, 39, 53-61; b) J.-C. G. Bünzli, N. André, M. Elhabiri, G. Muller, C. Piguet, *J. Alloys Compd.* **2000**, 303-304, 66-74.
- [199] R. J. Taylor, G. D. McAllister, C. D. Wilfred, *Synlett* **2002**, 1291-1292.
- [200] D. Kühne, F. Klappenberger, R. g. Decker, U. Schlickum, H. Brune, S. Klyatskaya, M. Ruben, J. V. Barth, *J. Phys. Chem. C* **2009**, 113, 17851-17859.
- [201] a) J. Reichert, M. Marschall, K. Seufert, D. Ecija, W. Auwärter, E. Arras, S. Klyatskaya, M. Ruben, J. V. Barth, *J. Phys. Chem. C* **2013**, 117, 12858-12863; b) M. Marschall, J. Reichert, A. Weber-Bargioni, K. Seufert, W. Auwärter, S. Klyatskaya, G. Zoppellaro, M. Ruben, J. V. Barth, *Nat. Chem.* **2010**, 2, 131-137; c) S. Stepanow, T. Strunskus, M. Lingenfelder, A. Dmitriev, H. Spillmann, N. Lin, J. V. Barth, C. Wöll, K. Kern, *J. Phys. Chem. B* **2004**, 108, 19392-19397; d) U. Schlickum, F. Klappenberger, R. Decker, G. Zoppellaro, S. Klyatskaya, M. Ruben, K. Kern, H.

- Brune, J. V. Barth, *J. Phys. Chem. C* **2010**, *114*, 15602-15606; e) M. Marschall, J. Reichert, K. Seufert, W. Auwärter, F. Klappenberger, A. Weber-Bargioni, S. Klyatskaya, G. Zoppellaro, A. Nefedov, T. Strunskus, C. Woll, M. Ruben, J. V. Barth, *ChemPhysChem* **2010**, *11*, 1446-1451.
- [202] Z. Shi, C. Zhang, S. Li, D. Pan, S. Ding, Y. Cui, N. Jiao, *Angew. Chem., Int. Ed.* **2009**, *48*, 4572-4576.
- [203] D. Kühne, F. Klappenberger, R. Decker, U. Schlickum, H. Brune, S. Klyatskaya, M. Ruben, J. V. Barth, *J. Am. Chem. Soc.* **2009**, *131*, 3881-3883.
- [204] J. V. Barth, *Annu. Rev. Phys. Chem.* **2007**, *58*, 375-407.
- [205] a) Y. R. Chen, W. L. Duan, *J. Am. Chem. Soc.* **2013**, *135*, 16754-16757; b) P. Reutenauer, M. Kivala, P. D. Jarowski, C. Boudon, J.-P. Gisselbrecht, M. Gross, F. Diederich, *Chem. Commun.* **2007**, 4898; c) Z. T. Fomum, P. F. Asobo, S. R. Landor, P. D. Landor, *J. Chem. Soc., Perkin Trans. 1* **1984**, 1079-1083; d) N. E. Heard, J. Turner, *J. Org. Chem.* **1995**, *60*, 4302-4304; e) V. V. N. S. R. Rao, B. P. B. Lingaiah, G. Ezikiel, R. Yadla, P. S. Rao, *Heterocycl. Commun.* **2006**, *12*, 275-280.
- [206] a) Y. Sohn, W. Wei, J. M. White, *Langmuir* **2007**, *23*, 12185-12191; b) Y. Sohn, W. Wei, J. M. White, *J. Phys. Chem. C* **2007**, *111*, 5101-5110.
- [207] M. Ruben, *Angew. Chem., Int. Ed.* **2005**, *44*, 1594-1596.
- [208] K. Kobayashi, N. Kobayashi, M. Ikuta, B. Therrien, S. Sakamoto, K. Yamaguchi, *J. Org. Chem.* **2005**, *70*, 749-752.
- [209] E. C. Constable, O. Eich, D. Fenske, C. E. Housecroft, L. A. Johnston, *Chem. Eur. J.* **2000**, *6*, 4364-4370.
- [210] P. Siemsen, R. C. Livingston, F. Diederich, *Angew. Chem., Int. Ed.* **2000**, *39*, 2632-2657.
- [211] G. Zhang, H. Yi, G. Zhang, Y. Deng, R. Bai, H. Zhang, J. T. Miller, A. J. Kropf, E. E. Bunel, A. Lei, *J. Am. Chem. Soc.* **2014**, *136*, 924-926.
- [212] A. C. Ferrari, J. C. Meyer, V. Scardaci, C. Casiraghi, M. Lazzeri, F. Mauri, S. Piscanec, D. Jiang, K. S. Novoselov, S. Roth, A. K. Geim, *Phys. Rev. Lett.* **2006**, *97*, 187401.
- [213] H. Estrade-Szwarczkopf, *Carbon* **2004**, *42*, 1713-1721.
- [214] I. Alexandrou, H. J. Scheibe, C. J. Kiely, A. J. Papworth, G. A. J. Amaratunga, B. Schultrich, *Phys. Rev. B* **1999**, *60*, 10903-10907.
- [215] A. Reina, X. Jia, J. Ho, D. Nezich, H. Son, V. Bulovic, M. S. Dresselhaus, J. Kong, *Nano Lett.* **2009**, *9*, 30-35.
- [216] R. Müller, S. De Jonge, K. Myny, D. J. Wouters, J. Genoe, P. Heremans, *Solid-State Electron.* **2006**, *50*, 601-605.
- [217] R. Müller, R. Naulaerts, J. Billen, J. Genoe, P. Heremans, *Appl. Phys. Lett.* **2007**, *90*, 063503.
- [218] I. J. Olavarria-Contreras, M. L. Perrin, Z. Chen, S. Klyatskaya, M. Ruben, H. S. van der Zant, *J. Am. Chem. Soc.* **2016**, *138*, 8465-8469.
- [219] S. Sangtarash, C. Huang, H. Sadeghi, G. Sorohhov, J. Hauser, T. Wandlowski, W. Hong, S. Decurtins, S. X. Liu, C. J. Lambert, *J. Am. Chem. Soc.* **2015**, *137*, 11425-11431.
- [220] a) S. Takahashi, Y. Kuroyama, K. Sonogashira, N. Hagihara, *Synthesis* **1980**, *1980*, 627-630; b) I. O. Koshevoy, C. L. Lin, A. J. Karttunen, J. Janis, M. Haukka, S. P. Tunik, P. T. Chou, T. A. Pakkanen, *Inorg. Chem.* **2011**, *50*, 2395-2403.
- [221] L. L. Schafer, J. R. Nitschke, S. S. H. Mao, F.-Q. Liu, G. Harder, M. Haufe, T. D. Tilley, *Chem. Eur. J.* **2002**, *8*, 74-83.
- [222] C. A. Martin, J. M. van Ruitenbeek, H. S. van der Zant, *Nanotechnology* **2010**, *21*, 265201.

- [223] C. A. Martin, R. H. Smit, R. van Egmond, H. S. van der Zant, J. M. van Ruitenbeek, *Rev. Sci. Instrum.* **2011**, *82*, 053907.
- [224] J. R. Widawsky, W. Chen, H. Vazquez, T. Kim, R. Breslow, M. S. Hybertsen, L. Venkataraman, *Nano Lett.* **2013**, *13*, 2889-2894.
- [225] S. Martin, I. Grace, M. R. Bryce, C. Wang, R. Jitchati, A. S. Batsanov, S. J. Higgins, C. J. Lambert, R. J. Nichols, *J. Am. Chem. Soc.* **2010**, *132*, 9157-9164.
- [226] a) D. J. Wold, R. Haag, M. A. Rampi, C. D. Frisbie, *J. Phys. Chem. B* **2002**, *106*, 2813-2816; b) C. J. Querebillo, A. Terfort, D. L. Allara, M. Zharnikov, *J. Phys. Chem. C* **2013**, *117*, 25556-25561; c) D. M. Adams, L. Brus, C. E. D. Chidsey, S. Creager, C. Creutz, C. R. Kagan, P. V. Kamat, M. Lieberman, S. Lindsay, R. A. Marcus, R. M. Metzger, M. E. Michel-Beyerle, J. R. Miller, M. D. Newton, D. R. Rolison, O. Sankey, K. S. Schanze, J. Yardley, X. Zhu, *J. Phys. Chem. B* **2003**, *107*, 6668-6697.
- [227] a) B. Capozzi, E. J. Dell, T. C. Berkelbach, D. R. Reichman, L. Venkataraman, L. M. Campos, *J. Am. Chem. Soc.* **2014**, *136*, 10486-10492; b) B. Q. Xu, X. L. Li, X. Y. Xiao, H. Sakaguchi, N. J. Tao, *Nano Lett.* **2005**, *5*, 1491-1495.
- [228] a) M. J. Ford, R. C. Hoft, A. McDonagh, *J. Phys. Chem. B* **2005**, *109*, 20387-20392; b) H.-Y. Gao, J.-H. Franke, H. Wagner, D. Zhong, P.-A. Held, A. Studer, H. Fuchs, *J. Phys. Chem. C* **2013**, *117*, 18595-18602; c) A. M. McDonagh, H. M. Zareie, M. J. Ford, C. S. Barton, M. Ginic-Markovic, J. G. Matison, *J. Am. Chem. Soc.* **2007**, *129*, 3533-3538.
- [229] S. Y. Quek, L. Venkataraman, H. J. Choi, S. G. Louie, M. S. Hybertsen, J. B. Neaton, *Nano Lett.* **2007**, *7*, 3477-3482.
- [230] a) T. Kakui, S. Sugawara, Y. Hirata, S. Kojima, Y. Yamamoto, *Chem. Eur. J.* **2011**, *17*, 7768-7771; b) C. Liu, D.-M. Shen, Q.-Y. Chen, *J. Am. Chem. Soc.* **2007**, *129*, 5814-5815; c) Y. Yamamoto, A. Yamamoto, S.-y. Furuta, M. Horie, M. Kodama, W. Sato, K.-y. Akiba, S. Tsuzuki, T. Uchimaru, D. Hashizume, F. Iwasaki, *J. Am. Chem. Soc.* **2005**, *127*, 14540-14541.
- [231] a) M.-s. Liao, S. Scheiner, *J. Chem. Phys.* **2002**, *117*, 205-219; b) K. M. Kadish, Æ. E. V. Caemelbecke, *J. Solid State Electrochem.* **2003**, *7*, 254-258.
- [232] K. M. Kadish, K. M. Smith, Â. S. Gabriel, R. Guilard, *The Porphyrin Handbook Editors*, Academic Press, **2003**.
- [233] a) S. Prathapan, T. E. Johnson, J. S. Lindsey, *J. Am. Chem. Soc.* **1993**, *115*, 7519-7520; b) R. Stranger, J. E. McGrady, D. P. Arnold, I. Lane, G. A. Heath, *Inorg. Chem.* **1996**, *35*, 7791-7797; c) V. S. Lin, S. G. Dimagno, M. J. Therien, *Science* **1994**, *264*, 1105-1111.
- [234] a) C. A. Hunter, J. K. M. Sanders, *J. Am. Chem. Soc.* **1990**, *112*, 5525-5534; b) C. J. Medforth, Z. Wang, K. E. Martin, Y. Song, J. L. Jacobsen, J. A. Shelnutt, *Chem. Commun.* **2009**, *9*, 7261-7277.
- [235] M. Inamo, H. Kumagai, U. Harada, S. Itoh, S. Iwatsuki, K. Ishihara, H. D. Takagi, *Dalton Trans.* **2004**, *11*, 1703-1707.
- [236] M. Okubo, E. Hosono, J. Kim, M. Enomoto, N. Kojima, T. Kudo, H. Zhou, I. Honma, *J. Am. Chem. Soc.* **2007**, *129*, 7444-7452.
- [237] Z. Zhang, H. Yoshikawa, K. Awaga, *Chem. Mater.* **2016**, *28*, 1298-1303.
- [238] X. Feng, W. Pisula, L. Zhi, M. Takase, K. Müllen, *Angew. Chem., Int. Ed.* **2008**, *47*, 1703-1706.
- [239] Y. J. Cheng, T. Y. Luh, *Chem. Eur. J.* **2004**, *10*, 5361-5368.
- [240] E. C. Constable, O. Eich, D. Fenske, C. E. Housecroft, L. A. Johnston, *Chem. Eur. J.* **2000**, *6*, 4364-4370.
- [241] L. H. Thoresen, G. S. Jiao, W. C. Haaland, M. L. Metzker, K. Burgess, *Chem. Eur. J.* **2003**, *9*, 4603-4610.
- [242] G. M. Sheldrick, *Acta Crystallogr., Sect. A* **2008**, *64*, 112-122.

-
- [243] O. V. Dolomanov, L. J. Bourhis, R. J. Gildea, J. A. K. Howard, H. Puschmann, *J. Appl. Crystallogr.* **2009**, 42, 339-341.

10. Appendix

10.1 Abbreviations

General:

1D	one-dimension
2D	two-dimension
3D	three-dimension
DOS	density of states
DFT	density functional theory
E_F	Fermi level
HOMO	highest occupied molecular orbital
LIBs	Lithium ion batteries
LED	light-emitting diode
LDOS	local density of states
LUMO	lowest unoccupied molecular orbital
min	minute(s)
ML	monolayer
OMBE	organic molecular beam epitaxy
OCV	open-circuit voltage
rt	room temperature
SAM	self-assembled monolayers
vs	versus

Chemicals:

Ac	acetyl group / acetate
Ar	aryl
CuDEPP	[5,15-bis(ethynyl)-10,20-diphenylporphinato]copper(II)
CuTPP	[5,10,15,20-tetraphenylporphinato]copper(II)
CB	carbon black
COF	covalent organic framework
CPDMS	(3-cyanopropyl)dimethylsilyl
CMP	conjugated microporous polymer
DCM	dichloromethane
dba	(1 <i>E</i> ,4 <i>E</i>)-1,5-diphenyl-1,4-pentadien-3-one
dppp	1,3-bis(diphenylphosphino)propane

dppf	1,1'-bis(diphenylphosphino)ferrocene
DMC	dimethyl carbonate
EC	ethylene carbonate
GY	graphyne
GDY	graphdiyne
HEB	hexakis[(trimethylsilyl)ethynyl]benzene
HOPG	highly oriented pyrolytic graphite
LiPF ₆	lithium hexafluorophosphate
Ln	rare earth metal, -ion
Me	methyl
MOF	metal-organic framework
NMP	<i>N</i> -methyl-2-pyrrolidone
Ph	phenyl
PPh ₃	triphenylphosphine
PVDF	poly(vinylidene difluoride)
PC	propylene carbonate
PP ₁₄ TFSI	1-butyl-1-methylpiperidinium bis(trifluoromethylsulfonyl)imide
R	organic group
SPhos	2-dicyclohexylphosphino-2',6'-dimethoxybiphenyl
TBAF	tetrabutylammonium fluoride
THF	tetrahydrofuran
TIPS	triisopropylsilyl
TMEDA	<i>N,N,N',N'</i> -tetramethylethylenediamine
TMS	trimethylsilyl

Measurement:

AFM	atomic force microscopy
ATR	attenuated total reflection
BET	Brunauer-Emmett-Teller theory
CV	cyclic voltammetry
EI	electron ionization
ESI	electrospray ionization
EDX	energy-dispersive X-ray spectroscopy

GC	gas chromatography
HR-TEM	high-resolution transmission electron microscopy
IR	infrared spectrometer
MALDI	matrix-assisted laser desorption/ionization
MS	mass spectrometry
MCBJ	mechanically controllable break junction
NMR	nuclear magnetic resonance
OM	optic microscopy
SEM	scanning electron microscopy
SAED	selected area electron diffraction
STM	scanning tunneling microscopy
STS	scanning tunneling spectroscopy
TEM	transmission electron microscopy
ToF	time-of-flight
TGA-DSC	thermogravimetric differential scanning calorimetry
UV-vis	ultraviolet-visible
UHV	ultra-high vacuum
XRD	X-ray diffraction

10.2 Publications

- [1] **Z. Chen**, S. Klyatskaya, J. I. Urgel, D. Ecija, O. Fuhr, W. Auwaerter, J. V Barth, M. Ruben, *Synthesis, Characterization, Monolayer Assembly and 2D Lanthanide Coordination of a Linear Terphenyl-di(propionitrile) Linker on Ag(111)*. *Beilstein J. Nanotechnol.* **2015**, *6*, 327-335.
- [2] B. Cirera, Y.-Q. Zhang, J. Bjork, S. Klyatskaya, **Z. Chen**, M. Ruben, J. V Barth, F. Klappenberger, *Synthesis of Extended Graphdiyne Wires by Vicinal Surface Templating*. *Nano Lett.* **2014**, *14*, 1891-1897.
- [3] I. J. Olavarria-Contreras, M. L. Perrin, **Z. Chen**, S. Klyatskaya, M. Ruben, H. S. J. Van Der Zant, *C-Au Covalently Bonded Molecular Junctions Using Nonprotected Alkynyl Anchoring Groups*. *J. Am. Chem. Soc.* **2016**, *138*, 8465-8469.
- [4] European Patent: M. Fichtner, P. Gao, **Z. Chen**, Z. Zhao-Karger, M. Ruben, *High Performance Organic Electrodes For Secondary Batteries*. 16000312.5, 08.02.2016.

11. Acknowledgements

First of all, I would like to thank all the people who helped, supported and encouraged me during my doctorate.

I would like to express my sincere gratitude to my supervisor Prof. Dr. Mario Ruben for providing me the opportunity to work in his group. His guidance in the research project, offering many training chances in different areas of knowledge, as well as his personal suggestions help me enormously during my PhD studies. I appreciated all the freedom and opportunities to work independently in his group.

I am very grateful to Dr. Svetlana Klyatskaya for her introduction into chemical syntheses, her continuous research advice, her patience, and efficient counter reading of my publication drafts as well as of the preliminary versions of my PhD thesis.

My heartfelt thanks also go to my colleagues. I would like to thank Yu Li for his cooperation in synthesis of graphdiyne. I would like to thank Senthil Kumar Kuppusamy for teaching me the usage of SEM and AFM. I would like to thank Dr. Yanhua Lan and Dr. Moreno Pinenda for sharing me a lot magnetic knowledge and also help for life and science research. I also greatly thank my current colleagues Dr. Bernhard Schäfer, Nithin Suryadevara, Concepcion del Carmen Molina Jiron de Moreno, Dr. Michal Valášek and Marcin Lindner, my former colleagues Dr. Veronica Gomez Piedrafita, Dr. Ping Du, Dr. Wen Yu, Dr. Schramm Frank, Dr. Ivan Šalitroš, Dr. Cyril Rajnak, Dr. Andrea Magri, Dr. Coral Herranz-Lancho and Amy Jane Hutchison. I kindly thank Andrea Magri for introducing usage of electrochemical measurement and Michal Valášek for the GC-MS measurement.

For proofreading and thesis correction, I would like to thank Dr. Svetlana Klyatskaya, Dr. Moreno Pinenda, Dr. Bernhard Schäfer, Nithin Suryadevara, Ping Gao and Dr. Tao Lin.

I would specially thank Hagen Sparrenberger for the help of chemical ordering, and daily laboratory support. I also thank Sven Stahl for help in the NMR, elemental analysis. Many thanks go to Olaf Fuhr for crystal data collection and refinement.

In our institute INT, I also would like to thank Dr. Jean-François Greisch, Dr. Nicole Rijs for the help of MALDI-ToF; Chaoming Wang, Suresh Kumar Garlapati, Simone Dehm, Dr. Matthias Hettler for the help of SEM problem solution; Dr. Romain Danneau and Dr. Renjun Du for the help of making devices; Dr. Christian Kübel, Dr. Di Wang and Shyam Kumar Chethala Neelakandhan for TEM measurements; Dr. Sergei Lebedkin for the help in Raman measurement.

For the battery work in chapter 6, I am pleased to acknowledge Prof. Dr. Maximilian Fichtner, Dr. Zhirong Zhao-Karger, Ping Gao (performance measurements) at KIT and the

University of Ulm. From Ping and Zhirong, I learned a lot basic knowledge of electrochemistry. They are always patient and kind with me.

For the STM research, many thanks go to Prof. Dr. Johannes Barth, Dr. Florian Klappenberger and Dr. Carlos-Andres Palma at Technical University of Munich who gave me the chance to use UHV-STM and SL-STM. During the learning and measuring time in TUM, Dr. Tao Lin, Dr. Yiqi Zhang, Liding Zhang, Dr. Juan Li and Raphael Hellwig give me valuable help to use STM. Here, I express my heartfelt thanks to them. I am also glad to have the good cooperation with Borja Cirera and Dr. José I. Urgel in the work of chapter 3.1 and 3.3. Thank Jonas Björk in Linköping University for the DFT calculation for 1D graphdiyne wires in chapter 3.1.

For the break junction application in chapter 5, I am glad to have the opportunity to collaborate with Prof. Dr. Herre van der Zant, Ignacio José Olavarria-Contreras (MCBJ measurement) and Mickael L. Perrin (DFT calculation) in Delft University of Technology.

Additionally, I would like to thank my friends Dr. Meng He and Yingzhao Ma in the group of Prof. Dr. Peter Roesky in KIT south campus for help of ATR IR measurement of graphdiyne films. I also would like to thank Dr. Christopher Anson for the help in practice to fulfil the requirement for PhD defense.

I would like to express my gratitude to my friends in Karlsruhe for their great company during my stay in Karlsruhe. And I would like to thank my family and friends in China, they are my import supporters.

I acknowledge the Karlsruhe Nano Micro Facility (KNMF) for provision of access to instruments (such as MALDI-ToF, SEM, AFM, single-crystal XRD) at their laboratories.

Finally, I would like to thanks of the China Scholarship Council for providing the financial support for my four years PhD study.